Development of carbon fibre reinforced carbon-silicon carbide composites for advanced friction brake applications

By

Andrew Leatherbarrow

Doctoral Thesis

Submitted in partial fulfilment of the requirements

for the award of

Doctor of Philosophy of Loughborough University

1st January 2011

Foreword

The industrial aspect of this project is represented by a consortium aforenamed *ReBrake*, which was formed to facilitate the sharing of information, technology and protect the intellectual property rights of the participating companies. Members of the consortium are identified in Table 1.

Table 1. Consortium companies and their representing area in the ReBrake project.

Company Name	Major role in the consortium
Loughborough University	Manufacture process development and understanding of friction
Meggit Aircraft Braking Systems	Aerospace application
AP Racing Ltd	Automotive application
Surface Transforms Plc	Industry scale manufacture development
Federal Mogul Friction Products Ltd	Pad material development
Wichita Ltd	Industrial braking application
Milled Carbon Ltd	Recycled carbon fibres
Airbus UK	CFRP waste supplier
Faiverley Transport	Rail application
Advanced Composites Group	Carbon fibre waste supplier

Abstract

In the present study, different origins of recycled carbon fibre and carbon are evaluated against virgin-based alternatives as cost-effective constituents inside carbon fibre/carbon-silicon carbide (C_f/C-SiC) composites. These include: recycled, end-of-life or reclaimed carbon fibre and pyrolytic carbon (pyC), which are investigated inside these composites for potential friction materials to replace or extend the life of current high-end automotive, industrial and aircraft brake discs.

The literature review begins by investigating the differences and implications of the applications on the requirements of the carbon fibre inside the composite and documents past and current progress made. The constituents that comprise these composites were investigated and the manufacture routes were reported in terms of their advantages and disadvantages. A three-step process was identified as the most cost-effective and promising route to manufacture these new C_f/C-SiC composites with suitably high mechanical properties: 1). Polymer infiltration (PI) and hot pressing (HP) to create a carbon fibre reinforced plastic (CFRP), 2). Pyrolysis to convert the CFRP into a porous C_f/C composite, 3). Liquid silicon infiltration (LSI) to introduce the silicon carbide (SiC) matrix.

Beyond this, the aims, feasibility and current progress of recycling carbon fibres were documented. It was found that current recycling technologies are in their infancy, in both academia and industry, although great commercial potential is recognised. Investigations herein revealed the capability to mechanically recycle carbon fibres from waste carbon fibre pre-pregs and CFRP spars, re-use end-of-life carbon fibre pre-pregs and reclaim carbon fibre from existing CFRP spars using pyrolysis.

Testing and analysis were split into two stages: firstly, how the pre-preg architecture changes during pyrolysis and secondly, the resulting C_f/C-SiC composites: microstructural evolution after LSI; physical, mechanical and micro-mechanical properties; frictional performance.

Pyrolysis of end-of-life pre-pregs revealed no significant difference in comparison to virgin carbon fibre pre-pregs. Instead, any differences were attributed to the: fibre orientation, preform architecture and resin carbon yield. Testing revealed that end-of-life pre-pregs and reclaimed CFRP’s were suitable for pyrolysis and further processing toward C_f/C-SiC composites. In addition, the architecture could be either customised or inherited from the original.

Physical and mechanical property testing revealed that C_f/C-SiC composites incorporating recycled, end-of-life and re-claimed carbon fibre could achieve comparable densities, open porosities and flexural strengths compared to similarly processed virgin C_f/C-SiC composites.

Microstructural examination by optical and electron microscopy revealed that the hierarchy order of the developed microstructure inside these composites by LSI was the same irrespective of the carbon fibre or carbon format. Combined TEM and XRD investigations indicated that the generated SiC and silicon belonged to the same polytypes regardless of the carbon format and that the most likely type was face-centered cubic (FCC) β 3C-SiC and cubic silicon respectively.

Small-scale dyno in a disc-on-pad configuration revealed that a C_f/C-SiC composite comprising end-of-life fibre could achieve the required mechanical strength to perform dyno testing and that the surface topography had a significant influence on the coefficient of friction (COF), COF stability and wear rate.

Acknowledgements

It is difficult to complete a project such as this without failing to acknowledge the contribution of the people who have come into contact with the project. I would firstly like to thank my academic supervisor, Dr. Houzheng Wu for his continued support, patience and guidance throughout this study. His efforts have been boundless in facilitating my development and I will be forever in his debt.

I would like to acknowledge the academic and technical staff in the department of materials at Loughborough University for any assistance I received with the many techniques used in this report. I would also like to acknowledge and thank the consortium members, the sports manufacturer who supplied virgin carbon fibre pre-pregs and the project co-ordinator Sue Panteny for their support and co-operation. Lastly, for their financial backing, I would like to thank the EPSRC and Technology Strategy Board* for making this research possible.

* The Technology Strategy Board is a business-led executive non-departmental public body, established by the government. Its role is to promote and support research into, and development and exploitation of, technology and innovation for the benefit of UK business, in order to increase economic growth and improve the quality of life. It is sponsored by the Department for Business, Innovation and Skills (BIS). For more information please visit www.innovateuk.org.

Table of Contents

List of Abbreviations

C_f	Carbon fibre
C_f/C/C	Carbon fibre reinforced carbon composite
C_f/SiC	Carbon fibre reinforced silicon carbide
C_f/C-SiC	Carbon fibre/Carbon reinforced silicon carbide
CMC	Ceramic matrix composite
CLVI	Chemical liquidised vapour infiltration
CVD	Chemical vapour deposition
CVI	Chemical vapour infiltration
CFRP	Carbon fibre reinforced plastic
CLVI	Chemical liquidised-vapour infiltration
COF	Coefficient of friction, μ
CTE	Coefficient of thermal expansion
Disc	Brake disc rotor
EDaX	Energy dispersive and X-ray (spectroscopy)
FEA	Finite element analysis (computer software)
FEG-SEM	Field emission gun-scanning electron microscope (spectroscopy)
FIB	Focused ion beam (spectroscopy)
FBP	Fluidised bed process
FRP	Fibre-reinforced plastic
I-CVI	Isothermal/Isobaric chemical vapour infiltration
LMC	Laminate matrix composites
LMI	Liquid melt infiltration (similar to LSI and RMI)
MMC	Metal matrix composites
MTS	Methyltrichlorosilane (CH_3SiCl_3)
LMI	Liquid melt infiltration
LP-CVI	Low-pressure chemical vapour infiltration
LSI	Liquid silicon infiltration (similar to LMI and RMI)
OM	Optical microscopy
P-CVI	Pressure/pulsed CVI
PIP	Polymer impregnation and pyrolysis
Pre-preg	Pre-impregnated
PAN	Polyacrylonitrile
PyC	Pyrolysed carbon
RMI	Reactive melt infiltration
Rotor	Brake disc rotor
RTM	Resin transfer moulding (manufacture)
SI	Slurry infiltration
SI-HP	Slurry infiltration and hot pressing
SCF	Supercritical fluids (chemical recycling)
TEM	Transmission electron microscope (spectroscopy)
UD	Uni-directional
XMT	X-ray microtomography

List of Tables

List of Figures

1. Introduction

1.1. Background

C_f/C-SiC and similar C_f/SiC materials were originally developed in the 1970's as lightweight re-entry heat shields for space applications due to their high temperature resistance and low specific weight. However, expensive gas-phase manufacturing techniques limited their application until the late 1980's when several researchers and companies developed alternate cost-effective routes such as liquid phase processing to create cheaper and similarly tailorable ceramic matrix composites (CMC). In the proceeding years, these materials have been developed for a range of low weight and high temperature applications, including friction materials which today, although in modified form, appear on several high performance cars such as the Porsche Carrera GT, Porche 911, Ferrari, Daimler AG and Audi cars [1].

1.1.1. What are brake discs

Brake discs are key components in modern braking systems that function on the principle that a driver actuates the brake and the speed of the vehicle, aircraft or machine is reduced or maintained. The three basic functions of the brake include: 1). Decelerating the vehicle or machine, including stopping; 2). Maintaining speed, including on descents where applicable; 3). Holding a stationary position (where applicable). Braking is achieved by converting the kinetic energy to heat through the friction force generated between the friction materials. Therefore, the performance of a braking system is based on the mechanical and tribological properties of the friction couple. The essential requirements that affect the brake performance are highlighted in Table 2.

Table 2. Essential requirements of a modern braking system.

Requirement	Property (where applicable)
1. Safety: extreme reliability, wear resistance and durability	• High resistance to shear and compressive loads • High wear resistance • Low Coefficient of Thermal Expansion, CTE α ($10^{-6}K^{-1}$) • High thermal conductivity (k) • Sufficiently high maximum operating temperature (including thermal shock resistance) • Non-catastrophic failure mode • Excellent corrosion & oxidation resistance
2. Tribology	• Minimal wear • Sufficiently high COF (μ) • Stable COF (μ)
3. Cost effective: raw materials and feasible manufacturing	• Cost versus performance
4. Recyclability	• Contribute to the adherence of legislation and directives
5. Ease of maintenance	
6. Low weight	

The dominant prerequisites for braking systems are safety and the tribological characteristics. Therefore, the friction couple must be extremely reliable, mechanically compliant and exhibit a sufficiently high and stable coefficient of friction, COF (μ). The frictional stability (S) can be defined as:

$$S = \frac{CoF_{Ave}}{CoF_{\max}} \quad (1)$$

where, CoF_{Ave} is the average COF over the whole braking and CoF_{Max} is the maximum COF recorded. In addition to these essential characteristics, the brake system should be tailored to the application.

1.1.2. Current materials

Brake disc materials are selected according to the application and specific property requirements. Grey cast iron brake discs are common for automotive and industrial applications because they are cheap, easy to manufacture and exhibit balanced tribological characteristics [2]. Conversely, grey cast iron has a high density of 7.2 g/cm^3

and limited corrosion resistance. Furthermore, the mechanical properties, including strength and thermal shock resistance rapidly decrease with increasing temperature [3], thereby restricting its' application to approximately 650ºC [4] depending on the brake pad material e.g. grey cast iron discs against organic pads can withstand up to 800ºC [3].

However, for automotive applications, cast iron discs do not normally fail because of insufficient strength, but due to propagation of thermally induced wear or cracks. This has led to the development of alternate metal alloys with lower strengths and an increased thermal conductivity to improve the thermal shock resistance [5]. For example, aluminium alloys possess high thermal conductivities between 202-285 W/m.K [4] or alternatively grey flake cast iron, which possesses a thermal conductivity between 293–419 W/m.K [6] due to the highly conductive flake graphite in the microstructure [7].

For weight sensitive applications, metal matrix composites (MMC) were developed that possess low densities between 2.8 and 3 g/cm^3 and high thermal conductivities between 200 and 400 W/m.K [8]. For improved wear resistance, particulate-reinforced metal matrix composites (PMMC) based on aluminium and ceramic particles were introduced [9]. However, MMC's and similar PMMC's are limited by their requirement of a compatible brake pad material, maximum application temperature of approximately 400ºC, low recycle fraction and high cost per unit weight [5].

For high performance applications such as Formula 1 racing and aircraft, where the performance requirements outweigh any high cost, carbon fibre reinforced carbon composites (C_f/C/C) are used [4, 10, 11, 12]. Such materials were originally developed for lightweight structures for military and space applications in the 1970's [13]. This class of composite exhibits: highly tailorability, low specific weight between 1.7 and 1.8 g/cm^3, high strength and stiffness in the range of 140 to 170 MPa and 50 GPa respectively [14] and a stable COF of approximately 0.35 [15] at temperatures above 400ºC [4]. Conversely, these materials suffer from low COF and high wear rates below 400ºC [16]. They are also comparatively expensive to manufacture and are prone to oxidation at temperatures above 650ºC [4], especially in high humidity environments [5]. Therefore, C_f/C/C's cannot be considered for long-term applications and have to be replaced frequently, making this class of material an expensive choice.

Non-oxide CMC composites such as C_f/C-SiC are considered to be the next link in the development of advanced high performance friction materials [3, 5, 17-21]. They offer similar mechanical and thermal properties to C_f/C/C materials, except their innate

oxidation resistance is superior due to the SiC matrix [17]. The properties have been widely investigated [22, 23] and include: low specific weight of around 2 g/cm^3, which equates to a significant weight savings compared to conventional automotive brake systems [14]; excellent mechanical properties including: a typical tensile and flexural strength of 120 and 280 MPa respectively, where the flexural strength varies considerably between 50 and 500 MPa depending on the architecture, constituent volume fraction and manufacture process; modest fracture toughness (K_{1C}) of around 6 MPa.m$^{1/2}$ [24]; high potential thermal conductivity between 14 and 70 W/m.K depending on the fibre orientation [14, 25]; low sensibility to the surroundings and oxidation [26], low CTE of -1 to 7 x10^{-6}.K^{-1} [17]; high thermal stability of up to 1400ºC [3]; excellent potential tribological properties [3, 17, 27] and adequate stability of braking against fade versus braking number and surface temperature [5].

1.2. Challenges facing C_f/C-SiC composites

1.2.1.1. Reducing the cost of the raw materials

Carbon fibre is the most expensive constituent in the composite and varies according to the grade, but typically costs between £6,000-7,000 per tonne for a virgin industrial grade [28]. Factors affecting the grade include: modulus and tensile strength, fibre length, number of tows/filaments e.g. 3,000 filaments, preform dimension e.g. unidirectional or woven and pre-treatment e.g. thermal. Incorporating a recycled, end-of-life or reclaimed carbon fibre will therefore significantly reduce the raw material cost of the composite whilst theoretically maintaining their properties.

1.2.1.2. Reducing the manufacturing costs

The most common and established method of manufacturing C_f/C-SiC composites is via the deposition of gaseous precursors into a porous carbon fibre preform by chemical vapour infiltration (CVI) [29, 30]. This gas-phase route creates high purity, well controlled and highly tailorable CMC's. However, due to the slow deposition rate and typical requirement of multiple impregnations, traditional CVI is very expensive [22, 31, 32]. Therefore, many derivatives of CVI have been developed to help alleviate these inherent weaknesses, including: Isothermal/isobaric CVI (I-CVI), temperature gradient CVI (TG-CVI) and forced CVI (F-CVI).

Meanwhile, alternate liquid phase routes: polymer infiltration and pyrolysis (PIP), liquid silicon infiltration (LSI) [33-35]; ceramic [31] and hot pressing (HP) [36] routes have also been developed to facilitate cost-effective processing. In addition, combinations of HP, PIP and LSI have been envisaged to create rapid and cost-effective C_f/C-SiC composites [20]. Therefore, incorporating: recycled, end-of-life or reclaimed carbon fibre should compound this cost saving and further reduce the overall cost of the C_f/C-SiC composite, which is one of the focuses of this research.

1.2.1.3. Development of a suitable automotive friction pad for a CMC disc

The friction pad constitutes as the sacrificial partner in the automotive disc-on-pad friction couple. Currently, there are very few publications in this field due to the perceived problems associated with gathering information, namely: the heterogeneity of the pad, repeatability of the experiment and the complex mechanical and chemical interactions at the disc-pad interface. In terms of tribology and heat generation, a C_f/C-SiC-on-pad friction couple functions in a completely unique manner compared to a classical 'grey cast iron-on-pad' friction couple.

In order to withstand the high temperatures generated by high performance automotive or alternative industrial applications, typically up to 600ºC for traditional materials [37] and up to 1000ºC for CMC friction couples, similar non-oxide CMC or MMC pads have to be used, which typically result in unstable COF values and inadequate wear rates. This problem was addressed by modifying the surface of the disc with a compatible coating. For example, a SiC-based coating for SiC matrices such as proposed and tested by Krenkel *et al* [3]. These early findings highlighted the necessity for continued research, but also the potential for such C_f/C-SiC composites to be the next major link in advanced friction brake materials.

1.2.1.4. Improving the coefficient of friction stability

The initial stage of braking is commonly referred to as the 'bedding-in' stage, which is typically characterised as the gradual increase or decrease of the COF, followed by a steady state COF. The development of which is widely attributed to the development and maintenance of a friction layer in-between the friction materials at the contact junction.

However, existing research [5, 17, 20, 22] and associated consortium companies have recognised an unstable COF trend that C_f/SiC and similar C_f/C-SiC composites generate. This is noted as being particularly relevant for aircraft disc-on-disc brake applications that are under significantly higher stresses for prolonged durations in comparison to automotive conditions. Instead of a gradual incline and steady state COF curve, such materials generate a high initial COF of around 0.35, which decreases to an unacceptably low 0.12 for a period of seconds before rising to a higher COF of approximately 0.45 toward the end of braking. If this class of composite is to truly replace or extend the life of existing material solutions based on carbonaceous matrices, a more stable COF must be achieved.

1.2.2. The need to recycle

Strict recycling legislation and directives [38], rising landfill taxes, high raw costs and increasing usage of carbon fibre [39] with additional associated off-cut waste has made it a necessity rather than a desire for companies to recycle the carbon fibre materials they manufacture. Today, these issues are particularly relevant in the wake of international environmental talks and a global recession, which encourage cost-saving opportunities such as recycling and re-use.

Therefore, in this research: a feasible recycling process will be identified and carbon fibre will be recycled, recovered from end-of-life carbon fibre pre-pregs and reclaimed from existing CFRP's. The fibre will be used to manufacture unique C_f/C-SiC composites that will be validated in terms of their final properties so they can be considered as viable additional options for automotive brake discs, industrial friction plates and aerospace brake discs.

1.3. Aims and objectives

The overall objective of this investigation is to develop and evaluate the feasibility of C_f/C-SiC composites comprising: recycled, end-of-life or reclaimed carbon fibre, including any carbonaceous interfaces for automotive, industrial and aeronautical friction brake applications. Considering the broad and complex undertaking of this project, the feedback methodology highlighted in Fig. 1 will be used to achieve a laboratory scale C_f/C-SiC composite.

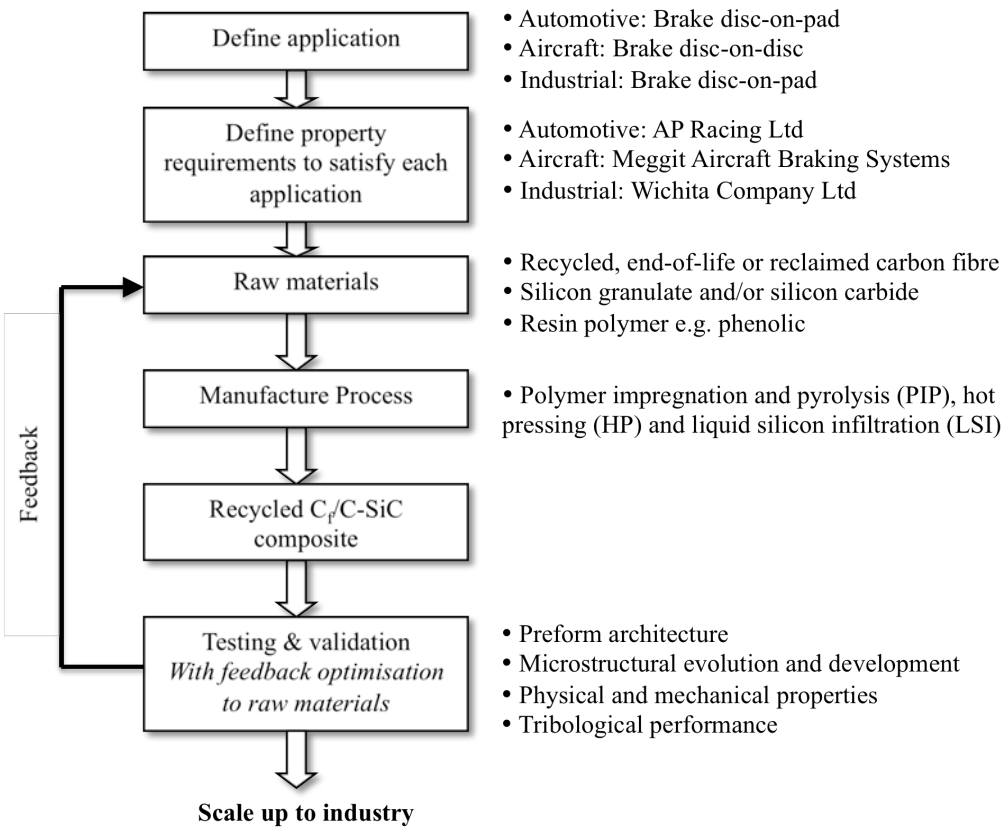

Fig. 1. Flow chart describing the methodology for producing a successful laboratory scale recycled C_f/C-SiC composite.

The first aim was to define the requirements of the applications and research the progress made in these areas according to academic and industry sources. The next step was to identify a recycle stream for the carbon fibre, which was satisfied by the consortium. Three categories of carbon fibre were supplied: recycled, end-of-life and reclaimed, in addition to alternate carbon sources: CVI-Carbon and graphite, which are described in *Section 3.1*.

The next step involved identifying a suitable manufacturing route that would be cost-effective and suitable for producing the composites. The inclusion of the new origins of carbon fibre could then be evaluated by investigating: the impact of pyrolysis on the preform architecture; evolution and development of the microstructure during and after processing; resulting physical and mechanical properties, and tribological characteristics. The techniques and equipment highlighted in Table 3 will be utilised in this study.

Table 3. Proposed analysis and corresponding equipment.

Analysis	Equipment
Surface microstructure	OM, FEG-SEM, FIB and TEM
Phase identification	TEM and XRD
Mechanical properties of phases	Nano indentation
Bulk density and open porosity	Archimedes method
Bend strength	Four-point bend test
Friction performance	Small-scale dynamometer

2. Literature Review

The literature review is split into four sections, where it is the intention of *Section 2.1* to identify the material requirements according to the applications that were outlined by the ReBrake consortium members. *Section 2.2* focuses on understanding the constituents inside C_f/C-SiC composites and how they could satisfy the outlined requirements. *Section 2.3* meanwhile investigates the different manufacture routes used to create these composites, while *Section 2.4* identifies progress made by industry and academia in the field of carbon fibre recycling.

2.1. Material applications and requirements

C_f/SiC and similar C_f/C-SiC composites were originally developed for friction applications in early 1990's and have since been explored as commercial friction materials for high performance vehicle applications, as replacement materials for traditional cast-iron brake discs for automotive vehicles, C_f/C/C brake discs for Formula 1 racing and C_f/C/C friction packs for aircraft braking systems [4].

In the proceeding sections, the material applications have been introduced, which include automotive brake discs, industrial clutch plates and aircraft brake discs. The requirements for a potential replacement C_f/C-SiC material have been identified and discussed. Beyond this, past and present material solutions were reviewed.

2.1.1. Automotive brakes

The two most common types of disc brake systems are 'floating' and 'fixed' as shown in Fig. 2 [40]. The driver pushes down on the brake pedal, which activates a master cylinder and forces the brake fluid through a series of metal brake lines applying pressure at each piston. The brake lines are known to be susceptible to heat radiation from the brake disc during service, therefore considering CMC discs reach much higher temperatures, it is important to minimise any heat radiation or shield the brake lines from any potential thermal damage. The housing of the 'fixed calliper' is fixed, therefore friction pads on both sides of the calliper housing independently grip the disc rotor.

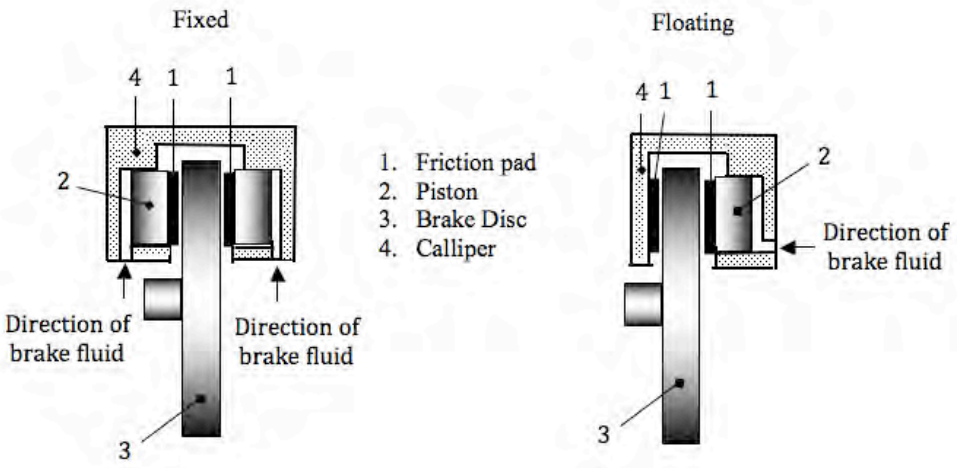

Fig. 2. Sectioned side view of a 'fixed' and 'floating' brake disc configuration [40].

Alternatively, the 'floating calliper' employs a single moving piston and friction pad on one side of the housing, which forces the disc against the fixed friction pad on the other side. The clamping force is typically generated through hydraulic power, although air power is common in some applications and forces the disc rotor, which is attached to the wheel to decelerate or stop the vehicle.

There are also different types of brake actuation, which have a profound effect on the disc during service. The most influential being the advent and implementation of anti-lock braking systems (ABS), which is as a closed loop safety feature. When activated, the brakes pulse on and off to prevent the wheels locking-up during harsh or emergency braking. This rapid engaging and disengaging of the brake pads on the disc reduces the contact time, thus greatly reducing any build up of heat and thermal stress, although exposes the disc to the oxygen in the surrounding atmosphere.

Discs are commonly ventilated to encourage airflow through the disc, which reduces the temperature induced by friction. Ventilation spacing typically varies between 6 and 9 mm. However, high performance cars such as the Porsche Carrera have additional air space (15.6 mm) to aid cooling [7]. In addition, strategically placed holes assist cooling by allowing air to pass through the disc and also help reduce the weight. Today, some of the largest production automotive discs are on Bentley cars, which vary in size up to and beyond 400 mm [41], whilst one of the heaviest reported cast iron disc is the Mercedes S-Class disc at 10.55 Kg [7].

2.1.1.1. Material requirements

The material requirements are based on the service application. Due to the significantly higher cost of CMC materials, only high performance brake discs for road and race car applications are considered, such as those supplied by AP Racing Ltd. Table 4 highlights the specific automotive requirements for a replacement C_f/C-SiC brake disc in comparison to traditional grey cast iron or C_f/C/C materials.

Table 4. Specific automotive brake disc property requirements.

Property	Automotive property requirements
Coefficient of friction, COF (μ)	• Brake disc material must provide an adequate and stable friction couple with the brake pad material in both wet and dry conditions e.g. COF of 0.3 to 0.4
Thermo mechanical	• Must be resistant to thermal shock. • Capable of operating at high surface temperatures e.g. 900 ºC including higher spike temperatures without oxidation.
Wear	• Disc wear rate is required to last for the vehicle life e.g. up to 200,000 km.
Durability	• Required to be capable of operation for the full vehicle life e.g. the assembly should be capable of withstanding corrosion influences, wet weather conditions and heat cycling. • Must be mechanically compliant and resist failure during braking life.
Manufacture	• Needs to be capable of being machined to circumferential parallelism
Cost	• Material needs to be economically machined in the shortest possible duration without high machine tool wear.
Physical	• Disc assembly weight and cost needs to be optimised.

2.1.1.2. Recycling and legislative requirements

The automotive end-of-life vehicle directive [38] states that at least 80-weight percent (wt. %) total vehicle waste must be reused or recycled with an additional 5 wt. % recovered. The European Union target for the year 2015 is 85 wt. % reuse, with a total of 95 wt. % reuse and recovery. Such legislation applies increasing pressure on manufacturers to make more and more of the vehicle recyclable.

2.1.1.3. Metal brakes

Cast iron brake discs such as grey cast iron have been, by far, the most popular materials used to date. This is because they possess satisfactorily high properties and are comparatively cheap. Such discs typically contain 95 wt.% iron, 1-3 wt.% silicon and 2-4 wt.% carbon. Additions of carbon act as hardening agent, which prevent dislocations in the iron atom crystal lattice from sliding past one another. Therefore, high performance discs generally contain a higher carbon wt. %, although most are in the medium carbon content range from 3.3 to 3.5% [7]. Other common alloying elements include: chromium ≤ 0.1%, copper ≤ 0.25%, molybdenum ≤ 0.1%, nickel ≤ 0.1%, tin ≤ 0.1% and titanium [7], which are added based on the application to further tailor the properties. However, irrespective of the additional elements added, the potential of cast iron brake discs for high performance applications is limited due to their innate high weight and low temperature capability.

2.1.1.4. Metal matrix composites

Virtually all European and several American automotive manufacturers have evaluated MMC brake discs including: BMW, Daimler AG, Renault, Peugeot, Ford and General Motors. Emphasis was being placed on particulate-reinforced metal-matrix composites (PMMC) because they were cheaper. Blau *et al* [42] validated an Al-based MMC brake disc in contact with a MOPAR^{TM} brake pad material in a simulated truck test at 60 mph. The friction couple performed favourably with an average COF of 0.21 and a low temperature rise of 46.2ºC over 30 seconds due to high internal thermal conductivity. However, MMC discs are limited by their high temperature capability of approximately 400ºC, which can exceed as spike temperatures in performance automotive applications.

2.1.1.5. Carbon fibre reinforced carbon composites

Carbon fibre reinforced carbon composite (C_f/C/C) brake discs have been used successfully for more than 30 years [4]. However, due to their high cost, unstable COF in humid conditions and at temperatures below 450ºC [4, 16], high pad wear rate and risk of oxidation at temperatures above 650ºC, such materials are only used for weight sensitive and high performance applications. C_f/C/C brake discs replaced metal brakes for Formula

1 applications because of their superior thermal, mechanical and physical properties in the early 1980's [43]. They are replaced frequently so long-term implications are avoided and the temperature can be maintained between 400 and 600ºC during service [44]. Furthermore, in this temperature range, oxidation is avoided and the COF remains relatively stable between 0.5 and 0.6, depending on the microstructure [4].

The cost and properties of C_f/C/C's are highly variable and depend on the preform dimension and microstructure, where cost-effective processing has been realised [11]. Gomes *et al* [45] investigated the tribological properties of a 2D-C_f/C/C disc using the pin-on-disc method. A stable and high COF of ~0.82 was exhibited between 300 and 600ºC depending on the sliding speed. However, the disc wear rate increased exponentially with increasing sliding speed, which was explained by the pins being applied perpendicular to the fibre orientation of the 2D rotating disc. This investigation confirmed the sensitivity of the preform dimension on the friction of brake discs with carbon fibres.

Today, companies such as Hitco Carbon Composites, Inc. [46], Messier-Bugatti Safran Group [47] and The German Aerospace Centre (DLR) [48] manufacture C_f/C/C discs for the automotive industry. Hitco Carbon Composites is a provider of aero-structures and material solutions for a variety of industries and currently develop and manufacture rocket nozzles, advanced composites for the defence industry, C_f/C/C brakes for military, civil and high performance race cars. The Messier-Bugatti Safran Group meanwhile, is predominantly an aircraft brake disc manufacturer, although still produce a limited number of C_f/C/C brake disc for the high performance automotive industry.

2.1.1.6. Ceramic matrix composites

Traditional two-dimensional (2D) C_f/C-SiC friction materials began competing with C_f/C/C's in high performance race applications in the 1990's [4]. Such materials were considered superior due to their enhanced thermal properties and innate oxidation resistance of the SiC matrix. However, their relatively poor frictional stability that ranged between 0.2 and 1 limited their application range [4]. Early standard 2D C_f/C-SiC composites investigated by Krenkel *et al* [5] with a fibre orientation parallel to the friction surface were paired with pads of a similar material because no other material could withstand the elevated temperatures of more than 1000ºC. The friction couple exhibited very low wear rates, a high and unstable COF that was attributed to the low transverse thermal conductivity and were also very expensive. It was not until the year 2000, when

the brake discs were optimised to exhibit a more stable COF in a special edition Mercedes S-class coupe and Porsche 911 Turbo [49], making this class of material the most promising to date.

Today's leading manufacturers and research institutions of non-oxide CMC composites for automotive applications include: Surface Transforms Plc [50], SGL Carbon [51], DLR [52], Schunk [53], SNECMA and MAN. Surface Transforms developed a combined CVI and reactive melt infiltration (RMI) fabrication process to produce C_f/C-SiC composites from a 2.5D bi-directional needled carbon fibre felt perform. The final composite has a carbon fibre volume fraction of around 22-25% and are machined to final tolerance. Unfortunately, the microstructural and tribological properties of such discs are currently confidential.

Meanwhile, SGL Carbon manufactures C_f/SiC automotive brake discs [14] using their oxidised poly-acrylic-nitrile (PAN) fibre called Panox™ [54], which is designed for processing into yarns, woven fabrics, non-woven materials and felts. C_f/SiC materials are produced under their trademark name Sigrasic™ and are manufactured by: mixing the fibre, additives and resin together; defining the shape compression; carbonisation to convert the resin into pyrolytic carbon (PyC); siliconisation in introduce the SiC matrix. Three grades are available, each with a different microstructure as described in Table 5.

Table 5. SGL Carbon material constituent percentage (%) [54].

SGL Carbon material properties		1500-J	6010-GNJ	3001-GSJ
Composition	SiC	35	60	50
	Silicon	17	10	35
	Carbon *	46	30	15
	Open porosity	2	0	0

*** Note:** The carbon value is assumed to be carbon fibre and any other regions of carbon and graphite.

Therefore, the composition of the discs were either fibre dominated or matrix dominated, or a mixture thereof in the case of 6010-GNJ, which are reflected in the properties in Table 6.

Table 6. Material properties of C_f/SiC composite from SGL Carbon [54].

			Fibre dominated ⟷ Matrix dominated		
SGL Carbon material properties		**Unit**	**1500-J**	**6010-GNJ**	**3001-GSJ**
Density		g/cm^3	2	2.4	2.7
Open porosity		%	2	<1	~0
Flexural Strength (3-point)		MPa	190	50-95	130-150
Compressive Strength (3-point)		MPa	470	250	1300
Fracture toughness (K_{1C})		$MPa.m^{1/2}$	-	-	5
Maximum temperature application		ºC	1350	1350	1350
Coefficient of thermal expansion ($x10^{-6}/k$)	at 25	ºC	-0.3	1.8	3.5
	at 200-1200		0-1.36	3	4.5
Thermal conductivity, k	at 20ºC	(W/m.K)	23	40	125
	at 1200ºC		20	20	80

The effect of the fibre or matrix dominated composition is highlighted in the mechanical and thermal properties. All three variations possessed a high maximum application temperature of 1350ºC, high thermal stability and low CTE, however, with increasing carbon fibre volume fraction from 15 to 46%, the density reduced from 2.7 to 2 g/cm^3 and the CTE improved from 4.5 to about 1.36 $x10^{-6}/K$ (between 200-1200ºC).

Conversely, as a consequence to the increase in carbon fibre, there is a significant reduction in the thermal conductivity, from 125 to 23 W/m.K (at 20ºC) and 80 to 20 W/m.k (at 1200ºC), most likely due to the reduction of silicon that possesses a superior thermal conductivity in comparison to the carbon fibre. 3001-GSJ claims to exhibit a compressive strength of 1300 MPa, although this value is most likely an anomaly due to the high matrix and low carbon fibre volume fraction. SGL [54] declared that the carbon fibre dominated structure: 1500-J is most suitable for self-supporting structures, high damage tolerant and high thermal shock resistant applications. The mixed microstructure: 6010-GNJ is similarly suited for high damage tolerant and high thermal shock resistant applications, whilst the matrix dominated: 3001-GSJ is aimed for oxidation resistant and low wear rate applications.

However, from Table 6 it is clear that a balance of all these properties is required for a successful brake disc, which is not represented in any one material from SGL and should be considered herein. The tribology and wear characteristics of SGL's discs is currently unavailable apart from Sigrasic 6010-GNJ which is known to exhibit a COF between 0.3 and 0.7 depending on pad material [54]. Such materials are discussed in more

detail later, including SiCralee™ coated (SiSiC) C_f/C-SiC brake materials from DLR, which been successfully equipped in the Porche 911, Ferrari, Daimler AG, and Audi A8 cars [17]. Fig. 3 meanwhile illustrates typical COF curves of different C_f/C-SiC disc-and-pad friction couples, reported by Krenkel *et al* [5].

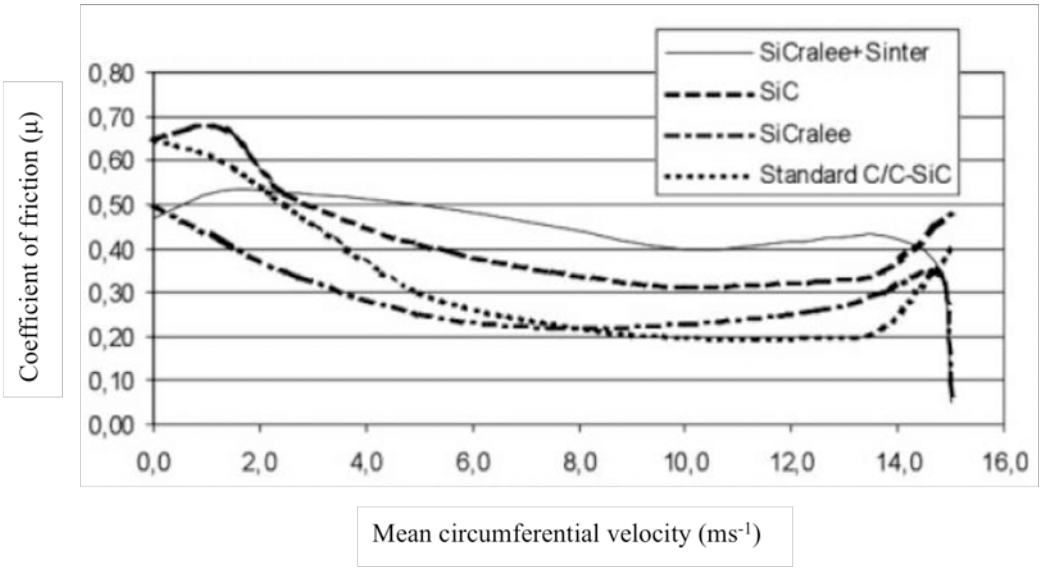

Fig. 3. Dynamometer results of different disc materials at 145 KJ with pads of identical materials except for SiCralee + sintered, illustrating how the COF (μ) varies as the mean circumferential velocity slows down (right to left) [5].

When the disc and pad material are the same, the COF was not sufficiently stable. The COF began relatively high at 15 ms^{-1} (right side), dropped to a steady state before gradually increasing to a maximum as the speed reduced towards zero. The SiCralee™ coated C_f/C-SiC disc and a sintered metallic pad exhibited a favourable COF between 0.4 and 0.55, with a far more stable COF stability. Addition of the SiCralee™ (SiSiC) surface coating was speculated to have improved the COF and COF stability by favourably modifying the surface temperatures due to the additional highly conductive silicon. Unfortunately, the composition of the sintered metallic pad is commercially unknown.

The investigation was extended to test the fade characteristics of the SiCralee™ coated C_f/C-SiC disc and sintered metallic pad [5]. The fading test investigated the COF and temperature during 21 repeated stops. The COF decreased from ~0.48 to ~0.45 after the initial stop, which lowered to ~0.38 and remained stable during the final stop. The temperature meanwhile increased from ~100 to ~200ºC after the first stop and increased

from ~450 to ~650ºC after the 21st stop. Therefore, when a suitable friction pad material and appropriate surface coating are selected; C_f/C-SiC composite brake discs can exhibit sufficiently high and stable COF, suitable for automotive applications.

In the same investigation, the wear rate was similarly investigated. The results are illustrated in Fig. 4, which shows no clear superior friction couple.

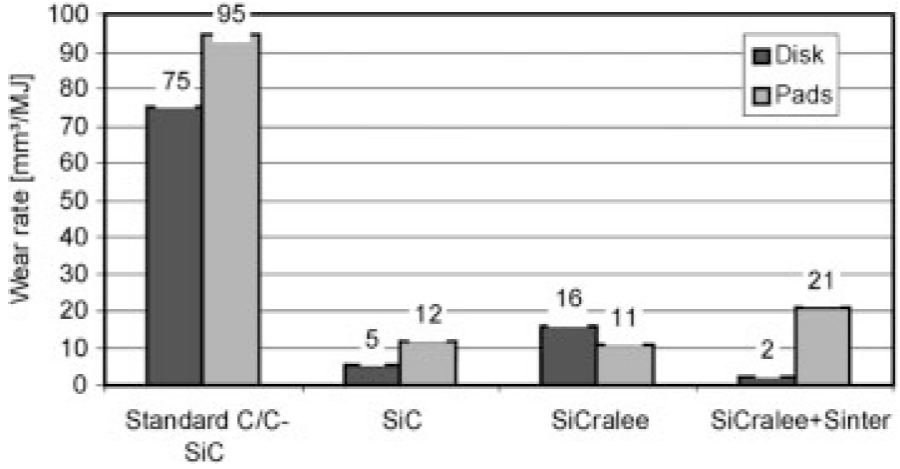

Fig. 4. Wear rates of different ceramic friction pairings at high-energy braking (pads and disks of identical materials, except for the combination SiCralee and sintered metallic pads) [5].

In comparison to the uncoated C_f/C-SiC friction couple, both the CVD-SiC and SiCralee™ coated C_f/C-SiC disc and pad friction couples exhibited significantly lower wear rates. The SiCralee™ coated C_f/C-SiC disc and pad did not reach the low wear rates that a CVD-SiC coating achieved, but was reported to be easier to tailor and cheaper to apply than the CVD-SiC coating. However, when the pad material was changed to a sintered metallic pad, the wear rate of the disc reduced significantly to just 2 mm^3/MJ. Unfortunately, the wear rate of the pad was almost twice that of the SiCralee™ or CVD-SiC coated C_f/C-SiC pads [5].

By comparison, Stadler *et al* [16] reviewed the tribological performance of a C_f/C-SiC disc, fabricated by liquid silicon infiltration with a reaction bonded ~300 µm SiC outer layer in contact with MMC sintered metallic pad using a dynamometer. The formulation of the pad was reported to contain different base metal powders: iron, copper, copper alloys or a mixture of these and frictional additives such as abrasives and solid lubricants.

The C_f/C-SiC disc against a MMC pad without graphite or SiC exhibited a COF of 0.55 and comparatively low wear rate of $9.3x10^{-6}$ m^3/MJ. When graphite was added to the pad, the mean COF marginally increased. It was assumed that the graphite acted as a lubricant and reduced the hardness of the material. Consequently, this caused an increase in the COF due to a speculated increase in contact surface area. By contrast, additions of SiC abrasives were speculated to have suppressed the displacement of the metallic phases, which limited any sintering of the upper matrix so it less dense. Consequently, the friction layer was thinner and not continuous, which reduced the COF and significantly increased the wear.

Meanwhile, it was recognised by Wu & Wang [55] that the tribological characteristics C_f/C-SiC composites were governed by mechanisms down to the nano-scale, which in turn are affected by the properties of the phases at this scale, in particular the fracture toughness. The most preferential phase was highlighted as silicon and to a lesser extent, the SiC regions, which exhibited a steady state relationship with the matrix and good longevity. By contrast, any carbonaceous regions such as C_f/PyC and general SiC regions were detrimental to the friction performance.

This is particularly interesting because it is SiC and not silicon that is by convention the most desired phase for friction applications due to its' higher 'bulk' fracture toughness and hardness, which should improve the wear resistance. This is investigated further in *Section 4.5*.

2.1.2. Industrial brakes

Braking systems within industry vary considerably depending on the scale and type of industry, making development of an industrial material 'niche'. Wichita Ltd represent the industrial link within the ReBrake project and want to improve the tribological characteristics of a clutch brake system, comprising a large reel, which is illustrated in Fig. 5.

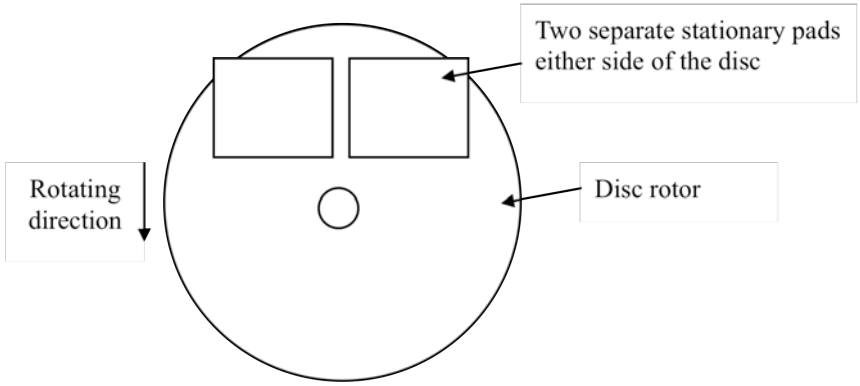

Fig. 5. Schematic of the clutch braking system at Wichita Ltd.

The friction couple currently consists of a grey cast iron brake rotor and organic friction pad, which apart from the scale and application is similar to that of an automotive braking friction couple. The mechanism is a calliper type brake system, which is designed to provide continuous slip and therefore stable COF for unwinding paper or corrugated cardboard. Depending on reel diameter and required linear pull off speed, the disc rotors vary from 250 up to 450 mm in diameter and operate at speeds from 50 to 2500 rpm for 20 to 40 minutes. Aside from significantly reduced weight, a C_f/C-SiC replacement disc could dramatically increase the life of the friction couple and achieve a COF of around 0.3.

2.1.2.1. Material requirements

The niche requirements for a C_f/C-SiC friction material for the large reel and clutch braking system are highlighted in Table 7. The main challenges facing a potential C_f/C-SiC material will be achievement of a stable COF between 0.7 and 0.8 whilst not excessively wearing the pads.

2.1.2.2. Material solutions

Grey cast iron or ductile cast iron for a high-speed option is currently used, primarily because it is cheap and delivers reasonable tribological performance. Typical properties include: tensile strength of 250 MPa, density of 7.2 g/cm^3, specific heat capacity of 500 J/Kg.K, thermal conductivity of around 47 W/m.K and CTE of 12 x10^{-6}/K. Currently, there is no commercially available information or test data regarding MMC's, C_f/C/C's or non-oxide CMC's for this type of continuous slip application.

However, it is envisaged that a C_f/C-SiC brake disc friction couple comprising the recovered carbon fibre can achieve the requirements highlighted in Table 7.

Table 7. Property and specific requirements for an improved friction couple.

Property	Specific industrial property requirements
Coefficient of friction, COF (μ)	• Stable COF of 0.7-0.8. • Brake disc material must provide a stable friction couple with the brake pad material. • Cold to hot coefficient change minimised to within 5%. • To increase the current COF without introducing any squeal/vibration.
Thermo mechanical	• Temperature capabilities are required to be greatly in excess of current.
Wear	• There should be no additional wear of the pad e.g. above 250 °C for organic based pads.
Physical	• Physical properties should be equal or superior to standard grey cast iron and organic pads.
Mechanical	• Strength should be comparable to existing grey cast iron.

2.1.3. Aircraft brakes

Aircraft brakes comprise of multiple brake disc rotors sandwiched between stators commonly made from C_f/C/C discs and/or metallic friction rings, as shown in Fig. 6 [56]. The discs are hydraulically squeezed together in a disc-on-disc configuration to generate enough friction force to stop the aeroplane. The rotating discs are driven by the wheel, while the torque tube restrains the stationary discs.

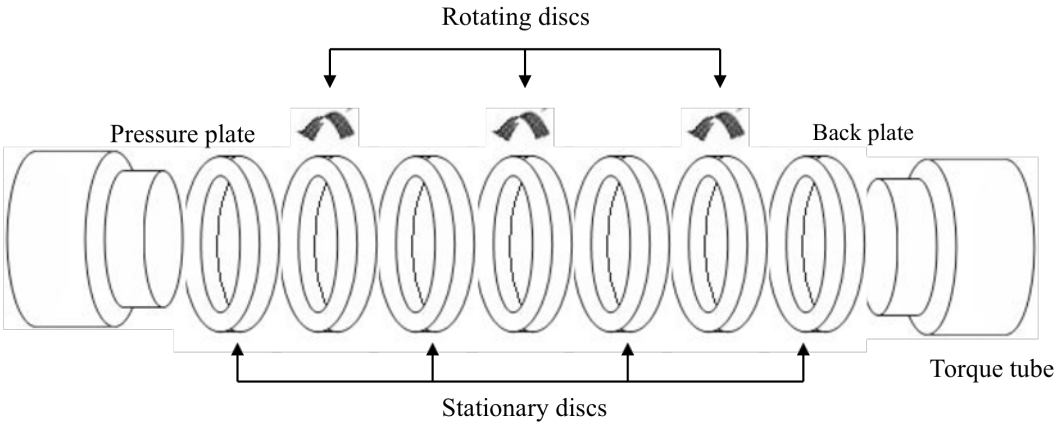

Fig. 6. Schematic exploded view of an aircraft brake disc pack.

2.1.3.1. Material requirements

Due to the required very high safety factors, the property requirements for a potential replacement C_f/C-SiC disc are numerous and vary considerably based on the size of the aircraft and dimensional constraints imposed by the wheel and brake design. Notable properties include: density of 2.10 g/cm^3 ±0.1, flexural strength greater than 100 MPa, wear rate of no more than 0.001016 mm/s/c (millimetre per second per cycle) and a service COF around 0.4. Prior research by MABS into this material highlighted areas of concern in the 'landing stop' frictional performance and brake dynamics, in particular the COF stability.

2.1.3.2. Recycling and legislative requirements

Aircraft composite recycling is increasingly important owing to the greater usage of these materials in the commercial aerospace industry. The impact of not recycling off-cuts pre-pregs and land filling end-of-life products constitutes as a significant potential cost saving. In addition, recycling and anti-landfill legislation is also applying pressure on the major aircraft manufactures and suppliers to adopt only composite materials that comply. Directives include: Council Directive, 1999/31/EC on landfill waste, Council Directive, 2000/76/EC on incineration of waste, Waste framework directive, 75/442/EEC, List of waste, (LoW) 94/3/EG, Hazardous waste directive, 91/689/EEC, Harmonisation of waste reduction programmes directive, 92/112/EEC, Shipment of waste directive, 120/97/EC, Municipal waste incineration directive, 89/369/EEC and 89/429/EEC and Harmonisation list of waste, com.dec.2000/532/EC, where 'B787 materials design' is based substantially on carbon fibres in an epoxy resin matrix for the fuselage and composite wings [57].

The airframe end of life sector is currently relatively obscure but is set to change according to a number of factors. These include: an increase in activity of airframe manufacturers in the self-regulation of disposal, increased awareness of product stewardship and associated part control issues by original equipment manufacturers (OEM) [57].

2.1.3.3. Carbon fibre reinforced carbon composites

Metal brake discs are not commonly used for large aircraft applications because of their high weight, poor performance at elevated temperatures and inadequate corrosion resistance [17]. Therefore, composites such as C_f/C/C's are used. First developments in C_f/C/C's for aircraft were by B.F. Goodrich, which were later licensed by Dunlop. Starting in the early 1970's with Concorde, Airbus and Boeing, most planes today including military aircraft now use C_f/C/C brakes due to their weight saving potential [58]; for example, a 900 Kg weight-saving on the Boeing 747-400 and high performance at elevated temperatures up to 2000ºC [4, 59].

Manufacturers of C_f/C/C brake discs for aircraft include: SGL Carbon, MABS and Messier-Bugatti. As well as producing brake discs for the automotive industry, SGL Carbon also fabricate aircraft C_f/C/C brake discs using their Panox™ precursor carbon fibre [60]. MABS manufacture a 2D stacked C_f/C/C either bi-directionally (0/90º) or with an offset fibre orientation of 10° for each layer. Densification of self-supporting preforms is achieved via CVI in large batches. Processing varies depending on the desired mechanical and physical properties e.g. density, finish required and quantity. An outer coating is applied for protection and also to modify the tribological performance. Details of the coating are confidential at this time.

Messier-Bugatti first introduced carbon brakes on the 'Airbus A310' in 1986 and today they offer their 3rd generation products: SepCarb®III and the SepCarb® III-OR (OR for Oxidation Resistant) to both civil and military programmes in the USA, including Boeing and Airbus. SepCarb® III-OR is fitted on all the Airbus A319s and A320s and on the 'C-17 Globemaster III's' [61]. Messier-Bugatti's '777LR SepCarb® III-OR' brake discs are claimed to be 15 Kg lighter than competitor C_f/C/C discs, which represents total weight savings of around 180 Kg per plane [62]. Messier-Bugatti is in the post development of a new antioxidant treatment, which hopes to deliver improved overall performance [61]. Meanwhile, SGL Carbon manufactures C_f/C/C brake materials on a number of military and commercial aircraft. However, no specific data is known regarding their discs.

2.1.3.3.1. Ceramic matrix composites

C_f/C-SiC and similar C_f/SiC composites are considered to be the next generation of high performance friction materials for aircraft applications [56, 63, 64]. Today, manufacturers include: MAN Technologie AG, SNECMA Group and Surface Transforms Plc. MAN Technologie AG manufactures C_f/SiC and SiC/SiC composites via Temperature gradient/pressure chemical vapour infiltration (TG/P-CVI) for the high performance space industries. SNECMA meanwhile is one of the world's leading aerospace companies that manufacture CMC's via I-CVI and also produce C_f/SiC and SiC/SiC composites. Surface Transforms Plc fabricate C_f/C-SiC brake discs for aircraft using a similar manufacture route as their C_f/C-SiC automotive brake discs, which implements a combination of CVI and LSI on a 2.5D bi-directional needled felt perform.

Table 8 shows the properties achieved by three research groups that have investigated C_f/SiC and similar C_f/C-SiC materials for friction applications. Fabrication by CVI notably creates CMC's with higher densities and superior flexural strengths, although are typically more expensive due to the extended manufacture times.

Table 8. Property summary for a C_f/SiC brake disc used in a disc-on-disc configuration.

Property		Research group		
		Zhang *et al* [22]	Fan *et al* [19]	Krenkel *et al* [14]
Reference		D	-	Silica XB
Preform dimension		3D	3D	3D woven
Fibre architecture		T300 3K 0º/90º	T300 12K 0º/90º	0º/90º
Interface coating		0.2µm pyC	None	None
Manufacture route		CVI	CVI & LSI	LSI
Constituents (%)	Carbon fibre	65	65	68
	SiC	35	27	30
	Silicon	-	8	2
Porosity (%)		4.4	5	3.5
Density (g/cm^3)		2.1	2.1	1.9
Flexural Strength (MPa) *		-	97 ⊥ 165 ∥	160
Average COF (µ)	Static	0.41	0.41	-
	Dynamic	0.34	0.34	-
Linear wear rate (µm/side/cycle)		1.9	1.9	-

Note: * directionally dependent, where ⊥ = perpendicular and ∥ = parallel

Optical micrographs in Fig. 7 illustrate the typical microstructure of a 3D C_f/SiC fabricated by a combination of CVI and LSI [19]. The microstructure consists of bi-

directional fibre architecture with dense C_f/C bundles consisting of tightly packed carbon fibres measuring approximately 7 µm in diameter. SiC is present in-between and surrounding the bundles, while un-reacted silicon exists beyond the SiC, which did not successfully react with the carbon/graphite. The enlarged image in Fig. 7(c) originated from Fig. 7(b) and identifies the closely packed nature of the carbon fibre bundles, although no scale was available. Also identifiable in this micrograph are gaps in-between the C_f/C bundles. These gaps likely exist because they were inaccessible during manufacture of the C_f/C preform and during siliconisation.

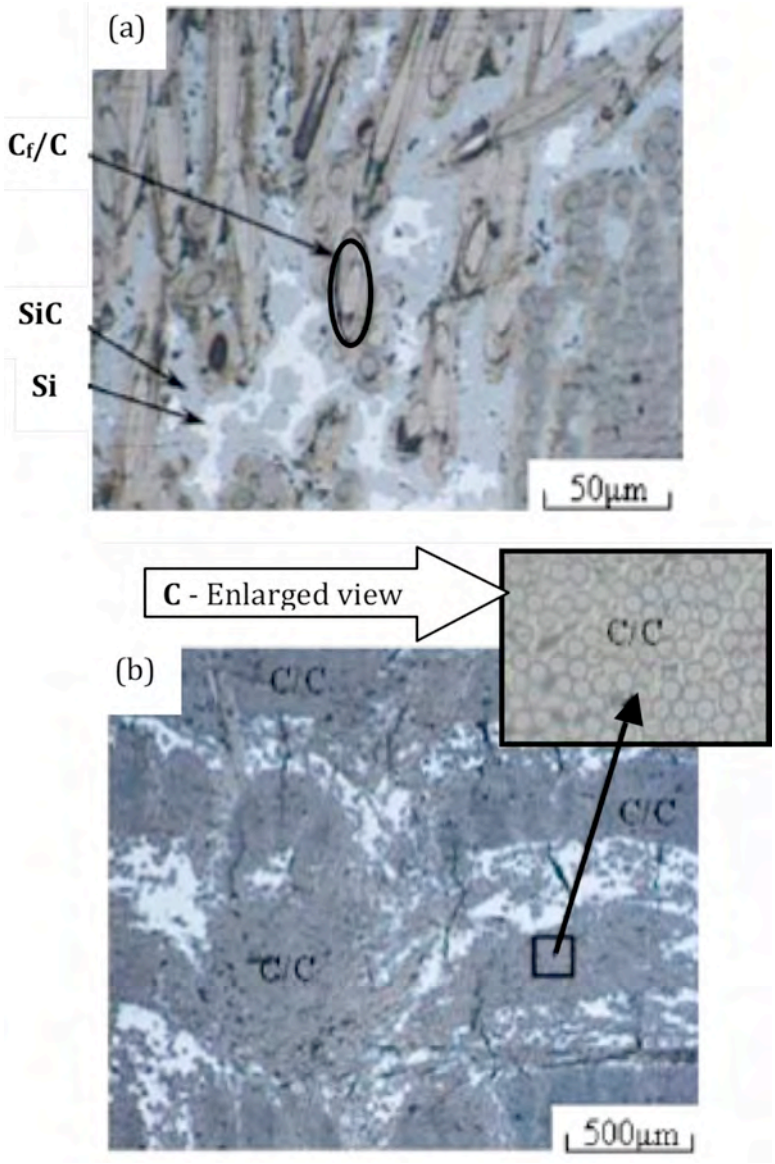

Fig. 7. Optical micrographs of C_f/SiC brake materials, illustrating the hierarchy of the phases in the microstructure: C_f/C, SiC, silicon and voids. No scale is available for 'C' [19].

2.1.3.3.2. Tribology

Comparative COF curves by Zhang *et al* [22], Fan *et al* [19] and Krenkel *et al* [5] are shown in Appendix A – Figures 1, 2 and 3 (and Fig. 8) respectively. The results were similar even though the testing conditions and their interpretations of the results differed. The COF profiles can be summarised into three parts: 1). Narrow high initial peak at the beginning of braking that ranged between 0.35 and 0.45; 2). A relatively smooth and stable middle stage; 3). Rapidly increasing COF to approximately 0.6 approaching the end, as discussed.

Part 1: Zhang *et al* [22] reported that the higher initial COF was mainly affected by the coverage of surfaces by absorbed water molecules during the cooling in the air after each braking stop as well as the response hysteresis of the testing apparatus. This was supported by a similar investigation by Xu *et al* [65]. Alternatively, Fan *et al* [19] attributed the pre-peak as being inevitable because of the existence of the large amounts of micro-peaks or valleys on the brake surface. These peaks and valleys meshed together, leading to deformation, shearing and breaking, which resulted in the higher initial COF. The initial peak reported by Krenkel *et al* [5] was slightly higher, between 0.4 and 0.45 and was attributed the higher initial peak COF to high contact temperatures created by the higher energy input of 0.8 MPa.

Part 2: In the relatively stable middle part, Zhang *et al* [22] concluded that the COF was determined by the solid–solid contact of asperities on surfaces of disks resulting in an adhesion force. The COF was established from the product of shear strength of adhesion junction or asperities and the true area of solid contact, which was in agreement with Xu *et al* [65]. Fan *et al* [19] meanwhile attributed the stable part to the micro-peaks on the surface being sheared or worn down, resulting in a gradual decrease of the COF. After being flattened, the micro-peaks now became wear debris that filled the micro-valley to form a friction film covering the worn surface of brake disks under the braking pressure. New wear debris was continuously formed as the retained debris in the friction film was progressively sheared off the braking surface. Therefore, the friction film reached a dynamic equilibrium and the COF became a smooth and stable third-body layered system.

Part 3: Toward the end of braking, Zhang *et al* [22] and Xu *et al* [65] reported that as the sliding velocity decreased, the surface temperature increased to about 500ºC in a short time. This enhanced the adhesion and abrasion of the contact conjunctions and asperities, thereby producing a higher mechanical deformation resistance and sliding resistance. The COF subsequently rose rapidly toward the end of braking. Fan *et al* [17] meanwhile reported that as the speed reduced, the amount of new debris falling off reduced. Consequently, the dynamic balance in the friction film was gradually broken. Therefore, the COF rose gradually and the tail peak appeared. Xu *et al* [65] concluded that generally within the same roughness, the higher the hardness is, the lower the COF.

The friction of a disc-on-disc friction couple is therefore influenced by: the mechanical deformation of the contact junction or asperities, groove effect of wear debris, adhesion and abrasion between the contact surfaces, surface coating, temperature at the friction interface and internal thermal conductivity.

Some of these factors could also affect the C_f/C-SiC composites manufactured herein. Therefore, friction trials were conducted, which are discussed in *Section 3.4.9*. The primary aim was to qualify the mechanical sustainability of the end-of-life preforms for further large scale testing, in addition to making comparisons between the generated COF between of similar sized and manufactured virgin and end-of-life C_f/C-SiC composites.

The next aspect in the development of the COF was to improve its stability, which was attempted by modifying the transverse thermal conductivity and altering the volume fractions of the constituents so that the discs exhibit different densities and surface proportions of the constituents, as discussed.

In an attempt to modify the transverse thermal conductivity, Krenkel *et al* [5] compared four C_f/C-SiC brake discs manufactured by LSI: a standard bi-directional C_f/C-SiC composite named Silica XB (Table 8) and three modified C_f/C-SiC discs that were based on Silica XB. The modified discs comprised: high heat conductive carbon fibres (Type 2), increased carbon fibre content in the axial direction (Type 3) and a microstructure with an increased SiC content (Type 4). The friction couple comprised two similar C_f/C-SiC stationary discs that began with a sliding velocity of 15 ms^{-1}, as shown on the right side of Fig. 8 and ended at standstill.

Type 2 exhibited the most stable COF, followed by Type 4, Type 3 and finally Type 1. Type 1 exhibited high contact temperatures caused by the high-energy input, which were responsible for the unacceptably low COF of 0.2. The stability of the COF exhibited by Type 2 was contributed to the high heat conductive carbon fibre. Meanwhile, Type 3 demonstrated that by increasing a greater proportion of carbon fibre in the axial direction, transverse heat flux was increased, which improved the COF stability.

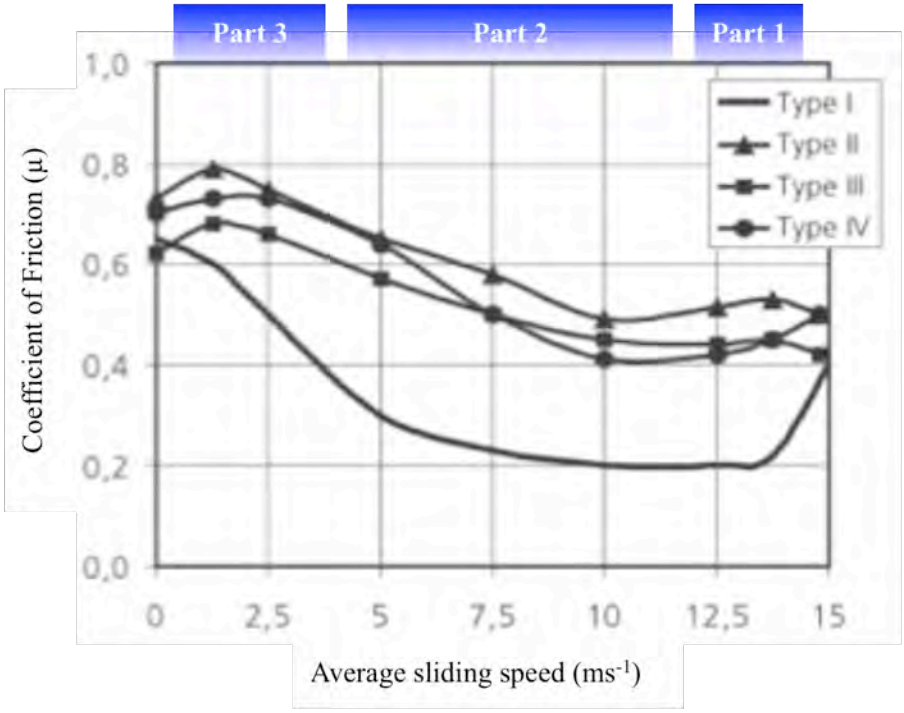

Fig. 8. Dynamometer COF curves, from right to left for the four different types of C_f/SiC reported by Krenkel *et al*. Type 1 represents the sample: Silica XB [5].

In addition, due to the SiC, silicon and related phases generating adjacent to the fibre structure, it could also be speculated that the volume fraction of these highly conductive phases was also increased in the axial direction. This could also aid the axial thermal conductivity. Type 4 was created by modifying the architecture to increase the SiC content.

Meanwhile, Zhang *et al* [22] varied the carbon fibre volume fraction and SiC inside four C_f/SiC composites, which consequently altered the density and investigated the impact on the COF. The composites were named: A, B, C and D and were fabricated by CVI. The properties of sample D were previously shown in Table 8, while Fig. 9 shows how altering the volume fractions affected the density of each sample.

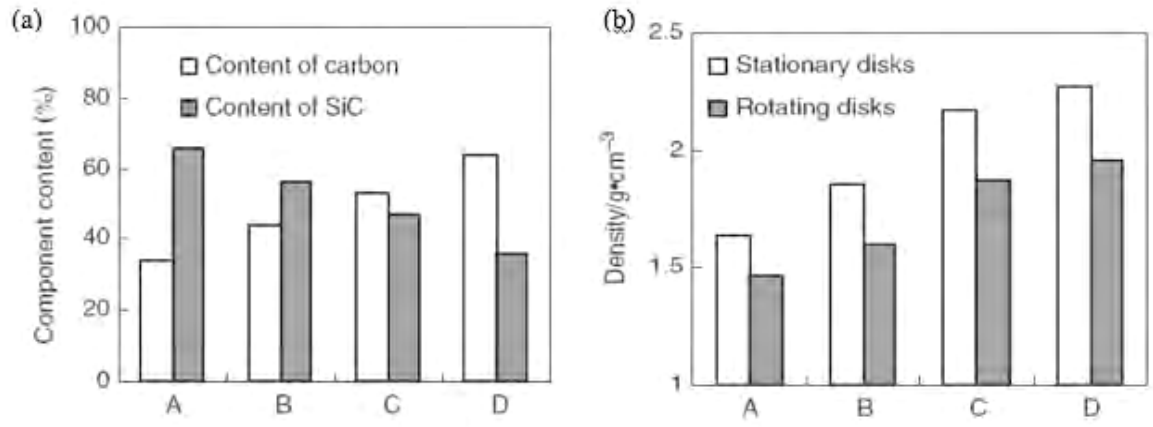

Fig. 9. Graphs showing (a) Relative carbon and SiC content (%) of four C_f/SiC composites and (b) Density (g/cm^3) comparisons of the stationary and rotating discs [22].

As the carbon fibre volume fraction (%) increased, the SiC volume fraction decreased, which increased the density from ~1.7 g/cm^3 (A) to a maximum of 2.3 g/cm^3 (D). The COF curves for samples A to D are shown in Fig. 10, which began at zero and ended when the disc stopped after a period of time (seconds).

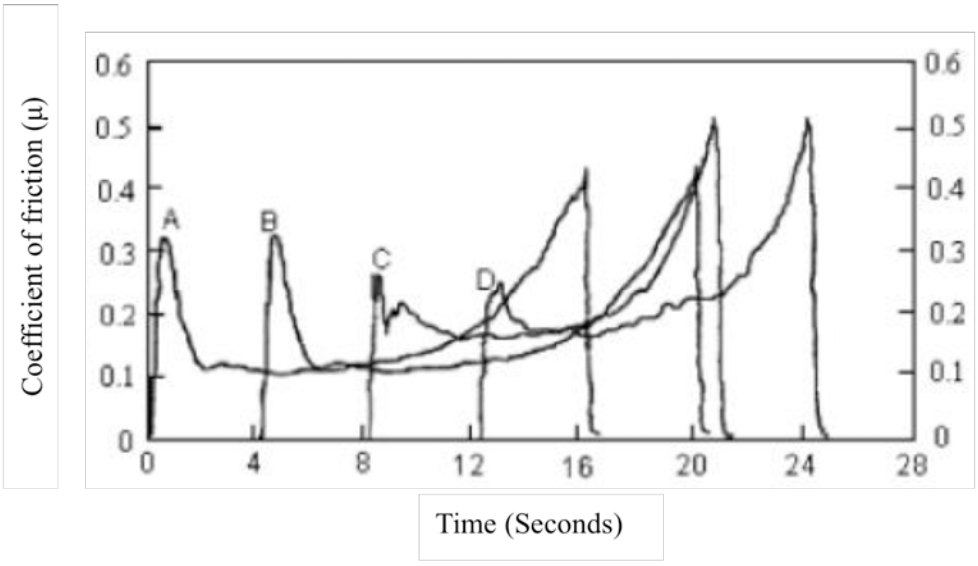

Fig. 10. The COF curves of the different C_f/SiC composites. Types A, B, C and D [22].

From left to right, each curve possessed the characteristic initial peak (Part 1), middle stable portion (Part 2) and final raised peak (Part 3) in common the previously discussed investigations. However, as the density increased from A to D, the average COF increased, the initial peak (Part 1) value decreased and the total breaking time

shortened. This was investigated further by comparing the COF (μ), COF stability (S) and density, as shown in Fig. 11.

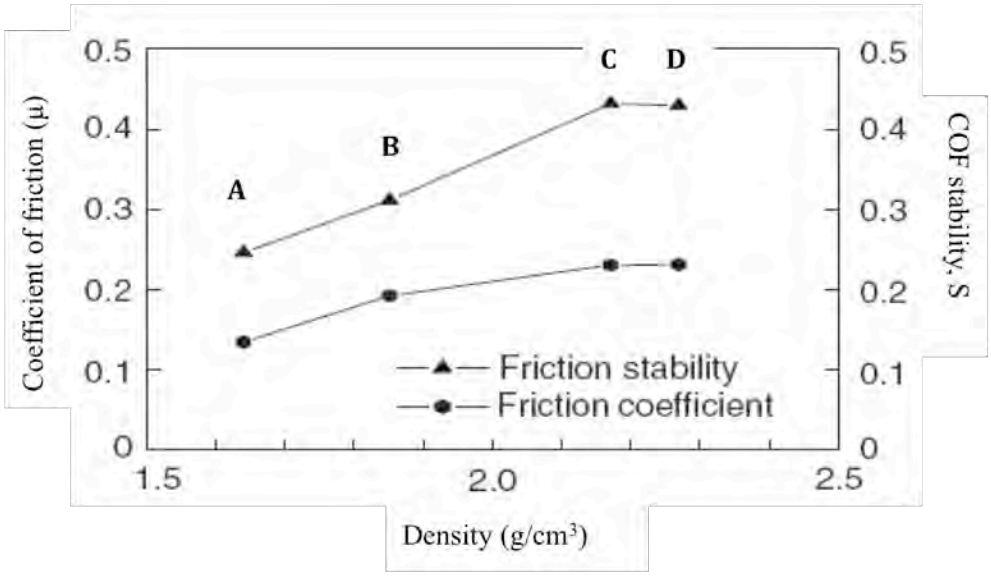

Fig. 11. The COF (μ) and COF stability (S) of C_f/SiC disks versus increasing density (g/cm^3) [22].

As the density increased, the COF and COF stability also increased. The lowering of the first initial peak (Part 1) was attributed to the increased rigidity i.e. shear modulus (G) of samples B-D, due to the high temperature graphitilisation processing and increased carbon content. Therefore, the COF and the COF stability of the 3D C_f/SiC composites improved by increasing the material density up to 2.3 g/cm^3 and carbon content (V_f) to at least 50%.

Widespread implementation of C_f/C-SiC composites has so far been limited by their poor frictional stability and high wear rates. From these investigations, the mechanisms at the friction interface are believed to be heavily influential and remain, even today not well understood. This is primarily because the mechanisms are complex, dynamic and completely dissimilar to the widely acknowledged mechanisms that occur for traditional cast-iron brake discs.

Therefore, research has focused on identifying the controlling mechanisms [55], which indicated the influence of the surface topography and effect of modifying the friction surface to improve the frictional stability and wear resistance. Modifications included efforts to promote the thermal conductivity [14] and incorporation of surface coatings [5], which were typically based on SiC.

Stadler *et al* [16] for example, demonstrated that a C_f/C-SiC brake disc with a SiC surface coating fabricated by LSI in contact with a metal matrix composite pad exhibited a low wear rate. Krenkel *et al* [14] meanwhile, revealed that a C_f/SiC brake disc with a SiSiC coating in combination with a sintered metallic pad produced a favourable frictional stability and wear resistance, especially in comparison to non-coated disc, although further improvements were still desired. Therefore, one possible direction to improve the COF and its stability could be to alter the volume fractions and surface proportions of the constituents at the surface. Therefore, composites comprising different volume fractions and surface proportions were investigated in this study. The results are shown in *Section 4.2.1*.

2.2. C_f/C-SiC composites

C_f/C-SiC composites comprise four main parts: the carbon fibre reinforcement that constitutes the preform architecture; interface, such as pyC, which is also sometimes considered as part of the matrix; SiC matrix and surplus silicon. However, after manufacture, the matrix in fact consists of multiple interfaces between the carbonaceous interface, SiC and free silicon, and typical microstructural features such as voids and grain boundaries. This is illustrated in the schematic in Fig. 12, which closely corresponds to previous micrographs, for example in Fig. 7.

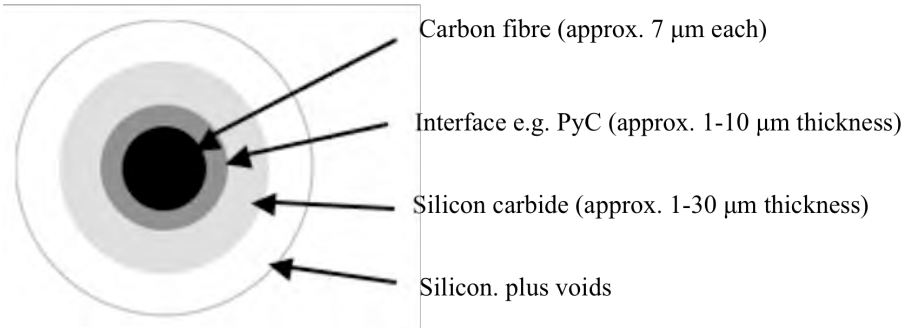

Fig. 12. Schematic of the hierarchal structure of a C_f/C-SiC composite (not to scale).

The properties of the composite are not determined by any single parameter, instead a combination of the constituent materials, preform architecture and manufacturing route that collectively dictate the physical, mechanical and thermal properties. It was therefore the purpose of this section to highlight the influence of each

on the properties, beginning with the influence and requirements of the preform architecture.

2.2.1. Preform architecture

The preform architecture comprises the carbon fibre reinforcement and may also include the interface, in particular when pre-preg materials are considered. The preform can exist in a number of permutations that dictate many of the physical, mechanical and tribological properties of the final composite. The most influential properties that the preform architecture influence, which are under investigation herein include: the open porosity, which changes during fabrication, and must be penetrated and fully densified if the composite is to achieve the desired mechanical performance; achievement of a satisfactory bend strength and failure mode, and a sufficiently high and stable COF.

Variables of the preform that are discussed in the proceeding sections include: shape and orientation, for example two-dimensional (2D), 2.5D, 3D or laminate; orientation; fibre size; fibre reinforcement volume fraction; and, the interface and its characteristics.

2.2.1.1. Preform dimension

The preform dimension i.e. 2D, 2.5D or 3D, fibre orientation and fibre volume fraction are of key importance with respect to the properties of the composite, especially when considering the added complication of directionality that conventional monolithic materials need not consider. Fibre reinforced composites are typically anisotropic, the properties vary along the three principle orthotropic axes: X, Y and Z, at 90º to each other. Fig. 13 shows some of the most common architectures [66], while other common reinforcement arrangements include woven and 2D with Z-needling i.e. 2.5D.

The preform dimension will dictate the potential mechanical performance of the composite, amongst other important parameters such as the internal architecture in-between the tows and fibres bundles, which will in-turn dictate the available open porosity. From Fig. 13(a), random short fibre composites such as non-woven structures are not commonly used for structural components, because of their lower mechanical properties in comparison to long fibre composites. More details are discussed about the properties of short fibre composites in *Section 2.2.2*.

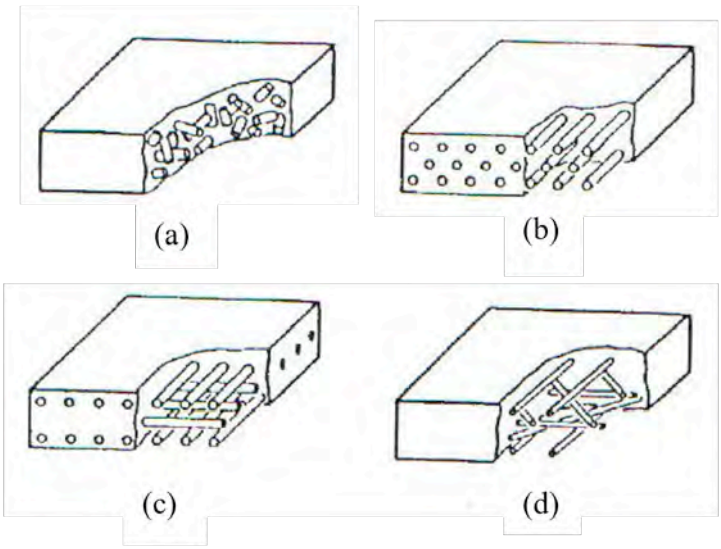

Fig. 13. Fibre reinforcement orientations: (a) Random short fibre, non-woven (b) Uni-directional, (c) Orthogonal directions e.g. 0°/90° and, (d) Multiple directions e.g. 0°/45°/90°, long fibre [66].

Meanwhile, a uni-directional (UD) composite is one in which the majority of fibres are straight, un-crimped and run in a single direction. An example of this is illustrated in Fig. 13(b)), although can also include a fibres in other directions to hold the primary fibres in position. UD composites therefore only generate properties in one direction, so are often aligned in alternating directions to achieve more balanced properties. For example in 0°/90° i.e. UD-weft or 0°/45°/90° directions as shown in Fig. 13(c) and (d) respectively.

However, it is also not uncommon to have a composite with a greater proportion of UD fibre in one direction, to enhance the properties in a specific direction whilst maintaining satisfactory properties in other directions. For example, a 0°/90° composite with 75% of the fibre in one direction and 25% fibre in the remaining perpendicular direction.

There are various methods of maintaining the fibres in position in a composite, which include webbing, weaving, stitching or needling. Some of the different woven architectures are shown in Appendix A – Figure 4 [67]. The woven architectures are manufactured by interlacing the warp fibres (0° orientation) and weft fibres (90° orientation) in a regular pattern. The most important parameters that the architecture dictates include the: direction of the properties, including stability; drapability i.e. ability to lay-up or follow a contour; and porosity, which are compared together with other commercial considerations [67]. As previously remarked, aligning more fibre in a specific

direction will aid the properties in that direction and forfeit the properties in the remaining directions. High drapability is an important parameter for intricate shapes or structures that require the weave to be flexible. Therefore, the drapability is improved when the fibre are not tightly woven e.g. basket weave.

The porosity in between the pre-pregs, tows and fibre is an important consideration when designing the preform architecture that will be densified. This was recognised by Yin *et al* [68] who used LSI to infiltrate molten silicon into a porous C_f/C architecture. The silicon melt was inefficient in penetrating the tows of dense weaves.

The porosity inside the woven structures is defined as the space in between the fibres, therefore in a similar respect to the drapability, the porosity increases when the fibres are not tightly woven. According to the manufactures data, shown in Appendix B – Table 1, the 'leno' architecture possesses the most porosity and the plain weave, which is the structure of several samples under investigation herein, has an intermediate porosity. Meanwhile, needling is performed in the vertical Z-direction and combines several adjacent layers together. After the fibres are orientated, resin is often impregnation into the preform architecture and semi-cured, creating a carbon fibre pre-peg that can be easily handled or transported. The resin can also be pyrolysed to convert it into pyC.

Micromechanics are often employed to predict the properties of materials, although, unlike homogeneous ceramic materials that exhibit the same properties in all directions i.e. isotropic, inhomogeneous composites exhibit anisotropic properties that must be individually resolved in each applicable orthographic direction. The stiffness, for example can be predicted in the in-plane (fibre direction) and transverse directions using the Voigt and Reuss expressions respectively. However, while micro-mechanic estimations are useful, they could never replace actual mechanical testing.

The two most important mechanical parameters that a replacement C_f/C-SiC must achieve are a satisfactorily high bend strength and non-catastrophic failure mode. The most common test method used to determine these parameters is the bend test using a three or four point jig. Materials that posses a non-catastrophic failure mode also have a high fracture toughness (K_{1C}), which is defined as the area under the stress-strain curve in Fig. 14 and is typically about 6 MPa.$m^{1/2}$ for C_f/SiC composites [24].

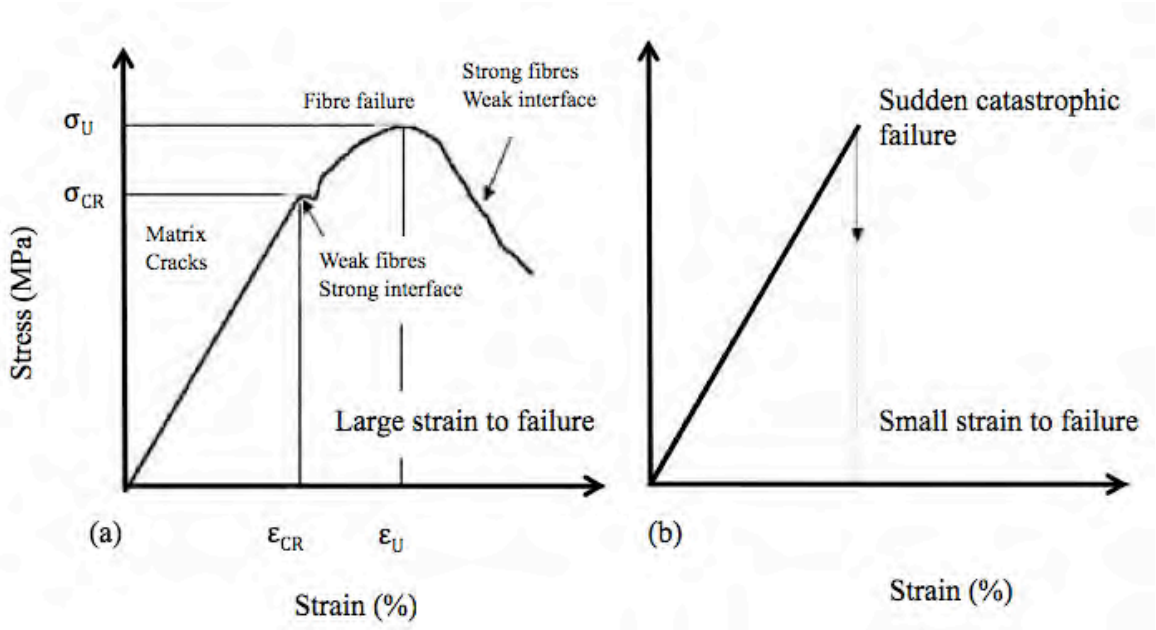

Fig. 14. Stress-strain curve illustrating: (a) non-catastrophic failure and (b) catastrophic failure [24].

While fibre reinforced composites cannot achieve the same toughness as conventional brake disc materials such as grey cast iron, a non-catastrophic failure mode is required; a characteristic not typical of homogeneous ceramics. Meanwhile, the flexural strength is derived from the ultimate strength, 'σ_U'. Further details regarding the mechanical properties are discussed further in *Section 3.4.4*.

A successful preform will provide the composite with failure mechanisms that include: crack deflection, delamination inhabitation, fibre bridging, fibre pull-out and fibre de-bonding. These properties will inhibit and deflect micro-cracking, dissipate energy and improve the failure mode i.e. fracture toughness (K_{1C}) as well as the flexural strength of the composite. C_f/C-SiC composites have been investigated [19, 24, 32] and were reported to exhibit several classical high toughness and non-catastrophic failure mechanisms including: single fibre pull-out, fibre bundle pull-out, fibre bridging and crack deflection properties, as shown in Fig. 15, which are directed related to the preform architecture.

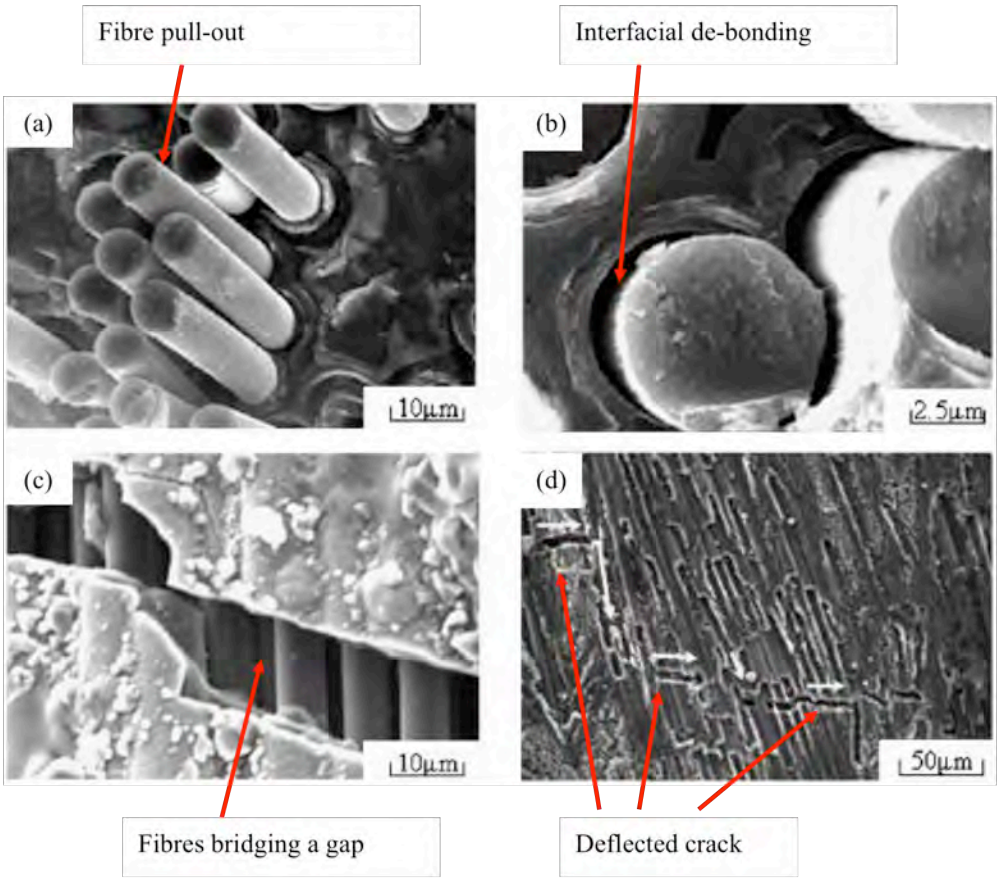

Fig. 15. SEM micrographs showing failure mechanisms of virgin C_f/C-SiC composites: (a) Fibre pull-out, (b) Interfacial de-bonding, (c) Fibres bridging a gap, and (d) Crack deflection [19].

However, as previously highlighted, the preform dimension can have a profound effect on the mechanical properties of the composite. This was demonstrated by Fan *et al* [19] in Fig. 16 when the stress-strain curve of a bend strength and tensile strength test were compared. In the bend strength test, the composite withstood greater stress in the direction parallel to the fibre orientation, but failed faster. The opposite scenario was evident in the perpendicular direction. By comparison, the fibre orientation had no influence of the stress-strain curve in tensile testing in Fig. 16(b). A non-catastrophic failure was exhibited due to successful failure mechanisms that included fibre pull-out, which is illustrated in Fig. 16(c).

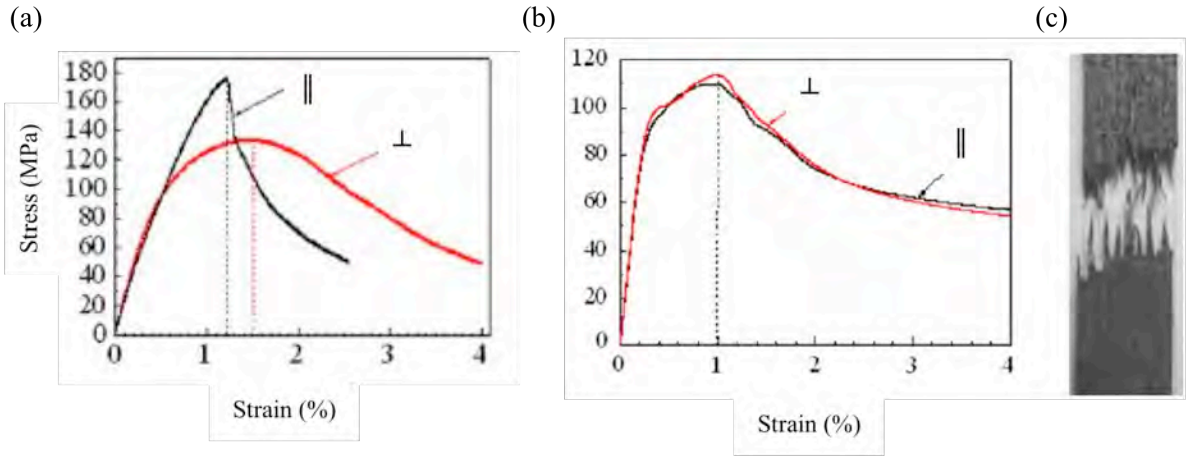

Fig. 16. Stress-strain curves of virgin carbon fibre C_f/SiC composites, from: (a) bend strength testing and (b) tensile strength testing. Black: Parallel to the fibre direction and red: perpendicular to the fibre direction. (c) Photograph of the C_f/SiC composite after tensile test illustrating fibre pull-out [19].

2.2.2. Carbon fibre reinforcement

The carbon fibre constitutes the reinforcement in the preform and is typically produced from a choice of two precursor materials: polyacrylonitrile (PAN) and petroleum pitch [69], although PAN-derived fibres are the most common [70].

2.2.2.1. Carbon fibre manufacture and treatment

Fig. 17 shows a flow chart of the manufacture process for as-received PAN and pitch-derived carbon fibre [71] that includes heat treatment methods such as carbonisation and graphitilisation, and stretching that are used to modify the carbon fibre properties.

The typical properties of carbon fibres are highlighted in Appendix B – Table 2, where advantages in comparison to other fibres include: high tensile strength-weight ratio, tensile modulus-weight ratio, low coefficient of linear thermal expansion, high fatigue strength and high thermal conductivity. Conversely, the disadvantages include: low strain-to-failure ratio, low impact resistance and high cost, depending on the tow count [71].

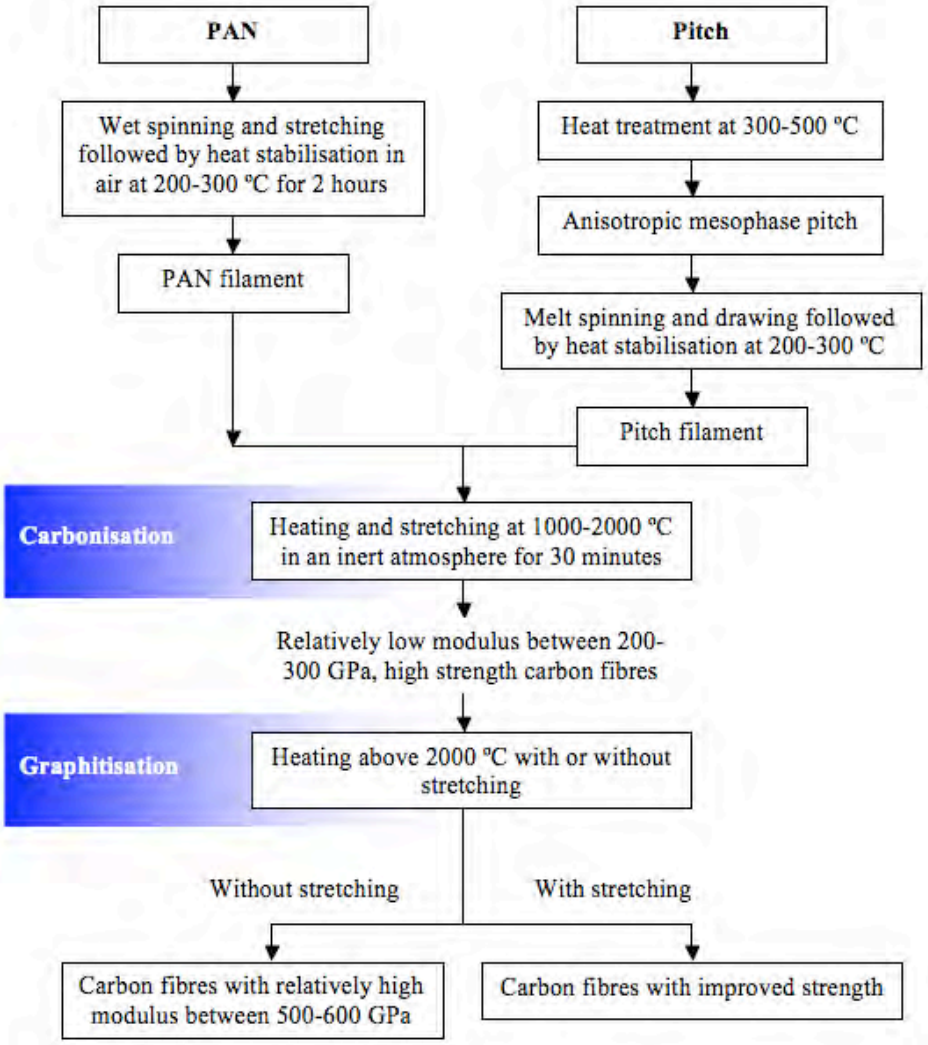

Fig. 17. Flow diagram of carbon fibre manufacture [71].

Carbon fibres are usually grouped according to their modulus and strength band, that include: high strength (HS), intermediate modulus (IM), high modulus (HM) and ultra high modulus (UHM) and typically vary in diameter between 5 and 10 μm. The table in Appendix B – Table 3 [67] lists many of the popular fibres according to the category and location of manufacture.

AS-4 fibres were are some of the fibres under investigation herein, which are recognised as being in the standard modulus band. The fibre gains its properties from its structure, which contain a mixture of amorphous carbon and graphitic carbon. The high tensile strength results from the graphite form, in which the carbon atoms are arranged in a series of parallel graphite planes. This is shown in Appendix A – Fig. 5. The carbon atoms in each plane are arranged at the corners of regularly re-occurring interconnecting hexagons. The distance between the planes, 3.4 Å is larger than that between adjacent

atoms, 1.42 Å [71]. Strong covalent bonds exist between the carbon atoms in each plane, unlike the bond between the planes, which is much weaker. This results in highly anisotropic mechanical and physical properties of the carbon fibre. The basal planes are aligned along the axis. However, in the transverse direction, the alignment can be either circumferential, radial, random or a combination of these arrangements, see Fig. 18 [71].

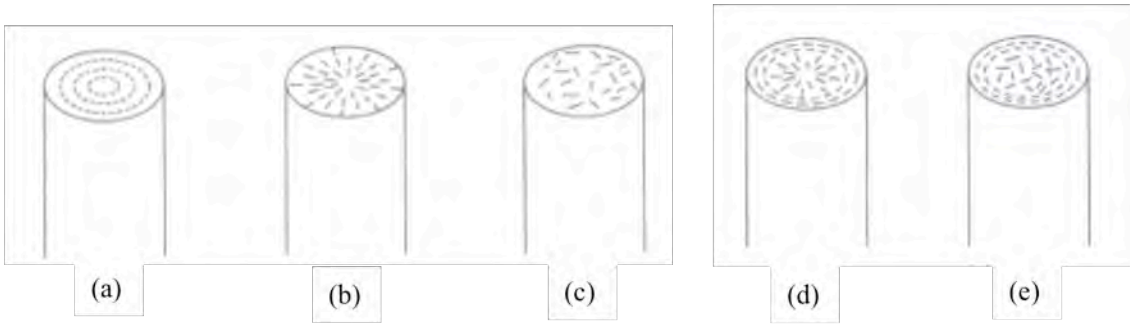

Fig. 18. Arrangement of the graphite crystals in the transverse direction (a) Circumferential, (b) Radial (c) Random, (d) Radial-circumferential and (e) Random-circumferential [71].

Depending on which arrangement exists, properties such as the Young's modulus (E) and coefficient of thermal expansion (α), in the radial (r) and circumferential directions (θ) of the fibre will vary compared to the axial or longitudinal direction. Commercially, a two-zone carbon fibre with a circumferential arrangement in the skin and either radial or random arrangement in the core is common [71].

The mechanical properties of carbon fibres therefore vary considerably depending on the type, manufacture process and applied post-treatment. Appendix B – Table 4 highlights some the structural features and controlling parameters that affect the properties of the carbon fibre [70], which can be compared to the properties previously highlighted in Appendix B – Table 2. PAN-derived fibres generally possess higher tensile strengths and a lower modulus, for example T-300 and AS-4 carbon fibre that is used in the end-of-life pre-pregs herein (Table 14). Alternatively, the ultra high modulus PAN fibres such as GY-70 possess a low tensile strength as well as the lowest tensile-to-strain ratio. While, a number of intermediate modulus (IM) fibres have since been developed, for example T-40 and IM-7 that possess the highest strain-to-failure among the carbon fibre types [71]. Low modulus fibres generally have a lower density, lower cost, higher tensile and compressive strengths and higher tensile-to-strain failures than high modulus fibres [70].

According to Fig. 17 and Appendix B – Table 4, the fibres are often heat-treated to improve their mechanical and thermal properties, which is also supported by Xingui *et al* [77] and illustrated in the graph shown in Appendix A – Fig. 6 [71]. From this graph, as the filaments are heat treated to and beyond 2000ºC, their structure becomes more ordered and progresses toward a true graphite form with increasing temperature. The fibre strength will increase to a maximum at approximately 1400ºC, then decrease as heat treatment continues, unlike the fibre modulus that will continue to rise with increasing heat treatment [71]. In addition to the modifying the mechanical and thermal properties, thermal treatment also permits the fibre inter-lamina shear strength (ILSS) to be tailored.

Use of commercially available as-received carbon fibre normally shows a high amount of active surface groups that increase the adhesion with the matrix leading to a strong fibre-matrix bonding [72] that can be measured in terms of their ILSS in the range of 40-50 MPa. Thermal pre-treatment deactivates and remove the surface functional groups at the fibre surface that progressively reduces the fibre-matrix bond strength i.e. ILSS with increasing temperature [73]. By comparison, conservative low temperature thermal pre-treatment between 600 and 900ºC creates an intermediate ILSS of approximately 30 MPa, while beyond 900ºC, the ILSS reduces further to 20 MPa for 2D CRFP's [74].

At higher thermal pre-treatment temperatures up to 1600°C in an inert atmosphere, the oxidation resistance of an ex-PAN T-300 2D C_f/SiC composite was enhanced by improving the thermo-physical characteristics of the ex-PAN fibre [75, 76]. At elevated temperatures above 2000ºC, carbon fibre undergoes graphitisation with a significant improvement in oxidation resistance [77], although is expensive [33].

In circumstances when the fibres are heated to elevated temperatures, an oxidised PAN fibre is recommended, which were developed in 1960 by Vosburgh and are more thermally stable in comparison to traditional PAN [78]. The fibre was originally called "black Orlon", which today is manufactured around the world (USA, Germany, UK, Japan, France, Isreal, Taiwan, South Korea etc) under a variety of trademark names including: Panox™ [79] and Sigrafil-O from SGL, Grafil-O from Courtaulds Ltd, Pyron from Zoltek and Celiox from Celanese [78].

Today, oxidised PAN carbon fibre (or PAN-OX) is used for a variety of applications, including automotive and aeronautical because it is relatively cheap in comparison to other thermally stable aromatic polymers and is widely available. This is the choice of fibre used by Surface Transforms Plc, 'ST' for the investigations herein.

The properties of these fibres are reported to depend on their manufacture, in particular the degree of drawing and tension during oxidation [78]. Typical properties include: density of 1.36 to 1.4 g/cm^3, high temperature resistance of >2000ºC, elastic modulus between 7 and 10 GPa, tensile strength of 200 and 400 MPa, low CTE and is highly compatible with SiC [78].

More recently, modified types of carbon such as those incorporating carbon nano-tubes or hollow carbon fibres with self-healing polymer matrices [80] have emerged and appear promising future candidates for advanced C_f/C-SiC, although today lack maturity.

In addition, the effect of the fibre length is also an important factor when considering the mechanical performance of the composite. Tucker *et al* [66] reported that for ceramic matrix composites containing discontinuous or short reinforcements; the stresses are transferred from the matrix to the fibres by shear forces i.e. ILSS at the fibre-matrix interface. The section at both ends of each fibre, where the tensile strength is still building to its maximum is where the reinforcing efficiency diminishes. In general, this leads to shorter fibres having less stiffness in comparison to continuous fibres, in particular <1 mm as is shown in Fig. 19 [66], while both the stiffness and strength improved to a maximum as the carbon fibre length increases beyond 1 mm and 5.5 mm respectively.

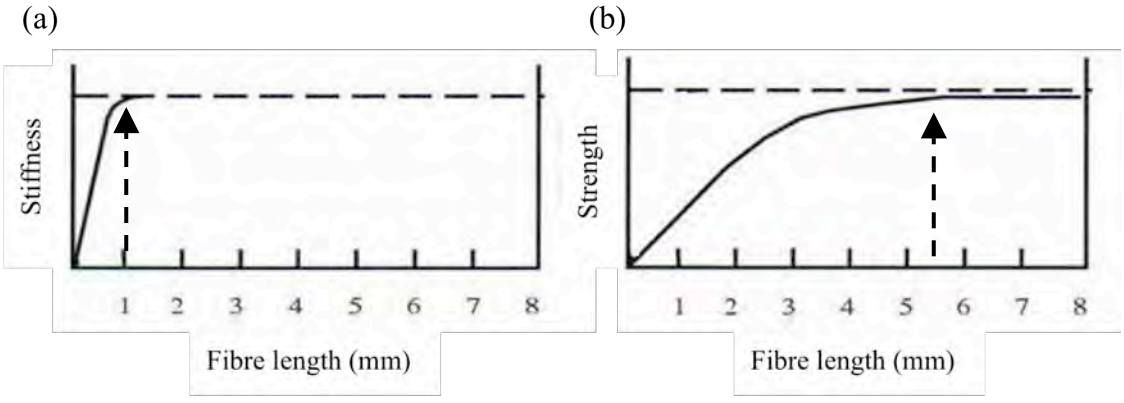

Fig. 19. Fibre length effect on the stiffness and strength of carbon fibres [66].

Meanwhile, as the diameter of the carbon fibre decreases, the tensile strength increases, which is shown in Appendix A – Fig. 7 [66]. Therefore, the optimum carbon fibre diameter is ~3 μm, where most commercial fibres are in the 3-10 μm range and ≥ 5.5 mm long. However, further research [66] revealed that only a carbon fibre length of at least 20 mm is necessary in order to start gaining the impact properties of a continuous

carbon composite. Fig. 20 shows how the four-point bend flexural strength of a C_f/C-SiC composite containing 50% carbon fibre volume fraction that was fabricated by LSI varied according to the fibre length [5].

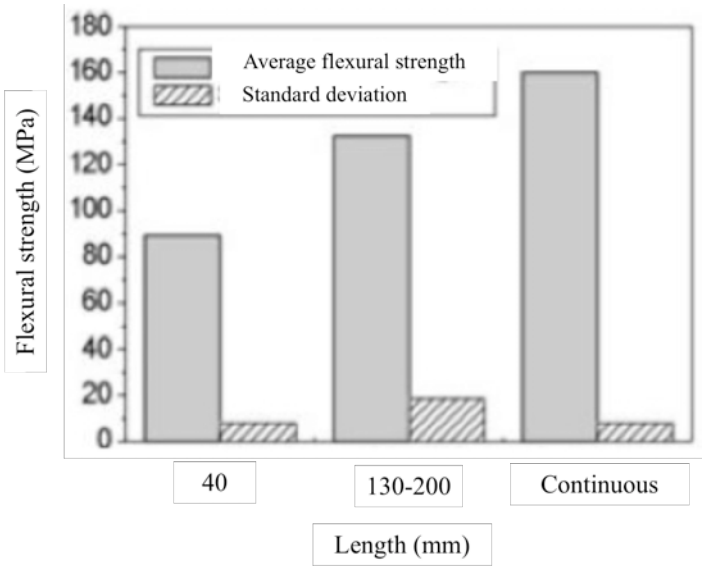

Fig. 20. Flexural strength of carbon fibres ranging from 40mm to continuous fibre length [5].

The strength of the composite was not solely dictated by the fibre strength. As the fibre length continues to increase beyond 5.5 mm (from Fig. 19), the strength of the composite increases to a maximum of 160 MPa (in Fig. 20), when the fibres became 'continuous'. By comparison, the flexural strength of similar discontinuous short fibre (SF) C_f/C-SiC composite manufactured by LSI from other companies include; DLR's short fibre silica: 90-140 MPa, SGL Carbon's 'HP and LSI' Sigrasic: 80 MPa, Daimler Chrysler's C-brake: 67 MPa and Schunk's FU2952: 65 MPa [14].

Meanwhile, when compared to alternate fabrication methods such as CVI and LPI techniques using continuous fibre reinforcements, the flexural strength increases significantly to 450 to 700 MPa [17]. However, a convincing way to reduce the cost of such composites is to simplify its' manufacture by using short fibre reinforcements and pressing techniques. The use of short fibre reduces the cost of the raw material by reducing the waste. Furthermore, short fibres are also considered to possess isotropic properties including the mechanical and thermal properties. For example, the thermal conductivity perpendicular to the friction surface is typically higher compared to other orthotropic composites, depending on the fibre volume fraction.

2.2.3. Interface

The interface that exists between the fibre and matrix and is typically introduced by gaseous phase or liquid based techniques, such as CVI or PIP respectively. Comprehensive interface design reviews exist [81, 82] that address the complex nature of incorporating a successful interface. It was reported that a successful interface acts to: protect the carbon fibre from environmental damage, such as oxidation by acting as a low oxygen permeable barrier over a range of temperatures throughout fabrication and during service, or alternatively any infiltrated corrosive vapour or silicon melt during siliconisation [83, 84]; facilitate impregnation and densification, as reviewed elsewhere [85, 86]; be mechanically compliant and act as a medium to transfer load from the matrix to the carbon fibre reinforcement.

Without an interface, the composite typically behaves like a monolithic ceramic [87]. However, if the interface is too weak, micro-cracks open widely under load and de-bonding occurs along the fibre. De-bonding can also occur over the whole fibre length, which exposes the oxidation-prone fibre. Alternatively, when the interface is too strong; the interface is strongly adherent to the fibre, the reverse situation is evident and the composite is known to exhibit a higher failure stress and a better oxidation resistance, but a more brittle failure [88].

Therefore, an ideal interface is characterised as mechanically compliant: strong enough to successfully transfer load, but weak enough to exhibit crack deflection, thus improving the mechanical performance of the composite by introducing an optimised failure mode through energy absorbing mechanisms [89, 90]. For example: crack deflection, crack bridging, fibre fracture and fibre pull out (Fig. 15).

The adjacent fibre and matrix must also therefore be considered, in particular with respect to the CTE mismatch. This is particularly relevant during PIP and LSI fabrication as previously highlighted, which is common among all manufacturing routes due to the necessary high temperatures. However, with respect to the ideal interfacial thickness, there is reported to be some conflict. Thicker coatings are assumed to reduce friction by decreasing the compressive residual stresses, although conversely increase the fracture surface roughness. By contrast, thin interfaces are assumed to reduce friction by minimising roughness but also are considered more susceptible to failing under stress [82]. An optimised layer thickness is therefore required that is not too thick to maintain good mechanical properties and adhesion, and not too thin to protect efficiently from oxygen

[91]. A common solution to this problem is the incorporation of a self-sealing glass or glass forming compound layers that seal any cracks that develop [32], or alternatively, a multi-layer interface.

Many different types of interface have been suggested, however, in terms of chemical compatibility; non-oxide reinforcements and matrices are favoured in-conjunction with non-oxide interfaces. The most common types include: single layer porous or weak interfaces that are therefore compliant, such as: PyC; layered crystalline interfaces, for example boron nitride (BN); multilayer $(X\text{-}Y)_n$ interfaces with alternating glass and a ceramic layers that are typically applied by gas phase techniques such as CVI or chemical vapour deposition (CVD). In such a case, modern derivatives such as P-CVI or P-CVD have the capability to deposit the interface, ranging from very thin e.g. 1 nm thick up to 25 μm. However, such thin interfaces are typically very weak and therefore offer little absorption or crack deflection capability. Cracks readily penetrate the interface and de-bond the fibre from the interface.

Layered crystalline interfaces are the most commonly applied to date and include turbostratic pyC or hex-BN. The layers are ideally aligned parallel to each other that progressively deflect micro cracks. It is speculated that more layers are beneficial depending on the fabrication deposition rate i.e. layer thickness and ILSS of each layer. However, in reality the layers are known not to be perfectly aligned and contain defects that undoubtedly reduce the ILSS.

PyC is similar to graphite, but with covalent bonding between its layers that are a result of imperfections in its production. The interface is typically produced gaseous precursors or alternate resin derivative e.g. phenol formaldehyde or epoxy resin to almost its decomposition temperature and permitting it to crystallise i.e. pyrolysis. Meanwhile, the thickness and texture of the pyC interface are known influential factors that control the matrix-to-fibre stress transfer [92], while the anisotropy of the pyC controls the rate of oxidation. For example, smooth i.e. none textural laminar pyC is reported to oxidise more slowly in comparison to rough laminar pyC [93].

The effect of heat-treatment on mechanical properties of pyC was investigated by Guellali *et al* [94]. Highly textured pyC matrices that were heat treated to 2900°C exhibited a distinct increase of the ductility accompanied with a flexural strength decrease. By contrast, samples with medium textured pyrocarbon matrices exhibited no significant changes in the mechanical properties after heat treatment.

When a classical optimisation of the ILSS is achieved, pyC can be an effective interface, especially in comparison to an interface-free CMC. PyC is known to be successful when applied to PAN derived carbon fibre [82] that were not smooth and possess micro-depressions also known as defects. The pyC layer effectively filled in the micro-depressions thus making the surface smooth and less susceptible to oxidation.

In addition, studies exist [83, 89, 82, 74] that confirm that C_f/C-SiC composites with pyC interfaces exhibit typical composite failure and protect also the carbon fibre from the corrosive silicon alloy melt during LSI manufacture [83, 84]. By contrast, the same composite without a pyC interfacial layer exhibited an obvious brittle failure mode, very low flexural strength and failure mode. However, pyC is known to be intrinsically prone to oxidation at temperatures as low as 500ºC [88] and therefore requires careful design and manufacture precautions in order to minimise and pre-oxidation.

According to the reported literature, it is clear that pyC can be used as a successful interface material inside C_f/C-SiC composites that have been manufactured by LSI. However, different origins of pyC have thus far not been investigated. This includes pyC derived from pyrolysis of end-of-life epoxy resin inside recycled carbon fibre pre-pregs. This was therefore investigated in *Section 4.1.1*.

2.2.4. Matrix

The matrix provides support for the carbon fibre reinforcement, distributes load via the interface (if present) and protects the fibre from physical and environmental damage, including oxidation. As previously identified, SiC has been proposed and successfully applied as a replacement for carbon inside C_f/C composites, mainly due to the innate oxidation resistance of SiC, which is discussed further in *Section 2.2.5.3*. However, SiC also possesses other favourable properties that includes: a low density of 3.2 g/cm^3, is chemically inert and is particularly suitable as the matrix material for friction applications [1] due to: high hardness, high temperature and thermal shock resistance, high creep resistance [32] and high thermal conductivity of approximately 90 W/m.k [95]. Meanwhile, in terms of wear, SiC-based coatings for disc-on-pad friction couples were reported to significantly reduce wear, in particular when manufactured by CVD [5].

However, work by Wu and Wang [55] indicated that the presence of SiC on the surface of uncoated composites could be detrimental to the friction characteristics. Therefore in order to address this, friction trials were performed using the newly created composites. The results are discussed in *Section 4.5.*

2.2.5. Oxidation

Oxidation has been mentioned on several occasions as an environmental process that is detrimental to the properties of the composite. It is therefore the purpose of this section to define and discuss the reported causes and effects of oxidation.

Early CMC studies measured the strength and load deflection i.e. flexural strength of composites with carbon-coated interfaces only at room temperature. These CMC's exhibited high strength, high strain-to-failure and a non-linear load-deflection behaviour. However, when tested at temperature beyond 900ºC, there was a significant loss in strength, which was initially attributed to the replacement of the carbon layer by SiO_2 that created a strong fibre-matrix bond. However, it is now known that oxidation of the reinforcing carbon fibre caused the substantial decrease in strength [82], which is known to rapidly oxidise at temperatures above 400ºC [96, 97].

Oxidation is a destructive reaction that occurs when there is a physical interaction between oxygen atoms in the atmosphere and the composite, which adversely affects the mechanical properties of the composite [24, 75, 76], primarily by attacking the carbon matter inside the composite, including the reinforcing carbon fibre. Therefore, all carbonaceous matter inside the composite, including the fibre reinforcement and carbonaceous interfaces are particularly vulnerable when temperatures exceed this threshold temperature and then protecting the carbon from oxidation becomes necessity rather than an additional property. Considering the significant impact of oxidation, it has been the focus of many studies [68, 88, 89, 97, 98, 99] and is summarised as the: -

1). Diffusion of oxygen into the boundary interfacial layer surrounding the carbon fibre reinforcement,
2). Surface diffusion of oxygen towards the active sites which are located at the defects of the carbon fibre,
3). Chemical reaction between the oxygen and the carbon fibre with formation of the oxide gaseous species,

4). Diffusion of the oxide gaseous species into the boundary layer.

The rate and extent of oxidation is typically quantified by measuring the relative percentage (%) mass loss of the composite on an electronic balance [98].

Oxidation reviews exist [82, 96] that provide historical data and an insight into the causes and effect of oxidation for CMC's. However, oxidation protection for non-oxide CMC's is still not widely documented, primarily because oxide CMC's are more mature and the emergence of new manufacturing routes.

Since oxidation can only occur when the composite physically interacts with oxygen, past and present protection has focused on understanding how oxygen is introduced [82] with subsequent incorporation of protection, where common methods include: modifying the vulnerable fibre with thermal fibre treatments, physical barriers at the fibre-matrix interface and outer surface coatings that form external barriers. Alternatively, the matrix can be substituted for a naturally oxidation resistant material such as SiC that forms a low oxygen permeable silica (SiO_2) layer during oxidation.

The flowchart in Appendix A – Fig. 8 highlights a hierarchy of considerations for implementing superior oxidation protection for a CMC. The service application is the overwhelming factor to consider, in particular the environment e.g. atmospheric pressures and service condition e.g. temperature, followed by the manufacture process [31]. The oxidation resistance therefore depends on relies on five key areas: 1). Carbon fibre reinforcement type and pre-treatment, 2). Interfacial layer, 3). Matrix selection, 4). Fibre architecture, 5). Outer surface coating, which are discussed.

2.2.5.1. Carbon fibre reinforcement

Different types of carbon fibre are commercially available that are derived from a range of sources such as polyacrylonitrile (PAN), pitch or less commonly rayon. The mechanical properties vary considerably depending on the type, manufacture process and applied post-treatment, while the rate of oxidation has been linked to the surface architecture of the fibre, including the texture [89].

Use of commercially available as-received carbon fibre normally shows a high amount of active surface groups that increase the adhesion with the matrix leading to a strong fibre-matrix bonding [72]. This is known to lead to brittle interfaces that readily crack under excessive stress created during manufacture by the CTE mismatch or

alternatively during service. Such cracking could facilitate the penetration of oxygen and permit oxidation.

This issue is typically addressed by thermally pre-treating the fibre, which as previously discussed, deactivates and removes the surface functional groups at the fibre surface. The fibre-matrix bond strength i.e. ILSS is subsequently reduced with increasing temperature [73]. In such a case, an oxidised PAN polymer e.g. Panox™ carbon fibre from the SGL group [100] that possesses greater thermal stability is recommended as an alternative to traditional PAN-based carbon fibre. Alternatively, the fibre can be thermally treated at elevated temperatures above 2000ºC. The carbon fibre undergoes graphitisation with a significant improvement in oxidation resistance [77], although is expensive [33]

2.2.5.2. Fibre-matrix interfacial layer

Of the different types of interfaces that were previously suggested in *Section 2.2.3*, the most common types are single layer porous or comparatively weak interfaces that are compliant, such as pyC. However, pyC is known to be prone to oxidation at temperatures over 500ºC, while oxidation occurs typically between 500 and 900ºC depending on the structure [185].

Therefore, in terms of oxidation resistance, alternatives are continuously being sought such as BN. BN, in particular α-BN has been studied as an alternative to carbon based interfacial coatings such as pyC, primarily because it is reported to be thermodynamically more stable in contact with SiC matrices and more oxidation resistant than carbon.

The microstructure and oxidation resistance of turbostratic BN depends primarily on the deposition parameters that define the structure, degree of crystallinity, crystallography, orientation and impurities [101]. Such interfaces are commonly applied by CVD [82], where at low temperatures BN is amorphous or turbostratic and known to possess impurities. Consequently, BN is most vulnerable and begins to oxidise between 700 and 800ºC [101] unless the CVD processing conditions are well controlled and the degree of crystallisation is increased by a post-elaboration heat treatment. In such a case, it is reported that the oxidation threshold can be increased to 950ºC [82, 102]. However, beyond 1000ºC a volatile oxide is produced [103]. Although, it was reported by Tressler [101] that doping the BN interface with Silicon could solve this issue [101]. At higher

temperatures, above 1500ºC, BN is known to be hexagonal with a similar structure to graphite making it more resilient [101]. Therefore, the major issue with BN is the intermediate temperature oxidation.

Today, interfaces have been modified into superior multi-layers that consist of two or more stacked layers that aim to gain the advantages of each complimentary layer while limiting their inherent drawbacks. For example, many such multi-layer interfaces possess a self-healing capability that includes one or more glass forming layers based on oxides like alumina or silica. Furthermore, when adjacent layers are mechanically and chemically compatible, fewer problems exist in terms of the local CTE.

Multi-layer interfaces already in use include: B-C, Si-B-C and Si-C [91], BN/C/BC, BN/C/Si_3N_4, SiC/C/SiC, hex-PyC/SiC, BN/SiC [104], $(PyC\text{-}SiC)_n$, $(BN\text{-}PyC)_n$ or $(BN\text{-}SiC)_n$ where 'n' is the number of layers with an overall thickness typically in the range of 0.1-1 μm. Such coatings are applied by gaseous phase infiltration such as CVI and CVD, or to a lesser extent via PIP using a liquid precursor such as phenolic or pitch for carbon. Such interfaces are far less controlled due to their kinetics of infiltration and conversion to pyC via pyrolysis, although can be rapidly applied and are therefore significantly cheaper.

2.2.5.3. Matrix

In terms of non-oxide matrices, carbon is both common and mature, although innately susceptible to oxidation. Therefore alternate matrices have been sought such as SiC that possesses superior oxidation resistance. This is due to the growth of silica (SiO_2), a similar CTE to carbon fibre of 4.8 $x10^{-6}$/°C and ≈1.3 $x10^{-6}$/°C respectively and additional properties that permits it to be particularly suitable for friction applications including: high temperature and thermal shock resistance, high creep resistance [32], high thermal conductivity up to 90 W/m.k [95]. SiC is most advantageous at temperatures between 1000 and 1200ºC [107], at which point the formation kinetics of SiO_2 is fast and the condensed oxide scale forms acting to protect by sealing/filling in the residual pores and micro cracks, thereby minimising any in-depth diffusion of oxygen. The necessary time for sealing (t_C) such cracks was derived by Yin *et al* [98] that was a function of the crack width, CTE and the parabolic rate, B (nm^2/min), where 'B' is the parabolic rate constant of SiC and is bigger than 181 nm^2/min in combustion environments at 1250ºC.

Xu *et al* [89] demonstrated that cracks with a maximum width of 4 µm were reduced to 2 µm at 1250ºC within 2.9 hours and closed completely within several hours. These results therefore indicate that an extended time period and high temperature would be required to seal any cracks, which would not be experienced in any traditional friction-braking scenario. However, the relative mass loss (rate of oxidation) continued to increase after the micro-cracks decreased in size. This indicated that the occurrence of micro-cracks was not the only reason for the oxidation of the carbon phase. In fact, it was most probably the porosity and quantity of interconnecting pores/voids within of the composite that was responsible for the continued oxidation, which relates directly to the fabrication route and preform architecture. It is therefore important to carefully consider a suitable manufacture processes that yields composites of low open and in particular 'interconnecting' porosity.

Multi-phase matrices like those found in alloy and functionally gradient matrix (FGM) composites were originally developed to further tailor and enhance the matrix properties, namely the thermal shock resistance and oxidation protection of CMC's [23, 186, 122, 123]. The material properties are continuously altered by gradually varying the dispersion to matrix ratio from one inside of the material to the outer surface and is advantageous in terms of oxidation resistance, mechanical and thermal properties because complimentary phases or layers are applied to minimise the impact of the CTE mismatch, deflect and inhibit the formation of the micro cracking and seal any crack formation with glassy compounds typically based on boron or silicon.

Gas phase processing is commonly used, for example CVD or CVI that can also simultaneously create the interface and outer surface coating. Lamouroux *et al* [87] fabricated a multi-layer FGM composite consisting of Si-B-C using P-CVI that composed of ceramic layers alternating with thin layers of a sealant material e.g. BN [105] that act as mechanical fuses to promote crack deflection and accommodate the CTE mismatch. Oxidation protection was postulated as being at least one order greater in comparison to a traditional single-phase matrix. Fabrication can also be achieved by hot pressing techniques to create composites with a graded matrix from carbon to SiC [122]. Strong bonding between the layers was successful and a density of 95% without pores was reported, while thermal testing revealed a higher thermal conductivity and thermal shock resistance compared to other CVI and CVD functionally gradient C_f/SiC composites. Even at high surface temperatures beyond 1200°C, no surface cracking was evident. Alternatively liquid phase routes are promising, for example LMI [106] that contained

boron compounds additives: B_4C, titanium borides (TiB_2) and boron silicates (SiB_6) that improved the oxidation resistance by sealing of the micro cracks.

Sol-gel processing is a valid alternative that is faster compared to gas phase processing and also has the capability to create multi-layer interfaces. Incorporating SiC particles has been shown to be effective for improving the oxidation resistance within FGM composites up to 1000°C [125]. According to Vandenbulcke *et al* [105], the best conditions for a multilayer matrix are evident when: the bonding between layers is strong, each layer is thin and well controlled near the fibres, different glass forming carbide layers are used in order to introduce a self healing capability e.g. B_xC, Si-B-C or SiC, inclusion of energy absorbing weak interfaces far away from the supporting fibres and finally to implement a complimentary multilayer interface to work in conjunction with the matrix to deflect and arrest micro cracking.

2.2.5.4. Composite outer surface coating

External coatings are applied for a number of beneficial reasons. These include: to seal open porosity, for example at the end of gas phase manufacture; reduce surface temperatures and theoretically improve the friction mechanism between the rotor and pad, including the COF stability; improve wear resistance; enhance the environmental protection of the brake couple by isolating the composite from the environment.

Today's knowledge of coatings is relatively mature for C_f/C/C's [107] and existing CMC's [5, 19, 22, 96], although material applications focus on aircraft disc-on-disc friction brakes only, which differs greatly compared to automotive disc-on-pad friction brakes. Common outer coatings include silicon-based ceramic coatings [96, 21] such as SiC, silicon nitride (Si_3N_4), yttrium silicate [108] and alternate boron carbides and boron nitrides [13, 82] that range in thickness between 30 and 300 µm.

However, in specific environments such as friction brake systems, the benefit of oxide films such as SiO_2 does not contribute to the tribology and are innately worn away. Much of the tribology research to date is led by Krenkel, which is still in early development. Silicon based outer coatings are promising, where SiC has been tested and proven as a sound starting point for further development. Such coatings deposited by CVD on the friction surface of C_f/C-SiC composites are known to significantly improve wear rates by up to 90% and only small thicknesses of 100-200 µm are sufficient for long-term applications [5]. For example SiCralee™ (SiSiC) [5] or a ~300 µm SiC [16]

coated C_f/C-SiC disc and a sintered metallic pad exhibited favourable wear rate and COF properties. SiCralee^{TM} coated C_f/C-SiC discs paired with similar pads with the same coating did not reach the extremely low wear rates of CVD-SiC, but significantly improved the wear stability in comparison to uncoated C_f/C-SiC brakes [5].

Successful oxidation protection systems for non-oxide CMC's are complex, primarily because of the high number of variables in the constituent materials, fabrication routes and varied service conditions. The extent of degradation caused by oxidation is dependent on many variables including: the fabrication process e.g. micro cracking is a typical phenomenon caused by the fibre-matrix CTE mismatch after pyrolysis and siliconisation; carbon fibre reinforcement: type, homogeneity and volume fraction; fibre-matrix interfacial layer: type, whether single or layered; and SiC matrix: constituents and volume fraction.

According to the reported literature [5, 19, 22, 96], it is postulated that an effective long-lasting protection against oxidation should comprise individually tailored constituents that extend beyond their primary function to inhibit oxidation during both fabrication and service. Each constituent must therefore be designed to be complementary to its' adjoining constituent, in particular with respect to the CTE mismatch and chemical compatibility to inhibit the in-depth infiltration of oxygen throughout the composite.

However, since the cost and origins of the fibres under investigation herein are fixed; a sufficient oxidation resistance must be compromised. This would include a protective and compliant pyC interface with SiC matrix introduced by cost-effective LSI.

2.3. C_f/C-SiC fabrication

Table 9 highlights the direct and indirection considerations when fabricating ceramic matrix composites.

Table 9. Direct and indirect manufacture considerations.

C_f/C-SiC manufacture considerations	
Indirect	**Direct**
• Cost: Raw materials, machinery, equipment and near net shape fabrication with limited handling capability	• Time duration: The fabrication route (and required microstructure) will dictate the manufacture time for each disc, which will heavily affect the overall cost
• Repeatability: In terms of scalability from the laboratory at Loughborough University (LU) to industry i.e. the consortium	• Open porosity (%): The matrix should be homogeneously distributed in the preform with limited residual porosity to maintain good mechanical and thermal properties
	• Oxidation protection: Sufficient protection must be applied during fabrication and for service.
	• Fibre-matrix bonding: Optimised, not too strong or too weak.
	• Properties: Desired mechanical and thermal properties. It is known the fabrication dictates the microstructure that directly affects the properties of the final composite.
	• Finish: Required extra manufacture stages. E.g. surface coatings, grinding, drilling, and polishing. All of which are heavily related to the overall cost

The most common manufacture routes for C_f/C-SiC and similar C_f/SiC composites are gas phase, liquid phase and hot pressing techniques. The flow chart in Appendix A – Fig. 9 highlights the most common gas and liquid phase processing routes [32], which are separated into the three key stages: 1). Preform fabrication, 2). Preform densification/impregnation, 3). Introduction of the SiC matrix. Meanwhile, hot pressing (HP), miscellaneous techniques e.g. sol-gel, and combinations of traditional routes are also becoming more popular because they alleviate some of the limitations of any one

single process. All of these manufacturing routes are discussed in the following sections in terms of their potential to manufacture C_f/C-SiC composites bearing different origins of carbon fibre.

The first step is to create the carbon fibre preform, which is a porous nD-fibre perform, where n = 1, 2, 2.5 or 3, unless sintering or alternate miscellaneous technique is employed. The preform is typically a 2D cloth [98, 109, 110], weave [111] or needled 2D yarn [112] that is self-standing, supported or held together with tooling, at least at the beginning of densification.

The carbonaceous interface is then introduced by partial densification using gaseous infiltration e.g. LP-CVI [98], H-CVI [109], P-CVI [110], F-CVI [111], traditional CVI [112] or impregnated with a polymer precursor e.g. epoxy or phenolic resin and pyrolysis (PIP), to protect fibres, improve the failure mode and supply a carbon matter for the molten silicon to react with in the case of LSI. Today, it is common for the preform to be infiltrated using a gas phase route, especially if the siliconisation is performed using a gas phase route. In this case, multiple preforms are simultaneously densified for improved economy. The gas phase routes are discussed followed by the liquid phase routes.

2.3.1. Gas phase routes

In the gas phase route, the interface, matrix and outer coating are deposited from gaseous precursors at temperatures typically ranging between 850 and 1000ºC under reduced or atmospheric pressure. In most cases, a methyltrichlorosilane (MTS, CH_3SiCl_3) precursor in a 10:1 (MTS: hydrogen) mole ratio is used for the deposition of SiC [110, 113, 114], because it contains the same number of silicon and carbon atoms in one MTS molecule. Therefore, MTS can easily prepare a stoichiometric SiC by CVD [115] or CVI [31].

Full densification of the preform is only feasible if the porosity is kept open until the end of the gaseous infiltration process. This is commonly achieved by keeping the pore entrances at low temperature i.e. by applying an inverse temperature gradient to the preform or periodic machining to re-open the sealed pores**.**

Meanwhile in terms of oxidation, gas phase processing produces composites with well-controlled high purity protective interfaces, coatings and matrices that are favourable for improving the oxidation resistance [125]. However, regardless of the derivative, manufacturing is performed at temperatures well beyond the vulnerable limit

for carbon fibre i.e. 500°C. Furthermore, oxygen is known to be present during manufacture in the residual water of the insulation materials due to the strong moisture absorption of the MTS precursor [89]. In addition, due to the high temperatures, the characteristic crack pattern caused by the CTE mismatch is created [98] and final composites are known to possess comparatively high porosity in the range of 10 to 20% [98]. All of these factors increase the composites' susceptibility to oxidation by exposing the vulnerable carbon fibres and interfaces.

These limitations and cost concerns have therefore facilitated the development of different gaseous phase derivatives and alternate processes such as: liquid phase routes, miscellaneous and hybrid routes, each of which possess their own challenges and are discussed in the following sections.

2.3.1.1. Chemical vapour infiltration

CVI is typically performed using an MTS precursor at temperatures between 850 and 1100ºC under pressure e.g. 17 kPa [116] using hydrogen [22, 116] or both hydrogen and argon [89] as a gas carrier. In order to maintain sufficient open porosity, the preform is removed from the CVI chamber and the outer surfaces are machined open, before being returned to the chamber for further CVI. This necessity therefore makes traditional CVI very time consuming and expensive, which facilitated the introduction of several derivatives.

2.3.1.1.1. Isothermal/Isobaric chemical vapour infiltration (I-CVI)

I-CVI functions under no temperature or pressure gradient and operates typically between 900-1100ºC under <100 kPa [114] with natural gas [117] or hydrogen and argon as carrier gases [114, 117]. A further CVD-SiC process is sometimes used to cover the fibre ends sealing any residual porosity [118, 119]. I-CVI is a mature and established technology, but similarly requires long manufacture times lasting from days to months due to the slow deposition rate.

2.3.1.1.2. Chemical liquid vaporised infiltration (CLVI)

CLVI was investigated by Wang *et al* [146] as an alternative to I-CVI using a liquid kerosene hydrocarbon precursor. Several advantages were identified including a significantly faster densification rate of approximately 150 minutes, which translates to being around 100 times faster compared to conventional I-CVI and a simplified fabrication procedure requiring only one cycle run. No visual damage of the carbon fibre was reported and the final composite possessed a good density of around 2 g/cm^3.

2.3.1.1.3. Low-pressure chemical vapour infiltration (LP-CVI)

LP-CVI operates in a similar respect to traditional CVI except at lower pressure, for example under 5 kPa. The temperature is typically around 1000ºC, for roughly 120 hours using hydrogen e.g. 350 ml.min^{-1} and argon flow e.g. 350 ml.min^{-1} to slow down the reaction [98].

2.3.1.1.4. Force-chemical vapour infiltration (F-CVI)

F-CVI is traditionally used for SiC/SiC composites, although research by Appiah *et al* [120] describes laminated alternating carbon and SiC layered matrix composites reinforced with carbon fibre produced by F-CVI. The preform was infiltrated at 1100-1200ºC under atmospheric pressure with an MTS precursor carried by 750 cm^3/min of hydrogen. The back-pressure was monitored and infiltration was ceased when a pressure of 6.9 x10^4 Pa was reached. The F-CVI process is attractive due to: the high purity, uniform distribution, minimal carbon fibre damage during fabrication, lower porosity and increased production rates as compared to standard CVI. In addition, the flexural and tensile strengths are reported to improve by approximately 10% [111, 121].

2.3.1.1.5. Heaterless-chemical vapour infiltration (H-CVI)

H-CVI, as reported by Tang *et al* [109] was used to introduce a SiC matrix into a 2D bi-directional PAN-based T700, 12 K tow carbon fibre preform. The complete process used to manufacture the C_f/C-SiC composite actually comprised three-steps: heat treatment of the carbon fibre in the preform at1200°C for 2 hours in a vacuum furnace; introduction of a pyC interface by pyrolysing natural gas for 10 hours at 1000°C using I-CVI; H-CVI of the SiC matrix, where the pyC coated preforms were clamped between

two graphite electrodes and directly heated using an electric current in a 50 kW cold-wall and normal-pressure furnace. The SiC matrix was introduced using an MTS precursor that was carried by bubbling hydrogen gas into the chamber at 1000ºC for 25 hours, using an inert gas such as argon to slow the reaction. The resulting composite possessed favourable damage tolerance, which was attributed to the presence of the pyC layer and favourable mechanical properties including: an average flexural strength of 163 MPa, compressive strength of approximately 300 MPa and fracture toughness of 6.5 MPa.$m^{1/2}$.

H-CVI has the advantage of being rapid in comparison to tradition CVI and can create composites with good mechanical properties, but only if the fibres are heat-treated and complimentary processes such as I-CVI are also used to introduce a pyC interface. Therefore, combining all three stages to produce the C_f/C-SiC composite still requires comparatively long manufacturing times. Consequently, alternate methods are more common as they are also more established and mature.

2.3.1.1.6. Pulse-chemical vapour infiltration (P-CVI)

P-CVI was first presented as a solution to shorten the overall densification duration of the preform in comparison to traditional CVI. The main advantage is the ability to yield highly engineered interfaces or matrices through the sequential use of several precursors [31, 110].

As reported by Sakai *et al* [110], P-CVI can be used in conjunction with MTS that is saturated using hydrogen as a carrier gas and bubbled into an MTS saturator and accumulates in a reservoir. The gas is fed into the reaction tube at up to 10 kPa for each pulse through an electromagnetic valve. After a specified holding time for the reaction, excess gas and by-product gas are evacuated using the vacuum pump. The preform is filled and evacuated periodically with a residence time of the gaseous precursor in the preform in the order of a few seconds. The total time for each cycle was typically between 2 and 3 seconds, which can be repeated as many times as is necessary up to 50,000 times. It was reported that additional cycles increased the flexural strength, where 16,000 pulses achieved a strength of approximately 110 MPa.

2.3.1.2. Gradient matrix composites

Functionally gradient matrix (FGM) composites were originally developed to further tailor and enhance the matrix properties, namely the thermal shock resistance and oxidation protection of CMC's [23, 186, 122, 123]. This was primarily achieved by inhibiting the crack formation caused by the CTE mismatch between the C_f/C and the SiC. Fabrication typically consists of several normal complementary processing routes, combined to produce a potentially superior composite. For example, Kawase *et al* [124] in 1999 fabricated a 3D woven carbon fibre preform solidified partially by phenolic resin (PIP), further carbon densified by propane TG-CVI and completed by CVD (carbon and dimethyldichlorosilane, DDS). CVI, although considered slow and expensive offers controllability of the thickness and composition of the C-SiC gradient layers while CVD offers a gradual homogeneous composition, low process temperature and near net shape production of the outer gradient ceramic layers. The gradient layers were crack-free and remained adhesive following rapid cooling tests from 1000 to 0ºC.

Meanwhile, Deng *et al* [125] fabricated a carbon felt gradient matrix C_f/SiC composite by I-CVI with co-deposition of carbon and SiC from Acetylene (C_2H_2) and MTS respectively. Testing showed a significantly improved oxidation threshold compared to C_f/C composites up to 1000°C, due to the SiC particles in the gradient matrix. Alternatively, Wu *et al* [122] fabricated a functionally gradient C_f/SiC composite, from carbon to SiC using a hot pressing powder metallurgy method with SiC, B and amorphous carbon powder. Thermal testing revealed a higher thermal conductivity and thermal shock resistance compared to other CVI and CVD functionally gradient C_f/SiC composites. Even at surface temperatures between 1227 and 1527°C, no surface cracking was evident. Strong bonding between the layers was successful and a density of 95% without pores was reported.

Chan *et al* [186] fabricated a C_f/C-SiC FGM. The final composite was very dense with no evidence of porosity, although problems were reported with the quality of fibre adherence to the matrix that was not understood and required further analysis.

In 2007, Krnel *et al* [23] fabricated and tested three types of gradient C_f/C-SiC composites using dispersed nano sized SiC particles and demonstrated the capability to create a rich SiC outer layer which gradually reduced toward the inner C_f/SiC core. As a result, the cracking issue previously identified due to the CTE mismatch was alleviated because the matrix carbon fibre to SiC was more gradual in comparison to traditional C_f/C-SiC composites.

2.3.1.2.1. Chemical vapour deposition (CVD)

CVD is typically used to deposit interfaces, coating and sometimes the matrix itself. There are several examples of researchers using CVD to create a functionally graded C_f/SiC material [126, 127], which was achieved by controlling the ratio of Si to C in the input gas.

As reported by Wang *et al* [126], a graphite substrate is heated to between 1400 and 1600ºC by an electric current in a cold-walled reactor using e.g. $SiCl_4$ (liquid) and C_3H_8-H_2 (gases) as source materials. The gas pressure is varied between 6.7 and 40 kPa and the $SiCl_4$ was kept at 20ºC, while its vapour was carried into the furnace via a bubbling hydrogen carrier gas. The C_3H_8 flow rate was kept constant throughout, while the silicon to carbon ratio varied between 0 and 1.9. The growth rate varied from 0.05 to 1.3 $mm.h^{-1}$ depending on the temperature and molar ratio. The optimum deposition temperature was 1327ºC, while below 1227ºC no deposits were obtainable. Meanwhile, above 1627ºC, deposits were porous due to the homogeneous reaction in the gas phase. The properties of CVD-SiC functionally graded materials continuously changed by gradually varying the matrix ratio from the inner to outer surface.

Although slow, where the growth rate varies from 0.05 to 1.3 $mm.h^{-1}$, CVD is effective due to the ease of controlling of the composition and microstructure, which creates composites with good oxidation and high thermal shock resistance. An improvement in the oxidation resistance was evident when a small amount of SiC (< 5 mol. %) is combined with the carbon matrix by CVD. In addition, CVD SiC-C, containing a trace of carbon was shown to be more resistant to abrasion than CVD SiC, while a small amount of free carbon accelerated the deposition of the SiC.

Subsequent experimentation by Wang *et al* [127] revealed that the Young's modulus and fracture stress increase with increasing SiC content and decreasing deposition temperature; the latter behaviour resulted from the lower density of the high temperature deposits. Meanwhile, the thermal conductivity ranged between 5 and 58 W/m.K, which decreased as the carbon content increased.

Gaseous phase deposition manufacture routes yield composites with high purity, a well-controlled composition and microstructure. Table 10 shows the typical properties achieved from CVI fabrication routes, I-CVI and p/T-CVI processing [17]. The composites typically possess high flexural and compressive strengths, especially in comparison to

LSI C_f/C-SiC composites (Table 11) that typically exhibit 160 to 300 MPa and 210 to 320 MPa respectively. Conversely, the internal porosity is high compared to other processes, in particular LSI, which leaves only 2 to 5%. The effect of a high internal porosity seems to reduce the internal thermal conductivity, depending on carbon fibre volume fraction. Apart from differences in the compressive strength between the I-CVI and p/T-CVI composites, the properties are very similar, which is a testament to the reproducibility of this gaseous process.

Table 10. Typical properties of I-CVI and p/T-CVI C_f/SiC composites [17].

Properties	Unit	Gas Phase Infiltration	
		C_f/SiC	C_f/SiC
Manufacture	-	I-CVI	p/T-CVI
Tensile strength	MPa	350	300-320
Strain to failure	%	0.9	0.6-0.9
Young modulus, E	GPa	90-100	90-100
Compressive strength	MPa	580-700	450-550
Flexural Strength	MPa	500-700	450-500
Interlaminar shear strength (ILSS)	MPa	35	45-48
Porosity	%	10	8-15
Fibre Content	Vol. %	45	42-47
Density	g/cm^3	2.1	2.1-2.2
Coefficient of thermal expansion (10^{-6}/K)	∥ ⊥	3 5	3 5
Thermal conductivity, (W/m.K)	∥ ⊥	14.3 - 20.6 6.5 - 5.9	14 7
Specific heat	J/kg.K	620 - 1400	-
Manufacturer	-	SNECMA	MAN

In addition, CVI is highly flexible and has the capability to simultaneously produce a large number of near net shape composites with low thermal and mechanical stress [31, 109 119]. Fibre degradation is also minimal due to limited handling during densification and a carbon fibre volume fraction of around 45% and final density of 1.9-2.3 g/cm^3 is achievable [22, 119].

Conversely, the process is relatively slow, up to several hundred hours [128], since it has to be performed at a low deposition rate in order to avoid a too rapid sealing of the

pore entrance by the deposit [109]. If the densification rate is too fast, surface machining may be required to re-open the porosity, with consequent handling and possible fibre degradation of the preform. Furthermore, whichever version of CVI is used, the resultant composite will possess significant residual porosity, which is detrimental to the thermal conductivity and oxidation resistance [31, 119].

The slow densification rate of CVI techniques can be improved by introducing an inverse TG-CVI, by replacing the slow diffusion mass transfer with the significantly faster convection mass transfer within the pore network (P-CVI) or a combination of TG-CVI and P-CVI i.e. F-CVI [88]. However, these improvements in the densification rate are at the expense of flexibility due to extra fixtures being required. Nevertheless, regardless of the drawbacks of traditional CVI, it has already been established at plant level, making it a mature and reliable process [113, 119, 129]: two factors that are very appealing to industry.

2.3.2. Liquid phase routes

Two different types of liquid silicon processing exist depending on whether the molten (pure or alloyed) silicon reacts with the preform or not. The reactive processes include reactive melt infiltration (RMI), liquid melt infiltration (LMI) or liquid silicon infiltration (LSI), while the non-reactive include liquid polymer infiltration (LPI) or polymer impregnation and pyrolysis (PIP). There is essentially no difference between these different reactive melt infiltration techniques. However, on occasion, a different acronym is used to distinguish the manner and timing in which the molten silicon makes contact with the preform. This is discussed further in *Section 2.3.2.2*.

Liquid siliconisation is performed after the preform is complete, including any carbonaceous interfaces or matrices. Table 11 shows the typical properties achieved via liquid phase manufacture from three different companies: DaimlerChrysler (PIP), MAN (PIP) and DLR (LSI) [17].

Table 11. Typical PIP and LSI C_f/C-SiC properties [17].

Properties	Unit	Liquid Phase Infiltration		
		C_f/SiC	**C_f/SiC**	**C_f/C-SiC**
Manufacture process		***PIP***	***PIP***	***LSI***
Tensile strength	MPa	250	240-270	80-190
Strain to failure	%	0.5	0.8-1.1	0.15-0.35
Young modulus, E	GPa	65	60-80	50-70
Compressive strength	MPa	590	430-450	210-320
Flexural strength	MPa	500	330-370	160-300
Inter laminar shear strength	MPa	10	35	25-33
Porosity	%	10	15-20	2-5
Fibre Content	Vol. %	46	42-47	55-65
Density	g/cm^3	1.8	1.7-1.8	1.9-2.0
Coefficient of thermal expansion ($10^{-6}.K^{-1}$)	∥ ⊥	1.16 4.06	3 4	-1 – 2.5 2.5-7
Thermal conductivity (W/m.K)	∥ ⊥	11.3-12.6 5.3-5.5	- -	17-22.6 7.5-10.3
Specific heat	J/kg.K	900-1600	-	690-1550
Manufacturer	-	Daimler Chrysler	MAN	DLR

According to the reported data, the mechanical properties of PIP-composites are superior in comparison to LSI-composites, apart from the Young's modulus. Furthermore, PIP-composites generally contain a lower fibre reinforcement volume fraction, possess a lower density and have a significantly higher porosity. While there are too many parameters to build conclusive relationships between the properties, there is a clear indication that the porosity could be an important factor, especially during manufacture.

For instance, the LSI-derived composites possessed lower porosities with correspondingly high thermal conductivities in both directions: parallel and perpendicular, which is a favourable property for tribological applications [25]. The opposite was the case for PIP-composites, which possessed higher porosities with lower thermal conductivities. However, there was no indication that a lower porosity granted or limited the mechanical properties. This is evident in Table 11, where the PIP-derived C_f/SiC in comparison to the LSI-derived C_f/C-SiC possessed a higher porosity and a significantly higher flexural strength, although the Young's modulus was comparable. More details of PIP and LSI are discussed in the following sections.

2.3.2.1. Polymer impregnation and pyrolysis

PIP or LPI is a non-reactive process that impregnates a Si-C based polymer e.g. polycarbosilane (PCS) into a porous carbon fibre preform, which is subsequently pyrolysed to create the matrix and complete the composite. The flow chart in Fig. 21 shows how different categories of carbon fibre could be manufactured into C_f/C-SiC or similar C_f/SiC composites by PIP.

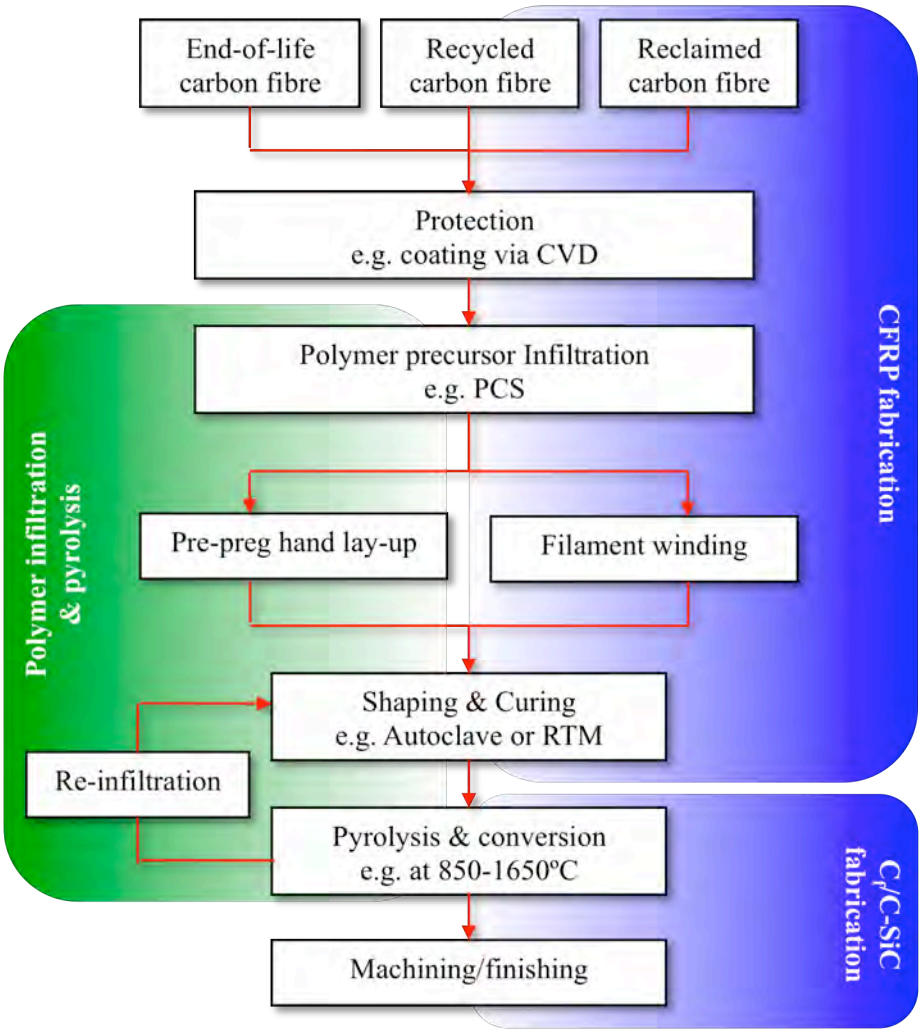

Fig. 21. Overview of C_f/C-SiC fabrication by polymer impregnation and pyrolysis, PIP.

2.3.2.1.1. CFRP fabrication

Preform fabrication is essentially the same as the gas-phase preform manufacture with the same cost implications based on quantity. Consequently, laboratory scale manufacture commonly employs hand lay-up [130, 131, 132], while industry utilises the more

expensive automated techniques such as autoclave moulding, resin transfer moulding (RTM) and hot pressing & filament winding.

The preform is impregnated with a Si–C precursor that possesses a high carbon yielding polymer that wets the carbon fibre, exhibits a low enough viscosity to flow in the pore network of the fibre preform and possess a high ceramic yield when pyrolysed. Common polymer precursors include:

- Polycarbosilanes (PCS) [31, 77, 132, 133] although this is currently expensive,
- Poly-(vinylsilanes) [134],
- Polysilazane [135],
- Hexamehyldisilazane (HMDS) [131], which is cheap and commercially available,
- Polymethlsilane (PMS) [131] is currently expensive,
- Polysilsesquioxane (for C_f/SiC_xO_y composites) [130] possesses high wettability and good adhesion to the carbon fibre.

Additives are commonly used, for example PCS:Xylene in a 50:50 wt.% [77] in molten state or in a solution of an organic solvent. Once the precursor has been infiltrated, the preform is now known as a 'green body', which is cured at room temperature [130], at 160ºC and 5 MPa [136], cured thermally or under radiation by gamma-rays or E-beam [31] to render the precursor infusible. The CFRP is now complete unless further post-curing is required, for example at 200ºC [136].

2.3.2.1.2. C_f/C-SiC fabrication

The CFRP is pyrolysed, during the latter stage of the PIP process in an inert [77], nitrogen [14, 33, 132] or argon [130] atmosphere at temperatures typically between 900 and 1200ºC, [14, 31, 77, 132] as low as 850ºC [131] and up to 1650ºC [33] to convert the polymer matrix into amorphous SiC.

Assuming that the precursor is a PCS type, the pyrolysis results in a matrix that can be SiC and carbon mixture or pure SiC depending on the nature of the atmosphere, where the ceramic yield can vary up to 90% [31]. Part of the carbon is lost as gaseous species even when pyrolysis is conducted under an inert atmosphere, with significant shrinkage evident after pyrolysis. As the pyrolysis temperature increases, the local

shrinkage stresses exceed the tensile strength of the matrix, which results in a subsequent crack formation.

The remaining pyC residue is porous and largely open, most likely from the gaseous species that was generated and escaped [31]. It is this porosity that makes it necessary for multiple PIP densification cycles. Re-infiltration of the polymer and additives is repeated until a sufficient density is reached. However, the chosen temperature-time-cycle will dictate the morphology of the resulting SiC matrix.

Xingui *et al* [77] reported after 10 PIP cycles that further densification was slow. Full densification of a T-800 3D braided carbon fibre preform and PCS precursor required no less than 15 PIP cycles. The final density, measured using the Archimedes method was 1.8 g/cm^3. In addition, the results showed that pre-heat-treatment of carbon fibre in combination with the PIP-process lead to C_f/SiC composites with excellent properties, which included: a flexural strength of 600.8 MPa, shear strength of 45.9 MPa and the fracture toughness of 18.5 MPa.m$^{1/2}$. The effect of fibre heat treatment was previously addressed in *Section 2.2.2.1*, while the potential of PIP-processing is clearly demonstrated here.

Meanwhile, Wang *et al* [132] required 10 PIP infiltration cycles of PCS to achieve a similar density of around 1.8 g/cm^3. The results showed that the composites without fibre pre-treatment possessed a modest flexural strength of 154 MPa and a fracture toughness of 4.8 MPa.m$^{1/2}$, while those with a carbon coating or thermal treatment had much higher strength and toughness of more than 400 MPa and 15 MPa.m$^{1/2}$ respectively. It was concluded that weak interfacial bonding and better in-situ strength of carbon fibre were the main reasons for mechanical property improvement with pre-treated fibre.

The main weakness of the PIP process is therefore the required number of infiltrations. One method to reduce the number of PIP cycles was reported by Naslain [31], which involved loading the polymer precursor with a filler that was essentially a powder with a fine granulometry. In the investigation, a mixture of SiC and additives, including a boron bearing species such as BC was used to entrap oxygen at medium temperatures in service conditions. However, loading the precursor with a powder significantly increases its viscosity, which is contrary to the requirement for effective penetration. In such a case, it would be necessary to simplify the preform architecture to cater for the increased viscosity. For example 2D-fabrics used in conjunction with a SI-HP technique [31]. In a later investigation by Naslain [88], it was reported that 6-10 PIP cycles were required for

full densification and even then, would yield composites with significant residual porosity.

2.3.2.2. Liquid silicon infiltration

Silicon treatments of C_f/C composites via liquid silicon melts were first patented worldwide by Schunk in 1979 [13]. LSI is based on the impregnation of a molten silicon into a porous C_f/C perform that reacts exothermically with any carbon matter to form SiC with some residual unreacted silicon. The phase diagram for Si-C is illustrated in [137].

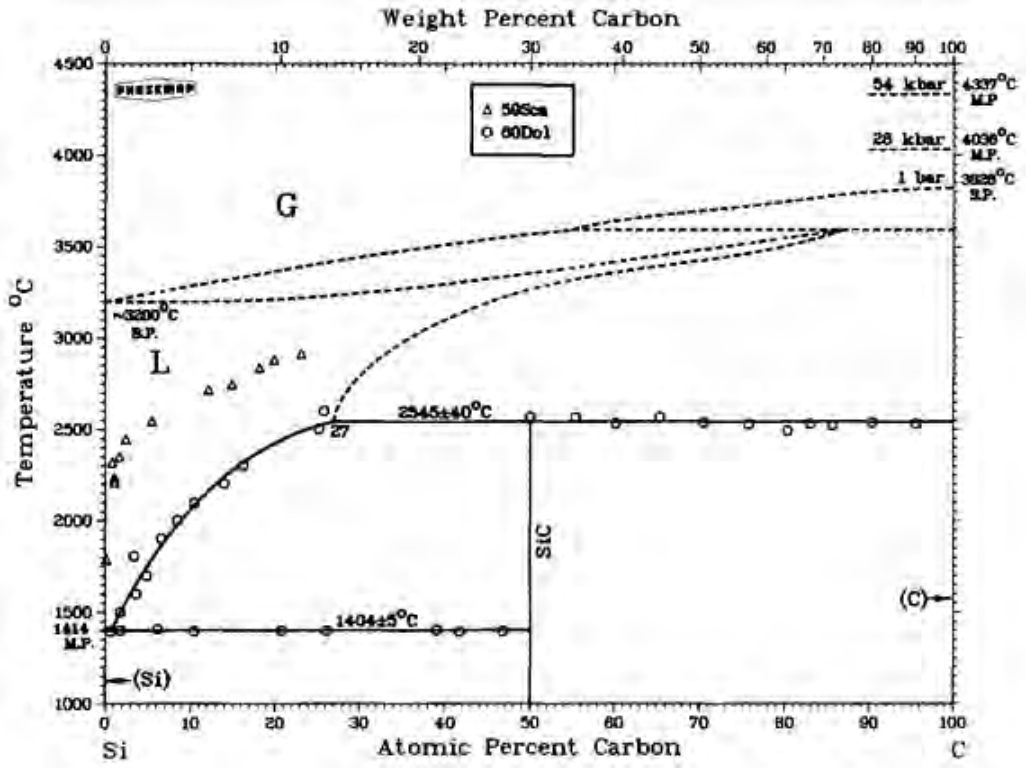

Fig. 22. Phase diagram for Si-C [137].

First investigations by Evans *et al* [138], Hillig *et al* [139] and Gadow [140] revealed that the carbon fibre had to be protected prior to the infiltration of the molten silicon to reduce the extent of carbon fibre degradation, which resulted in CMC's with a low fracture toughness. From these initial investigations, stable forms of protection were found to be either heat-treated i.e. highly graphitised carbon fibre as previously discussed, or high modulus carbon fibre, both of which add expense to the composite [33]. Mentz *et al* [141] also identified this problem and attempted an inner siliconising process, similar in respect to PIP processing. Meanwhile, in 1990, DLR established their three-

step LSI process [14], which was patented in 1996 and extended manufacture to in-situ internally ventilated discs [5, 27, 142]. An overview flow chart for manufacturing C_f/C-SiC composites by LSI using different categories of carbon fibre is highlighted in Fig. 23.

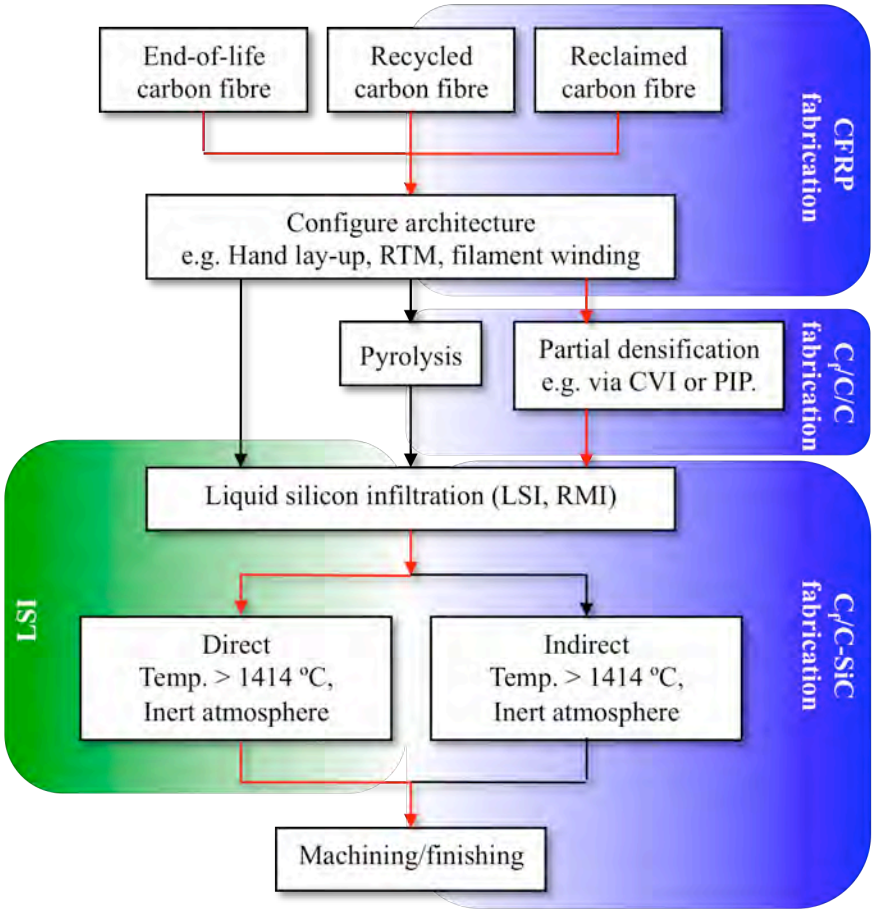

Fig. 23. Overview of the C_f/C-SiC manufacture process by LSI. The red line highlights the route used to manufacture the C_f/C-SiC composites herein.

2.3.2.2.1. CFRP preform fabrication

A partially densified porous nD-fibre preform, where n = 1, 2, 2.5 or 3 is constructed. Early preforms were made by stacking up woven fabrics [25, 73], for example in bi-directional 0º/90º orthotropic orientations. Modern shaping and orientating is heavily influenced by the production volume and available funds. Some common methods include: -

- Hand lay-up. In particular for low volume, low budget or cost-effective processing.

- Resin transfer moulding, for example: high tenancy (HT) carbon fibre with a volume fraction content ~58% CVD-PyC coated plain weave fabric [74], as-received and thermally pre-treated carbon fibre woven fabrics [73], XP60 resin with a carbon fibre content of around 60% [143] or alternatively curing a green body at 208ºC under a pressure of 2 MPa and post-cured at 240ºC under ambient pressure [144].
- Autoclaving under heat and pressure, for example using phenolic resin with a carbon fibre volume fraction of around 60 % [143].
- Filament winding, for example: Toray 3K yarn i.e. spun fibre with phenolic resin [34]. Hot pressing (HP) technique [33], for example: HT chopped (10-200 mm) short carbon fibre (V_f = 30-60%), which are cured at a maximum temperature of 250ºC for 2.5 hours under 5-10 MPa pressure [142].

The two most important factors to consider are that the preform architecture has to be protected and inherently porous to facilitate the liquid impregnation of the molten silicon. Protection is required because liquid silicon is a corrosive medium to the carbon fibre reinforcement. Therefore, a suitable protective interface is required that acts as a physical barrier and mechanical fuse as previously discussed. Common protection methods include: carbon fibre heat treatment or fibre coatings by CVD, CVI or alternate PIP.

In the case of PIP, a resin is then used such as epoxy or phenolic. The earliest commercial synthetic resin was based on a phenol formaldehyde resin, which is a low cost basic resin with the commercial name Bakelite^{TM}. The low viscosity (<500 cPs) allows for various composite applications techniques and processing conditions, primarily by RTM automated processes where a high degree of fire safety, excellent mechanical properties and resistance to high temperatures is required [145].

2.3.2.2.2. C_f/C/C fabrication

If the preform architecture is sufficiently protected and porous, then conversion by pyrolysis or partial densification is omitted and the preform is siliconised. Alternatively, the CFRP is converted into a porous C_f/C composite by pyrolysis with the same shrinkage issues as PIP, and/or partially densified for protection and supply of carbon for LSI reactions, and then siliconised.

Partial densification is achieved by: either CVI, for example I-CVI [33], CLVI [146] or alternate gaseous technique as previously discussed, or PIP [73, 74, 143], which performed at 900ºC [33, 143, 74, 147] or between 900-1650ºC [14, 147, 148, 149] under an inert atmosphere, for example nitrogen [34, 147] or vacuum conditions [14, 35, 73].

When the preform is constructed or the CFRP is converted into a porous C_f/C composite, the impact of the preform architecture is realised. This is because the internal architecture is created that represents the porosity for the liquid silicon to penetrate and densify the composite. However, after infiltration, the composite is rarely fully converted to SiC or completely dense, where porosity is almost always present. This is despite investigations into LSI of porous structures [150] and efforts to predict the ideal preform porosity and density [85] and attempts to engineer the internal architecture [86, 151, 152]. The internal architecture i.e. porosity, is based on three factors: preform architecture; the densification route; impact of pyrolysis on the fibre architecture and polymer inside the CFRP, which are discussed.

1). Influence of the preform architecture:

As previously identified, porosity exists inside the architecture, between the fibre pre-pregs and even inside the fibre bundles. It is this porosity that must be penetrated by the polymer during the CFRP manufacture, gas or liquid during the creation of the protective layer, and silicon during LSI.

Wang *et al* [152] manufactured five different porous carbon structures and investigated the effect of the infiltration process on the properties of reaction-formed SiC manufactured by LSI. It was reported that the porosity of the carbon preform and infiltration process were highly influential on the reaction rate and infiltration rate of molten silicon inside porous carbon fibre architecture. Five different porous carbon preforms with porosity that ranged between 35 and 67% with a pore size from 0.03 to 2.58 μm were infiltrated with liquid or silicon vapour. Under the same experimental conditions, silicon vapour infiltration lead to a deeper infiltration than liquid silicon infiltration. The best result was obtained by silicon vapour infiltration with a relatively smaller scale porous carbon preform that possessed a density of 0.92 g/cm^3. The final composite exhibited a high flexural strength 630 MPa, density of 3.12 g/cm^3 and Si-content 8 vol.%.

These results provide enough motivation to further explore different virgin and recycled carbonaceous materials in order to identify if there are any differences in the

developed microstructure after LSI. One difference could be the thickness of the developed SiC, which is investigated in *Section 4.2.4.1*.

Meanwhile, Bae *et al* [153] investigated the effect of initial porosity on the physical and mechanical properties of LSI-C_f/C-SiC composites. Lower initial densities lead to overall higher C_f/C-SiC densities of around 2.22 g/cm^3. A higher initial porosity also resulted in higher free silicon volume fraction (%) content with no direct correlation to the residual open porosity in the final C_f/C-SiC. The flexural strengths meanwhile ranged between 80 and 95 MPa, which was attributed to unprotected fibres that degraded during LSI.

Alternatively, Margiotta *et al* [86] attempted to engineer the internal architecture by blending crystalline cellulose and phenolic resin in various mass ratios as carbon precursors to create a porous carbon preform. The bulk density, median pore diameter, and overall chemical reactivity of C_f/C preforms could be adjusted. Based on a prior investigation by Chiang *et al* [154] who reported the minimum median pore diameter necessary for infiltration was 1 μm, and calculations indicating the ideal density of the preform should be 0.964 g/cm^3, a porous carbon structure with a density of 0.791 g/cm^3 with median pore diameters of 1.45 μm was created. After LSI conditions at 1800°C, under low pressure for 120 minutes, a C_f/SiC product was produced with a bulk density of 2.96 g/cm^3 with an estimated proportion of 82.5 vol. % pure β-SiC.

2). Influence of the densification route:

According to information in Table 10, gaseous phase manufacture typically yields very dense composites with low porosities in the 8 to 15% range. This compares to the liquid phase routes that typically create higher porosities in the 15 to 20% range (Table 11), although could be as low as 5% in optimised conditions.

3). Shape change of the carbon fibre architecture due to pyrolysis:

Meanwhile, pyrolysis at elevated temperatures leads to shrinkage of the resin inside the CFRP, which is hindered by the carbon fibre reinforcement that constitutes as the preform architecture. This shrinkage causes a build up of residual stress and a dimension change. A translaminar crack pattern forms in the matrix based on the CTE mismatch between the: fibres, interface and matrix. The extent of the resin shrinkage directly affects the formation kinetics of the translaminar crack pattern, which in turn

contributes to the internal open connected porosity [31] and is penetrated equally infiltrated by the molten silicon.

Early investigations by Krenkel *et al* [155] reported that 900°C pyrolysis of 2D CFRP green bodies resulted in 0-10% shrinkage, depending on the orientation and 15-20% open porosity. These results were supported by a subsequent investigation [142] that revealed the shrinkage of a 3D CFRP after pyrolysis of around 1% in the in-plane direction and around 5% in the press direction. These results support previous theories that the fibre inhibits macroscopic changes in dimension in the direction of the fibre, and is supported elsewhere [144, 156].

Kochendorfer *et al* [156] predicted that at temperatures between 900 and 1650ºC under inert conditions, the original polymer volumetric shrank by 50-60%. However, the bi-directionally reinforced composite with in-plane reinforcement i.e. 2.5D exhibited little to no shrinkage. The only shrinkage observed was in the perpendicular to the fibre orientation (in-plane) that shrank between 2 to 10% due to the limited impedance of the fibre.

Meanwhile, Schulte-Fischedick *et al* [144] concluded that a CFRP did not exhibit any shrinkage in the fibre direction after pyrolysis. Unlike a 60 wt.% highly aromatic resin that shrank by approximately 20%. This was in agreement with Krenkel [33] who demonstrated that a carbon precursor (XP-60) shrank by 26% at 900ºC in all three spatial axes. A volumetric contraction of the matrix of 60% was calculated, while the average mass loss from an XP-60 resin at 900ºC and at 1550ºC was 36 and 39% respectively. This shrinkage phenomenon was accredited to the fibre-matrix bonding mechanism, which was investigated by Krenkel *et al* [157, 158, 159]. Thermo-optical analysis revealed that the first fibre-matrix debonding occurred beyond 505°C for bi-directional reinforced CFRP with a 60% carbon fibre volume fraction. Below this temperature, the carbon fibre and matrix was submitted to tensile stresses parallel to the carbon fibre axis and compressive stresses perpendicular to the carbon fibre axis. These stresses were attributed to the CTE mismatch between the carbon fibre reinforcement and the matrix i.e. the fibre-matrix bonding interface.

Meanwhile, beyond 505°C, a reverse stress state was evident. The carbon fibre was submitted to compressive stress while tensile forces act perpendicular to the fibre axis. With increasing pyrolysis temperature, the tensile stresses exceeded the tensile strength of the matrix resulting in a relaxation by cracking. The extent of cracking will

directly affect the siliconisation kinetics, because of the increased preform surface area and access points for a reaction to take place.

In addition, it was demonstrated that the fibre-matrix bonding could be tailored by thermally pre-treating the carbon fibre. Untreated (as received) carbon fibre exhibits a high amount of active surface groups, which increases the adhesion to the polymer matrix. Consequently, the fibre-matrix bonding force i.e. ILSS is high. Typical values for fabric based CFRP range between 40 and 50 MPa. After pyrolysis, a high fibre-matrix bond results in a translaminar crack pattern with dense C_f/C segments, which are hardly accessible to the silicon during siliconisation [33]. However, these narrow communicating channels could generate high capillary forces that could aid siliconisation infiltration, in particular when using liquid melts of low viscosity [157]. This paradoxical phenomenon was also confirmed by Naslain [88] and was studied further in *Section 4.2*.

Meanwhile, heat-treating the carbon fibre between 600-900ºC removed a proportion of the functional surface groups, which consequently reduced the fibre-matrix bonding forces to intermediate levels of around 30 MPa (2D CFRP laminates). During pyrolysis, at 900ºC these fibre-matrix bonds are strong enough to form a translaminar crack pattern, similar to a high fibre-matrix interface, but the carbon fibre bundles are additionally inter-spread with small cracks making them more vulnerable to being attacked by the molten silicon during siliconisation [157].

Additional heat-treating of the carbon fibre beyond 900ºC further reduced the ILSS to below 20 MPa. During pyrolysis, no geometric reduction is observed in the laminates thickness and the individual fibres remain in their original position. The resulting C_f/C composite is completed microcracked but not delaminated, which results in a microstructure without any segmentation. Consequent siliconisation fills in all of the extra micro-cracks resulting in higher densities of around 2.3 g/cm^3 [157]. The carbon fibre is now exposed to the molten silicon (alloy) melt, which results in the silicon heavily reacting with the carbon fibre fibres. This reduces the load bearing capability of the carbon fibre considerably and the fracture behaviour becomes brittle, very similar to monolithic ceramics [157].

Krenkel [33] subsequently reported that a 2D-laminate CFRP performs with carbon fibre volume fractions between 50-70% created porosities between 30% (low fibre-matrix bonding) and 11% (high fibre-matrix bonding). As a result of this research, Krenkel [17] attempted to solve this CTE mismatch issue and created a graded C_f/C-SiC composite

that consisted of 26-stacked layers across four thermal treatment zones, which is shown in Appendix A – Fig. 10.

By progressively increasing the thermal pre-treatment, the fibre-matrix bond strength gradually reduced in the transverse direction. This resulted in the increasing uptake of silicon with subsequent SiC formation from the centre to the outer friction surface. Due to the higher CTE of the outer SiC rich layers, more transverse cracks were evident after cooling, which ranged in width between 17 and 19 μm, ran in-plane in rectangular order with a distance of between 1 and 2 mm from each other and stop when they reach the first intact in-plane fibres. The cracks reduce the overall strength of the composite but allow a greater uptake of SiC near the surface, which could potentially increase the in-plane thermal conductivity, wear and oxidation resistance. An improved in-plane thermal conductivity also has the potential to reduce surface temperatures, which could aid stabilisation of the COF.

Krenkel *et al* [25, 73, 143] investigated the effect of fibre architecture and used a woven carbon fibre fabric for preforms, which were compared to short fibre (SF) carbon fibre reinforcements that represented a reduced material cost of up to 50% [156] making the technology viable for the cost sensitive automotive industry. Five different C_f/C-SiC composites were manufactured by LSI and investigated, including: XB: basic woven structure, XT: high tenacity carbon fibre, XD: functional composite with a highly dense matrix, XG: graded composite and SF: Short fibre composite, the properties of which are compared in Table 12 [17].

Table 12. Mechanical and thermo-physical properties of different LSI-derived C_f/C-SiC composites [17].

Property	Unit		XB	XT	XD	XG	SF
Density	g/cm^3		1.9	1.9	2.3	2.2	2-2.1
Open porosity	%		3.5	3.5	1	<5	<3
Interlaminar shear strength	MPa		28	33	-	-	-
Flexural Strength	MPa		160	300	80	65-80	90-140
Tensile Strength	MPa		80	190	30	-	-
Strain to failure	%		0.15	0.35	0.04	-	0.15-0.25
Young's modulus, E	GPa		60	60	100	-	50-70
Coefficient of thermal expansion (10^{-6}/K)	100ºC	∥	-1	-1	1.5	-	0.5
		⊥	2.5	2.5	4.5	-	1
Thermal Conductivity (W/m.K)	200ºC	∥	22.6	22.6	33.7	-	-
		⊥	10.3	10.3	18.2	-	25-30

All of the composites exhibited a low open porosity, which is a testament to the capability of LSI. However, the mechanical and thermo-physical properties varied quite significantly. Replacing standard fibres with high tenacity alternatives increased the ILSS from 28 to 33 MPa, which consequently almost doubled the strain-to-failure ratio and flexural strength, while the tensile strength increased from 80 to 190 MPa. However, the stiffness remained the same. Meanwhile, the tenacity of the fibre had no effect on the CTE or thermal properties. By contrast, the function (XD), graded (XG) and SF composites exhibited: higher densities, most probably due to an increased SiC content; variable porosities (except for XD); but significantly lower mechanical properties, which reiterates the influence of the preform architecture: continuous fibres, preform dimension and fibre volume fraction.

Furthermore, the mechanical properties of the XG and SF were variable, which could be attributed to their varied architecture. Unfortunately, only limited information was known about the graded composite with respect to its mechanical and thermal performance. However, the remaining composites could be compared in terms of their CTE and thermal performance. The additional SiC in the XD structure improved the in-plane and surface thermal conductivity by approximately 50%, although conversely almost doubled the CTE. SEM micrographs of the Type XB and SF microstructures are compared in Fig. 24(a) and (b) respectively [17].

The bi-directional fibres in the weave can be clearly identified, which had a volume fraction of approximately 60%. However, the silicon melt was still able to successfully penetrate the weave and react creating the limited SiC matrix. The white region in the middle areas of the SiC is this unreacted silicon, which did not make contact with the fibres. However, the silicon was unable to penetrate the tightly packed carbon fibre bundles, which remained as closed porosity.

By comparison, the SF C_f/C-SiC composite exhibited a very different isotropic microstructure, which was similarly fully penetrated. The silicon was able to infiltrate more regions of the architecture and therefore created more SiC, which increased the density by approximately 10%. Also recognisable in the microstructure are voids in-between relatively large regions of tightly packed fibres. According to microstructure and the estimated porosity of <3%, it can be assumed that the closed porosity was evident throughout the microstructure but not connected.

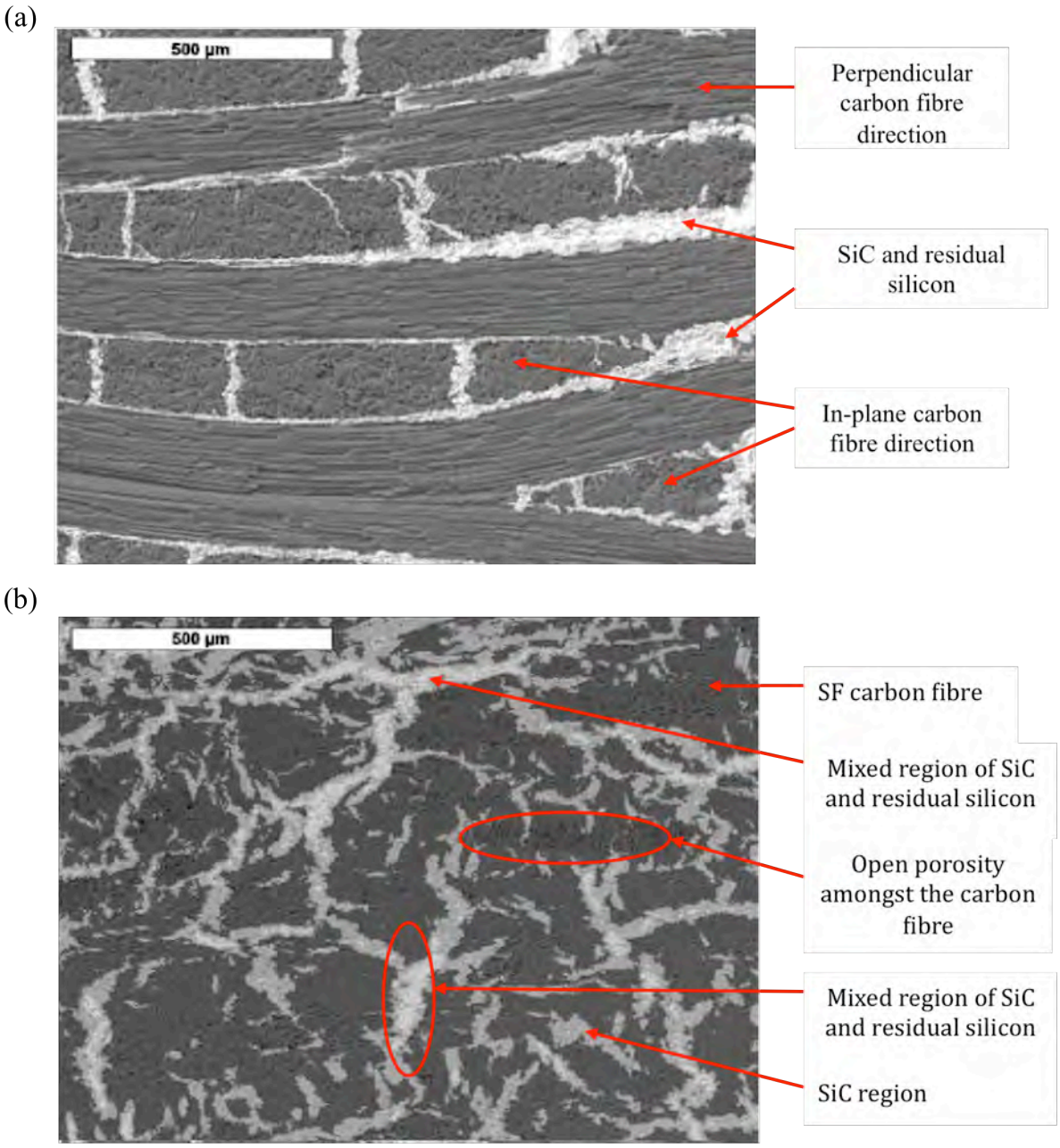

Fig. 24. SEM micrographs of (a) Type-XB woven C_f/C-SiC from DLR and (b) short fibre (SF) C_f/C-SiC from DLR. C_f/C (dark grey), SiC (grey), silicon (white) and voids (black) [1].

2.3.2.2.3. C_f/C-SiC fabrication

Molten silicon or an alternative silicon alloy is infiltrated into the porous architecture at: 1500ºC [4], 1600ºC [31, 153], 1650ºC [34, 73, 74, 143, -144, 147] or 1700ºC [172] under argon gas [171] or vacuum conditions [4, 34, 112, 147, 160, 161, 172]. There is a subsequent evolution of heat, as the reaction is exothermic where the estimated heat of reaction is -

115 KJ/mol [162] and enthalpy of solution is estimated at -247 KJ/mol [162, 163] with an associated volume expansion [31, 88, 153]. With the release of heat, the local temperature can rise significantly, by as much as an estimated 500ºC [164], which was confirmed by Pampuch *et al* [165, 166] by differential thermal analysis.

Covalently bonded SiC generated is considered to be temperature dependent, where SiC is known to exist in as many as 240 crystalline forms. Commercially speaking, alpha SiC (α-SiC) is the most commonly encountered polymorph, which possesses a hexagonal crystal structure and is postulated as forming at temperatures greater than 2000°C. In contrast, the beta form (β-SiC) is considered to form at temperatures below 2000°C and possesses a face centered cubic (FCC) crystal structure. After LSI was performed in this study to manufacture the composites, a combined effort using transmission electron microscopy (TEM) selected area diffraction (SAD) patterns and X-ray diffraction (XRD) was used to extrapolate the most probably type of SiC. Further details can be seen in *Section 4.2.4*.

After siliconisation, the composite microstructure comprises: the carbon fibre architecture; residual pyC matrix if a pre-preg was used; an interface e.g. pyC derived from PIP; SiC matrix, and free unreacted silicon. The mechanisms governing the microstructural evolution during LSI have been investigated elsewhere [144, 163, 167, 168], although only limited and in some cases conflicting experimental support is available. According to these investigations however, the LSI mechanism can be broadly summarised into four stages, which are discussed:

1). Silicon vapour infiltration into the porous preform prior to reaching the melting point of the silicon that creates a nano-sized SiC layer;
2). Infiltration of the silicon melt through the accessible open interconnecting porosity of the architecture creating the bulk SiC;
3). Diffusion of the carbon through the evolving SiC layer (and visa versa) for continued and rate limiting step growth of the bulk SiC layer;
4). Development of the silicon phase with dispersed SiC islands, the formation mechanism of which is still not agreed upon.

Furthermore, in addition to these mechanisms, other factors that affect LSI must also be considered, which include: type of siliconisation i.e. direct or indirect; quantity of silicon, related to the internal open porosity and the silicon phase transition anomaly;

manufacture conditions e.g. temperature; and, addition of further elements i.e. silicon alloy melt to infiltrate a instead of pure silicon, and are also discussed.

1). Silicon vapour infiltration:

Schule-Fischedick *et al* [144] documented the presence of a fine SiC layer and attributed its formation to silicon vapour that readily accessed this open porosity at temperatures prior to reaching the melting point of the silicon. The mean layer thickness was approximately 3 μm with a mean size of around 100 nm, as shown in Fig. 25(a). Verala-Feria *et al* [164] observed a similar fine SiC layer, but it was not present throughout the entire structure; they attributed this to the effect of LSI temperatures and possible higher localised reaction temperatures of up to 500°C, which was supported by Pampuch *et al* [165, 166] who performed differential thermal analysis. However, according to Schule-Fischedick *et al*, XRD (Fig. 25(b)) and SAD patterns from TEM (Fig. 25(b) inset) suggested that the SiC was a mixture of α and β-SiC.

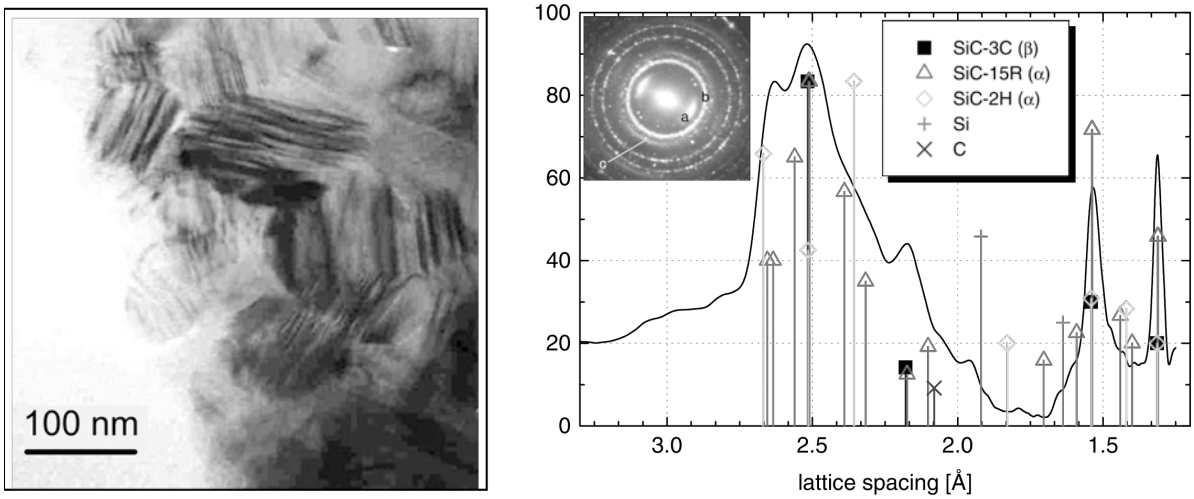

(a) (b)

Fig. 25. TEM micrographs illustrating: (a) the nano-sized SiC layer at the C/SiC interface and (b) XRD pattern of the SiC with inset SAD pattern [144].

However, considering highest mean temperature was only 1650°C, it was unlikely but still feasible that local temperatures could exceed 2000°C resulting in the β to α-type transformation. Using computer simulations, the possible occurrence of β-SiC in the diffraction profiles was investigated by Pujar and Cawley [169]. It was revealed that this feature might have been caused by stacking faults in β-SiC and not due to the presence of

other polytypes. Therefore, the nano-crystalline SiC layer was thought not to consist of a mixture of polytypes, but instead, of β-SiC with a high density of stacking faults that can be seen in Fig. 25(a).

Only a limited number of investigations exist that discuss the mechanisms of silicon vapour infiltrating porous carbonaceous materials. One such was by Qian *et al* [170] who similarly reported that growth of the SiC layer was dependent of the diffusion of silicon vapour through the primary porous SiC layer and further gas–solid reaction of silicon and carbon at the C/SiC interface. Meanwhile, as previously reported, Wang *et al* [151] used silicon vapour to infiltrate different porous carbon preforms with porosity that ranged between 35 and 67% with a pore size from 0.03 to 2.58 μm that were infiltrated with silicon vapour. The final composite was successfully infiltrated possessing a density of 3.12 g/cm^3 and Si-content 8 vol.%. However, the implications of a silicon vapour generated SiC layer followed by SiC generated by a silicon melt were not reported.

2). Silicon melt infiltration:

Beyond the melting point of the silicon, the silicon infiltrates the porous architecture, reacting with any carbonaceous matter to create a SiC. The reaction is very rapid, lasting seconds [171]. The mean thickness of the coarse SiC layer ranged from between 1 and 30 μm in all reported investigations [144, 163, 164, 167].

Favre *et al* [163] used direct-LSI at 1600°C and investigated the thickness change in the SiC with increasing time. SEM micrographs in Fig. 26 illustrate the hierarchy and format of the microstructure. The hierarchy remained the same, irrespective of the reaction period or type of LSI (direct or progressive). In fact, the hierarchy of the microstructure was the same in all reported investigations. Meanwhile, additional information regarding the impact of using progressive or direct LSI on the infiltration height of the SiC in these composites is discussed later. Meanwhile, TEM and XRD investigations throughout the literature (Fig. 25(b)) indicated that the polytype of the coarse SiC when manufactured at temperatures under 2000°C was face centred cubic (FCC) β 3C-SiC, while at temperatures above 2000°C, hexagonal α-SiC was observed [144, 168, 163, 247].

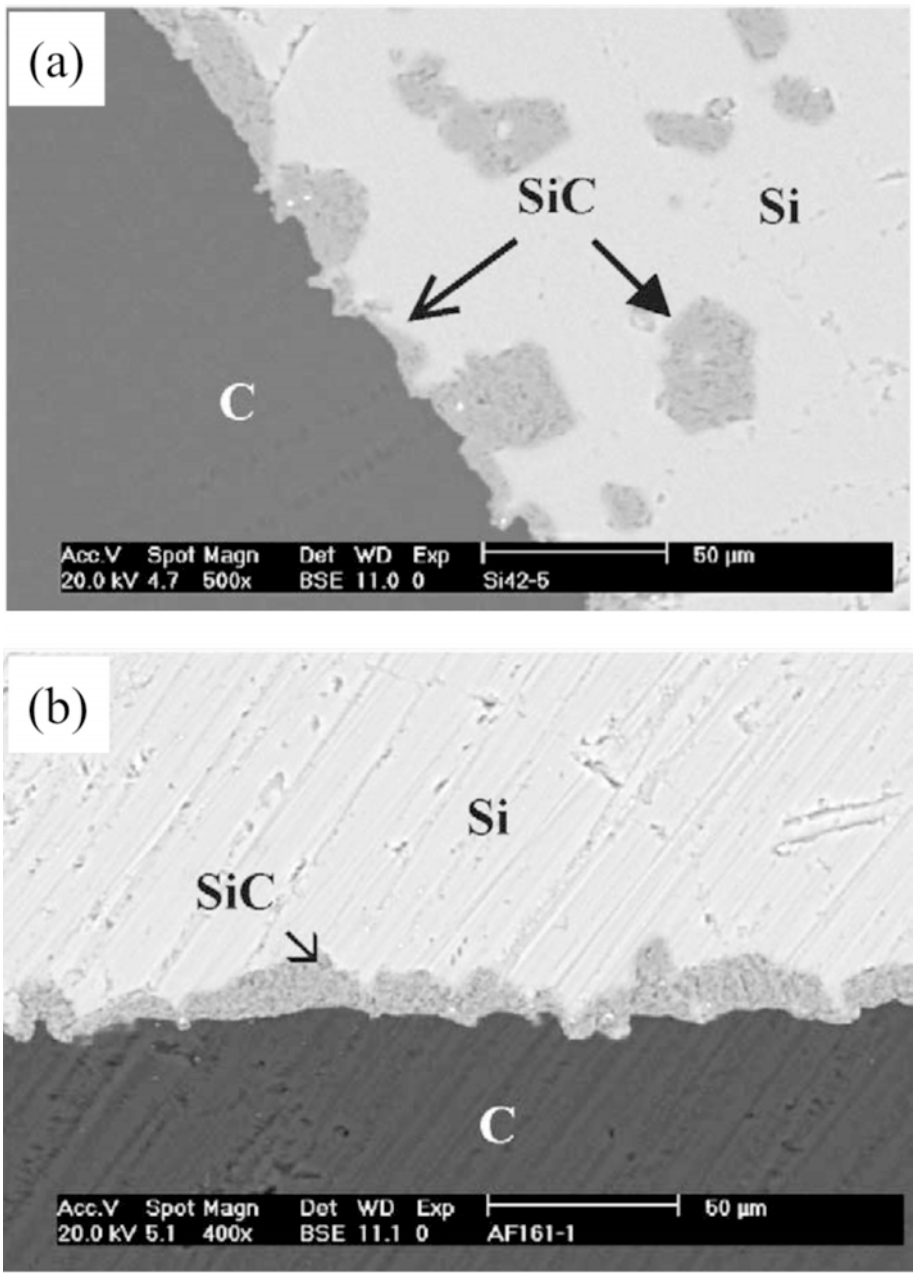

Fig. 26. SEM micrographs illustrating the same hierarchy in the microstructure after LSI at 1600°C for (a) 7 minutes and (b) 90 minutes [163].

A fast reaction can only occur under the condition of accessible pores and a large surface area [172], where the infiltration of porous bodies is described by the well-known Washburn equation [173].

$$x^2 = \left(\frac{\gamma.\cos\theta}{2\eta}\right)\cdot r \cdot t \qquad (2)$$

where, ‘x’ is the infiltration depth, ‘r’ the pore radius, ‘t’ the infiltration time, ‘η’ the viscosity, ‘γ’: surface tension and ‘θ’ the contact angle, which was investigated [150, 172, 174]. The term in brackets is the so-called ‘penetration coefficient’. The typical values for pure liquid silicon are shown in Appendix B – Table 5.

Gern and Kockendörfer [174] presented a model to predict the infiltration kinetics of molten silicon in idealised tubes, which was in agreement with LSI experiments. The C_f/C architecture was a T-300 plain weave, which was pyrolysed at two temperatures: 900 and 1600°C in an attempt to vary the internal architecture and make comparisons. The infiltration dynamics were modelled and the statistical frequencies of the capillary diameters were measured, which are shown in Fig. 27(a) and (b) respectively.

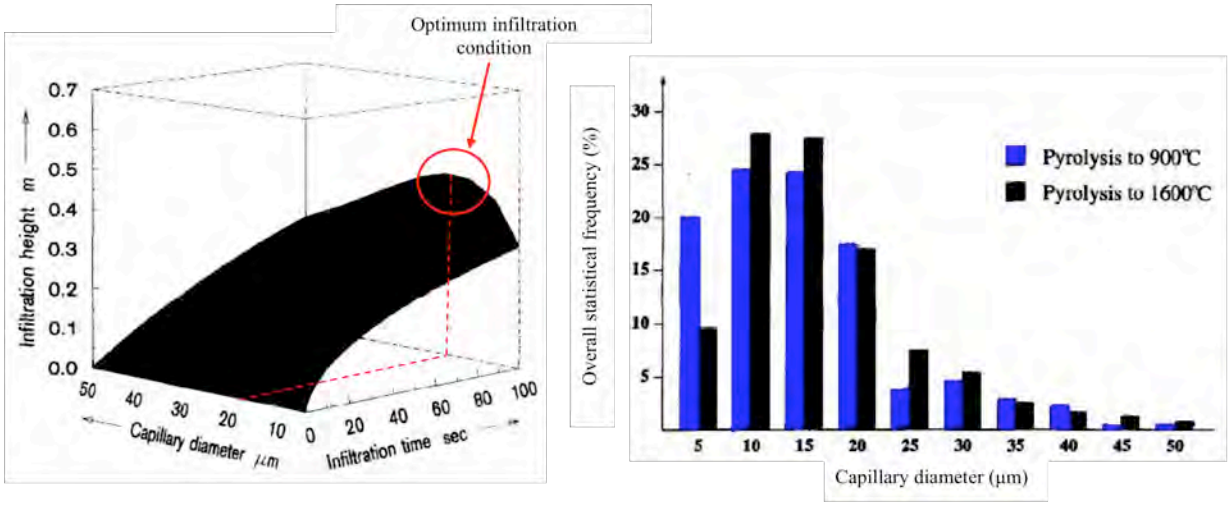

(a) (b)

Fig. 27. Graph showing (a) the infiltration dynamics of a single capillary system, with the optimum infiltration condition highlighted, and (b) the measured statistical frequency of capillary diameters for two different pyrolysis temperatures [174].

Based on the model in Fig. 27(a), it was predicted that the optimum infiltration conditions that generated the maximum infiltration heights were tubes measuring 20 μm with an infiltration time of 100 seconds. Meanwhile, according to Fig. 27(b), it was found that pyrolysis at 900ºC would favour more narrow tubes, especially around 5 μm. While at 1600ºC, the statistical frequency of wider diameters was increased, in particular 25 μm. This would indicate that for this study, the ideal pyrolysis temperature was between these two temperatures. However, since there is an almost indistinguishable difference for the

statistical frequency for 20 μm between 900 and 1600ºC, there is no clear advantage of either pyrolysis regime.

Meanwhile, an investigation by Raether *et al* [172] compared the pure silicon infiltration depth (mm) of a straight tube for two different infiltration temperatures, one just above the melting point of pure silicon, at 1485ºC and a higher temperature; 1700ºC. The results are illustrated in Appendix A – Fig. 11. It was from the results that an increase in temperature significantly improved the silicon infiltration height with time. This is supported by the physical properties of silicon melt, namely the viscosity that reduces as the temperature increases. However, these results correspond to a theoretical tube geometry. Therefore, it is unlikely that a real multi-dimensional fibre architecture would demonstrate similar infiltration kinetics.

This field of research was furthered by Yang *et al* [150], who used a modified version of the Washburn equation that also took into consideration the capillarity and resistance of the viscous and gravity forces of the liquid melt inside a porous preform, and also included a turtuosity factor to represent a more realistic wavy internal porosity:

$$\frac{dh}{dt} = \frac{C}{8\mu h}\left(\frac{2\sigma.\cos\theta}{r(t)} - \rho g h\right) r(t)^2 \qquad \textbf{(3)}$$

where ‘h’ is the infiltration height, ‘t’ the time, ‘μ’ the viscosity, ‘σ’ the surface tension, ‘θ’ the contact angle, ‘r(t)’ the mean pore radius, ‘g’ the gravity, ‘ρ’ the density, and ‘C’ the turtuosity factor, whose value was taken to be 1/3 that assumed isotropic porous media. Using the equation, theoretical liquid silicon infiltrations were preformed based on (3) at 1527 and 1627ºC [150], the results are shown in Appendix A – Fig. 12.

Naturally, as the infiltration time increased, the height and diameter increased. However, an increased height was reached at 1527ºC in comparison to 1627ºC. This was attributed to an increase in the infiltration index and correspondingly, the infiltration capacity. It was speculated that at the higher temperature, the chemical reaction rate increased, which resulted in a rapid build-up of SiC that reduced both the pore size and subsequently the infiltration rate.

The effect of the pore size and contact angle for unidirectional capillary infiltration of molten silicon on carbon was studied by Asthana [175]. A schematic of the

model is shown in Fig. 28, where it is evident that the angle of contact between SiC layer and silicon plays an important role for silicon infiltration.

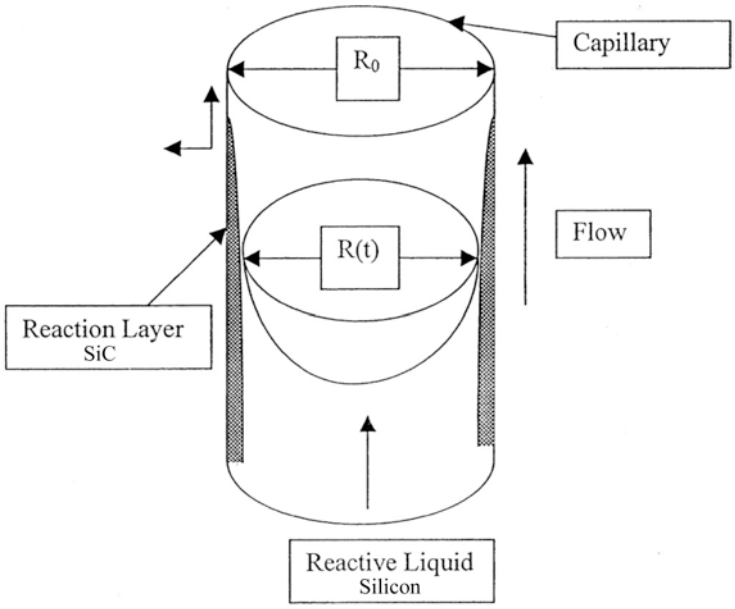

Fig. 28. Schematic of the reactive infiltration of molten silicon, illustrating the dynamic evolution of the capillary radius and contact angle due to interphase formation via chemical reactions [175].

The contact angle varies from 0 to 22º for silicon versus carbon under vacuum [162, 175] and also varies with reaction time [175]. It was reported that a capillary-driven flow analysis from the Washburn equation overestimated the infiltration kinetics, whereas an analysis that considers pore shrinkage with decreasing capillary radius, 'R' ('r' in equation (3)) but assumes the contact angle 'θ' and the capillary pressure, 'P_c', where $P_c = \sigma.\cos\theta(t) / R(t)$ to be constant during flow, thereby underestimating the kinetics.

More recently, Kumar *et al* [162, 176] developed a theoretical model using the modified Washburn equation to investigate the infiltration height of molten silicon and the thickness of developed SiC in a 3D stitched C_f/C preform. The theoretical model was based on a modified version of the Washburn equation. However, their model included a parabolic-reaction rate constant, 'M', which was introduced to account for any changes in the pore radii size in the preform, where: $r(t) = r_0 - M\sqrt{t}$ (from the Washburn equation), 'r_o' is illustrated in Fig. 28 and contact angle 'θ', which varies between 0 and 22°. Values for 'M' and 'θ' were validated using experimental testing, which was conducted on preforms measuring: 150 mm long, 17 mm wide and 50 mm thick. Each preform was suspended inside a furnace and lowered by hydraulic means into a pool of molten silicon,

for different time periods ranging from 6 to 180 seconds. The heating rate was maintained to achieve the temperature rise in the range of 10–15°C/min and held at 1650°C under vacuum conditions. The infiltrated height of the silicon inside the carbon fibre preforms was estimated using X-rays, which have been added to Appendix A – Figure 13 [162].

Under these test conditions, the infiltration height of the silicon increased up to the maximum height of the preform (150 mm) with increasing time. Comparisons between the theoretical and experimental tests are shown in Appendix A – Figures 14(a) and (b) respectively. It shows a close match when the parabolic-reaction rate constant, 'M' and contact angle 'θ' was 1.75 $x10^{-7}$ $m/s^{1/2}$ and 22°, respectively; indicating that the model used could be used for 3D stitched C_f/C preforms. However, it is also clear from the images that the infiltration height reached was not uniform, which was attributed to a non-uniform local pore size and complex architecture. Not only will the size of the pores inside the preform have been variable prior to LSI, but also will have become smaller as SiC formed. In fact, as the SiC layer developed inside the pores, depending on their size, would not have been uniformly thick. The maximum thickness would be at the mouth of pores and at the bottom, while the thickness would be negligible at the top of the infiltrated height. This is illustrated in the schematic in Fig. 29, which shows an idealised SiC development in (a) and a more realistic development in (b).

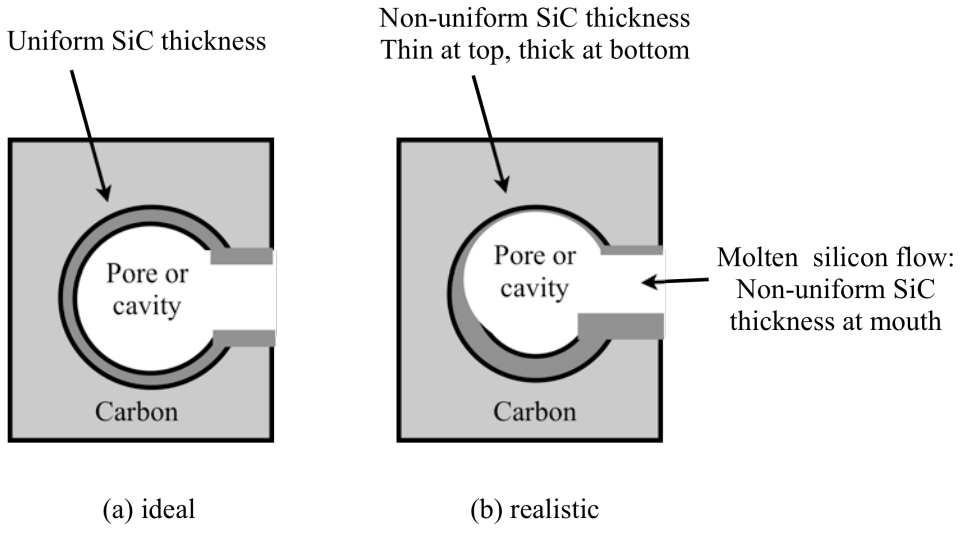

Fig. 29. Schematic illustrating (a) an ideal uniform SiC formation and (b) a more realistic non-uniform SiC formation at the mouth and inside the pore or cavity.

However, their Washburn version/modification of the equation assumed uniform thickness throughout the infiltrated height in the pores, and is equal to that at the pore

mouth. Furthermore, it was shown in their experimental study that a contact angle of 22° was the closest match. It is however, unlikely that the contact angle remained constant throughout siliconisation, especially if a narrow SiC layer developed prior to melt infiltration as previously identified by Schule-Fischedick *et al* [144].

The preforms that were infiltrated for 30 and 180 seconds were cut along the X-section and studied using an optical microscope, which are shown in Fig. 30. In these micrographs: white is silicon, grey is SiC and black is the carbon. The micrographs illustrate the typical microstructure: a continuous and non-uniform thick SiC layer surrounding the carbon matter, with the SiC islands embedded in the silicon pools. It appears that there was an increased proportion of SiC in the microstructure as the reaction time increased from 30 to 180 seconds, although no statistical data was gathered. However, it could be easily envisaged that an increased reaction time could promote more SiC, but this would also depend on the available and supply of carbon i.e. architecture.

Meanwhile, the theoretical calculation used for estimating the thickness of the developed SiC on a flat horizontal surface is shown below [162]:

$$\delta = \sqrt{\left(\frac{2D}{\rho} C_{si,l}\right)\sqrt{t}} \qquad \textbf{(4)}$$

where ‘δ’ is the thickness of SiC layer (m), ‘ρ’ is the density of SiC, 3217 kg/m^3, ‘$C_{Si,l}$’ is the density of silicon in the liquid phase, 2500 kg/m^3, ‘t’ is the reaction time (seconds) and ‘D’ is the diffusion coefficient of the silicon through the SiC layer (m^2/s), which has the Arrhenius form of:

$$D = D^o e^{-E/RT} \qquad (5)$$

where ‘E’ is the activation energy of 132 kJ/mol, ‘D^o’ is the diffusion constant of 2x10^{-6} cm^2/s, ‘R’ is the Regnault constant of 8.314472 J.K^{-1}.mol^{-1} and ‘T’ is the temperature (k) [162].

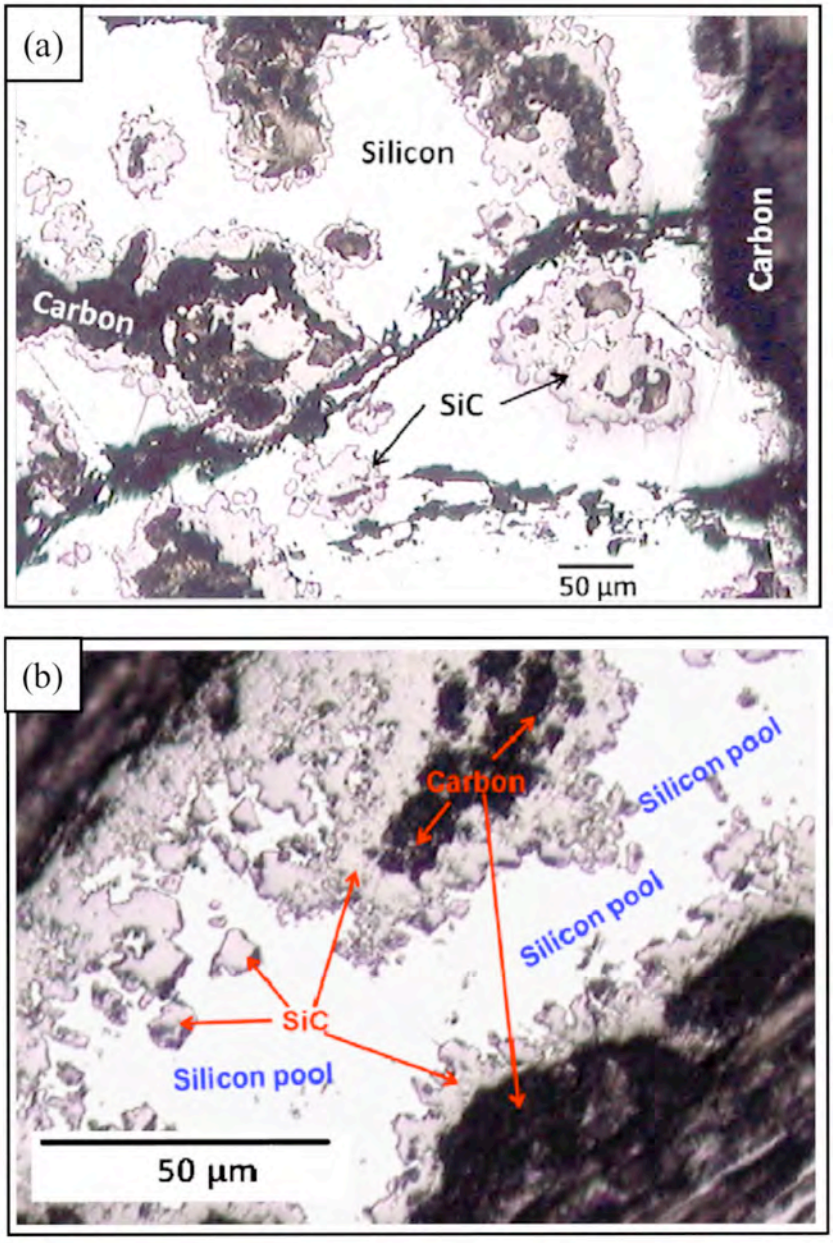

Fig. 30. Optical micrographs of C_f/C preform after direct-LSI at 1650 °C after (a) for 30 seconds and (b) 180 seconds [162].

Therefore, at a siliconisation temperature of 1650°C, equation (4) now varies with time, where: $\delta = 2.841 \times 10^{-7} \sqrt{t}$. However, it should be acknowledged that the thickness of the SiC layer (δ) would grow in the two opposite directions away from the SiC/silicon interface: into the pool of molten silicon and also into the carbon.

Favre *et al* [163] meanwhile, in a continuation of the previous investigation, analysed how the SiC thickness changed with increasing time period and types of LSI: progressive and direct, at 1500 and 1600°C. The results are shown in Appendix A – Figure 15. As the reaction time increased to approximately 140 minutes, the average SiC

thickness increased to a maximum of around 10 µm. Meanwhile, when direct and progressive-LSI were compared at the same temperature (Appendix A – Figure 15(b)), both followed the same trend: rapid increase at the start followed by a gradual increase to a steady maximum of approximately 10 µm at approximately 140 minutes. However, progressive LSI was more variable, in particular at the beginning of LSI up to 30 minutes, where thicknesses of between 5 and 20 µm were evident.

However, in these investigations, there was no indication of the possible impact of significant local temperature increases, caused by the exothermic reactions; or the 'Venturi effect', which might be attributed to the over simplified models without adjoining perpendicular tubes. According to the Venturi effect, which is illustrated in Fig. 31, the pressure increases as the speed slows in larger regions of the tortuous architecture. Consequently, as the liquid silicon or even silicon vapour travels down the tube, it is likely to be drawn into adjoining tube networks depending on the width of the tubes.

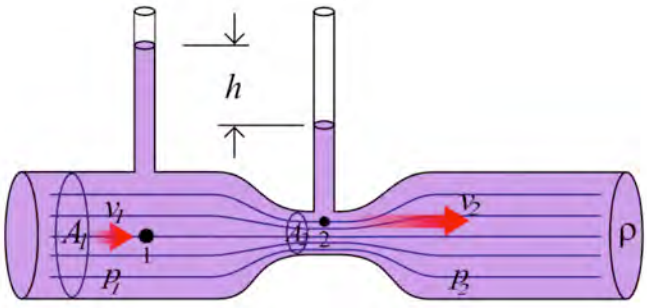

Fig. 31. Schematic illustrating the 'Venturi effect' and the impact of the area (A) on the flow speed (v) inside the tortuous tube. An increased pressure is exerted at '1' in comparison to at '2', which increases the relative height uptake (h) at '1'.

The scope of the published research to date prompted further questions regarding the effect of the carbon source, thickness of the carbon matter and dependence of the architecture on the thickness and proportion of the generated SiC. Since there was currently no published data addressing these parameters, each was address in *Section 4.2*.

3). Diffusion mechanism and continued growth of the SiC layer:

As the SiC forms by infiltration of the melt, a layer is generated that becomes thicker in nature and a barrier is created between the carbon and molten silicon, which increasingly inhibits further conversion reactions. Diffusion of carbon through the evolving SiC is the widely accepted mechanism for the continued creation of the bulk

SiC layer, which eventually ceases. However, considering the work by Hon *et al* [177, 178] who found that the lattice self-diffusion coefficient rate of carbon was up to 100 times higher than silicon, it is more likely that the carbon diffuses outwards through the evolving SiC layer.

4). Silicon and SiC islands beyond the SiC layer:

As the evolving SiC layer grows thicker, infiltration and diffusion reactions are progressively inhibited to the point at which they cease. Consequently, a region of unreacted re-solidified silicon exists beyond the SiC. However, in this region, SiC islands can be observed, the formation mechanism of which is still not agreed upon. It has been speculated that the mechanism is a combination of solution and precipitation [144, 165]. Favre *et al* [163] alternatively hypothesised alternating periods of crystallisation and breaking away of SiC from the SiC region. Zollfrank *et al* [167] believe the mechanism to be one of diffusion, dissolution and re-crystallisation. Further investigations into the mechanisms governing the SiC thickness and the crystallographic structure and polytype of SiC created by different carbonaceous sources have been discussed in *Section 4.2.4*.

5). Other influences:

(a) Type of siliconisation

There are two main types of LSI, progressive and direct that were previously highlighted in the manufacture flow chart in Fig. 23. During progressive siliconisation, porous C_f/C preform is placed in direct contact with the silicon at room temperature and heated beyond the melting point of the silicon for pure silicon and permitted to infiltrate the preform.

The reaction between the carbon e.g. pyC and silicon begins immediately after the silicon or related silicon-based alloy makes contact. By contrast to progressive siliconisation, during direction siliconisation, the silicon is heated up separately and poured directly onto the carbonaceous matter e.g. porous C_f/C preform at or beyond the meting point of the melt. This method avoids any early reaction between the silicon and the pyC and/or interface beyond the silicon melting point.

From an earlier investigation by Yang *et al* [150], the infiltration kinetics of progressive and direct-LSI were compared at two different temperatures: 1427 and 1487°C (1700 and 1760 K respectively), which is illustrated in Appendix A – Fig. 16.

Since the silicon is heated up whilst in contact with the carbon preform during progressive-LSI, the preform would be susceptible to silicon vapour reactions at temperatures prior to and after reaching the silicon melting point (1414°C), which could affect the infiltration mechanism.

Furthermore, contrary to the time scale of the progressive-LSI infiltrations, as shown in Appendix A – Fig. 16(a) and (c); the actual reaction time period for the melt would begin immediately after reaching the melting point and would be dependent on the heating and cooling rate beyond 1414°C. This would undoubtedly add a significantly longer period of time to the overall reaction time in comparison to direct-LSI. When comparisons are made between the progressive-LSI and direct-LSI, it can be seen that a greater height is reached by progressive-LSI, which could be attributed to the pre-infiltration of silicon vapour, but is most likely due to the extended reaction time. This is in accordance with previous investigations discussed.

Meanwhile, the effect of temperature had little effect on the infiltration kinetics according to the model. Only a slight increase was observed in the maximum infiltration height, although could be in agreement with work by Raether *et al* [172], who demonstrated a more rapid increase in height with temperature.

(b) Silicon phase transition anomaly

Due to the standard silicon phase transform anomaly, the purity of the silicon plays in important role in effective LSI. According to the data in Appendix B – Table 5, the density of solid silicon, ~2.34 g/cm^3 is lower than the silicon melt, ~2.53 g/cm^3, therefore as the silicon cools down, it expands or contracts. The preform is therefore at risk of damage or cracking if too much silicon is infiltrated into the preform or if restricted due to the carbon fibre. This could however possibly be alleviated by either using an alloy melt, as discussed in (c); ensuring sufficient open porosity; or alternatively, prescribe an exact silicon dosage. However, the dosage is particularly difficult to determine because of the variable quantity of internal connecting porosity [33].

This was investigated by Margiotta *et al* [86], who defined the fractional volume upon conversion of solid carbon to porosity-free SiC, and concluded that the ideal bulk density of the porous carbon preform would be 0.964 g/cm^3 based on a minimum pore size of 1 µm, as previously highlighted. It was further speculated that when carbon pore diameters insider the porous carbon structure drop below approximately 1 µm, the volume increase caused by SiC formation at the carbon preform surface could lead to a

'pore-choking' that inhibits and restricts further silicon infiltration, resulting in early termination of the reaction near the carbon pre-form outer surface.

(c) Liquid silicon alloy infiltration

Instead of using pure silicon during LSI, the melt can be modified with a number of additives, such as: iron, chromium, titanium, molybdenum, molybdenum disilicide ($MoSi_2$), nickel or aluminium [31, 84, 179] to facilitate infiltration or tailor the final properties of the matrix. For example, Gadow *et al* [179] showed a particular preference to a silicon melt containing 5 to 50% weight of iron and 1 to 10% by weight of chromium, where the iron lowered the melting point of the silicon and was suspected to enhance brake performance by improving the compatibility with traditional brake linings.

Esfehanian *et al* [84] made comparisons between silicon alloy infiltrated carbon fibre preforms, which resulted in a C_f/MoSiTi composite and traditional silicon infiltrated C_f/SiC composites. Two different preform architectures were investigated: a short non-coated carbon fibre felt and a bi-directional pyC coated woven C_f/C preform. SEM micrographs of the C_f/MoSiTi composites with corresponding stress-strain curves derived from bend strength tests are shown in Appendix A – Fig. 17(a) and (b) respectively.

It was reported that additions of chromium, titanium, molybdenum, nickel or aluminium resulted in a reduction in the solidification volumetric increase, in comparison to pure silicon. This is supported in the micrographs, because there is no evidence of any characteristic cracks that result from the CTE mismatch between the silicon alloy and preform. Also from the micrographs, the proportion of the matrix (white and grey) inside the felt preform is significantly greater than compared to the woven C_f/C preform. This is likely attributed to the much higher open porosity and lower density of the felt preform prior to infiltration, which was 40-42% and 0.13-0.15 g/cm^3 respectively for the felt preform and 6-8% and 1.6-1.65 g/cm^3 respectively for the woven preform.

As a consequence of this high porosity during infiltration, both the silicon and alloy melt would have easily accessed the unprotected fibres of the felt preform and significantly degraded their properties. This is confirmed in the bend strength stress-strain curve for each preform, which shows that both felt preforms failed catastrophically.

In contrast, it was reported that the pyC coated fibres inside the woven C_f/C preform exhibited a good resistance against the melt and formed a weakly bonded interface with the matrix after infiltration. These characteristics should provide a non-catastrophic mode, which can be seen in the stress-strain curve (Appendix A – Fig.

17(b)). The results were 199 ±3 and 206 ±19 MPa for the C_f/C + MoSiTi and C_f/C + Si respectively. Furthermore, the strength of these samples increased at 1600°C, to 244 and 246 MPa respectively, which was related to an increase of the strength of the fibres themselves.

Meanwhile, Yang *et al* [150] investigated the infiltration kinetics of silicon alloy melts containing aluminium and copper. It was reported that aluminum generally suppressed the infiltration rate, while the influence of copper depended on the composition. Infiltration was enhanced for low concentrations of copper and attenuated for higher concentrations, while increasing the temperature enhanced both the infiltration capacity and the reaction rate.

2.3.2.3. Oxidation issues associated with the liquid phase routes

A notable property of LSI CMC's is the potential of low porosities, which is favourable for oxidation resistance, where optimised LSI can create CMC's with porosities as low as 2-5% [143], although LPI manufacture generates higher porosity in the 15-20%. However, one of the fundamental issues with liquid phase processing is the CTE mismatch between the fibre-matrix (up to several orders) and matrix-surface coating during both heating i.e. pyrolysis [87] and cooling. As the pyrolysis temperature increases beyond 505°C, high fibre-matrix bonding stresses locally exceed the tensile strength of the polymer matrix that results in a relaxation by cracking throughout the fibre bundles, which will facilitate the in-depth infiltration of oxygen [76].

This phenomenon was confirmed by Bae *et al* [153] for as-received carbon fibre during LSI, which resulted in significant degradation of the fibre. Although, from a processing standpoint, a micro crack network appears beneficial because it aids thorough infiltration of the silicon melt into the preform during liquid phase routes. In addition, it permits gaseous precursors to readily penetrate. However, liquid silicon melts are corrosive to any carbon fibres that are not sufficiently protected, which necessitates the requirement for an interfacial layer on the fibre [139, 138, 140].

The mechanisms governing the microstructural evolution during LSI have been reviewed [144, 163, 167, 164, 168] and can be summarised in three steps: infiltration of gaseous silicon at temperatures under 1414ºC; silicon infiltration into the architecture at temperatures above 1414ºC to create the bulk SiC; and finally, diffusion of carbon

through the evolving SiC layer. Beyond the bulk SiC lies a region of unreacted re-solidified silicon with SiC islands that were interspersed in close proximity to the SiC/Si interface. However, only limited and in some cases conflicting experimental support has been available. Therefore, an investigation was designed to try and understand the microstructural evolution further, which has been added to *Section 4.2*.

2.3.3. Slurry infiltration and hot pressing

Slurry Infiltration and Hot Pressing (SI-HP) methods using different carbon fibre volume fractions in the range of 28 to 55 vol.%. The raw materials required to form the matrix are a mixture of nano β-SiC powder, required to lower the sintering temperature e.g. Marketech International Inc., America [180]; the composition comprised of SiC > 95%, free carbon 1-2% and oxygen 1-1.5%, with an average diameter typically below 30 nm but as high as 60 nm and typical sintering additives of (6 wt.%) Al_2O_3 and (4 wt.%) Y_2O_3. The nano-SiC powder and additives are typically ball milled for 3-4 hours, for example using SiC balls. After drying, the powders are dispersed in xylene with polycarbonsilane (PCS) [36, 180] to form the slurry. The slurry infiltrates into and in between the carbon fibre tows, which are wound to form aligned uni-directional composite sheets and later stacked in the desire orientation. After drying, the sheets are typically cut to size and pyrolysed in an inert atmosphere such as argon. The sheets are stacked in a graphite die and sintered by hot pressing at high temperature; 1850ºC under 20 MPa [36, 181] or 1720-1780ºC under 15-20 MPa [180]. Machining and polishing ensues to complete fabrication of the C_f/C-SiC composite.

Typical properties include: a density of between 2.27 and 2.6 g/cm^3, low open porosity between 2.4 and 4.8% and a high variable flexural strength between 198 and 500 MPa depending on the carbon fibre volume fraction [36]. Hot isostatic pressing (HIP) has also been identified as a potential fabrication route, but is associated with high cost and several known fabrication difficulties [181]. Optimisation and adoption of hot pressing techniques relies primarily on an effective densification process, but also the incorporation of a suitably protected carbon fibre preform architecture in order to avoid fibre degradation caused by the high temperature.

If the densification process is effectively promoted, the sintering temperature and pressure should be as low as possible. Dong *et al* [180] reported such a method using Al_2O_3 and Y_2O_3 as additives; then lower temperature densification of SiC was possible.

Meanwhile, research by Ding *et al* [36] showed that the densification process became increasingly difficult with increasing carbon fibre volume fraction and some small pores were still distributed in the intra-bundle regions of the composites. However, increasing the carbon fibre content improves the mechanical properties, in particular the fracture toughness.

2.3.4. Miscellaneous routes

A variety of miscellaneous routes have been developed to try and alleviate some of the inherent disadvantages using traditional techniques, including: sol-gel processing, electrophoretical deposition/infiltration [182, 183], rolling [26] and carbothermal reduction reaction [184, 185], powder compaction [186] and spark plasma sintering [187].

2.3.4.1. Sol-gel processing

Sol-gel research thrived particularly in the 1990's, which led to a range of products and applications for sol-gel derived materials including C_f/SiC composites. Modern sol-gel processing has potential to not only fabricate C_f/SiC composites but also provide adequate oxidation protection [188, 189] in the form of coatings [190], by dip coating or spin-coating. For example, fluoride rich sol-gel derived coatings provide oxidation protection via the silica formation process and flexible coatings, which are reported to not crack [188].

In a typical sol-gel process, the precursor e.g. distilled water, hydrochloric acid (HCl) and/or ethonol and tetraethyl-orthosilicate (TEOS) [188], or alternatively tetraethyl orthosilicate (TMOS) [189] in specific concentrations is subjected to a series of hydrolysis and polymerisation reactions to form a colloidal suspension i.e. the 'sol'. This 'sol' is then infiltrated into a typical porous carbon fibre mat or fabric, which constitutes as the preform. When the 'sol' is cast into the preform, a wet gel will form. With further drying, pyrolysis heat-treatment up to 2000ºC and/or pressing up to 30 MPa [189], the gel is converted into a ceramic, in this case: a SiC matrix.

Attributes of the route include: the capability of forming homogeneous high purity matrices, potential for creating a multi-phase uniform matrix, low processing temperature, potential to fabricate intricate shapes and capability to create an in-situ oxidation protective coating [190]. However, the apparent major disadvantage of the sol-

gel processing is the large volume shrinkage during the curing and pyrolysis stages that could make the preform susceptible to oxidation because of the induced cracks.

2.3.4.2. Electrophoretical deposition

Electrophoretical Deposition (EPD) is used in industry particularly for applying coatings to metal fabricated products, although has been recently developed to fabricate C_f/SiC composites [182]. A characteristic feature of EPD is that colloidal SiC particles are suspended in a liquid medium, migrate under the influence of an electric field (electrophoresis) and are deposited onto an electrode. Due to the electrical conductivity of carbon fibre, it can be directly used as the deposition electrode, while another set of counter-electrodes are used to complete the circuit. The carbon fibre preform is submerged into a container or vessel that holds the SiC solution before applying a direct current, using typical voltages between 25-400 volts DC. After deposition, the preform is normally rinsed to remove the undeposited bath.

Advantages of EPD include: processing is completely automatable, thick and complex ceramic pieces are feasible as are tailorable microstructures, such as functional gradients and laminates through suspension control during processing. One of the main challenges facing EPD is the requirement of the SiC powder to be well dispersed inside the carbon fibre mat/roving for successful infiltration. Therefore, nano sized SiC powders are ideally used to facilitate sintering and infiltration between the carbon fibre roving's. However, such powders are currently very expensive [182], making the process unfeasible for cost-effective processing.

2.3.4.3. Rolling

C_f/SiC composites have also been fabricated through continuous rolling of carbon fibre, by soaking it with SiC on a mandrel [26]. After an initial sintering stage, the large 'doughnut' shaped composite could then be sliced to the desired thickness. The slices could then be sintered to actual size or built up through a series of layers depending whether further internal treatment was required. However, composites manufactured by rolling were reported to exhibit a high open porosity of around 23%. In addition, the surface fibres were fractured as a result of the slicing and micro-cracking was evident, which was caused by handling and the CTE mis-match between the matrix and

reinforcement. Therefore, for these reasons, the technique is not commonly employed as a primary route for C_f/SiC composite fabrication.

2.3.4.4. Carbothermal reduction reaction

Carbothermal reduction synthesis of SiC is a relatively old process that was developed at the end of the 19th century and was termed the 'Acheson process'. Today, the process can be used to produce commercial SiC powder through the reduction of SiO_2 by carbon.

As reported by Lin *et al* [184] for SiC modified C_f/C composites, the process is performed at 1400-1800°C; where solid silicon dioxide, $SiO_{2\ (s)}$ reacts with solid carbon, $C_{\ (s)}$ to produce SiO gas and CO gas. The SiO gas then reacts with the solid carbon to form solid SiC and CO gas. In their reported work, the C_f/C was fabricated by impregnating a 2D carbon fibre cloth that contained pure phenolic resin or 20 phr (parts per hundred) of silicon dioxide with phenolic resin, which was then placed inside an oven at 70°C for 2 hours to remove the excess solvent. The pre-preg were then stacked and pressed at 160°C under 2000 psi (about 13.7 MPa) for 30 min. Composites were cut and post-cured at 230°C for 8 hours, prior to being pyrolysed at 1000°C under an inert nitrogen atmosphere for 30 minutes. The C_f/C was then heat treated/carbonised inside a graphite furnace at 1600 to 2200°C, where heat treatment affected the mechanical properties of the C_f/C composite. It as concluded that since the structure of carbon fibre is more ordered than that of the carbon matrix; therefore, the SiO gas reacted with the carbon matrix, rather than the carbon fibres. However, there was reported to be variability in the mechanical properties, which required further work to gain a more thorough understanding. Consequently, the process still lacks maturity to be considered as a commercial process.

2.3.5. Combination fabrication routes

Combinations of traditional routes are becoming more popular because of their capability to alleviate the limitations of any one single process.

2.3.5.1. Isothermal/isobaric- chemical vapour infiltration and reactive melt infiltration

CVI, in its I-CVI or P-CVI versions, is the method of choice for the deposition of simple or highly engineered interfaces since it yields deposits of relatively uniform composition, structure and thickness, even with preforms of complex fibre architecture. RMI can then be utilised to fill the residual open porosity. I-CVI and RMI are complementary because of the residual porosity of CVI-composites, which can be fabricated at a suitable state of densification and be filled via an RMI-step [88].

2.3.5.2. Slurry infiltration, polymer impregnation & pyrolysis and pressurised-chemical vapour infiltration

SI-HP techniques [36, 88, 180] notably yield composites of almost no residual porosity, which is favourable for improving the oxidation resistance. Conversely, SI-HP is a high temperature and pressure process in the range of 1700-1800°C and 25 MPa respectively and therefore suffers from a significant CTE mismatch, with subsequent micro-crack formation. The extent of which is dependent on the interfaces between the fibre-matrix and matrix-outer surface, and fibre distribution within the matrix.

However, as an alternative; it could be possible to densify a carbon fibre preform combining: an impregnation with a SiC powder slurry, to introduce a significant amount of SiC in the preform; several PIP sequences with a polymer precursor to consolidate the SiC particulates deposited from the slurry; and deposit the SiC matrix from a gas phase via P-CVI, to alleviate some of these innate disadvantages.

2.3.5.3. Hot pressing, polymer impregnation & pyrolysis and liquid silicon infiltration

HP, PIP and LSI are complimentary processes, which can be used as a combined process to fabricate C_f/C-SiC composites in a rapid and effective manner. HP will be used during the CFRP fabrication, whilst PIP and LSI will be conducted in a ‘single-shot’ inside the alumina tube furnace. In this process, the preform is orientated and a polymer such as epoxy is impregnated and cured under pressure (HP). The temperature is then raised to 900ºC, held for complete pyrolysis of the polymer into pyC, prior to adding the

silicon, which is heated beyond its melting point (1414ºC) and permitted to infiltrate the porous C_f/PyC architecture.

2.4. Recycling carbon fibre

Academic institutions and companies have recently combined their efforts in the world's first conference dedicated to carbon fibre recycling [191]. Companies and institutions involved include, from the UK: Nottingham University, Warwick University, Sheffield University, Imperial College London, Technical fibre products, Adherent technologies and Recycled carbon fibre Ltd (which used to be Milled carbon Ltd); from Germany: CFK valley stade recycling, Airbus and Fraunhofer Ict; the USA: Boeing, Aircraft fleet recycling association (AFRA) and Firebird advanced materials. According to their outcomes, the key challenges facing carbon fibre recycling today are: recycled composites must be product oriented, by designing the system to produce materials that can be integrated into existing markets; the continued need for collaboration and input from the supply chain industries to identify the challenges in shipping scrap in a format that is easy to recycle, which could help facilitate commercial acceptance; achieving consistency in product quality and supply.

2.4.1. Supply and demand

The continued expansion and growth of the worldwide carbon fibre market will inevitably facilitate the continued research and development into carbon fibre recycling [192, 193, 194]. Since the first commercial production of carbon fibre in the late 1960's, the price for the basic high strength grade was about £200/kg, which due to the continued expansion of the industry, has dropped to between £13-40/kg for an equivalent high strength grade [39].

According to a recent study by Roberts [195], the global investment in carbon fibre was $820 million between 2005 and 2008, which aimed to increase the carbon fibre capacity by 78% to coincide with the increasing demand of carbon fibre tow; estimated as 27,000 tonnes in 2006, into which, CFRP's were estimated to be worth some $9.9 billion. By 2010, the global demand of carbon fibre tow increased to a predicted 34,000 tonnes, which translates to an estimated value in the CFRP market of around $13.6 billion. The forecast for the future is one of growth, where by 2025, global sales of CFRPs are

expected to be worth over $25 billion a year. In terms of global consumption, the market is divided geographically as follows: Europe 30%; North America 35%; Japan 15%; and the rest of the world 20% [195], where the reported global end-use demand for carbon fibre in 2006 was: aerospace/defence 28%, industrial 50% (including infrastructure, wind power and oil and gas) and sports goods 22% [195].

Historically speaking, in Europe the use and consumption of carbon fibre composites has been steadily growing with recent growth from approximately 2,500 t/year in 2002; of which approximately 80% was pre-preg, [196] an estimated 3,000 t/year in 2004 and 10-15% each year since until 2007 [28], which declined in 2008 due to the effects of the global recession. Although, with the new developments in the aerospace industry combined with growing demand in the aerospace industry and other end users, such as military, automotive, wind energy and sporting goods; it is expected that carbon fibre consumption achieve a similar expansion rate of 15% from 2010 [39].

However, the growth of the carbon fibre industry has been characterised by cycles, going from high capacity utilisation with associated supply difficulties and high prices with associated over-supply and falling prices. To illustrate this, between 2008 and 2009, the price of industrial grade carbon fibre has dropped approximately 40% from around £22/kg to £13/kg as a result of falling demand and new supply [39]. In the USA a common reference is that for carbon fibre to breakthrough in such applications as automotive, its price needs to drop to 5 $/lb, which is the equivalent of about £7.5/Kg.

Therefore, considering the current high cost of virgin carbon fibre and the re-use of scrap carbon only accounts for typically 20% of the cost of comparable new carbon fibre; increasing usage with corresponding waste; impending legislation and government strategies, reported elsewhere [194], especially in the automotive sector; rising land fill costs; recycling will inevitably become more appealing and the technology will increase in demand.

However, if recycling is to become part of the mainstream, then there must be a strong market confidence that can only be possible by identifying a sustainable carbon fibre source. One such possible source, at least in today's climate, could be end-of-life and off-cut carbon fibre from aerospace companies such as Airbus and Boeing, because of four factors: firstly, their predicted rate of growth is forecast to account for 15-20% of the worldwide small tow carbon fibre usage by 2010 [195]; secondly, the fibre pre-pregs are of a very high grade to satisfy the highly demanding nature of the application; thirdly, as a consequence of the high grade, such pre-pregs are usually very expensive and

therefore represent a significant potential cost-saving; and finally, due to the manufacturing technologies used today, there is also a high waste percentage that ranges between 30 and 40% as off-cuts [196, 197].

However, in this case, the type and form of carbon fibre would vary depending on the manufacture process, of which there are multiple options depending on the aircraft. For example, hot drape forming (HDF) of pre-pregs and resin transfer infusion (RTI) of dry carbon fibre material, as reported by Airbus. If the HDF technique was used, the amount of carbon fibre composite material used per wing set would be at least 2700 Kg minimum for all spars. The types of waste would then be either: uncured UD pre-preg off-cuts (1 layer) from the first step of the Automatic Tape Laying (ATL) process; uncured quasi-isotropic pre-preg stack off-cuts (5 to 10 cm thick) from the flat panel, also formed in ATL; or cured off-cuts from the trimming of the final part formed by hot forming and autoclave curing.

Alternatively, if the RTI technique was used, the amount of carbon fibre composite material used per wing set would increase to at least 2900 Kg for all spars. The types of waste in this case would be either: dry matrix-free carbon fibre off-cuts from the creation of the part structure or cured off-cuts from the trimming of the final part formed by hot forming and autoclave curing. However, once the carbon fibre is reclaimed, an appropriate recycling technique is required, which are discussed in the proceeding sections.

2.4.2. Carbon fibre recycling techniques

The main challenges in recycling composites are two-fold: firstly, composites comprise multiple constituents that are manufactured using different materials that necessitates the added cost and difficulty of separation, therefore simple composites are favoured such as CFRP's, and secondly, recovery of the fibre is difficult because commonly used thermoset polymer resins such as epoxy and phenolic cannot be recycled by re-melting and de-polymerisation processes. This has facilitated the development of different methods, typically based on thermal and chemical treatment to separate the composite constituents as efficiently as possible to recover the fibre.

However, in addition to simply recovering the fibre, further considerations should also be made to the carbon fibre length and fibre quality. CFRP's are particularly suitable for this because of their high thermal and chemical stability [198]. Long clean fibres have

been demonstrated to retain the bulk of their virgin characteristics, including: Young's modulus, tensile strength and impact strength [194]. Meanwhile, the contribution of matrix degradation during recycling was revealed to play a secondary role [199]. In contrast, milled short fibre products are readily available in the market and have little intrinsic value because they offer low mechanical properties and are produced from milled waste at very low cost [197]. Furthermore, the surface quality of the recycled fibres is typically of high importance. This is because after reclaiming the fibres, another resin is typically impregnated to generate a new matrix. However, in the case where a ceramic matrix is being introduced instead, such as for the composites in this study, protecting the fibre from any corrosive melt, gas or oxidation becomes an additional requirement.

In general, there are four technically feasible methods, miscellaneous techniques being the fourth to recycle carbon fibre from CFRP's. These include: mechanical, chemical and thermal [194, 196, 198], which are discussed in terms of their potential, advantages and disadvantages in the following sections.

2.4.2.1. Mechanical recycling

Mechanical recycling processes break down the composite by cutting, shredding, crushing or milling. In recent times, there has been significant interest in mechanical recycling, mainly because of its accessibility since only low-tech equipment is required, its rapid processing time and economy. However, depending on the requirements of the recycled material, the drawbacks of mechanical recycling can negate any possible benefit, which include an inability to maintain fibre architecture and fibre length. Consequently, only a limited number of applications are feasible, which are typically low value.

Very few companies currently use mechanical recycling at the production level. Two such companies are Milled Carbon Ltd and the European Composites Recycling Services Company (ECRC). However, Milled Carbon Ltd also thermally treat their fibre via pyrolysis as is discussed in *Section 2.4.2.3*. Meanwhile, the main focus of the ECRC is to develop recycling solutions that will meet the demands of the recently implemented European end of vehicle life (EVL) directive [38] and therefore deal with a wide range of different composites.

In terms of carbon fibre composites, research has thus far focused on low temperature milling, autoclaving and pressing of composites that comprise thermoset

polymers as either a cured or uncured pre-preg matrices. The parts are typically cut or crushed to between 50 and 100 mm in the first instance and ground into a finer product in the order of 10 mm down to 50 µm. The scrap can then be used in subsequent autoclave or pressing techniques, typically as fillers [198, 200].

Alternatively, Lester *et al* [197] recycled uncured pre-pregs by initially freezing them using liquid nitrogen followed by cutting using a saw-mill and then manufactured into short fibre composites using similar autoclave and pressing techniques. However, according to research by Fukui *et al* [201], creating short fibre composites typically forfeits many of the mechanical properties. For example, the Young's modulus and flexural strength of chopped fibre (6mm) from a crushed CFRP was about half and one third respectively in comparison to long virgin fibre.

Takahashi *et al* [202] proposed injection moulding as a method to manufacture new CFRP's as secondary structures in cars from existing CFRP that were crushed. The property demands were lower in comparison to typical primary structures and therefore were able to achieve comparable or superior properties in comparison to the virgin CFRP. However, the chemical properties were inferior, which highlighted the necessity to use a suitable resin or even to replace the matrix altogether with a ceramic.

The consortium company MABS offers two categories of recycled carbon fibre. The first is manufactured by mechanical chopping following by milling of the carbon fibre into a C_f/C particulate dust. Currently, the dust is typically land filled at an additional expense, but could instead be utilised as a filler material. However, the second category is manufactured by pressing carbon fibre off-cuts into a disc shape, followed by densification using their standard CVI process that completes a C_f/C composite. The material for this process could also be readily supplied by the aerospace sector, as previously highlighted by Airbus UK as being either: dry carbon fibre off-cuts (matrix-free) or cured off-cuts. The latter could be converted back into carbon fibre with a residual carbon matrix using pyrolysis, which is detailed further in *Section 2.4.2.3*. A photograph of the disc is shown in Fig. 32. The fibre lengths vary considerably and are randomly orientated, which can be seen in Fig. 32(inset). The physical, mechanical and tribological properties of this disc are currently unknown, although are anticipated in order to validate the potential of this novel route. Meanwhile, the disc could also be conveniently converted into a C_f/C-SiC composite by only partially densifying the preform and introducing a SiC (or alternate) matrix by any one of the techniques previously outlined, such as CVI or LSI.

Fig. 32. Photographs of a recycled C_f/C/C brake disc made from off-cut carbon fibre. Inset is an enlarged photograph illustrating the random fibre orientations.

2.4.2.2. Chemical recycling

In the chemical recycling processes, heat and catalysts are applied, usually in an inert atmosphere to break down the thermoset polymers to recover hydrocarbon chemicals and any remaining fibre reinforcement. For example: catalytic solutions [203, 204], benzyl alcohol [205] and supercritical fluids (SCF) [206, 207, 208] that are typically applied at lower temperatures, under 350°C. The advantages these chemical recycling techniques are: high potential for fibre recovery and high mechanical property retention, while disadvantages include: potential scalability issues and potential environmental hazards.

One of the early processes, reported by Alldred *et al* [203] was a tertiary catalytic conversion process that was used to recover the fibres via a pyrolysis process in the presence of a catalyst. The polymer matrix was removed from the fibres at temperatures as low as 200ºC and could be recovered as hydrocarbons that may be suitable for use as chemicals or fuel. According to SEM studies, the fibres were generally clean, although a small amount of resin or char remained particularly when the fibres are in a woven form. Meanwhile, only a 9% loss the tensile strength of the fibres was recorded in comparison to virgin unwoven fibres.

In a subsequent investigation by Allred *et al* [204], the same process was used to recover carbon fibres of a CFRP with a thermoset epoxy matrix. After processing, the fibres reached 99.8% carbon values, i.e., 0.2% residual resin. Tensile strength testing revealed that the fibres exhibited an 8.6% reduction after reclaimation indicating that the process had little damaging effect on the fibre. Potential applications for the recycled fibres were identified as thermoplastic and thermoset moulding compounds and non-woven sheet reinforcements. An economic analysis of a recycling business based on the catalytic depolymerisation process revealed that it should be profitable provided that adequate scrap composite feedstock could be obtained.

Lui *et al* [209] meanwhile processed a CRFP with an epoxy matrix using a solvent method comprising a nitric acid solution. The fibre was recovered with its length preserved from the matrix after a period of 12 hours in the solvent. The fibres were undamaged exhibiting only a 1.1% tensile strength loss from single fibre testing.

More recently, Nakagawa *et al* [205] developed a recycling process using benzyl–alcohol and a catalyst in an inert nitrogen atmosphere. The process was used to successfully reclaim carbon fibre from end-of-life components originating from the sports and aeronautical industries.

SCFs are fluids at temperatures and pressures that are typically just above a critical point where the fluid is in a supercritical phase with multiple characteristics. For example, liquid-like density with dissolving power and gas-like viscosity with diffusivity [210]. SCFs therefore have the capability to penetrate porous solids and dissolve organic materials, making them suitable for CFRPs, while still being relatively inert under atmospheric conditions [28]. A number of SCF have been studied to date for recycling carbon fibres, which are typically coupled with alkali catalysts. These include: water [206], methanol, ethanol, acetone [207] and propanol [28, 207, 208].

Pinero-Hernanz *et al* [206] investigated the potential for recycling CFRP's with epoxy matrices in water at supercritical or near critical conditions. Experiments were performed in a batch-type reactor (10 mL) without agitation or stirring, using temperatures ranging from 480 to 752°C, pressures from 4.0 to 27.0 MPa and reaction times from 1 to 30 minutes. Resin removal efficiency reached 79.3 wt.% under supercritical water conditions with further improvement through the use of potassium hydroxide as an alkali catalyst of up to 95.3 wt.%. The tensile strength of the reclaimed fibres was between 90 and 98% in comparison to virgin fibres.

Hyde *et al* [28] used the supercritical process using propanol to extract and remove epoxy resin from the surface of a carbon fibre composite. The process appeared to be effective when operating above 450ºC at a pressure 5 MPa, which recovered carbon fibre that was almost as strong as virgin carbon fibre in terms of tensile strength, indicating that only minimal if any damage was done to the fibres during recycling.

Also using supercritical propanol, Jiang *et al* [208] compared the mechanical properties of recycled carbon fibres versus as-received carbon fibres inside epoxy matrices. The properties maintained, however, the surface oxygen decreased significantly due to the decrease of surface C–OH group. This resulted in a reduction of the interfacial bonding strength to from between 60-80 MPa to 59-70 MPa for virgin and recycled fibre respectively. According to previous findings, these values are still comparatively high and should create a strong fibre-matrix bond.

By comparison, Pinero-Hernanz *et al* [207] used supercritical methanol, ethanol, acetone and propanol at temperatures between 200 and 450ºC to recover carbon fibres from a CFRP comprising an epoxy matrix. SEM and tensile strength studies revealed that the reclaimed fibres were clean and retained 85 to 99% of their strength, which ranged between 3.7 and 4 GPa in comparison to 4 GPa for comparable virgin fibres. This compared to 3.05 and 3.26 GPa for fluidised bed and microwave reclaimed fibres respectively. This indicates the potential of SCF recycling and shows in the case of propanol that it was superior to alternative methods such as the FBP or microwave heating. However, the batch system did not have any agitation means to avoid fibre damaging, which implies there is still scalability issues to overcome if SCF recycling was to become commercialised.

Using SCF, in particular propanol for recycling CFRP's is a relatively modern approach, although has already demonstrated significant potential in terms of retaining the mechanical properties of recovered fibres and for permitting the recovery of chemicals from the matrix. However, one conclusion from all existing research is that further work is required in order to refine the operating conditions.

2.4.2.3. Thermal recycling

The most common thermal route employed today is pyrolysis, which is one of the most widespread recycling processes for CFRP composites. The objective is to recover

clean fibres and fillers from mixed and contaminated composites with energy recovery from the polymer where possible.

Pyrolysis is thermal decomposition of organic molecules in an inert atmosphere, such as nitrogen or argon at high temperatures. During pyrolysis recycling, the CFRP is heated up to 450 to 700°C in the inert atmosphere; the polymeric matrix is volatilised into a lower molecular weight and the fibres can be recovered [211, 212]. Advantages of thermal recycling include: high retention of the mechanical properties of the fibres; potential to recover chemical feedstock from the polymer matrix and in some cases depending on the final component dimensions, it may also be possible to inherit the fibre length and architecture.

Meyer *et al* [211] reported the potential of pyrolysis as a route to recover fibres from CFRP's and showed that the modulus and strength were comparable to that of virgin fibres. This was in agreement with prior research by Ushikoshi *et al* [199], who used an optimised pyrolysis process for recycling carbon fibre composite scrap. The method applied was aimed at the carbon fibre in CFRP's, from which thermo-gravimetric analysis (TGA) indicated that the carbon fibre began to oxidise after almost all the resin disappeared by pyrolysis. Subsequently, by pyrolysing the CFRP under appropriate conditions, it was possible to recover the carbon fibre with an almost 100% yield. The recovered carbon fibres were reusable, exhibited comparable mechanical properties (tensile strength) to virgin alternatives and possessed an excellent surface condition that was qualified using SEM.

The consortium company in this study: Milled Carbon Ltd, developed a heating process in 2003 that continuously recycles cured and uncured carbon fibre composite parts that are up to 2 m wide, 250 mm high, with a thickness of up to 25 mm. The process is performed using a semi-open continuous-belt fed furnace that has a controlled atmosphere to avoid char formation. In addition, the resin's calorific value is recovered and fed back in the process. However, according to Alsop [213], material-recovery from the polymer is not economically viable. To date, the process has been used successfully to recycled fibres from virtually all types of waste. This includes off-cut or end-of-life unused rolls of pre-impregnated carbon fibre material, as well as already formed cured carbon fibre parts. Development studies are on going in an attempt to improve the consistency and alleviate any limitations on the size of the samples that can be processed. Two notable recycled products recycled to date include a milled carbon fibre particulate created by milling the chopped fibre; and secondly, a non-woven mat, which was

manufactured using a poly-vinyl alcohol (PVA) binder and traditional paper-making technique that was outsourced from a third party company. As previously discussed, milling composites in to particulate size offers little intrinsic value. Although, manufacture of the non-woven mat presented a novel option to test that also possessed good handleability. More details of this sample are described in the testing section.

Meanwhile, the Japan Carbon Fiber Manufacturers Association (JCMA) began work on recycling CFRP's using pyrolysis in 2006. Unfortunately, details of their process itself, the mechanical properties and quality of the fibres have so far not been disclosed.

In the USA, Materials Innovation Technologies RCF (MIT-RCF) began recycling CFRP in 2008 also using an undisclosed pyrolysis process [214]. Similar to Milled Carbon Ltd, their approach includes a preliminary step of chopping the feedstock to a consistent length, which was then pyrolysised. An in-house developed manufacturing process: three-dimensional engineered preforming (3-DEP) was then employed for re-manufacturing the recycled material [194]. No further details are available.

In Germany, Airbus is working with CFK Valley Stade Recycling GmbH & Co. KG (CFK) to develop a continuous pyrolysis process that incorporates an additional oxidation step for char removal. The 1000 tonne/year pilot recycling plant is being setup to recycle both CFRP and decommissioned Airbus aircraft and produce milled fibres, chopped fibres, and textile products [215, 216].

In Italy, Karborek S.p.a. [217] uses a combined pyrolysis and oxidation process to recycle carbon fibres and avoid char formation. Although the fibre-length is preserved during recycling, the main products are milled and chopped fibres, as well as blended non-woven veils with carbon and thermoplastic fibres [194].

An alternative to the pyrolysis process uses a continuous microwave approach, which avoids char formation. As reported by Lester *et al* [197], the microwave heating process has potential for recycling of both the polymer and the carbon fibre. By heating the fibres directly through the use of microwaves, there is potential to reduce the energy input compared with other processes. This permits the recovery of clean high quality fibres and the valuable chemical products simultaneously. Initial investigations confirmed that the polymer could be separated from the carbon fibre in a multimode microwave cavity. The fibres recovered were relatively clean, although some small changes in the surface morphology were evident after processing. Fibre strength retention was encouraging and superior in terms of the tensile strength to that of other existing recovery processes based on fluidised bed volatilisation, as shown in Appendix B – Table 6.

Microwave heat recycling appears technically feasible. However, it is clear that more work will be needed to establish whether it is a more viable technology than other techniques including a fluidised bed system. Additional work is still necessary in order to characterise the extracted polymer and to verify the properties of the recovered fibres. Furthermore, an investigation is also required into how different polymer coatings would respond to microwave heating [197].

Irrespective of the apparent maturity and encouraging results of thermal recycling today, large amounts of energy in the form of heat are required and the process can generate substantial pollution. Consequently, alternate routes are continually being sought; these are discussed below.

2.4.2.4. Miscellaneous techniques: Fluidised bed process

One such process is the fluidised bed process (FBP), which is today seen as a very efficient method for the recovery of carbon fibres. The FBP has been developed prominently and implemented by Pickering *et al* at the University of Nottingham. During recycling, the CFRP scrap is pre-cut to approximately 25 mm and is fed into a bed of silica on a metallic mesh. A hot air stream is passed through the bed and decomposes the resin. Both the oxidised molecules and the fibre filaments are then carried up within the air stream, where heavier metallic components sink in the bed. The main weakness of the FBP is that the fibre product is typically in fluffy form of mean length between 6 and 10 mm. The fibres however were clean and possessed little to no surface contamination.

Yip *et al* [196] further validated the FBP process by recycling a cured UD pre-preg comprising epoxy resin. The scrap was fed into a bed of silica sand, nominal sand particle size of 0.85 mm that is fluidised with heated air. After processing, the polymer was volatilised, leaving only clean fibres that were released into the gas stream as individual mono-filaments.

However, one of the most promising ways to reduce the cost of C_f/C-SiC composites is to simplify the manufacture by using short fibre reinforcements and pressing techniques. The use of short fibre reduces the cost of the raw material by the reduction of waste in comparison to other fibre architectures like bi-directional woven fabrics.

2.5. Literature review summary

The aim of the literature review was to investigate and document the requirements and implications of using different recycled origins of carbon fibre and pyC as key constituents inside a new class of recycled C_f/C-SiC composites. Each constituent inside these composites was investigated, where the main role of the fibres was to reinforce the matrix. The importance of the preform architecture e.g. woven, UD, 2D, 2.5D, and to a lesser degree, volume fraction was highlighted. In between the fibre and matrix is the interface, which was identified as being a critical part of the composite to: improve the failure mode; protect the fibre against oxidation and corrosion from the silicon during LSI processing. Different interface materials were identified and pyC was deemed to be the most suitable for manufacturing in this study. This was because of its compatibility with the carbon fibres; maturity and reported successes of it inside other reported C_f/C-SiC composites; low cost when derived from PIP; ease of production; compatibility with the LSI process.

A thorough review of C_f/C-SiC manufacturing processes revealed that a three-step combination route would be the most cost-effective and suitable process to create the new recycled composites: polymer infiltration (PI) and hot pressing (HP) to create the CFRP, pyrolysis to convert the CFRP into a porous C_f/C composite and LSI to introduce the SiC matrix.

Supply of the recycled carbon fibre used to create these composites was satisfied by the consortium; namely, Milled Carbon Ltd and Airbus. The fibres were split into three categories: recycled, end-of-life and re-claimed, which were based on their origin and processing. Details of all of the samples are shown in Table 14. The new C_f/C-SiC composites were designed and manufactured for three different potential applications: automotive, industrial and aerospace, where the specific property requirements were highlighted for each application in Table 4, Table 7 and Table 8 respectively. Therefore, the requirements in Table 13 are proposed for a baseline laboratory scale C_f/C-SiC composite. The properties in this table will be revisited in *Section 5* in order to gauge any successes of the project.

Table 13. Baseline properties for a laboratory scale C_f/C-SiC disc.

Property	Requirements
Recyclability	• Carbon fibre source should be predictable and the potential supply recognized. • History of the fibre should be traceable. • The length of any recovered fibres should be maintained. Minimum length of >5.5mm should be sought to maintain mechanical properties. • Recycling process should aim to recover clean fibres. Fibres without any residual carbon or damage. • Recycling process should limit any toxic emissions.
Manufacture	• Needs to be capable of being machined to circumferential parallelism.
Physical	• Porosity (%) should be as low as possible in order to promote the mechanical strength e.g. bend strength, and thermal conductivity. • Target density of at least 1.8 g/cm^3 for an automotive disc. • Target density of at least 2.1 g/cm^3 for an aerospace disc. • Target density less than grey cast iron, 7.2 g/cm^3 for an industrial disc.
Mechanical	• Bend strength of 100 MPa for an aerospace application. • Must withstand a pressure of 1 MPa for dyno testing.
Tribological	• Must provide an adequate COF of between 0.3 and 0.4 for automotive with a pad, between 0.7 and 0.8 for industrial applications and around 0.4 for aerospace applications. • COF for all applications should be predictable and stable. • No additional wear of the pads at temperatures above 250°C
Cost	• Manufacture process should be rapid to improve the economy. • The disc needs to be economically machined, in a short period with minimal tool wear.

3. Experimental details

3.1. Raw materials

3.1.1. Carbon fibre

All of the carbon fibre materials were supplied by members of the ReBrake consortium, except the Airbus UK and 'carbon fibre supplier' samples that were kindly donated.

Table 14. Carbon fibre materials under investigation.

Name	Fibre category	Fibre type	Architecture	Matrix
Non-woven mat	Recycled	Mixed[1]	Non-woven chopped short fibre (SF) mat	Mixed[1]
Chopped C_f		Mixed[2]	Non-woven chopped SF	CVI-C
5133	End-of-life pre-preg	AS4 PAN-12K[3]	UD	34% epoxy[6]
5164		AS4 PAN-12K[3]		34% epoxy[6]
5466		AS4 PAN-12K[3]		34% epoxy[6]
5471		AGP280-3K[4] (55.29% V_f)	Weave (5HS)	37% epoxy[6]
Cured spar	Reclaimed CFRP	AS4 PAN-12K[3]	Inherited UD (0°/45°/90°)[5]	34% epoxy[6]
ST	Virgin	PAN-OX (22-25% V_f)	2D + Z direction	CVI-C
V1	Virgin[7] pre-preg	PAN-3K	Plain weave	45% epoxy[9] (by weight)
V2		HS40 PAN-12K[8] (60% V_f)	UD	40% epoxy[9]
V3		HR40 PAN-12K[8] (60% V_f)		40% epoxy[9]

Notes:

SF: Fibres were denoted as short fibre (SF) if they were proportionally longer in comparison to their width and were less than 5mm in total length.

1 Mixed types of industry grade carbon fibres and epoxy resin from pre-pregs and CFRP.

2 Mixed carbon fibre and CVI-C from aerospace grade C_f/C composites

3 HexTow™ AS4 carbon fibre (Hexcel Ltd). Fibre density: 1.79 g/cm^3 [218].

4 HexTow™ AS4 carbon fibre (Hexcel Ltd). Fibre density: 1.77 g/cm^3 [218].

5 Fibre orientation was inherited from the original spar (0/45/90).

6 Hexply™ 8552 (Hexcel Ltd) [219].

7 Samples were mailed and stored in a non-refrigerated environment. However testing was performed immediately upon receiving the samples.

8 Pyrofil™ carbon fibre [220].

9 Epoxy resin 250F (Mitsubishi Rayon #350 resin).

In addition to the carbon fibre materials and pre-pregs outlined in Table 14, graphite (MABS, UK) was supplied so comparisons could be made to the end-of-life epoxy resin and virgin phenolic resin. This was an industrial grade graphite that was carbonised at elevated temperatures beyond 1000°C.

3.1.2. Resin

The two most common resins used to manufacture CMC's are epoxy and phenolic. The end-of-life pre-pregs: 5471, 5164, 5466, 5471 and cured spar samples contained epoxy resin, the composition of which has been added to Appendix B – Table 7. Epoxy resin is a thermoset polymer that is selected for its advantageous properties, which include: excellent mechanical properties and high glass transition temperatures (T_g).

A phenolic resin (Hexion Ltd, UK) was used to infiltrate the carbon fibre preforms during CFRP manufacture. The composition is shown in Appendix B – Table 8. The phenolic resin was selected because of its low viscosity of between 270-500 cPs, which should facilitate penetration and characteristic high carbon yield of approximately 52% after pyrolysis. This compares to a significantly lower typical carbon yield for industrial grade epoxy resins, which can be as low as 5% [221]. However, a disadvantage of phenolic resin is that they are characterized by a complex process of polymerisation during curing with the generation of water and formaldehyde, which is known to create voids [222].

3.2. C_f/C preform manufacture

The C_f/C fabrication route was a two-step process beginning with the creation of a CFRP via polymer impregnation and hot pressing using a custom designed die. Appendix A – Fig. 18(a) shows three-orthographic views of the die with a 3D colour illustration, while (b) shows an 'exploded view' of the die with the fixing screws omitted. Two of these dies were constructed, each comprising two closing cavities measuring 100 x 10 mm (LxW). To alleviate any potential opening and closing issues, the die was designed so that it could be completely opened and sealed using screws. In the second step of manufacture, the CRFP is converted into a porous C_f/C preform by pyrolysis at 900°C for 30 minutes in alumina tube furnace (Lenton, High Wycome, UK).

3.2.1. Process for recycled carbon fibre

The manufacturing routes for the four starting materials are described below in Fig. 33.

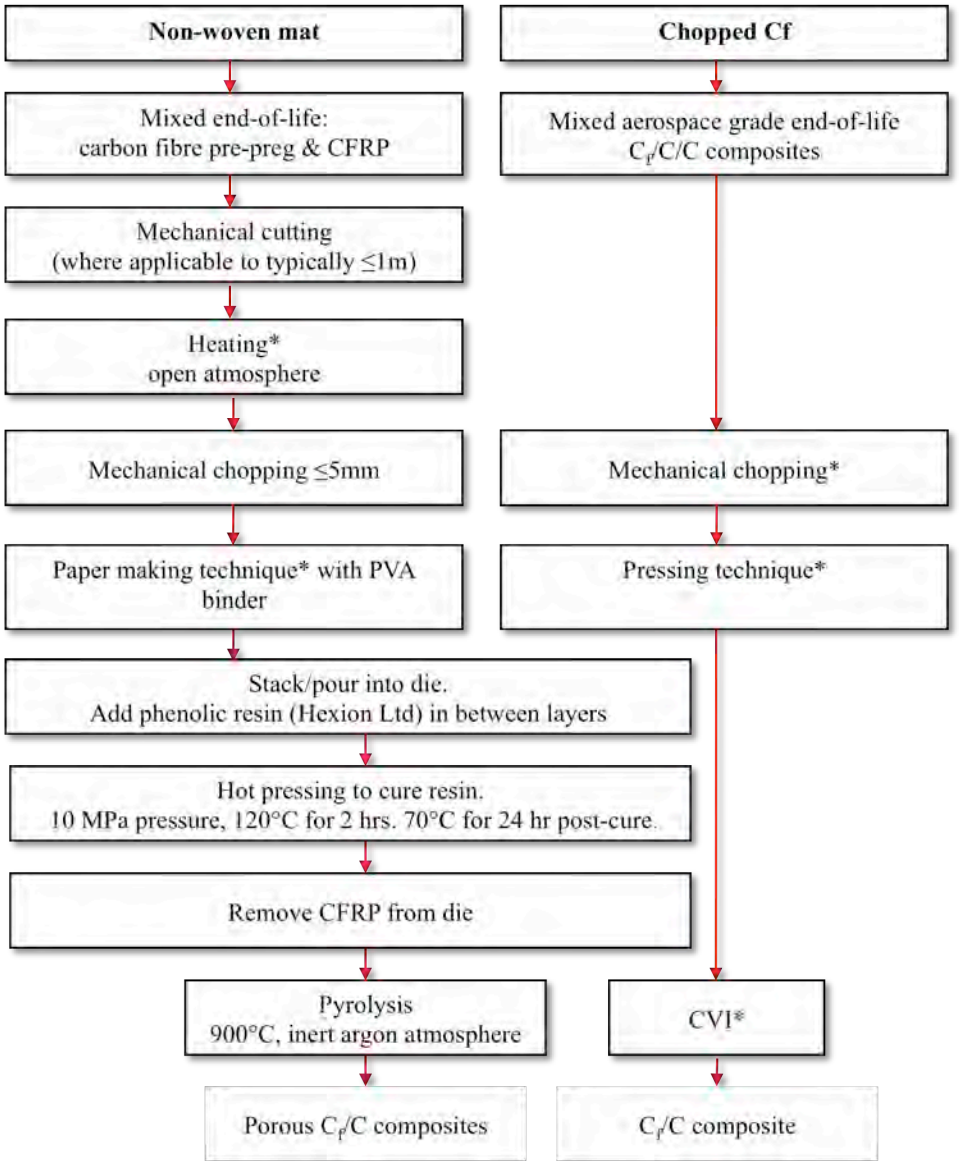

Fig. 33. Flow chart illustrating the recycled carbon fibre manufacture routes. * denotes commercially confidential.

The short fibre 'non-woven mat' (Milled Carbon Ltd, UK) was recycled from various mixed end-of-life carbon fibre pre-pregs and CFRP's, which were typically very large, ranging up to 2m in size and were therefore mechanically cut to ≤1m so they would fit on the conveyor belt and pass through the heater. Heating was performed at elevated

temperature, approximately 900°C in a semi-open atmosphere to effectively remove most of the resin within the samples. The non-woven short carbon fibre mat was fabricated using a commercially unknown process, although was based on a traditional papermaking technique that bonded the fibres together using a poly-vinyl alcohol (PVA). A photograph of the mat is shown in Appendix A – Fig. 19. The 'chopped C_f' sample (MABS, UK) comprised mixed variants of aerospace grade C_f/C composites. However, this was an experimental test and the composite was not converted into a C_f/C-SiC composite.

The 'non-woven mat' was made into a CFRP by stacking/pouring the fibre into the steel die. Phenolic resin was added and the die was closed, prior to being hot pressed under pressure and heat to complete the CFRP. The polymer matrix was then converted into pyC via pyrolysis to create a porous C_f/C composite, which was now ready for LSI.

3.2.2. Process for end-of-life pre-preg and reclaimed CFRP spar

Two origins of carbon fibre were reclaimed. The first were aerospace grade woven and UD carbon fibre pre-pregs that comprised epoxy resin and the second was a cured CFRP spar from an aeroplane. A photograph of the spar has been added to Appendix A – Fig. 20.

Since the pre-pregs were supplied on large rolls and the CFRP spar was an 'L' shape, both were mechanically cut so they would fit inside the furnace. Pyrolysis was used to convert the epoxy resin inside the pre-pregs into pyC and recover the fibre from the spar. The layers were stacked in the steel die and impregnated with a phenolic resin. The layup architecture of the UD and woven pre-pregs was maintained. Meanwhile, the architecture of the cured spar was inherited from the original spar, in a 0/45/90 configuration. Hot pressing was performed under pressure and heat to complete the CFRP's, which were removed and re-pyrolysed under the same conditions to convert them into a porous C_f/C composites. It should however be noted that each composite now possesses a dual pyC interface; one derived from the original epoxy and second from the phenolic resin.

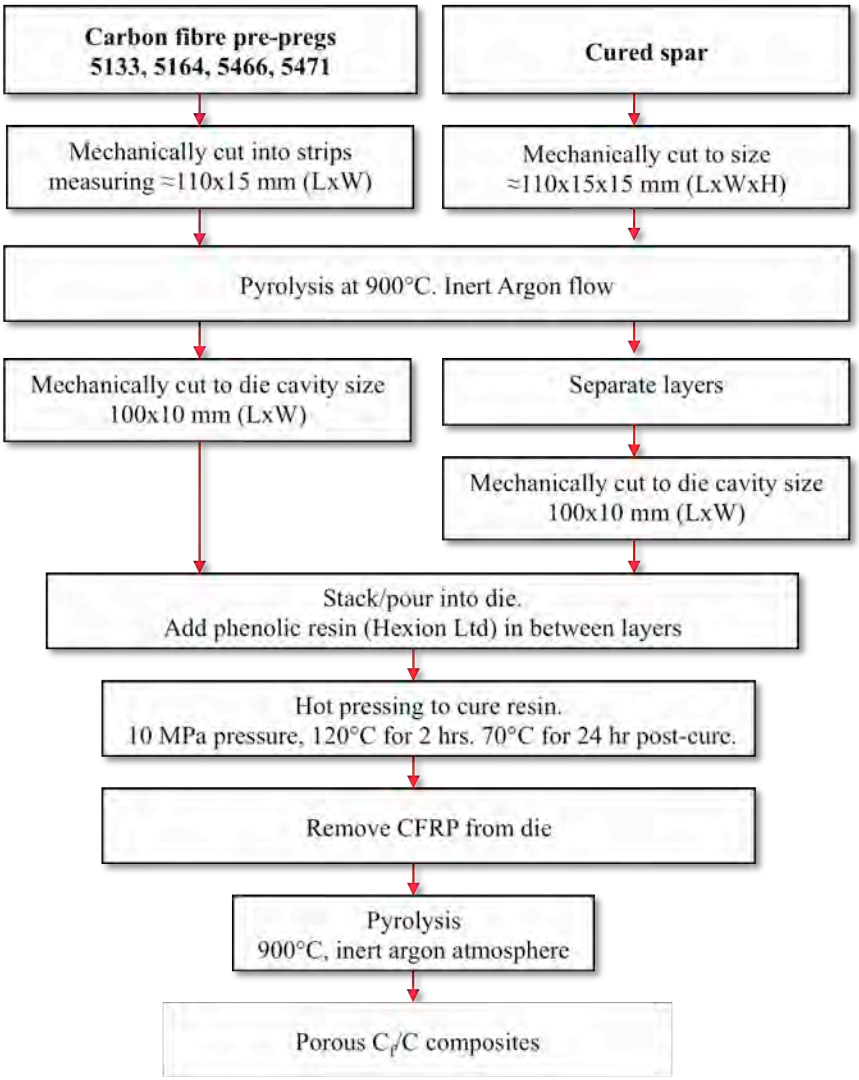

Fig. 34. Flow chart describing the manufacture routes for the end-of-life carbon fibre and cured spar.

3.2.3. Virgin carbon fibre

For comparative testing, a commercial carbon fibre manufacturer (Harrisons Advanced Rods Ltd, UK) and Surface Transforms Plc supplied virgin grade carbon fibre pre-pregs and a 2.5D preform, respectively. The manufacture routes are described in Fig. 35.

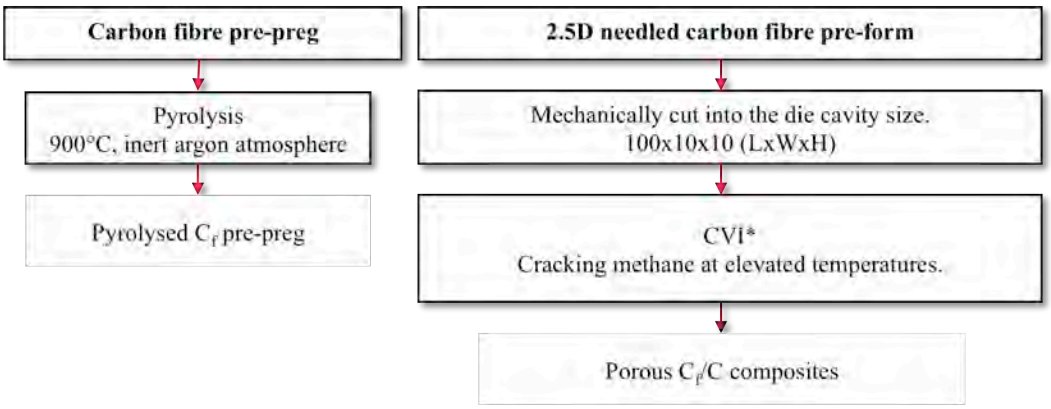

Fig. 35. Flow chart describing the virgin carbon fibre C_f/C manufacture route. * denotes commercially confidential.

The carbon fibre pre-pregs were used as comparative pre-pregs against the end-of-life pre-pregs in the pyrolysis investigation, in *Section 3.4.2*. Meanwhile, the 2.5D lay-up architecture of the ST preform is shown in Appendix A – Fig. 21. The preform comprised bi-directional (0/90) fibres held by a web with Z-direction needling. The preforms were partially densified using CVI through the cracking of methane at elevated temperatures.

3.3. C_f/C-SiC manufacture

All of the samples, unless otherwise specified were converted from porous C_f/C preforms into C_f/C-SiC composites by LSI, which was performed inside an alumina tube furnace (Lenton, High Wycome, UK). The preform was placed inside an alumina crucible and directly covered with commercial grade silicon granulate (Surface Transforms Plc, UK), which was 99.9% pure. LSI was performed in an inert argon atmosphere according to the following heat regime: -

1). Heat from room temperature by 5°C/min up to the target temperature of 1500°C,
2). Dwell for 3 minutes,
3). Cool by 5°C/min back to room temperature.

3.4. Testing and characterisation

3.4.1. Sample preparation

Samples were prepared by cutting, mounting and polishing as described in the following sections for the microstructure, mechanical and friction tests.

3.4.1.1. Cutting

After being removed from the furnace, samples were cut using a diamond tipped saw on an automated cutting machine (Struers Accutom-5), which has a positioning accuracy of 5-µm, adjustable feed speed and force limit.

3.4.1.2. Mounting

Two types of mounting were available: hot mounting (Struers/Pronto press-10) and cold resin mounting (Struers/EpoFix Resin). Hot mounting created a conductive mount, although was not suitable for fragile or porous samples because the process is performed under pressure. Cold resin mounting used a non-conductive resin and hardener mixture that self cured at room temperature over 24 hours, but did not damage fragile samples because no pressure was applied, and the resin would access relatively porous samples.

3.4.1.3. Polishing

The polishing regime was fully automated using a TegraPol-25 base unit with variable speed and disc size of 250 mm, TegraForce-5 designed to handle both single or multiple specimens under individually customisable forces, and a TegraDoser-5 equipped with up to 7 peristaltic pumps, 6 for diamond suspensions or lubricants. The following grinding (Struers, UK) and polishing (Struers, UK) regime was used to prepare each sample prior to microscopy: -

1). Grinding: MD-Piano 63-µm (grade-220) for 1 minute,
2). Grinding: MD-Piano 13 to 16-µm (grade-600) for 1 minute,
3). Grinding: MD-Piano 4.5 to 6.5-µm (grade-1200) for 2 minutes,
4). Polishing: MD-DAC 3-µm diamond suspension for 5 minutes.
5). Polishing: MD-DAC 1 µm diamond suspension for 5 minutes.

3.4.2. Shape change and mass loss during pyrolysis

Pyrolysis of the pre-preg is defined as the thermochemical decomposition of the resin with an evolution of gaseous emissions in the absence of oxygen. During pyrolysis, which is the intermediate stage in the manufacture of pre-pregs towards a CMC, two events occur: firstly, the resin is progressively converted into pyC with an evolution of the gaseous emissions. The rate of pyrolysis from end-of-life pre-pregs has so far not been documented; secondly, the carbon fibre preform undergoes certain geometric changes that alter the internal architecture. Therefore, seven different pre-pregs were investigated so comparisons could be made. These included four end-of-life: 5471, 5133, 5164, 5466 and three virgin-based: V1, V2, V3. The test procedure was performed as follows: -

1). Cut each pre-preg was into a small rectangular strips measuring approximately 25mm x 8mm (L x W) in size. The dimensions were measured using the digital vernier calliper (Cole-Parmer/Electronic 12 inch), which is accurate to 0.1 mm. Since the thickness of the woven pre-pregs (5471 and V1) varied slightly according to the position of calliper, a ‘mean thickness’ was calculated using six randomly measured points. Photographs of the strips are shown in Appendix A – Fig. 22.
2). Each pre-pregs was pyrolysed for 30 minutes in an alumina tube furnace (Lenton, LTF-1700) using an inert nitrogen atmosphere. The heat cycles were: 300ºC, 400ºC, 500ºC, 600ºC, 700ºC, 800ºC and 900ºC.
3). Seven additional strips of sample 5471 were pyrolysed at 500, 700 and 900ºC under the same pyrolysis conditions, in order to calculate a mean mass change (%) using a digital balance (Kern/EG).
4). After pyrolysis, the samples were re-weighed and the dimensions were re-measured using the digital calliper.
5). The cross-section of each pre-preg was investigated by optical microscopy (MEF-3), while sample: 5471 was further investigated using an electron microscope (FEG-SEM). Since each pre-preg was very fragile, the cold mounting process was selected, which is detailed in *Section 3.4.1.2*. However, since the cold mounting resin itself comprised epoxy, each pre-pregs was covered with sellotape prior to

being mounted. The celotape acted as a barrier to avoid any contamination. An annotated photograph of this has been added to Appendix A – Fig 23.

3.4.3. Bulk density and open porosity test

The bulk density (ρ_b) and open interconnecting porosity (π_a) of four different C_f/C-SiC composites was calculated using the Archimedes method using equations (6) and (7) respectively.

$$\rho_b = \frac{m_1}{m_3 - m_2} \cdot \rho_l \tag{6}$$

$$\pi_a = \frac{m_3 - m_1}{m_3 - m_2} \cdot 100 \tag{7}$$

where, 'ρ_b' is the bulk density (g/cm^3), 'm_1' is the dry mass, 'm_2' is the apparent mass of the immersed specimen, 'm_3' is the wet mass of the soaked sample and 'ρ_l' is the bulk density of the immersed liquid, where distilled water is approximately 0.9975 g/cm^3 at room temperature (23ºC). The test procedure was carried out in accordance with BS EN 1389:2003: -

1). Each sample was weighed (m_1) using a balance (Kern/EG), which was accurate to 3 decimal places.
2). Each sample was supported by a thin piece of wire and gradually submerged in to distilled water over a period of 3 minutes,
3). Each sample was placed inside a vacuum chamber. The pressure was lowered to less than 2500 Pa for a period of at least 15 minutes.
4). The samples were removed and weighed whilst still supported by the wire and submerged in the water (m_2).
5). The samples were re-weighed after being removed from the water with any surface water removed (m_3). A fine non-absorbent cloth was used to remove any water from the surface of the sample prior to weighing in accordance the standard.

Four different samples were investigated, which are detailed in Table 14 and included: 1). Recycled ‘short carbon fibre mat’, 2). End-of-life UD ‘5164’, 3). End-of-life 2D woven ‘5471’ and 4). Reclaimed UD ‘cured spar’, which were tested at each stage during processing: CRFP, C_f/C/C and C_f/C-SiC, and after an additional PIP or LSI where applicable. In addition to the manufacture, sample: 5471 received an additional PIP and LSI, under the same conditions.

3.4.4. Mechanical properties

3.4.4.1. Bend strength

The four-point bend strength ‘σ_f’ of: the recycled ‘non-woven mat’; end-of-life: 5164 and 5471; reclaimed ‘cured spar’ was measured using equation (8):

$$\sigma_f = \frac{3F_m(L - L_i)}{2bh^2} \tag{8}$$

where ‘F_m’ is the flexural force (N), ‘L’ is the outer span length (mm), ‘L_i’ is the inner span (mm), ‘b’ is the width (mm) and ‘h’ is the height (mm). The samples were prepared and tested in accordance with BS EN 658-3:2002. Details of the sample preparation are as follows: -

1). Each sample was cut to approximately 85x10x2.5 mm (L x W x H) and ground/polished to a tolerance of ±0.1mm, which was validated using a vernier calliper.
2). The samples were polished to a 1-µm finish as previously described.

The jig was custom built with adjustable rollers that were 4 mm in diameter; an inner span of 25 mm and outer span of 75 mm was used for all tests. The loading rate was 1 mm/sec.

3.4.5. Microscopy

3.4.5.1. Optical microscope

An optical microscope (Reichert-Jung, MEF-3) was used to generate images at magnifications up to 1000 times (x) under standard bright field, polarised and/or differential interference contrast (DIC) light conditions.

The bright field mode was used to image the carbon fibres inside the microstructure of different carbon fibre pre-pregs. Meanwhile, the polarised and DIC modes were used when imaging multiple phases or interfaces inside the microstructure of C_f/C-SiC composites. The polarized filter permits the light to be polarised, while the DIC create a physical relief effect, which aids the distinction between the phases and interfaces. The three-dimensional relief is created due to variations in the optical density, A, also known as the 'absorbance' of the sample, which is the intensity of light at a specified wavelength, λ that has passed through the sample i.e. transmitted light intensity and is proportional to the thickness of the sample and the concentration of the absorbing species. Therefore, the image created by the DIC is not topographically accurate.

Images were taken using an incorporated digital camera, which were directly saved or transferred to other image analysis software, such as 'GIMP', which is detailed further in *Section 3.4.6*.

3.4.5.2. Field emission gun-scanning electron microscope

A field emission gun-scanning electron microscope (FEG-SEM, Carl Zeiss Leo 1530VP) was used to characterise microstructural features in the secondary electron mode at 5 kV. Since the carbon fibre and SiC samples were innately conductive, no additional coating was required, unless the sample was mounted in a non-conductive resin, in which case, a gold coating was used and silver paste.

3.4.5.3. TEM sample preparation

TEM (JEOL 2000FX) samples were prepared using a Focused Ion Beam (FIB, FEI Nova 600 Nanolab) microscope. The FIB comprised a high-resolution field emission electron column and gallium source ion column, which was used generate images of the desire area and remove cross-sections across the C/SiC/Si interfaces inside the C_f/C-SiC composites. The size of the cross-section measured approximately 20-μm wide by 200 nm thick and were used to make comparisons between the different origins of carbon and fibre, and investigate the siliconisation mechanisms.

General imaging using the FIB was performed in the secondary electron (SE) mode at 15 kV; milling was performed in the ion beam mode using a current of 20 nA and voltage of 30 kV. The cross-section was removed in five stages, as illustrated in Fig. 36 and described below: -

1). A suitably sized interface was identified in the imaging mode and a 20-µm wide by 3-µm high platinum layer was deposited on the sample to avoid ion damage during milling.
2). Two rectangular craters were milled into the sample, either side of the platinum strip.
3). The sample stage and sample were tilted and the cross-section sides were cut, leaving only a small edge for support.
4). The cross-section was attached to a retracting tip via platinum
5). The remaining edge was removed and the cross-section was lifted to a sample holder (copper grid) for TEM analysis.

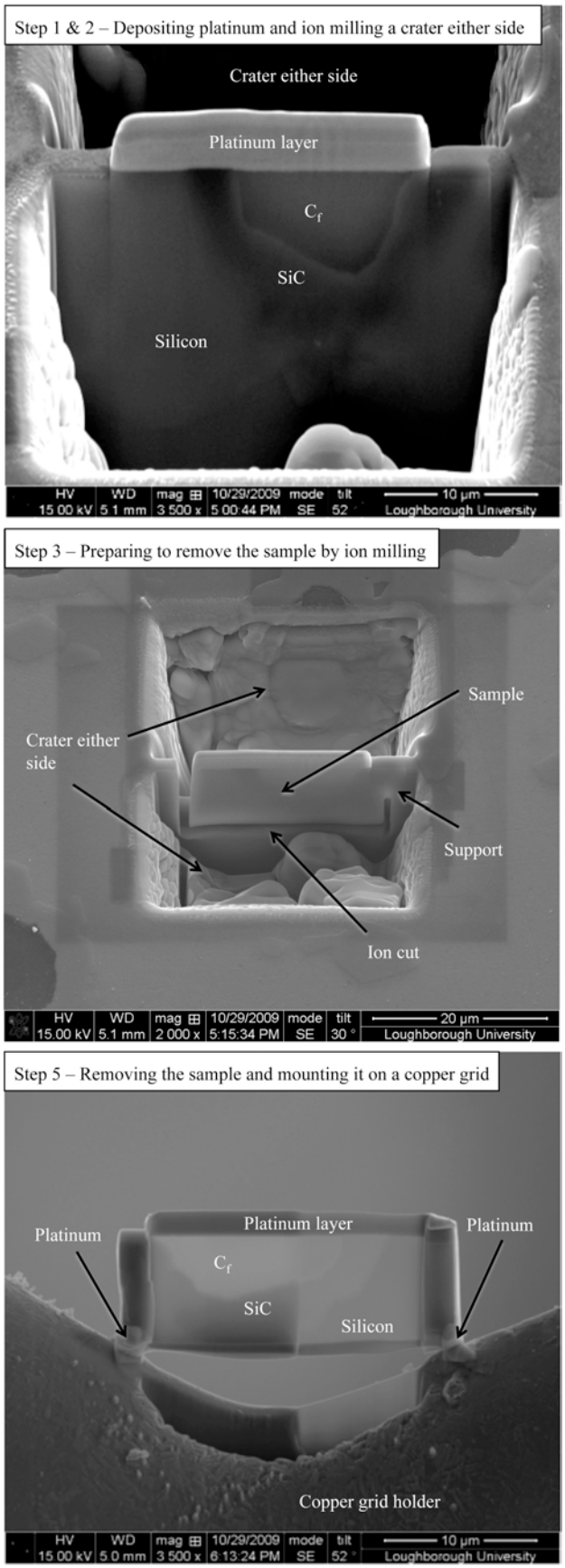

Fig. 36. FIB micrographs of sample 'ST' illustrating the key steps in preparing a TEM sample.

3.4.5.4. TEM analysis

The TEM was used in two imaging modes: bright field and dark field, in addition to generating selected area diffraction (SAD) patterns. Images were generated using a dual tilt arm, at a camera length of 100 cm and filament voltage of 200 keV.

In the bright field mode, the contrast is formed directly by occlusion and absorption of electrons in the sample. Therefore, thicker samples or specimens with a higher atomic number will appear darker in comparison to thin samples, or regions with no sample in the beam path, which will appear bright (white) i.e. hence the name.

The dark field mode excludes the transmitted beam from the image. Consequently, the field around the specimen is dark. The image is in fact generated by altering the objective aperture to be in a different diffraction plane so that the main beam is avoided and only scattered electrons are collected through that specific aperture. This method is typically used to identify any lattice defects in crystals, although was used herein to confirm the presence of any fine (nano-sized) SiC crystals inside the TEM micrographs. This was achieved by first generating an SAD ring pattern of the SiC crystal; identifying a diffraction spot; bringing the diffracted spot to the centre of the screen; adjusting the objective aperture to a smaller size to form an image using only the diffracted electrons. This resulting micrograph is called a ‘centred dark field’ image.

SAD patterns were generated to characterise the crystallinity and crystallographic structure of the carbon and SiC. The following equation (9), derived from the Bragg diffraction condition was used to calculate the d-spacings’ of the SiC and nano-crystalline SiC crystal planes (Å): -

$$d = \frac{\lambda L}{R} \tag{9}$$

where, ‘λ’ is the wavelength of electrons 2.5 picometres, ‘L’ the camera length of 100 cm and ‘R’ the distance of the diffraction spot to the central spot or radius of the diffraction ring (mm).

The measured d-spacings from the SAD were matched to values that could be acquired from the international powder diffraction database and correlated to the d-spacings measured from XRD spectra to ascertain the most likely polytype of the SiC and silicon. Meanwhile, indexing consisted of two stages: the first determines the general

(hkl) indices of the spot, without definite values or signs. The second stage assigns specific (hkl) indices to individual spots and the beam direction.

1. Camera constant method

This method assumes that the camera constant is known while material data is not essential. The crystal spacing distance, 'd' is calculated and correlated to standard ASTM or alternate international powder diffraction profiles, using equation (9), where, 'λ' is the electron wavelength, 2.5 pm at 200 kV, 'L' was camera length at 100 cm and 'R' the distance (mm) between the central spot and the corresponding diffracted spot.

2. Method of ratios

The second method assumes the material is known and camera constant unknown. It begins by measuring distance 'R' between the central spot and diffraction spots relative to each other and comparing against standard tables of ratios of 'd' spacing's for low index planes. In this case, the 'FCC' formula is adopted: -

$$\frac{1}{d} = \frac{h^2 + k^2 + l^2}{a^2} = \frac{N}{a^2} \qquad (10)$$

where, 'a' is the cell width lattice parameter that is known from the X-ray powder diffraction database, e.g. a = 4.3589. The indexing results are discussed in *Section 4.2*.

3.4.6. Image analysis and quantification

Two lightweight freeware image analysis software packages were used in conjunction with optical and SEM micrographs to quantify the surface volume fraction (%) and scale/range of specific regions and features inside carbon fibre pre-pregs, C_f/C preforms and C_f/C-SiC composites. These were 'Image-J' [223] and 'Gimp' [224] respectively.

Image-J was developed by the National Institute of Health and was used to estimate the volume fraction (%) of the phases: C_f/C, SiC, silicon and voids inside the different C_f/C-SiC composites, in accordance with the British standard test: general and texture properties [225]. To achieve this, an optical microscope (MEF-3) was used to gather no fewer than five micrographs at two magnifications: 200x and 500x. A

combination of polarised and DIC light was used in order to aid distinction between the phases and interphases. Once the micrographs were transferred to 'Image-J', they were converted into 'greyscale' images and the 'threshold contrast' was altered accordingly. This permitted isolation of the phases so each proportion could be measured as a percentage of the total micrograph area. 'Image-J' was used for two investigations: -

1). To understand the impact of different preform architectures on the volume fraction of the generated phases (*Section 4.2.1*);
2). To understand the impact of the volume fraction of the phases inside different C_f/C-SiC composites comprising virgin and recycled material during a friction trial. The results have been added to *Section 4.2.1*.

Meanwhile, Gimp was used to gather four sets of data: -

1). Measure the distances between C_f/C bundles inside different carbon fibre pre-pregs after being pyrolysed at different temperatures.
2). Measure and compare the thicknesses of the carbon interfaces and SiC inside C_f/C-SiC composites with different architectures that were manufactured by LSI. No fewer than one hundred thicknesses were measured in random positions throughout each microstructure, at intervals no less than 15-µm apart. An example of how the statistics were measured has been added to Appendix A – Fig. 24.
3). Measure and compare the thicknesses SiC inside C_f/C-SiC composites with different carbon sources that were manufactured by LSI. Similarly, no fewer than one hundred thicknesses were measured in random positions throughout each microstructure, also at intervals no less than 15-µm apart.
4). Nano-indentation: Measure the crack lengths generated in the different phases created by the nano indenter, which is detailed further in *Section 4.3*.

3.4.7. X-ray diffraction

An XRD (Philips, PW17-30) was used to characterise the crystallographic polytype of the SiC using CuK_α incident radiation through a 2θ range, from 0º to 90º with a step rate of 1º/min.

3.4.8. Nano-indentation

Today, nano-indentation techniques and equipment have improved to the extent that very small regions, down to 500 nm and up to 20-μm can be investigated [226-229]. Therefore, multi-phase composites such as C_f/C-SiC can be tested [230]. As a consequence of the small indentation sizes, tiny loads are typically used between 20 and 250 mN to measure the: hardness, Young's modulus and even estimate the fracture toughness. Indentation is performed using a ball, three- or four-sided point of known geometry; the three-sided Vickers or four-sided Berkovich indenter are commonly used, partly because they are easy to grind to a sharp point. An in-situ microscope, usually an optical microscope is used to identify the indentation location, and electron and/or atomic force microscopy utilized for post-analysis.

A nano indenter (Micro materials Ltd, UK), a schematic of which is shown in the Appendix A – Figure 25 [231] was used in conjunction with a Berkovich tip to generate indents inside the different phases of different virgin and end-of-life C_f/C-SiC composites. The samples were tested using the following regime, which is described inside the equipment test manual [231]:

1). Mounted and polished C_f/C-SiC samples were glued on to the sample holder (stub).
2). Fixed inside the nano-indenter, which is enclosed inside a temperature and humidity controlled chamber.
3). An optical microscope capable of x400 magnification was used to identify the location of each indent. Each location was programmed into the 'Micro labs Ltd' software. The testing parameters were setup to automatically calculate the results using 'Micro labs Ltd' software [231].
4). The indents were performed using a force of 100 mN (unless otherwise specified) and a loading rate of 2.5 mNs^{-1}.

The testing parameters were based on the *Power law* fit method from Oliver and Pharr in 1992 [226], which was updated in 2004 [227]. Data collected included: maximum depth (nm), plastic depth (nm), maximum load (mN), plastic work (nJ), elastic work (nJ), hardness (GPa) and reduced modulus of elasticity (E_r). The Young's modulus (E) and

fracture toughness (K_{1C}) were calculated separately, as discussed in *Section 3.4.8.1* and *3.4.8.2* respectively.

3.4.8.1. Hardness and Young's modulus

During indentation, a record of the load and depth of penetration is made and the values are plotted on a graph to create a load-displacement curve, as shown in Fig. 37 [227].

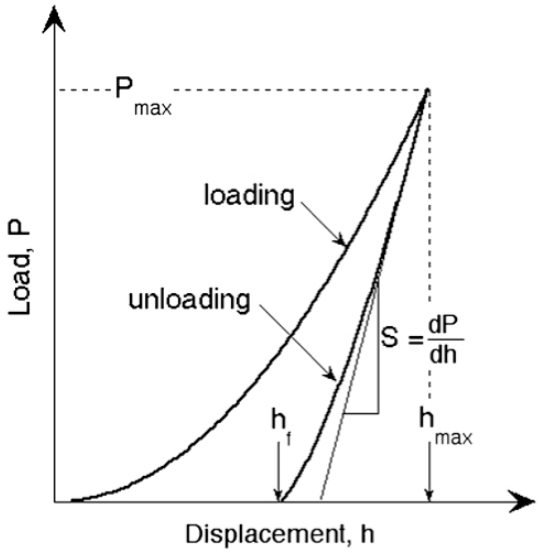

Fig. 37. Schematic of a load-displacement curve generated by the nano-indentation [227].

Three values can be extracted: maximum load, (P_{max}), maximum displacement, (h_{max}), and the elastic unloading, which is indicative of the stiffness (S), where $S = dP/dh$ and is defined as the slope of the upper portion of the unloading curve during the initial stages of unloading. Using the Berkovich tip i.e. pyramidal analysis, the load vs. displacement unloading data is fitted to either a:

- L*inear fit* (Doerner and Nix fit) [232], which is a tangent to the unloading curve at the maximum load and assumes the contact area remains constant as the indenter is withdrawn, which results in the unloading curve being linear, or alternatively;
- *Power law* fit (Oliver and Pharr method) [226, 227], which in contrast to the Linear fit, as experiments have shown that unloading curve is distinctly curved (see Fig. 38) and

is therefore well approximated by the power law relation. It was therefore used herein and has the form of equation (11) [227]:

$$P = \alpha(h_{\max} - h_f)^m \tag{11}$$

where, 'h_{max}' is the maximum depth reached by the indenter into the sample and 'h_f' is the depth of the indent after indentation (Fig. 38). 'α' and 'm' are the *power law* fitting constants for a calibration test performed periodically by the nano-indenter. For this test, a diamond indenter is used on fused silica, where 'α' = 0.05 and 'm' = 1.25 [227].

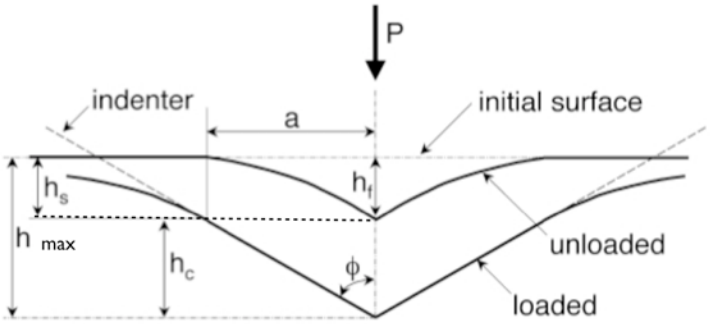

Fig. 38. Schematic illustrating the loading and unloading process showing parameters characterising the contact geometry. 'a' is the radius of contact. [227].

From Fig. 38, the plastic depth (h_c) is estimated using equation (12) [227]:

$$h_c = h_{\max} - h_s \tag{12}$$

where 'h_s' can be replaced, creating equation (13) [227]:

$$h_c = h_{\max} - \varepsilon(CP_{\max}) \tag{13}$$

where 'C' is the 'contact compliance' equal to the maximum force (tangent) and also the inverse of the stiffness (S), as represented below [227]:

$$h_c = h_{\max} - \varepsilon\frac{P_{\max}}{S} \tag{14}$$

where, 'ε' is a constant, the value of which depends on the geometry of the indenter, for a

Berkovich indenter, 'ε' is 0.75 [227, 231]. As previously highlighted, on unloading, the elastic component of the displacement starts to recover producing a sloped rather than horizontal unloading curve.

It is from this slope that the elastic and plastic properties can be derived. In order to determine the contact area (A), one of three methods can be used: 1) An in-situ atomic force microscope can be used, 2) Optical or electron microscopy after testing, or 3) Using an area function 'F(d)' that uses the plastic depth, 'h_c' and describes the projected i.e. cross sectional area, where [227]:

$$A = F(h_c) \tag{15}$$

The hardness, 'H' (GPa) is then estimated using the maximum load (P_{max}) and the projected area of contact (A_r) [227]:

$$H = \frac{P_{\max}}{A_r} \tag{16}$$

To obtain the reduced elastic modulus (E_r), the unloading portion of the load-displacement curve is analysed according to the following relationship [227], which is dependent on the contact area:

$$C = \frac{\pi^{1/2}}{2E_r A^{1/2}} \tag{17}$$

where, 'C' is the contact compliance again and 'E_r' is the 'reduced modulus of elasticity'. This value generally includes a contribution from both the material being tested and the response of the test device itself. The Young's modulus of the specimen 'E_s' is represented through the following relationship [227]:

$$\frac{1}{E_r} = \frac{(1-v_i^2)}{E_i} + \frac{(1-v_s^2)}{E_s} \tag{18}$$

where, 'E_i' is the Young's modulus for the indenter, 'E_s' is the Young's modulus for the sample, 'E_r' is the reduced modulus of elasticity (GPa) and 'ν' is Poisson's ratio. For a diamond indenter tip, E_i =1141 GPa and ν_i = 0.07.

The Poisson's ratio varies according indented phase and crystal orientation. The most common orientation was assumed and a value designated, where: PAN-derived carbon fibre varies from 0.20 (UHM) to 0.25 (UHS) [233]; a typical AS-4 carbon fibre, ν_S = 0.23 [234]; monolithic pyC, ν_s = 0.27 [235]; SiC, ν_s = 0.188 [236]; silicon, ν_S = 0.27 in the [111] orientation [237]. In the event where an indentation was made across two interfaces, the test was omitted.

3.4.8.2. Fracture toughness

The Vickers indentation fracture (VIF) method is used to generate an indent with propagating cracks, the length of which are used to estimate the fracture toughness (K_{1C}) [238, 239]. An estimate of the fracture toughness is calculated using the equation introduced by Lawn *et al* [240] in 1980, which has the form:

$$K_C = \delta \cdot \left(\frac{E}{H}\right)^{0.5} \cdot \frac{F_m}{c^{3/2}} \tag{19}$$

where, 'E' is the Young's modulus (GPa), H is the hardness (GPa), 'F_m' is the maximum applied force (mN), 'c' is the length of the crack path from the centre of the indent and 'δ' is an empirically determined calibration constant. For the Berkovich tip, which possesses the same depth-projected area ratio as a Vickers indenter, 'δ' is taken as 0.016 [241].

It should, however, be acknowledged that although there is no reported issue with using the Berkovich tip with equation (19), Quinn *et al* [242] reported that cracks are more readily produced at lower comparable indentation test loads in comparison to the Vickers diamond pyramid. This was attributed to the more sharp triangular geometry of the three-sided Berkovich indenter in comparison to the four-sided Vickers indenter. It could therefore be anticipated that any fracture toughness value generated by the Berkovich indenter would be slightly lower than in comparison to a value derived using a Vickers indenter.

However, there has always been scepticism regarding the accuracy of the indentation fracture method in estimating the fracture toughness. Kruzic *et al* [243] investigated the four most common test techniques in terms of their suitability for assessing the fracture toughness. These included: Vickers indentation fracture (VIF) test, Cube corner indentation fracture (CCIF) test, Vickers crack opening displacement (VCOD) and the Interface indentation fracture (IIF) test. It was concluded that no method granted sufficient accuracy to be implemented as a standard test, although, could be used with care for comparative studies within the same material. This was in agreement with Quinn *et al* [242] who questioned the accuracy of equation (19), concluding that the VIF method was unsuitable for determining the fracture toughness of any material. This was attributed to frequently encountered highly complex residual stress conditions that were often accompanied by extensive spalling of material from around the indentation, which created an incredibly complex crack tip arrest environment.

Therefore, for testing in this study, the indentation fracture method was used with a Berkovich tip to fracture different phases inside the composites and make comparisons with similar composites. Any successful propagating cracks were imaged using optical microscopy, at magnifications up to 1000x (times) and at higher magnifications using the FEG-SEM, which could clearly identify any cracks. The crack lengths were measured from the centre to the outer tip of the crack using the image measurement software previously discussed: GIMP.

3.4.9. Friction testing

A dynamometer (dyno) is often employed to test the friction and wear characteristics of materials, which replicates the action of the braking system in a controlled environment. The main advantage of using a dyno is the convenience of testing under the same test conditions. However, limitations exist by the assumptions incorporated to represent any variables. Such variables could include: weather conditions such as humidity, moisture, water; air flow around the disc; rolling weight of the vehicle; scale, which was the main consideration herein. To help alleviate this potential issue, any COF recorded was only intended for comparative reasons between similar sized C_f/C-SiC discs.

An air-powered small-scale dyno was used to validate the mechanical sustainability and friction behaviour of three different C_f/C-SiC composites, including

those comprising end-of-life carbon fibre pre-pregs. A schematic of the dynamometer layout is illustrated in Appendix A – Figure 26. Testing was performed using: an air pressure of 0.34 MPa (50 Psi) to power the motor and load cell, which generated a rotating speed of 11,000 RPM and a brake force of 550 N, respectively. The testing procedure for 200 stops was as follows: -

1). The surface of the disc was ground flat using a grinder (Axminster SIEG U2 Mill/Drill/Grinder) and polished to a 1-µm finish.
2). Two small holes measuring 10 mm (diameter) were drilled into each disc, which were then screwed into place, adjacent to the pad.
3). The computer, data-logger and air were switched on.
4). Once the pressure and speed was reached, the brakes were applied, stopping the disc.
5). Repeat immediately.

The COF and COF stability (S) of the C_f/C-SiC discs were tested against industry standard pads. The formulation of the standard pad was confidential but was noted to contain the following elements: iron, copper, zinc, calcium, aluminium, tin, sulphur and phosphorus. The COF was calculated according to equation (20) and multiplied by a calibration factor: 2.03, which was based on the angle of inclination of the shaft in relation to the load cell, and the load cell itself.

$$CoF = \frac{T_L}{R_N \times d_r} \tag{20}$$

where, 'COF' is the coefficient of friction (µ), 'T_L' is the torque measured by the load cell, 'R_N' is the normal force, 550 N and 'd_r' is the effective radium of the disc, 22 mm. The friction stability (S) was calculated according to (1), defined as:

$$S = \frac{CoF_{Ave}}{CoF_{\max}} \tag{1}$$

where, 'CoF_{Ave}' is the average COF over the whole braking and "CoF_{Max}' is the maximum COF value.

4. Results and analysis

4.1. C_f/C preform development

4.1.1. Effect of pyrolysis on carbon fibre pre-pregs

It was previously established in *Section 2.2.1* that the architecture of the carbon inside the preform is a critical factor that influences the penetration capability of the molten silicon during LSI manufacture. If the carbonaceous architecture surrounding the fibres and fibre bundles is too narrow, closed or orientated in a very complex format; access to the silicon will be inhibited or even stopped. The consequence of this would be incomplete penetration with a limited conversion of the silicon in to the desired SiC. Therefore, the effect of pyrolysis on different virgin and end-of-life pre-pregs were investigated at temperatures between 300 and 900°C. The aims of the investigation were as follows: -

1). Identify the rate and extent of pyrolysis, which was quantified by measuring the relative weight loss after pyrolysis using a digital balance (Kern/EG).
2). Identify and discuss any change in the architecture amongst the fibres and fibre bundles. Optical microscopy was used in the bright field mode to characterise the architecture of the fibres at 500 times magnification. Image analysis software was used to measure any in between the fibres or bundles.
3). Identify and discuss any change in the bulk geometry: length, width and thickness. Any geometric change was estimated by taking measurements prior to and after each pyrolysis cycle using a digital vernier calliper.
4). Discuss the role and function of the resin.

After pyrolysis, all of the virgin and end-of-life pre-pregs exhibited a weight loss as the resin was converted into pyC and any volatile species were lost through gaseous emissions. This is illustrated in Fig. 39, which shows an increasing mass change (%) with increasing pyrolysis temperature. The results are tabulated in Appendix B – Table 9.

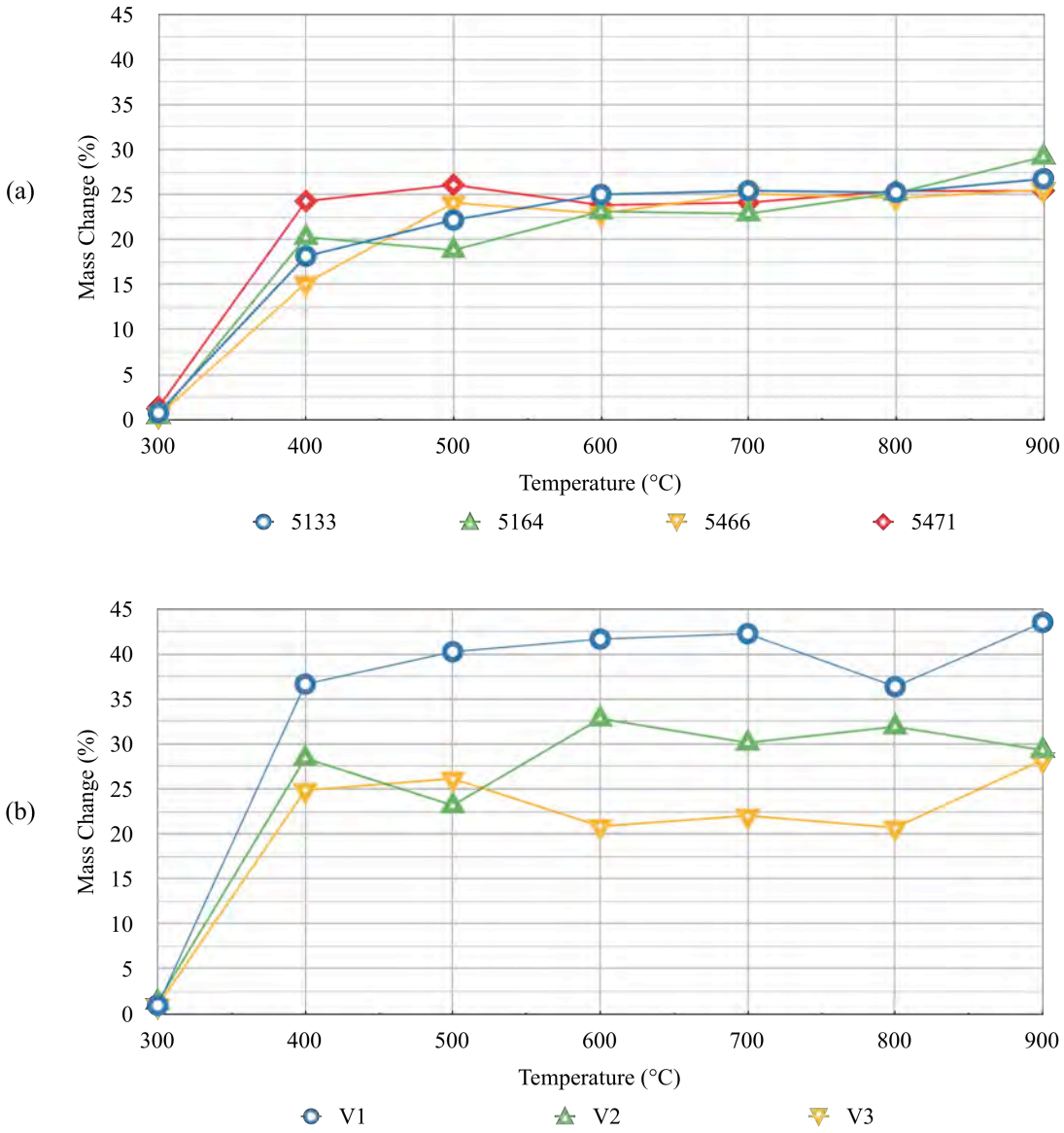

Fig. 39. Graphs showing the increasing mass change (%) of: (a) the end-of-life pre-pregs and (b) the virgin-based pre-pregs as they were progressively pyrolysed from 300 to 900°C in 100°C steps for 30 minutes.

After being pyrolysed for 30 minutes at 300°C, none of the pre-pregs exhibited any noticeable mass change. However, after 30 minutes at 400°C, a significant weight loss was evident from all of the samples. Beyond 400°C, all of the pre-pregs continued to exhibit a mass loss, although to a much lesser extent. These results indicate that most of the resin remained intact at temperatures up to 300°C, while between 300 and 400°C; the maximum rate of pyrolysis was evident, which is represented by the steep gradients in Fig. 39. The maximum rate of epoxy conversion

into pyC and release of any gaseous emissions therefore occurred between 300 and 400°C. In addition, since only a minor weight loss was exhibited between 400 and 900°C, it could be assumed that almost all of the conversion reactions occurred and emissions were lost between 300 and 400°C.

Apart from sample V1, there was no significant difference between: the virgin and end-of-life pre-pregs, pre-pregs with different fibre tow counts or different architectures (woven and UD). The additional mass change exhibited by V1 is likely attributed to the higher initial proportion of resin inside the pre-preg, which was 45% in comparison to the other pre-pregs that ranged between 37 and 40%. This therefore assumes that the fibres exhibited no weight loss during pyrolysis up to 400°C, which is reasonable considering that the fibres should be stable up to this temperature.

In order to reduce the possibility of errors, further tests were performed and a mean was calculated using seven of the '5471' pre-pregs under the same pyrolysis conditions at 500, 700 and 900°C for 30 minutes. The results are tabulated in Appendix B – Tables 10, 11 and 12 respectively, and show that the mean mass change (%) at each temperature was 24.04 ±0.43, 25.36 ±0.16 and 26.09 ±0.41, which were very similar to the results in Fig. 39.

4.1.1.1. Internal microstructure

FEG-SEM micrographs in Fig. 40 illustrate the microstructure of the woven end-of-life pre-preg 5417 after 30 minutes at 300, 500 and 900ºC. From Fig. 40(a), after pyrolysis at 300ºC, the fibre architecture appeared to be unaffected with a significant quantity of resin remaining in between the fibres and fibre bundles. After increasing the temperature to 500ºC (Fig. 40(b)), gaps became noticeable between the fibres, while further pyrolysis to 900ºC generated significantly larger gaps up to and beyond 20 µm. Larger gaps greater than 20 µm were also evident, but only in specific regions. For example, in between fibres in different perpendicular orientations, which is shown in Fig. 40(c).

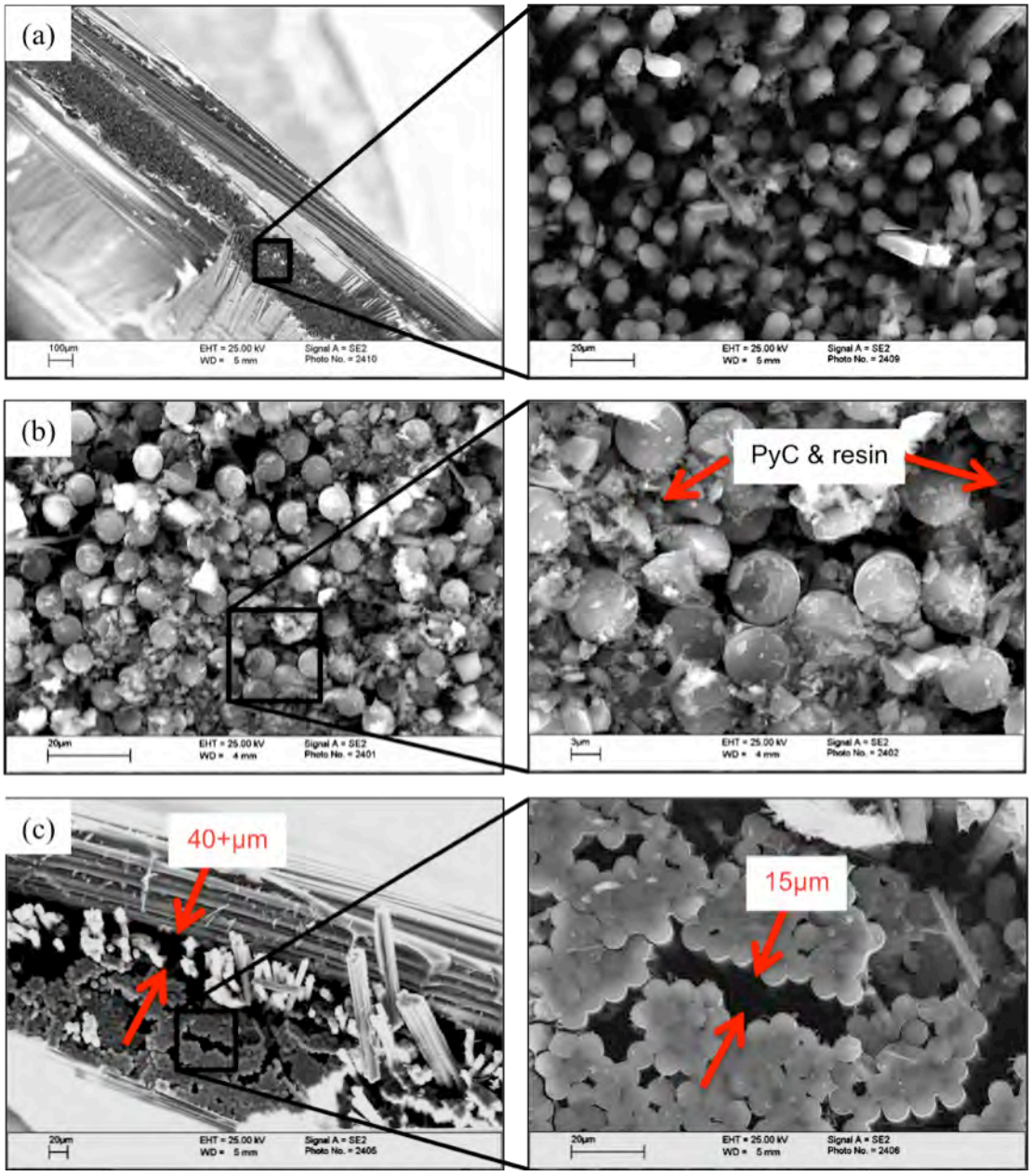

Fig. 40. FEG-SEM micrographs of end-of-life pre-preg: 5471, illustrating the progressive conversion of epoxy resin at (a) 300ºC, (b) 500ºC and (c) 900ºC, with inset micrographs at higher magnifications.

As the temperature increased, the resin was progressively converted into pyC with the corresponding release of gaseous emissions. As the resin depleted and converted into brittle pyC, it is apparent from the micrographs that the bonds between the fibres must have become weaker and inevitably fractured. However, the fibres did not split up individually. Instead, they split up as bundles of fibres, with each bundle typically comprising between 10 and 40 fibres that were held together by the pyC and

any remaining resin. According to the micrographs in Fig. 40(b), this was not evident after pyrolysis for 30 minutes at 500ºC, which indicates that fracture and separation probably occurred between 500 and 900ºC. This could be related with findings by Schulte-Fischedick *et al* [157], where thermo-optical analysis of multi-layered CFRP's by pyrolysis revealed that the first fibre-to-matrix debonding occurred at 505°C.

Nevertheless, these results prompted further analysis of the remaining pre-pregs, in order to further understand how pyrolysis affects the internal fibre architecture and whether there are any differences between the virgin and end-of-life based pre-pregs.

The remaining woven (V1) and UD pre-pregs are shown in Fig. 41, Fig. 42 and Fig. 43 respectively. Optical micrographs of each pre-preg were combined together using image manipulation software. According to the micrographs, there were no clear differences between the virgin-based and end-of-life pre-pregs. Instead, only subtle differences are evident, which are related to the fibre architecture, being either woven or UD. The microstructure of the woven pre-preg (V1) appeared comparable to the previously described end-of-life 5471 pre-preg in Fig. 40(c). It comprises similar tightly packed C_f/C bundles, which also consisted of approximately 10 to 50 fibres that were typically 10 to 50 µm apart. Micrographs of the UD pre-pregs in Fig. 42 and Fig. 43 were also comparable to each other apart from 5164 (Fig. 43(c) and (d)), irrespective of the origin of the pre-preg.

V1

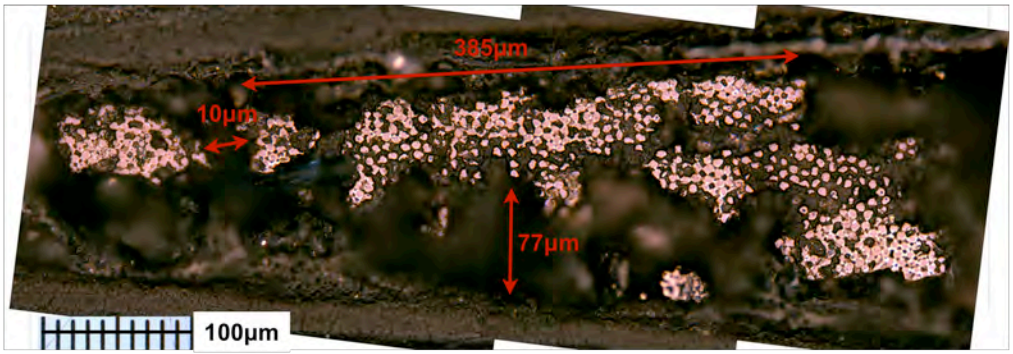

Fig. 41. Reconstructed optical micrograph of the virgin woven fibre pre-preg 'V1' after 30 minutes pyrolysis at 900°C.

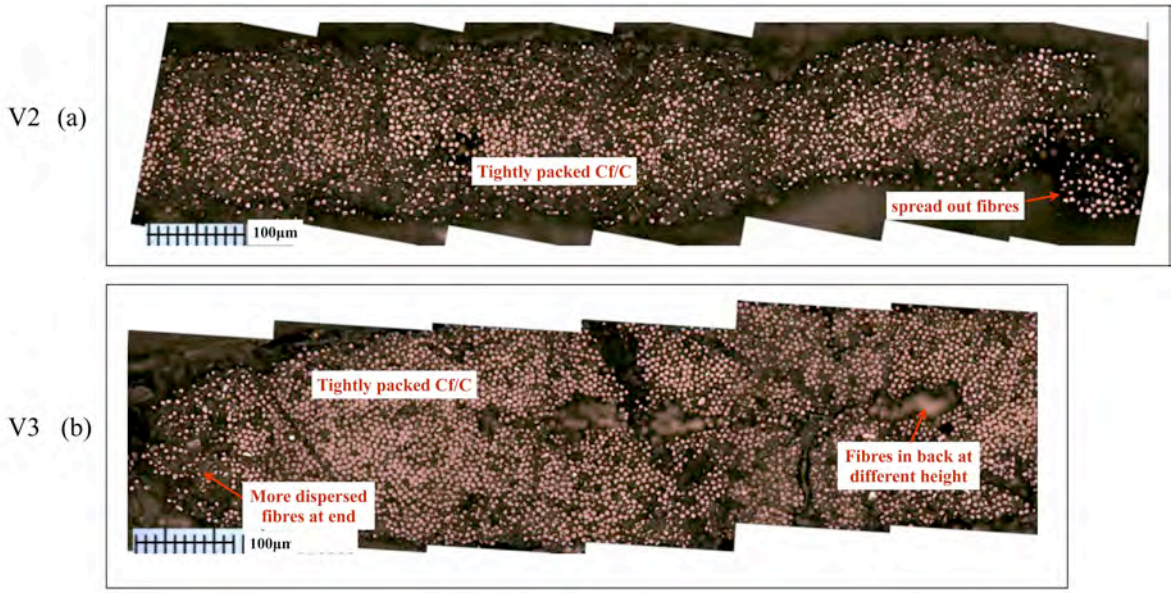

Fig. 42. Reconstructed optical micrographs of the fibre architecture inside the virgin-based UD pre-pregs after 30 minutes pyrolysis at 900°C.

Only apparent differences are evident with pre-preg 5164 because the fibres were at different heights. By adjusting the focus of the microscope, fibres could be observed in a similar architecture, although in the background. This was evident to some extent inside all of the micrographs and was likely caused by the nature in which the pre-preg fibres were cut, by hand using scissors. Therefore, it is reasonable to assume that some fibres would have been cut slightly shorter than others. In this case, only a few microns difference in the fibre length could account for the observed differences in the micrographs. For example, this can be seen in Fig. 41, which shows a number of blurred fibres in the background.

One difference between the woven and UD pre-pregs is the number of tows, where V1 has 3,000 compared to 12,000 in all of the other pre-pregs. However, since the dimensions of the pre-pregs were not restricted when they were sealed, it could be assumed that the fibres were not artificially ‘squashed together’. This could therefore, at least in part account for the increased space between the fibres of V1 in Fig. 41.

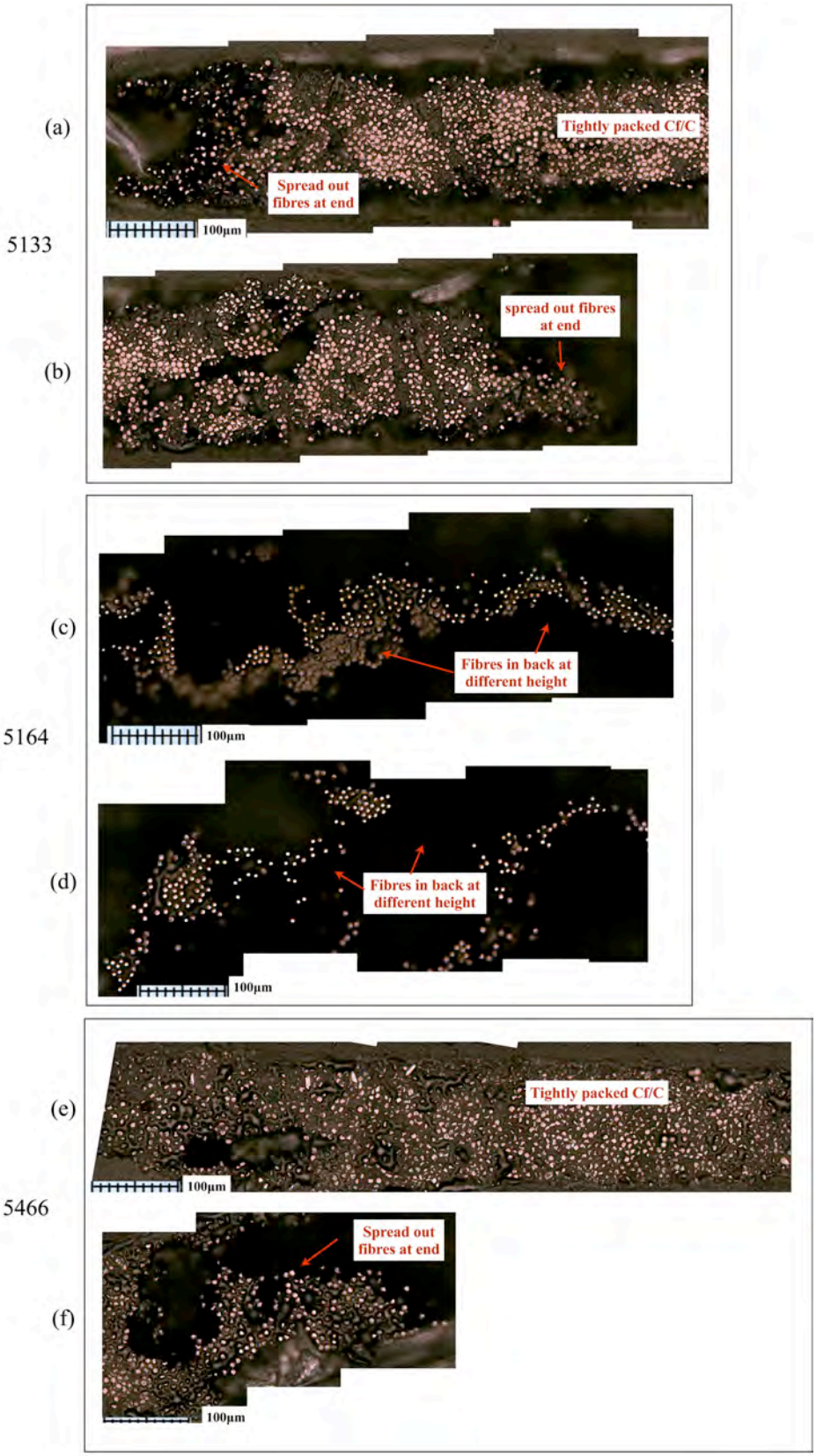

Fig. 43. Reconstructed optical micrographs of the fibre architecture inside the end-of-life UD carbon fibre pre-pregs after 30 minutes pyrolysis at 900°C.

In fact, the architecture of the UD pre-pregs is essentially the same as the woven pre-pregs, which also comprise UD tows. However, the UD tows inside the oven pre-pregs are bi-directional and overlap each other. Therefore, any differences between the UD and woven pre-pregs should be as a result of these inter-woven fibre tows that could restrict any movement to the adjacent fibres or tows, irrespective of the conversion and depletion of the resin.

The only information that can be extracted from these micrographs, at these scales is that the fibres inside the woven pre-pregs appear to have separated more as C_f/C bundles as can be seen in Fig. 40(c) and Fig. 41. The fibres inside the UD pre-pregs were also tightly packed, but in contrast to the woven pre-pregs, significant gaps were not evident in between the smaller C_f/C bundles.

In addition, there is also evidence that the fibres spread out individually at the edges of the pre-preg, which is highlighted in Fig. 42(a), (b) and Fig. 43(f). These fibres likely spread out at the edges because there was insufficient pyC to bond the fibres together and insufficient adjacent fibres restricting their movement. This phenomenon was not observed inside the fibres of the woven samples.

Another consideration that might contribute to the observed results is the fibre-matrix (F-M) bond strength, which was previously discussed in *Section 2.3.2.2.2*. It was previously identified that the F-M bond strength could be measured in terms of the ILSS, where a typical virgin ILSS ranges between 40 and 50 MPa [159]. The Pyrofil^{TM} fibres in the virgin-based pre-pregs are reported to possess a very high ILSS of 83 MPa, in comparison to a comparatively high ILSS of approximately 61 MPa [244] for the AS4 carbon fibres inside the end-of-life pre-pregs. This could offer some support as to why the fibres in the microstructures predominantly stuck together. This is in accordance with Krenkel *et al* [33], who stated that a high F-M bond strength would lead to C_f/C structures that are characterised by segments of C_f/C bundles. A clear example of these segments can be seen in Fig. 40(c) inset, which shows multiple fibres stuck together that were separated by a proportionally large gap.

4.1.1.2. Dimensional changes

The effect of pyrolysis on the length, width and thickness of each pre-preg was compared prior to and after pyrolysis at each temperature between 300 and 900°C at

100°C intervals for 30 minutes. The results are shown in Fig. 44, Fig. 45 and Fig. 46 and tabulated in Appendix B – Tables 13 to 15 respectively. Expansion and contraction in the graphs were represented by positive and negative geometric changes (%) respectively.

4.1.1.2.1. Length direction

There was negligible change in the length direction after pyrolysis for all of the pre-pregs, which is shown in Fig. 44. Additional graphs with smaller scales have been included in Appendix A – Fig. 27. The negligible change is likely attributed to the reinforcing nature of the fibres, which relates to the fibre orientation and was previously illustrated in the schematic in Fig. 37. Both the UD and woven pre-pregs possessed fibres in the 'length orientation', which consequently inhibited any geometric change. In fact, all of the fibres in the UD pre-preg and half of the fibres in the woven structures were orientated in the length direction. Therefore, considering the length changes were similarly small for both architectures, these results also suggest that only a proportion (half in this case) of the fibre is required to be orientated in a specific direction to effectively inhibit any geometric change during pyrolysis.

Investigations by Krenkel *et al* [142, 157], Kochendorfer *et al* [156] and Schulte-Fischedick *et al* [144] revealed that a 3D, bi-directionally reinforced composite with in-plane reinforcement i.e. 2.5D and woven CFRP respectively also exhibited little to no geometric change (shrinkage) in the fibre direction (length and width) due to their reinforcing nature after similar pyrolysis at 900°C. However, it should be noted that the pre-pregs tested herein were single layer and not the multi-layered structures that were tested in the highlighted investigations. This should however, have little impact on any dimension change in the length direction.

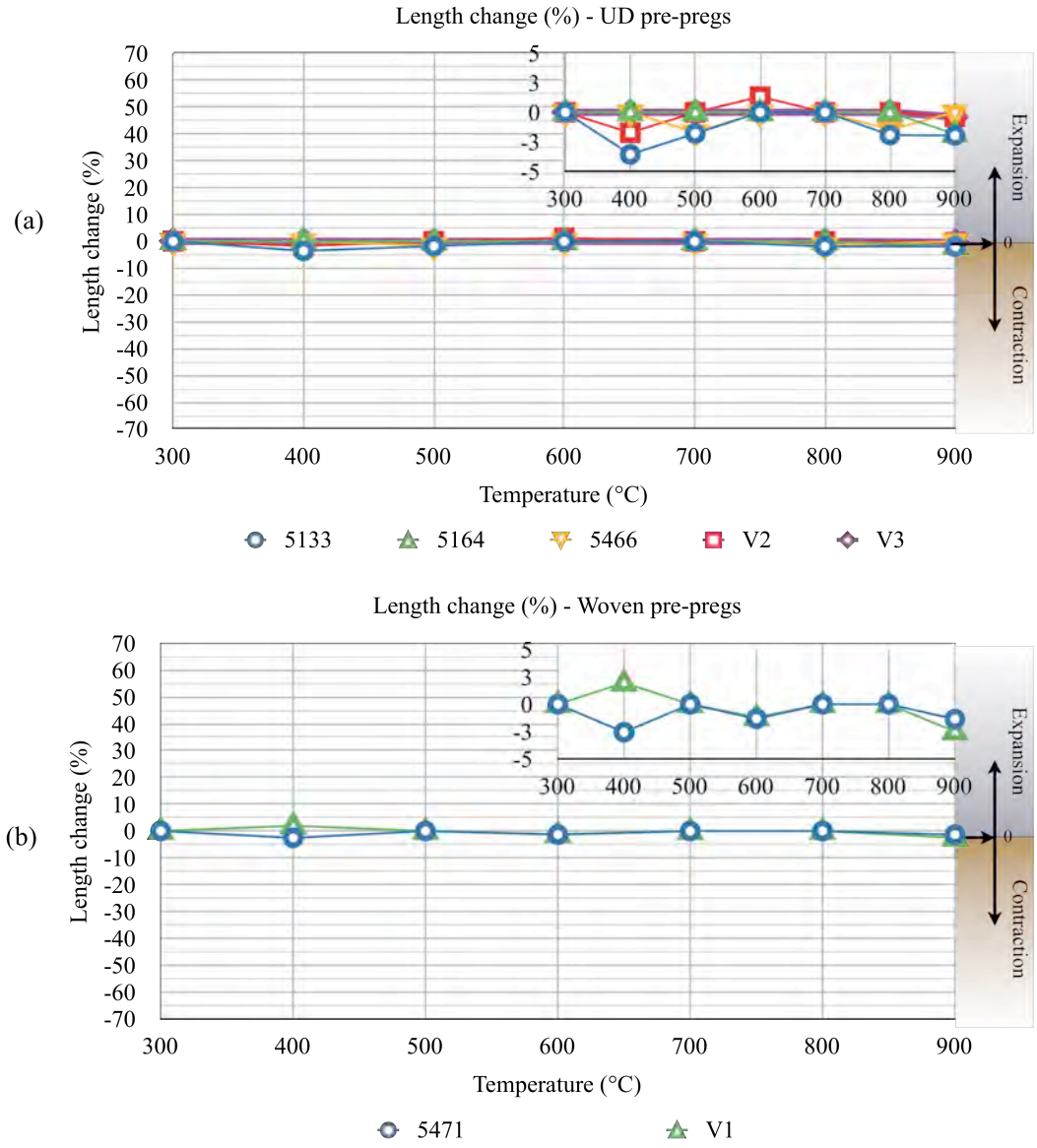

Fig. 44. Graphs illustrating the negligible length change of: (a) UD pre-pregs and (b) Woven pre-pregs as they were progressively pyrolysed from 300 to 900°C in 100°C steps for 30 minutes.

4.1.1.2.2. Width direction

The width change (%) results are shown in Fig. 45, while additional graphs with smaller scales have been added to Appendix A – Fig. 28. None of the pre-pregs exhibited any significant expansion in the width direction. Instead, each pre-preg typically contracted, which was evident at temperatures as low as 300°C and could be similarly attributed to the proportion of fibres existing in the width direction.

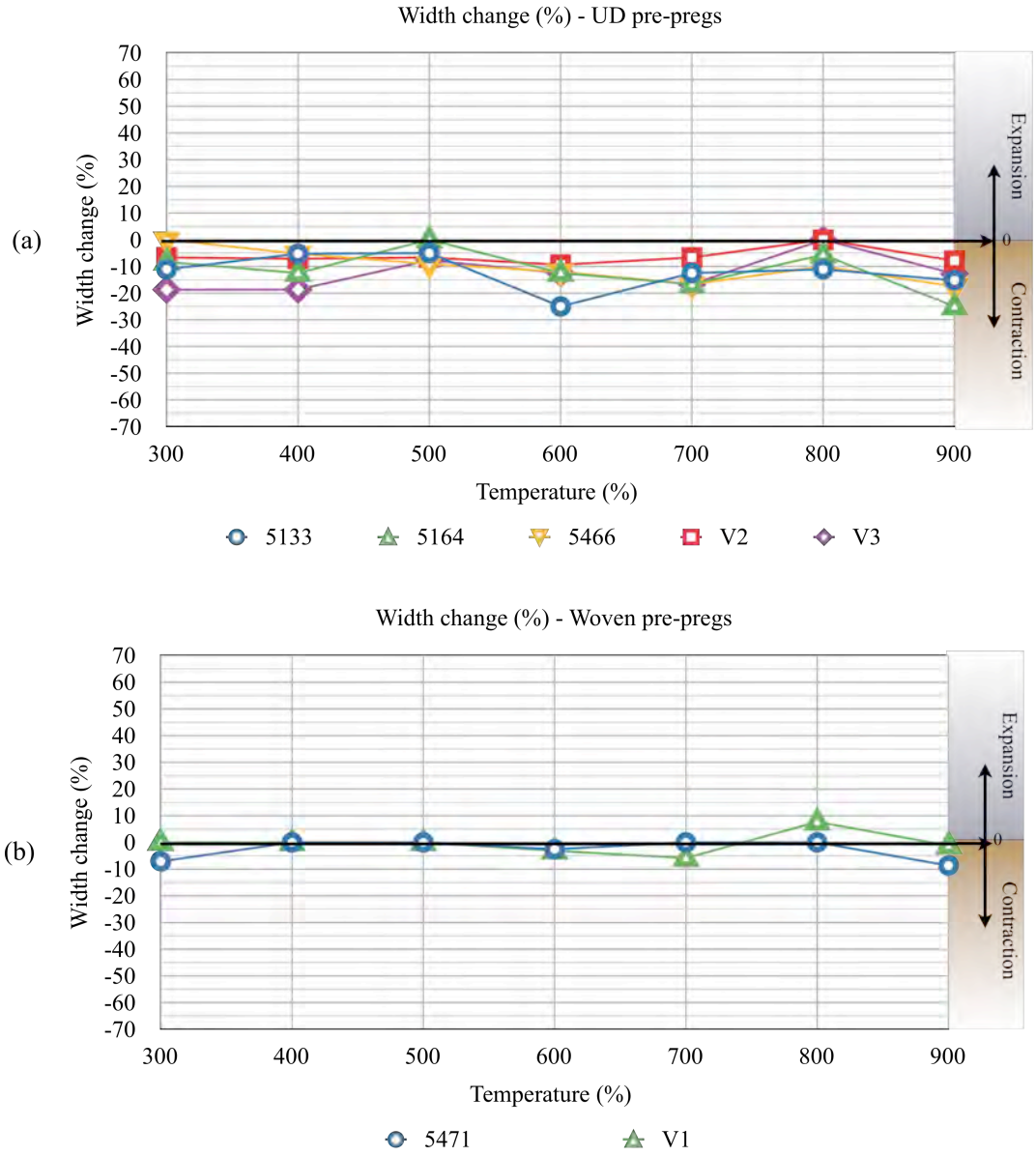

Fig. 45. Graphs with line of best fit showing the width changes of: (a) UD pre-pregs and (b) Woven pre-pregs as they were progressively pyrolysed in 100°C steps for 30 minutes from 300 to 900°C.

Referring back to the schematic in Fig. 37, the fibres inside the UD pre-pregs are now perpendicular and therefore were unable to inhibit any movement during pyrolysis. Consequently, a significant contraction was exhibited of up to 25% for the end-of-life pre-pregs and a comparable 18% for the virgin-based pre-pregs. By way of contrast, as previously highlighted, the woven pre-pregs comprised reinforcing fibres in both orthographic directions (length and width) and therefore did not exhibit any significant change in the width direction. In a similar respect to the length direction,

this was in accordance with the other reported investigations [142, 144, 156, 157], which also tested multi layer composites and would have had little impact on any dimension change in the width direction.

4.1.1.2.3. Thickness direction

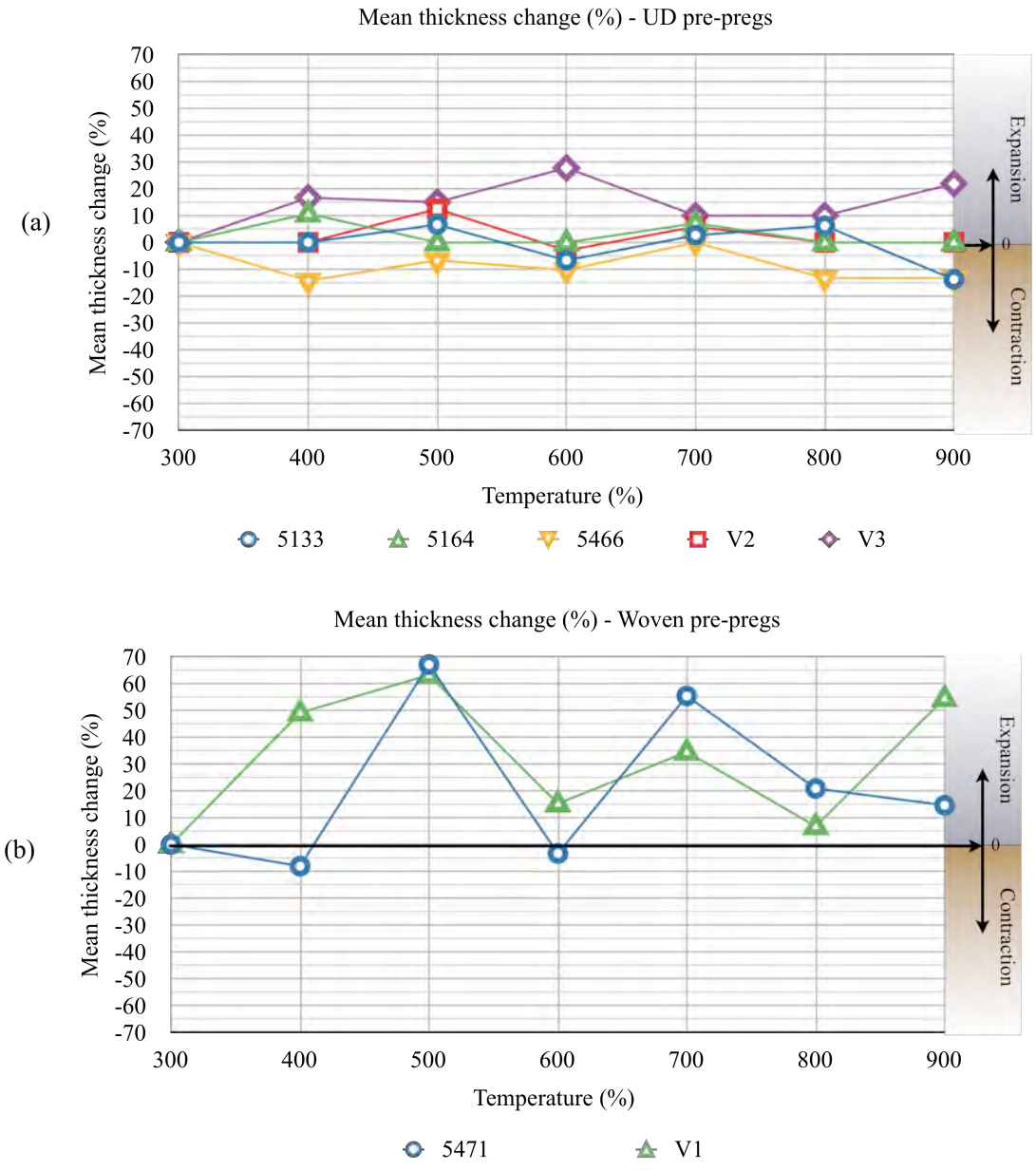

Fig. 46. Line graphs illustrating the width changes of: (a) UD pre-pregs and (b) Woven pre-pregs as they were progressively pyrolysed from 300 to 900°C in 100°C steps for 30 minutes.

After pyrolysis, there were no obvious differences between the virgin-based and end-of-life pre-pregs. However, differences were apparent between the UD and woven architectures, which are illustrated in Fig. 46(a) and (b) respectively. Individual graphs with smaller scales have been added to Appendix A – Fig. 29.

None of the pre-pregs exhibited any variation in the thickness until reaching 300°C. Beyond this temperature, all of the pre-pregs exhibited some variation in the thickness, in particular the woven pre-pregs. None of the UD pre-pregs exhibited any significant expansion or contraction, apart from V3. However, there was no significant difference between V2 and the end-of-life pregs, so no conclusive difference can be drawn between these virgin-based and end-of-life pregs.

By comparison, the woven pre-pregs responded very differently to the UD pre-pregs. Apart from the initial difference between 300 and 400°C, the reason of which is unclear but could be related to the additional resin in V1, both pre-pregs responded in a similar manner after pyrolysis. A significant expansion was exhibited by both pre-pregs at approximately 500°C, which could be related back to the previously discussed fibre/matrix debonding phenomenon at 505°C. Meanwhile, beyond 500°C, both pre-pregs shrank back to almost their original shape at 600°C, before expanding and contracting once again.

This could be attributed to a ‘kinking’ effect, which by definition in this context is described as the ‘bunching-up’ of the fibres (see Fig. 48). It could be envisaged that as the fibres bend or ‘kink’ during pyrolysis, the internal pressure inside the fibres would build up. Then, due to the elastic recovery, the fibres would possess a strong tendency to become straightened i.e. as the Gibbs free energy ΔG becomes less than zero. However, as the pyrolysis temperature increased, there was a progressive depletion of the resin with an associated contraction. This could increase the pressure inside the fibre, which could promote the fibres to move i.e. ‘kink’ in the direction where the fibres were least hindered by either the adjacent fibres or the resin/PyC.

To understand this further, the schematic in Fig. 47 illustrates the three degrees of either movement or restricted movement inside the UD and woven architectures. The red arrows identify the observed restricted movement direction and where adjacent fibres could hinder any potential movement.

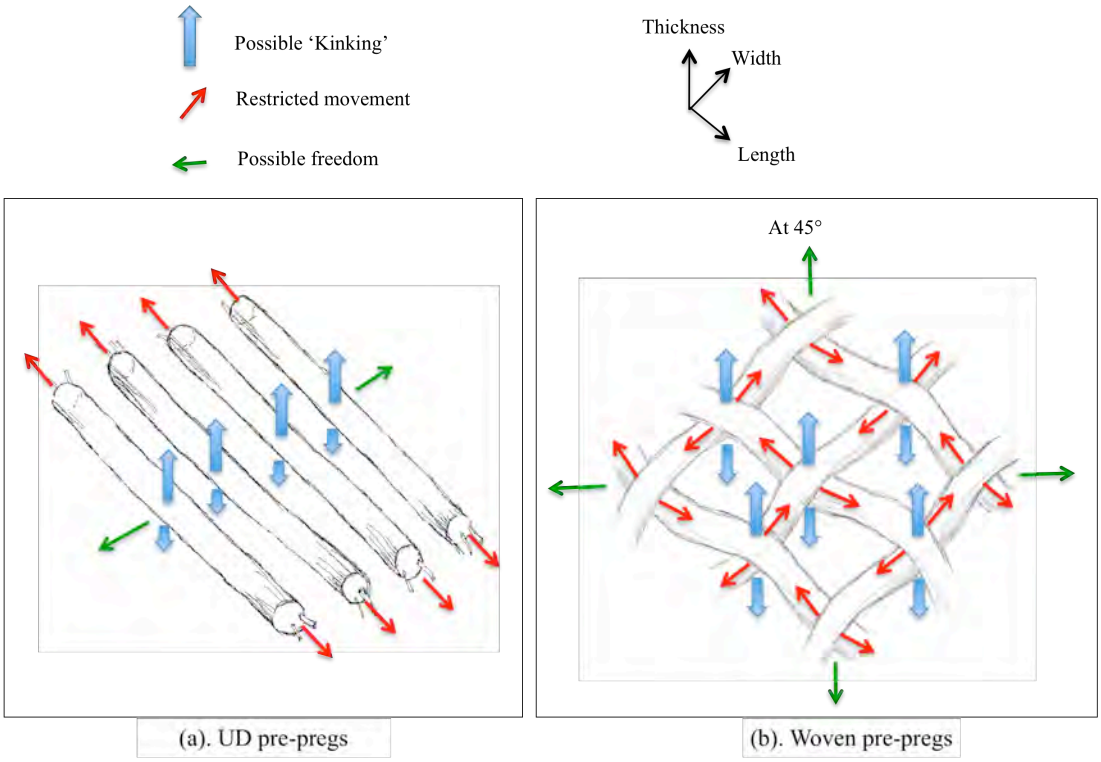

Fig. 47. Schematic illustrating the restricted directions (red), possible 'kinking' directions (blue) and possible freedoms of movement (green) for: (a) UD and (b) woven pre-pregs during pyrolysis.

Meanwhile, an additional freedom of movement could exist for the woven structure at a 45° angle to the length and width direction. However, the potential movement in this direction should be significantly less in comparison to the freedom of the UD pre-pregs in the width direction.

One possible explanation could be that during pyrolysis, the fibres inside both the UD and woven pre-pregs were able to move in the thickness direction (blue arrows in Fig. 47 and Fig. 48), which permitted the fibres to 'kink'. As the fibres would 'kink' during an expansion, the fibres in the length (and width for the woven pre-preg) would be pulled, causing a slight reduction in the length and width. The opposite would by the case during a contraction. In this case, the fibres would be pushed, causing a slight increase in the length (and width for the woven pre-preg).

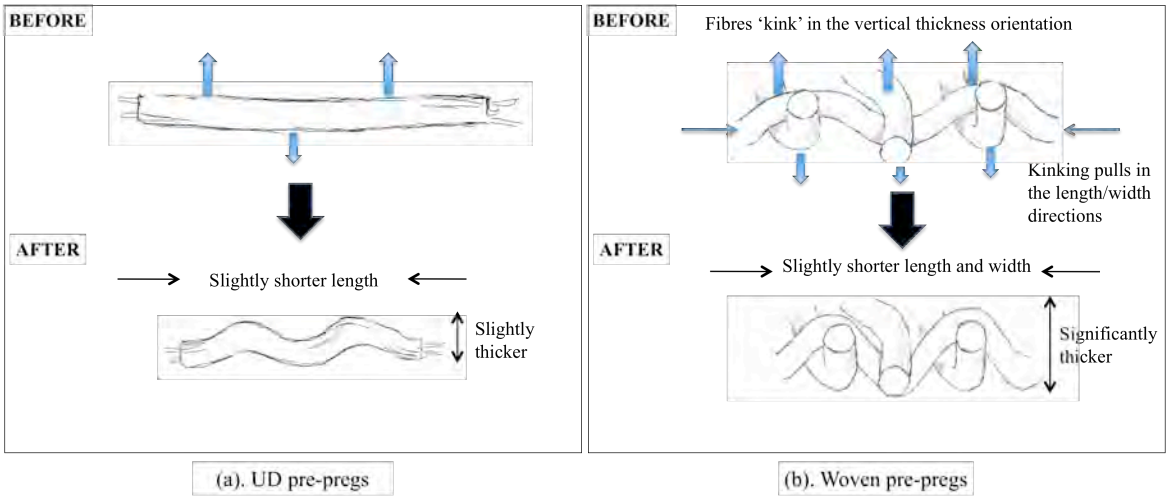

Fig. 48. Schematic side view illustrating the consequences of the 'kinking' effect of (a) UD pre-preg and (b) woven pre-preg, after pyrolysis.

This phenomenon could account for the observed results, but are in contrast with the typical minor shrinkage of around 5% commonly observed by multi-layered CFRP structures [142]. However, as previously stated, by comparison a multi-layered CFRP would be restricted, at least in part by the adjacent pre-pregs in the thickness direction. This could explain why such multi-layered architectures exhibited such a low dimension change.

Therefore, the degree of curvature of the kink in this case could be related to either: (i) the presence of any adjacent fibres; (ii) proportion of resin, which according to prior weight analysis, gradually depleted with increasing pyrolysis temperature. This could account for the smaller variation in thickness at the higher temperature of 700°C in comparison to 500°C that was observed in Fig. 46; (iii) the fibre-matrix bond strength (ILSS), which would also likely reduce as the resin depleted.

In summary:

- There was no significant difference between virgin-based and end-of-life carbon fibre pre-pregs in terms of weight loss after pyrolysis.
- As the resin pyrolysed with an evolution of gaseous emissions, the resin inside each pre-preg progressively pyrolysed into pyC.
- The greatest rate of pyrolysis inside all of the pre-pregs was between 300 and 400°C, which coincides with the maximum rate of weight loss. Beyond 400°C,

pyrolysis continued for all of the pre-pregs, although to a much lesser extent. There was no evidence that complete pyrolysis occurred at 900°C.

- Dimensional analysis confirmed that in the aligned direction to the fibres inside of all the pre-pregs, any significant variation in the geometry was restricted. This was observed in the length direction for both the UD and woven pre-pregs and the width direction for the woven pre-pregs.
- By contrast, any variation in the geometry was not inhibited in the perpendicular directions to the fibres. Therefore, the UD pre-pregs exhibited significant shrinkage in the width direction. Meanwhile, in the vertical thickness direction, both the UD the woven pre-pregs exhibited some variation, in particular the woven pre-pregs, which could be attributed to a kinking effect.
- The internal microstructure of the pre-pregs after pyrolysis at 900°C for 30 minutes was investigated by FEG-SEM and optical microscopy. There was no observed difference between the virgin-based and end-of-life pre-pregs. The microstructures comprised C_f/C segments, which was attributed to the high F-M bond strength of the fibres.
- The role of the resin inside these composites is to: support the fibres in a preferred orientation. This enables convenient transport of the pre-pregs and allows the fibres to be laid up in a desired architecture to modify the mechanical properties in a specific direction; generate a pyC interface after pyrolysis to help protect the fibres from environmental damage. For example, oxidation or alternatively the corrosive melt during LSI.

4.2. C_f/C-SiC microstructure characterisation

The aims of the microstructure characterisation were two-fold: firstly, to investigate and qualify the incorporation of the different recycled origins of carbon fibre; secondly, to identify the most appropriate carbon source and format of carbon fibre for manufacturing the C_f/C-SiC composites.

4.2.1. Volume fraction of the phases

Optical micrographs were taken to inspect the hierarchy of the developed microstructure of each composite. Image analysis software (GIMP) was then used to quantify the volume fraction (%) of the phases generated inside each composite, which were then compared to a virgin C_f/C-SiC composite. The raw materials used to construct the four C_f/C-SiC composites are detailed in Table 14 and included: (a) Recycled 'non-woven mat', (b) End-of-life UD pre-preg '5164', (c) End-of-life 2D woven pre-preg '5471', and (d) Virgin 2.5D preform 'ST', which were manufactured using a single LSI.

Optical micrographs in Fig. 49 illustrate the similarities in the hierarchy of the microstructure amongst all of the composites, irrespective of their preform architecture, carbon fibre source and carbon interface type.

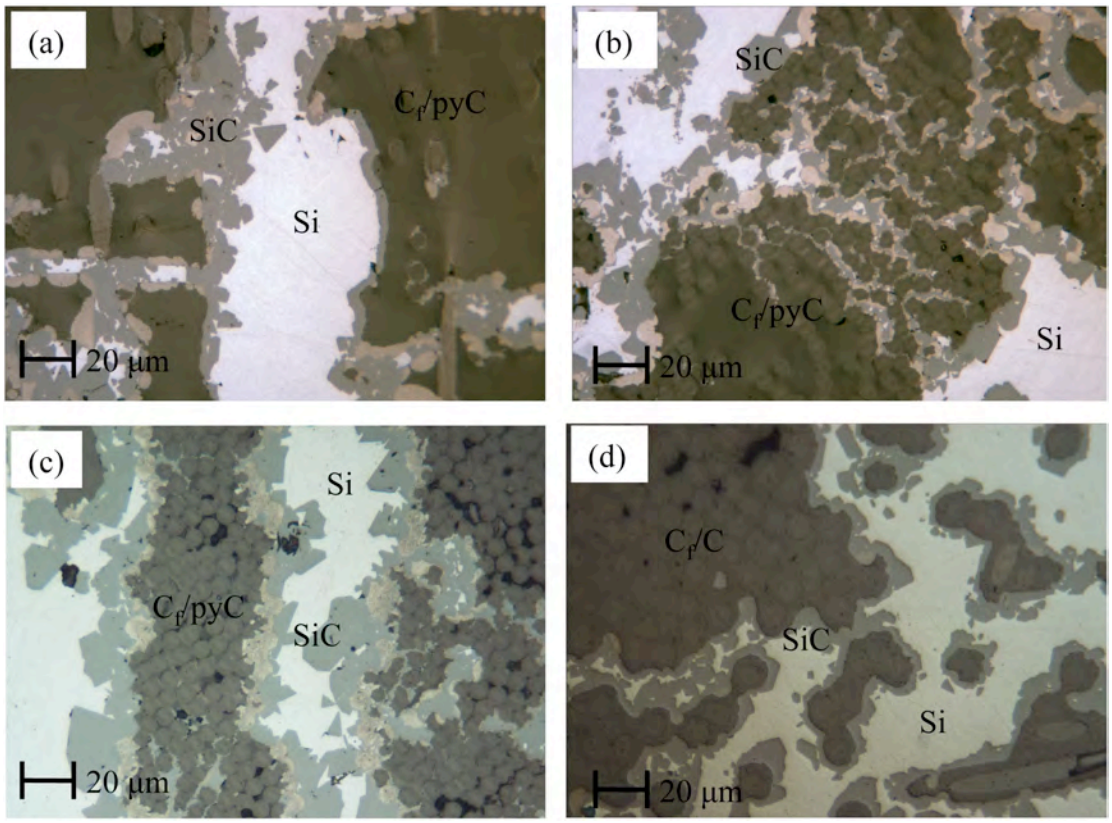

Fig. 49. Optical micrographs under polarised and DIC light conditions illustrating the format of the hierarchy order and morphology remained the same in (a) Recycled 'non-woven mat', (b) End-of-life UD pre-preg '5164', (c) End-of-life 2D woven pre-preg '5471' and (d) Virgin 2.5D preform 'ST' C_f/C-SiC composites.

From the inside of the microstructure, the following hierarchy is observed: C_f/C (dark grey/brown) with voids (black) in-between the bundles, SiC (grey), silicon (white) and additional voids. The overall microstructure of each composite was similar and also closely resembled that of a virgin LSI-derived composite, which was previously reported in Fig. 30. However, the apparent proportion of the phases differed, which could be influenced by either the preform architecture or the carbon source. Both of these factors are investigated in the proceeding sections.

The results of the average volume fraction (%) are shown in Fig. 50 and tabulated in Appendix B – Table 16. The C_f/C region was estimated as the proportion remaining after the SiC, silicon and voids were subtracted.

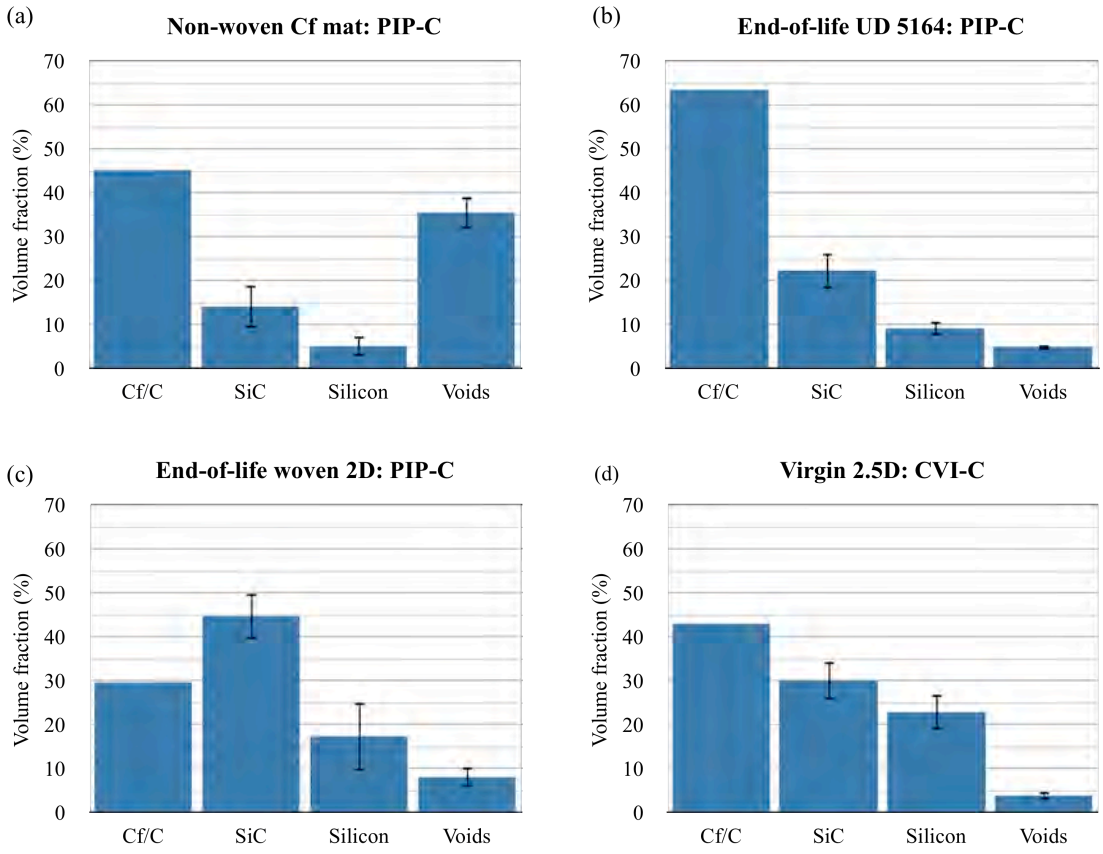

Fig. 50. Average composition by volume (%) of: C_f/C, SiC, silicon and voids inside C_f/C-SiC composites with different architectures and fibre origins: (a) Recycled 'non-woven mat', (b) End-of-life UD pre-preg '5164', (c) End-of-life 2D woven pre-preg '5471', (d) Virgin 2.5D preform 'ST'. Error bars represent the standard deviation.

4.2.1.1. C_f/C and silicon carbide regions

The UD architecture in Fig. 50(b) possessed the highest C_f/C volume fraction, followed by the non-woven, 2.5D and 2D architectures. The elevated proportion in the UD architecture could be attributed to the closely packed fibre bundles and absence of any gaps or voids created by the overlapping fibres in woven structures or fibres in alternate orientations. According to micrograph, much of the C_f/C was in fact pyC that probably formed due to the unidirectional channels of porosity that were aligned with the fibre direction.

However, a higher proportion of pyC did not generate a proportionally higher quantity of SiC, which could be explained since most of the pyC inside the UD architecture was confined inside the carbon fibre bundles and unable to react with the silicon. The pyC was essentially inaccessible by the silicon melt and beyond the range of diffusion for conversion reactions to occur.

Therefore, the contact surface area of the pyC could be an influential factor, instead of just the volumetric proportion. For example, flat carbonaceous regions tended to develop similarly flat SiC regions that would contour to the carbon interface, as previously shown in Fig. 49(b)-(d). However, in enclosed areas as are evident in Fig. 49(a), the relative proportion of SiC is noted to be greater. This is illustrated in the schematic in Fig. 51(a) and (b) respectively.

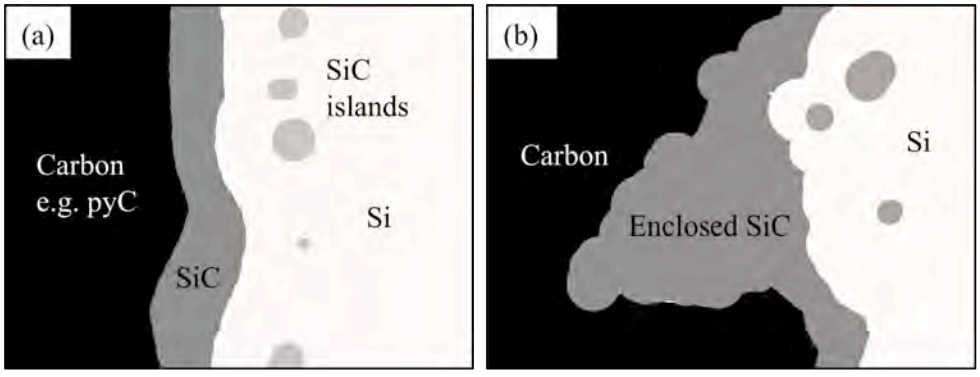

Fig. 51. Schematic of a typical microstructure, illustrating: (a) typical flat carbon microstructure and (b) enclosed carbonaceous region, which created a greater proportion of SiC.

The 2D weave architecture generated the greatest proportion of SiC, yet possessed the smallest proportion of C_f/C. This indicates a woven fibre structure, which likely possessed a comparatively high surface contact area readily granted access to the silicon melt during infiltration. In fact, when also considering the low proportion of unreacted silicon, 17%, the internal porosity could be considered the most optimal of the samples tested herein in terms of the ratio between the desired SiC and undesirable silicon. The results for the mean thickness of the carbon interface and SiC are shown in Fig. 52.

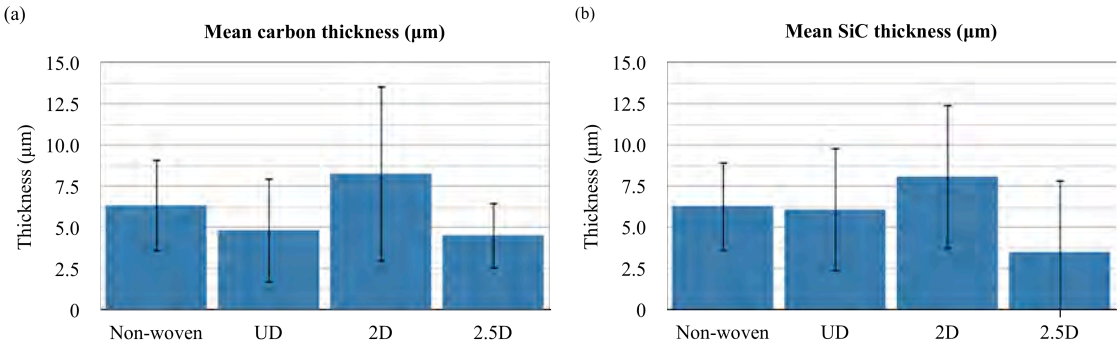

Fig. 52. Mean statistical thickness (µm) of: (a) carbon interface and (b) SiC bulk layer. The error bars represent the standard deviation.

It should, however, be acknowledged that the UD and 2D end-of-life preforms comprised a dual pyC interface, which could overestimate their thicknesses in Fig. 52. During manufacture, which is detailed in *Section 3.2*, each preform was pre-pyrolysed to convert the epoxy resin inside the pre-preg into the first inner pyC layer. Phenolic resin was then impregnated and cured under heat and pressure to complete the CFRP, which was subsequently pyrolysed to create the secondary outer pyC layer. However, according to TEM micrographs of the C_f/PyC/SiC interface in Fig. 53, the pyC derived by the epoxy was significantly thinner than compared to the PyC derived from the phenolic. This is likely due to the significantly higher proportion and higher carbon yield of the phenolic resin. Therefore, any contribution of the pyC derived from the epoxy would have been minimal.

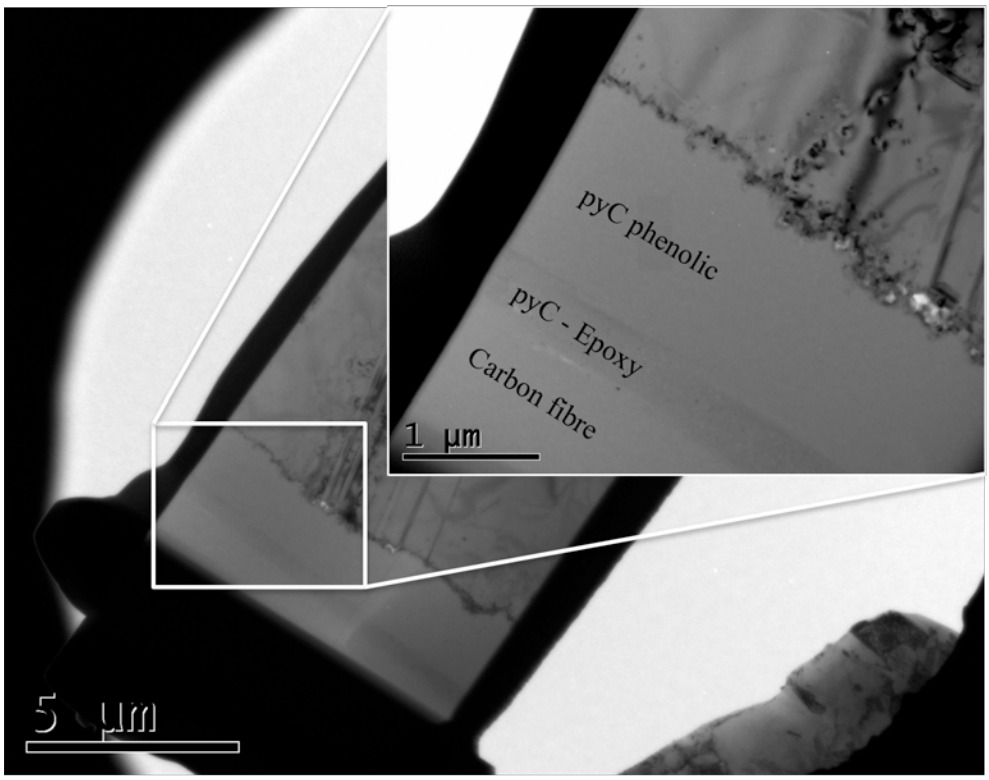

Fig. 53. TEM micrograph at 30k times magnification of the cross-section across a C_f/PyC-SiC interface. Inset is an enlarged image showing that the PyC-phenolic layer is significantly thicker than the PyC-epoxy layer.

Taking this into consideration and despite variations in the results, as indicated by the standard deviation, it is evident that the 2D architecture generated the greatest mean thickness of SiC. These results might gain support by referring back to equation (4), which was used by Kumar *et al* [162] to estimate the generated thickness of SiC on a flat surface, which is also the case in this study. However, their equation must be modified in terms of the reaction temperature (1500°C) and total reaction time period. Therefore, equation (4) alters to: $\delta = 2.004 \times 10^{-7} \sqrt{t}$, where the total reaction time, 't' is from 1414 to 1500°C at 5°C/min heating, 3 minutes dwell and 5°C/min cooling. This equates to 34.4 minutes or 2064 seconds. Therefore, using these values, the estimated SiC thickness is 9.47 µm. This is a good approximation based on the results in Fig. 52.

However, it is apparent that a thicker pyC interface generated a thicker SiC layer. This could be explained, at least in part by the increased surface contact area of the carbon matter, as previously described in Fig. 51, combined with the additional carbon and shorter distances that the carbon must diffuse through.

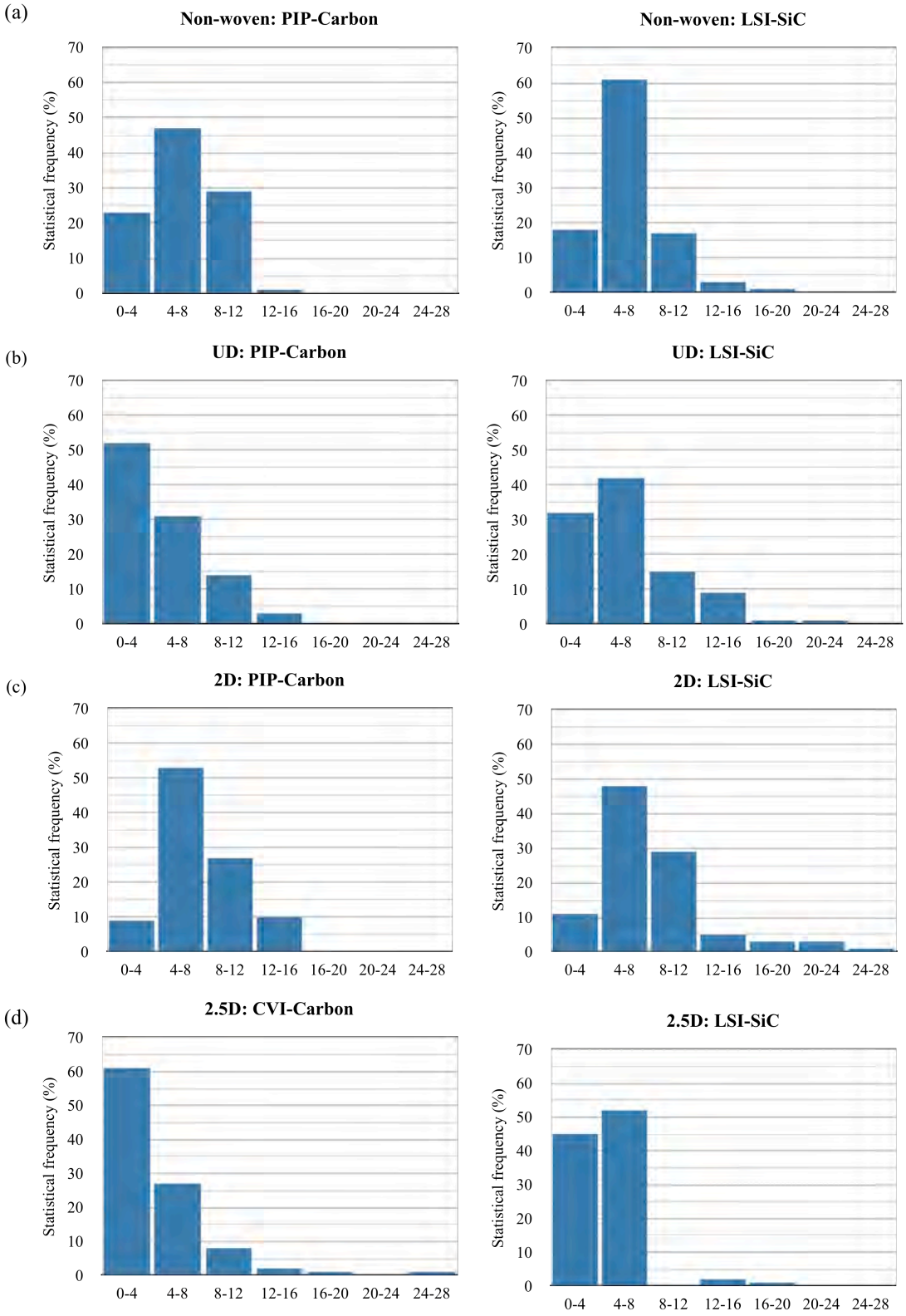

Fig. 54. Statistical frequency distribution (%) of carbon and SiC inside: (a) Recycled 'non-woven mat', (b) End-of-life UD '5164', (c). End-of-life 2D woven pre-preg '5471' and (d) Virgin 2.5D 'ST' C_f/C-SiC composites.

Therefore, quantifying the average composition of the pyC and SiC phases might provide a clearer indication of the impact of the pyC thickness in relation to the generated SiC thickness, as shown in Fig. 54.

The increasing thickness of the SiC in the non-woven, UD and 2D architectures correlated to an increasing thickness in the pyC layer. As the mean statistical frequency of the pyC increased, the proportion of SiC similarly increased, where it was noted that the 2D architecture created the fewest narrow bands of SiC and also the thickest, ranging up to 28 µm. It was evident in the UD architecture that more narrow bands of carbon existed that created fewer thicker bands of SiC.

By contrast, in the 2.5D architecture, only narrow bands of carbon were deposited by CVI that generated proportionally more SiC. This is particularly evident in the 4-8 µm range, which is shown Fig. 54(d). This could be explained by the reactivity of the carbon, but further testing would be required to qualify this theory. Nevertheless, as previously remarked, processing by CVI will generate more narrow bands of carbon throughout the architecture (Fig. 52(a)), which are more uniform in geometry and will favour the formation of narrower layers of SiC.

(ii) Silicon and void regions.

It is proposed that the molten silicon infiltrated into the architecture and reacted, where possible, with the carbonaceous matter to create SiC. Silicon that was unable to make contact with the carbon either through direct physical means or by diffusion through the evolving SiC layer re-solidified back into silicon.

According to Fig. 50, the quantity of un-reacted silicon in each microstructure was less than the SiC. This implies that few if any large open areas could have existed inside the architectures, which due to the limited surface contact area would promote the production of large proportions of free un-reacted silicon.

The highest void content was evident in the randomly orientated fibre structure of the non-woven mat composite, followed by the woven 2D and UD architectures, and finally the 2.5D architecture, but to a much lesser extent. The additional porosity inside the non-woven mat composite was likely attributed to the large gaps in between the fibres of the mat itself and also possibly between the fibres layers. Evidence of these gaps or channels can be seen in Fig. 49(a), which can also evident in Fig. 49(b)

and (c) for the 2D and UD architectures. However, in these cases, silicon has successfully infiltrated these gaps/channels and reacted with the pyC to generate the desired SiC.

By contrast, the 2.5D architecture created the fewest voids, which was attributed to a combination of two factors: 1). Z-needling through the thickness of the preform, which likely inhibited any delamination or change in the geometry as a result of the C_f/C preform or volumetric change of the SiC during LSI; 2). Higher penetration capability of the CVI-C that would have more effectively densified any narrow C_f/C regions in comparison to the resin.

4.2.2. Carbon fibre

According to the micrographs in Fig. 49 (and later in Fig. 56), the carbon fibres in all of the microstructures were similar. All of the fibres existed as either single filaments or C_f/C bundles that were encapsulated in either pyC from PIP of resin or carbon deposited from CVI. There was no indication that the virgin, recycled, end-of-life or reclaimed fibres suffered any degradation during their processing or in-house LSI manufacture. These micrographs also compare favourably to the microstructures of in Fig. 24 of the virgin C_f/C-SiC composites reported in the literature review.

4.2.3. Pyrolytic carbon

As previously highlighted, the fibres were encompassed by pyC from either PIP or carbon deposit from CVI, where PIP of a higher carbon yield resin such as phenolic should be included to ensure sufficient pyC exists for the LSI reactions. An example of this is shown inside Fig. 49(b) and (c), which illustrate that some of the fibres reacted directly with the silicon melt during LSI. Further support might be gained from the TEM micrograph in Fig. 53, which shows that the pyC derived from epoxy was very thin; about 1 μm.

In contrast, during CVI, the carbon precursor being gaseous should be more capable of penetrating the porous preform and coat the architecture with a dense and uniform band of carbon. However, neither the end-of-life PIP-PyC nor virgin CVI-

Carbon completely accessed the tightly packed carbon fibre bundles, which was evident by the void content in Fig. 49(c) and (d). This was also evident inside all of the virgin-based microstructures reported elsewhere (Fig. 24(b)), as either closed or both open and closed porosity.

According to the literature, differences in the molecular structure of the typically used materials, could lead the pyC, on heat treatment to a state varying from amorphous to highly crystalline [94, 245]. This was in agreement with Zollfrank *et al* [167] who stated the microstructure was dependent on the initial morphology of the carbon as well as the process parameters of reaction time and temperature, where short reaction times and low temperatures favour nano-sized SiC grains and extended reaction times and high temperatures favour the formation of a coarse grained SiC.

Meanwhile, Favre *et al* [163] made comparisons between glassy carbon, that was heat-treated to 2500°C, and polycrystalline graphite. The determining mechanism and microstructure after LSI were found to be similar, which leads to speculation of how different carbon morphologies or structures, including those derived from end-of-life origins could influence the development of the microstructure inside these composites.

The most common carbonaceous sources used for generating SiC inside these composites include carbon deposited by CVI and PIP of polymeric resins, while industrial grade graphite could also be considered. Therefore, four unique samples were prepared bearing each of these carbon sources, with the intention of using TEM SAD patterns to investigate and make comparisons between the morphologies of each. These included: (a) Virgin CVI-C that was deposited inside the 2.5D ‘ST’ preform; (b) Virgin industrial grade graphite, which was supplied by the consortium; (c) Virgin PyC-phenolic that was derived from phenolic resin and was impregnated inside the 2D woven ‘5471’ preform; (d) End-of-life PyC-epoxy that was inside the 2D woven ‘5471’ pre-preg. Each sample was siliconised by LSI, using a single LSI as described in *Section 3.3*.

4.2.3.1. Structure of different carbonaceous sources

The results of the TEM SAD patterns for each carbon source are shown in Fig. 55, which illustrate the differences in the carbon morphology inside each sample and

the similarities between the virgin and end-of-life resin derived pyC in Fig. 55(c) and (d) respectively.

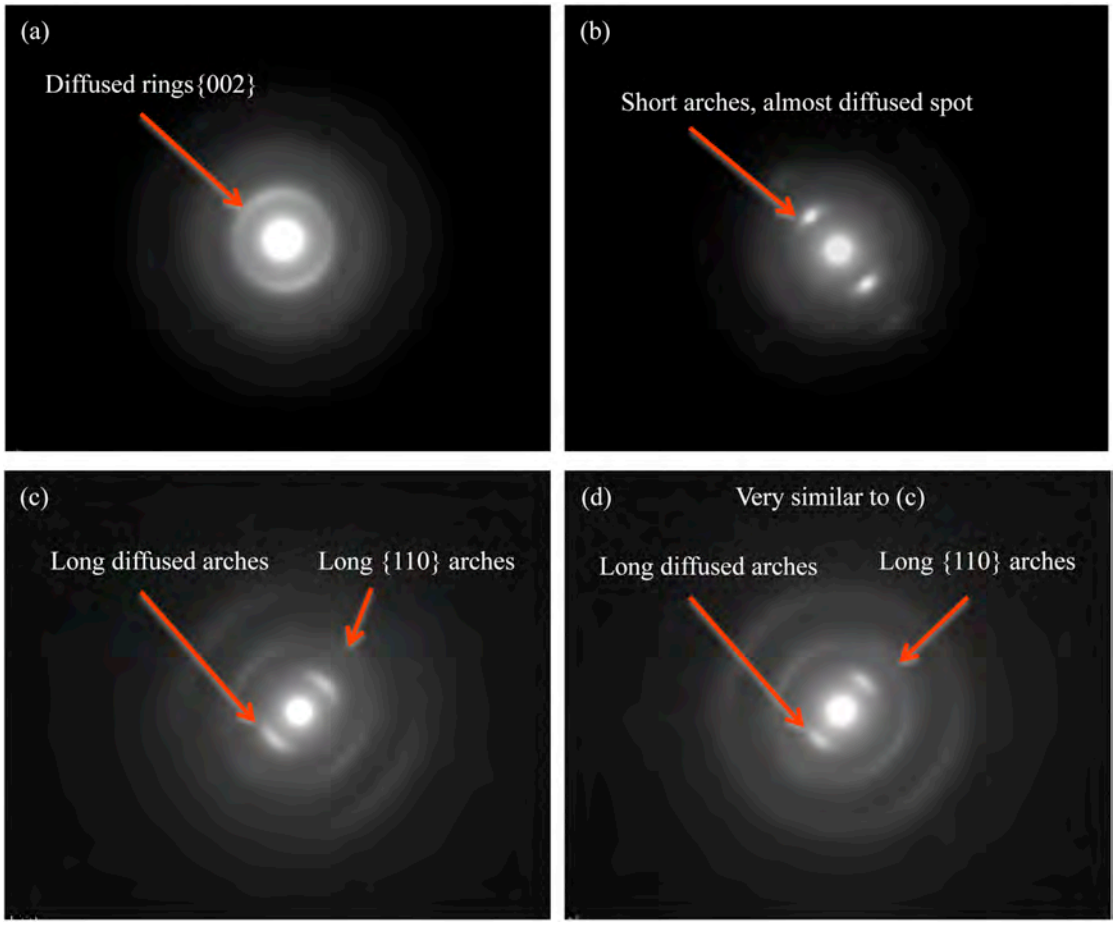

Fig. 55. SAD patterns of the different carbon phases inside (a) Virgin CVI-Carbon, (b) Virgin industrial grade graphite, (c) Virgin PyC-Phenolic and (d) End-of-life PyC-Epoxy.

From Fig. 55(a), the {002} reflections of the carbon from the CVI-carbon sample give well defined circles in the SAD pattern; those from the other three samples present a short arch, whilst the lengths of the arches in virgin PyC-phenolic and end-of-life PyC-epoxy are clearly similar and longer than those in graphite.

The length of the arch is likely to be related to the size and the orientation of the graphite units. These results show that the industrial grade graphite in Fig. 55(b) contained large graphite units, and/or smaller orientation angle among the units, in comparison to the other samples. Meanwhile, the pyC derived from the two types of

resin were very similar, irrespective of their origin and possessed large graphite units, and/or smaller orientation angles, in comparison to the CVI-carbon.

In fact, the ring in the diffraction pattern indicates that over the length scale, defined by the SAD aperture, the carbon was nearly isotropic in the CVI-carbon. The diffusion of the {002} reflections only has a marginal difference between the CVI-carbon, PyC-phenolic and PyC-epoxy, apart from graphite where the reflections are less diffused. A similar level of diffusion of the reflections provides a clear indication that the graphite units have a fairly close $d_{(002)}$-spacing distribution and/or similar thickness along the normal direction of the basal plane of the graphite units. In addition, the reduced diffusion in graphite indicates that the $d_{(002)}$–spacing is slightly more consistent and/or the thickness along the normal direction of the basal plane is larger in comparison to the other three samples.

Fig. 55 also shows that the {110} reflections have much longer arches than the {002} arches, for all of the samples. It is believed that the prismatic planes of the graphite units could be heavily distorted, whilst the graphene layers are more defined and stacked together. The SAD patterns reveal that the state of the carbon generated from the different carbonaceous sources and manufacturing process routes has introduced differences in size and orientation of the graphite unit, but not significantly, in the degree of graphitisation. This can be defined by the temperature regime used in this study; except the graphite, the other three samples were pyrolysed under 2000°C, which is a temperature regime where only a limited amount of graphitisation could be completed. This was indicated in Oberlin's study on the pyrolysis of different carbonaceous materials [245].

4.2.4. Silicon carbide

It was previously highlighted in *Section 4.2.3* that the carbon source could be responsible for altering the mechanism, which could in turn influence the proportion of SiC generated. Furthermore, the type of SiC generated could also be influenced inside these composites. Therefore, the generated thickness and polytype of SiC was investigated with respect to the different origins of carbon introduced in the previous section.

4.2.4.1. Thickness of the SiC generated by different carbon sources

The thicknesses of the SiC were similarly measured using optical micrographs and image analysis software (GIMP). Optical micrographs in Fig. 56 show that the hierarchy of the microstructure remained the same irrespective of the fibre and carbon origin, in a similar respect to varying the preform architecture (Fig. 49).

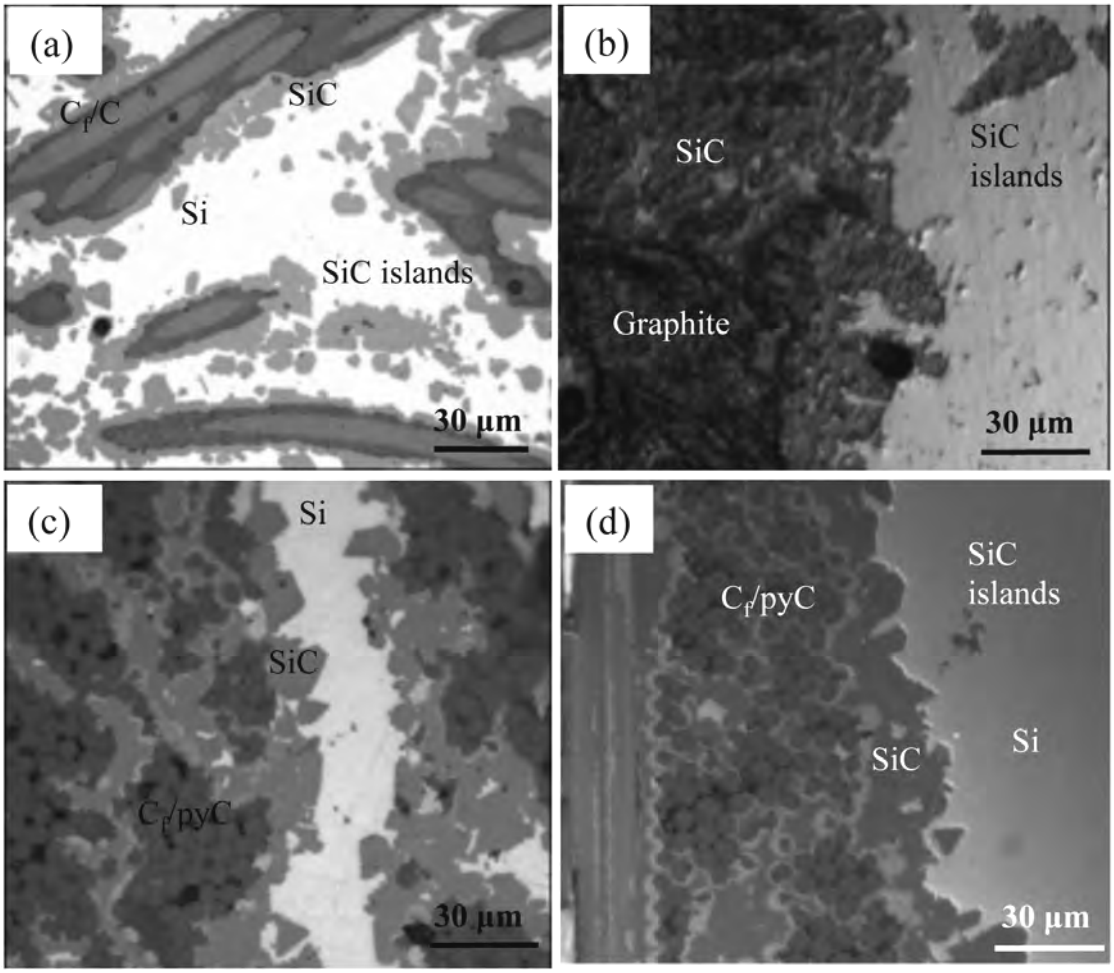

Fig. 56. Optical micrographs illustrating the microstructure generated by (a) Virgin CVI-Carbon, (b) Virgin graphite, (c) Virgin PIP-Phenolic, (d) End-of-life PIP-Epoxy, C_f/C-SiC composites.

Based on the optical micrographs, the estimated thickness of the SiC layer ranged between 1 and 30 µm. This is in agreement with reported data from the literature [144, 163, 167] and only extended further in specific regions where the carbonaceous material was enclosed as discussed, for example in Fig. 51(b). The

thinnest SiC layer was observed from the CVI-carbon that ranged between 5 and 10 μm, increasing to 10-20 μm for both PyC-derived samples and further still to 10-30 μm from the graphite.

The results of the mean SiC thickness are shown in Fig. 57, which are supported by the statistical distribution measurements in Fig. 58. The pyC from the virgin phenolic and end-of-life epoxy generated a similar thickness of SiC, which surpassed that of the graphite and CVI-carbon. In fact, the CVI-carbon generated the thinnest SiC layer, with an average thickness of around a half in comparison to graphite and about a third compared to the pyC derived from the different resins.

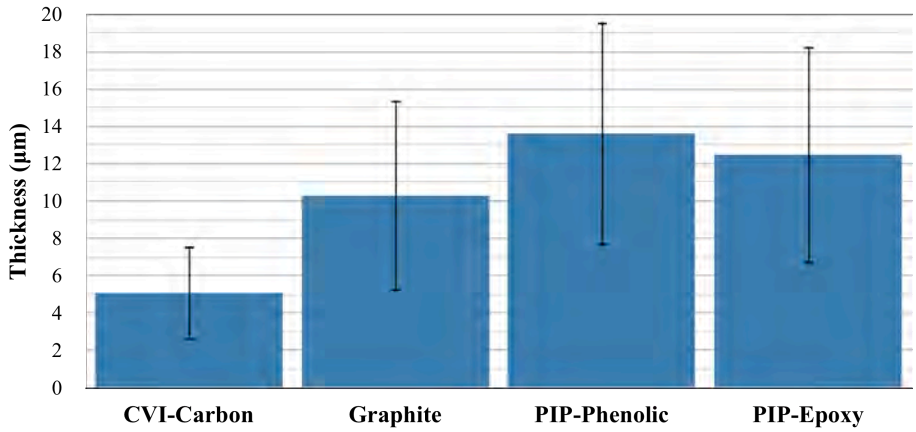

Fig. 57. Mean SiC thickness generated from the different carbon sources. Error bars represent the standard deviation.

The statistical results in Fig. 58 provide a more detailed breakdown of the SiC thicknesses, generated in each range. A Gaussian distribution is not clear, but could be easily envisaged if thousands of measurements were taken and a finer resolution chosen for the SiC thickness i.e. 0-1 μm or even less.

In the CVI-carbon sample, about 40% of the measured thicknesses were inside 4 μm, but in the other three composites, such thicknesses account for less than 5% in this range. The most likely thickness generated by the graphite was in the 4-8 μm range, which extended up to 8-12 and 12-16 μm for the end-of-life epoxy and virgin samples respectively. It is believed that SiC was initially generated by silicon vapour that created a nano-sized layer and then by the silicon melt during impregnation, creating a much thicker SiC layer.

Differences in the thicknesses could be explained, at least in part, by the diffusion mechanism governing the formation of the SiC. For sustained reactions and growth of the SiC, the carbon must either diffuse to the silicon region or vice versa. However, considering the work by Hon *et al* [177, 178] who found that the lattice self-diffusion coefficient rate of carbon was up to 100 times higher than silicon, it is more likely that the carbon diffuses outwards through the evolving SiC layer.

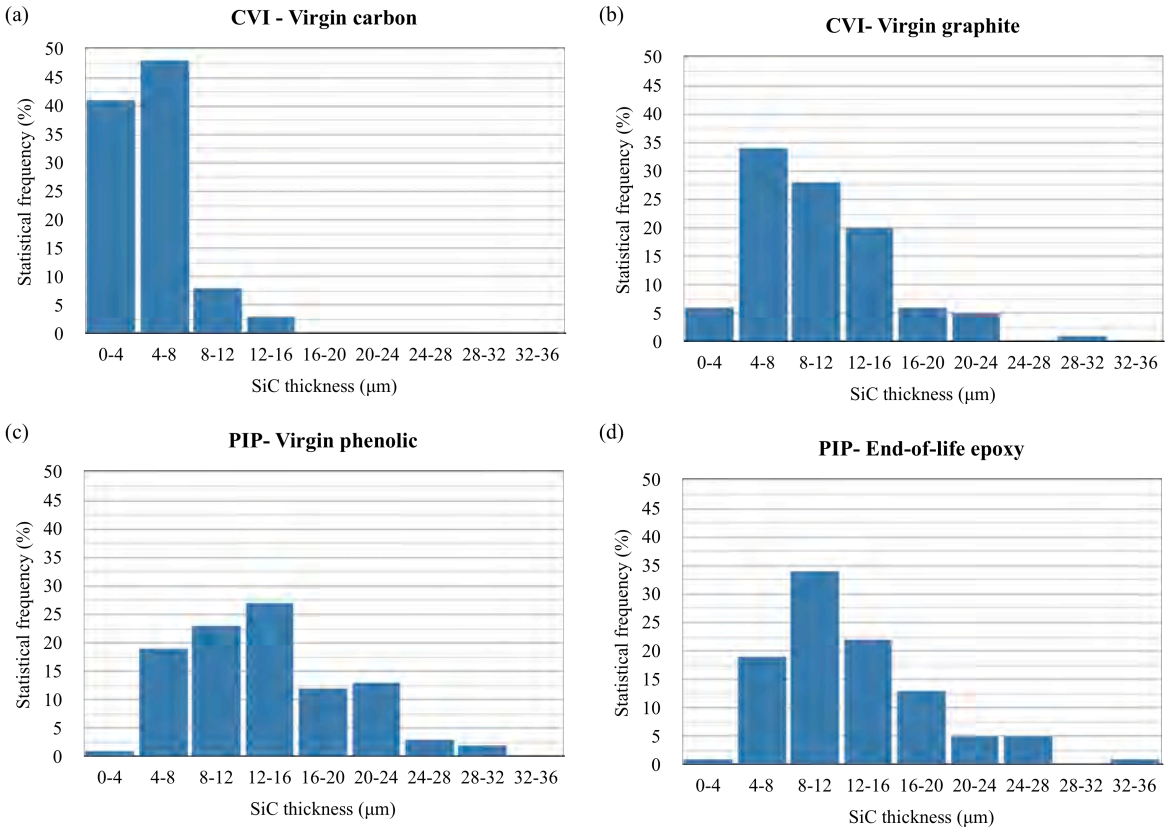

Fig. 58. Statistical frequency (%) distribution of the SiC thickness generated from (a) CVI of virgin carbon, (b) CVI of virgin graphite, (c) PIP of virgin phenolic resin and (d) PIP of end-of-life epoxy resin.

Support could be gained by examining the cross-section of each microstructure using the TEM, which are illustrated in Fig. 59. It is evident that all of the microstructures followed the same hierarchy format observed in the optical micrographs, irrespective of their origin: carbon, existing as either virgin CVI-C, virgin industrial grade graphite, pyC derived from end-of-life epoxy and phenolic resin or pyC derived solely from end-of-life epoxy resin; fine particles, thought to be SiC; coarse SiC; silicon.

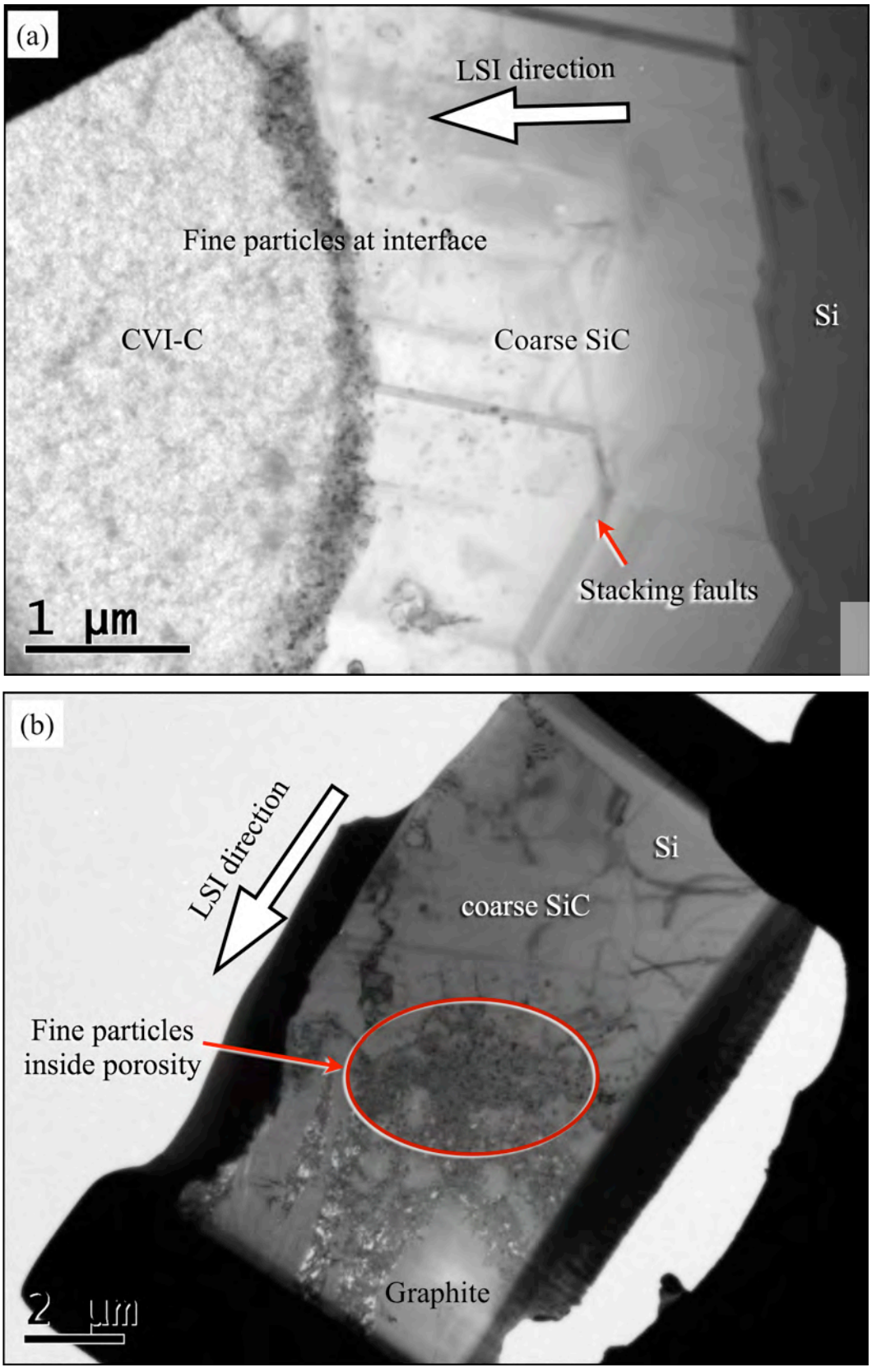
(a)
LSI direction
Fine particles at interface
CVI-C
Coarse SiC
Si
Stacking faults
1 µm
(b)
LSI direction
Si
coarse SiC
Fine particles
inside porosity
Graphite
2 µm

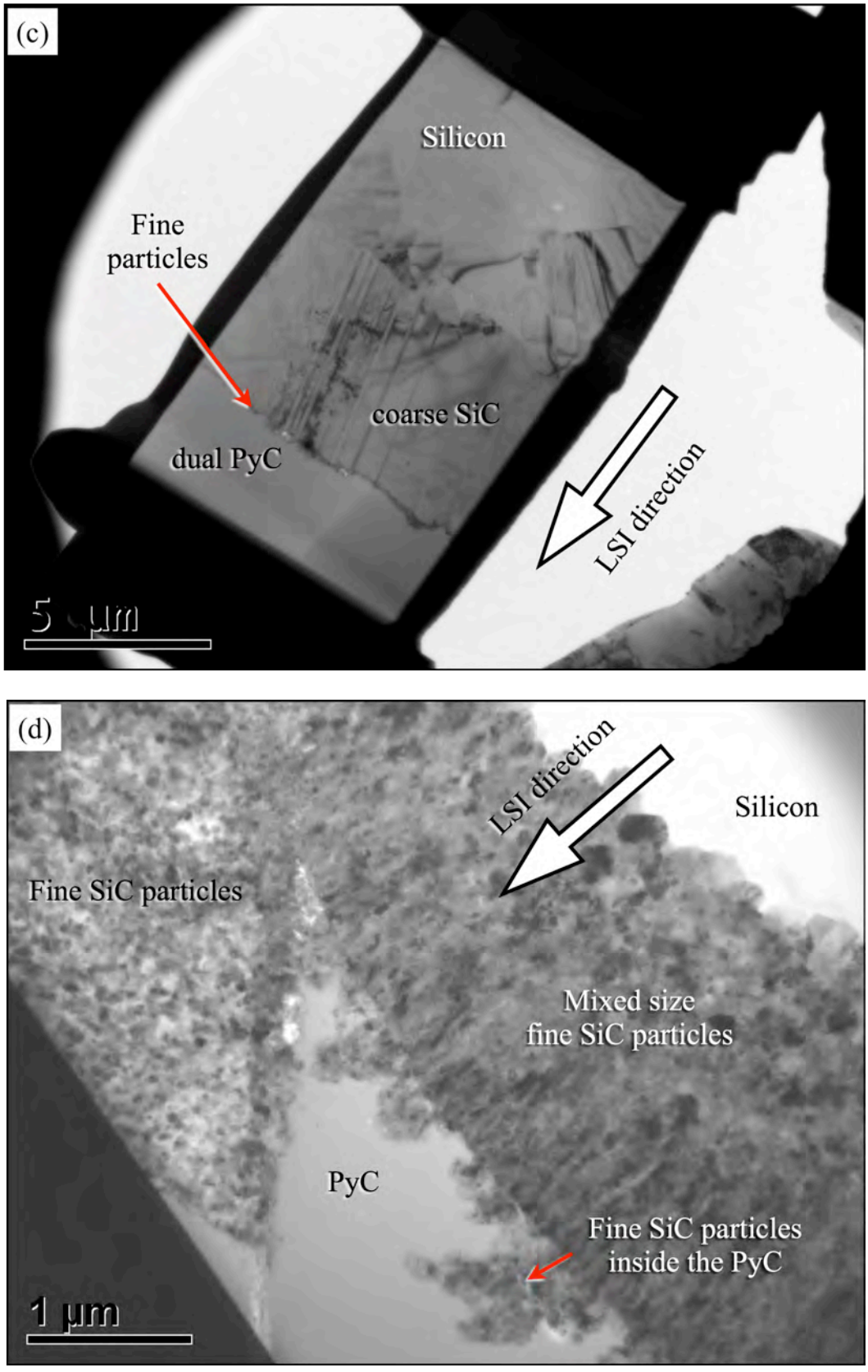

Fig. 59. Cross-section TEM micrographs of each composite: (a) CVI-carbon, (b) Industrial grade graphite, (c) PIP-Phenolic and (d) PIP-Epoxy.

It was highlighted in the literature review by Schulte-Fischdick *et al* [144] that fine particles existed at the interface. Details of these particles and the coarse SiC were investigated by TEM SAD patterns in *Section 4.2.4.2*. However, if this diffusion mechanism does exist, it would assume that the SiC was of the same type, which is currently unknown for these materials and was therefore investigated using the TEM and XRD.

The d-spacing's for each sample were calculated using the TEM SAD patterns and then correlated to the corresponding peaks from the XRD spectrum. The XRD spectrum for each sample is shown Appendix A – Fig. 30, where the correlating peaks have been highlighted. Any correlating results are detailed further in Appendix B – Table 17.

According to the results, the coarse and fine (nano-sized) SiC belonged to the same polytype in all of the four samples. The coarse SiC was highly crystalline; the calculated d-spacing from the diffraction pattern in Fig. 60(a) were 2.54 Å for $(\bar{1}\,\bar{1}\,1)$ crystal place, 2.19 Å for (200) and 1.56 Å for $(\bar{2}\,2\,0)$, and in Fig. 60(b) are 2.52, 1.54, 1.31 for (111), (220) and (113), respectively.

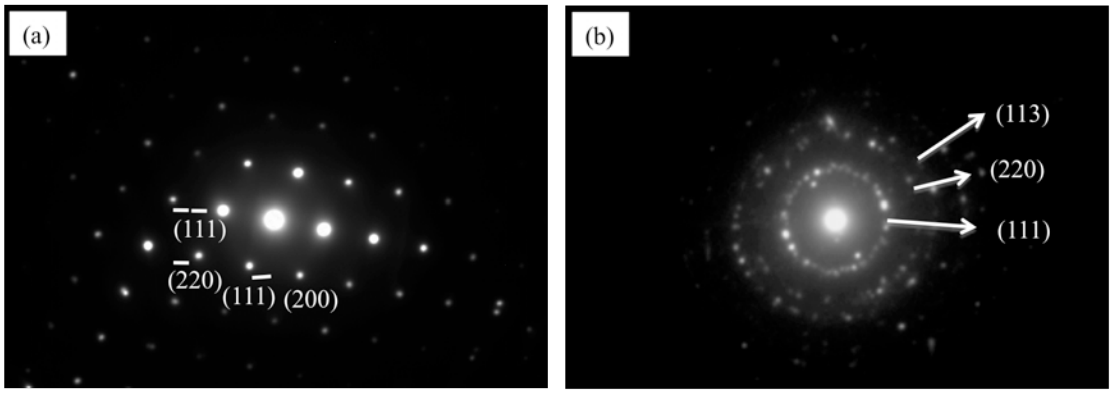

Fig. 60. TEM SAD pattern from PyC-Phenolic of (a) the coarse SiC region with a [110] zone axis and (b) nano-crystalline SiC.

These measurements closely match the international powder diffraction data sheet (00-029-1129) [246], which indicates the polytype should be face-centred cubic (FCC) β 3C-SiC, which is in accordance with other investigations [144, 167, 168, 247].

It was previously highlighted in the literature review that α-SiC is promoted when the local temperature exceeds 2000°C, which was unlikely in this study considering the LSI temperature was only 1500°C. Although, it was hypothesised by

Favre *et al* [163] that local temperatures could increase due to the exothermic reactions during LSI, where Pampuch *et al* [165, 166] estimated increases by as much as 500°C. Therefore, only in the most extreme case could the maximum temperature reach 2000°C, which is in agreement with Schulte-Fischdick *et al* [144] and seems unlikely herein considering the TEM SAD and XRD results.

Therefore, if the crystal structures of the SiC products were the same, the carbon diffusivity through SiC regions must also have been similar. In this case, the average SiC layer thickness developed during LSI should also have been very similar among these four preforms, which was clearly not the case in previous optical and TEM micrographs, which therefore required further investigation.

One proposed explanation for the observed differences in the thickness could be matter transportation through diffusion, which could boost the development speed of the SiC. For instance, connected micro-channels or pores in the pyC or graphite could lead to a quick 'sucking-in' capillary effect of the silicon vapour and melt into the carbon matrix and then a reaction between carbon and silicon would convert the region into SiC completely.

This therefore implies that the structure of the carbon could play an essential role in determining the production rate of the SiC layer under the current regime. As previously remarked, it would not be an unreasonable assumption that the carbon region of the graphite sample would be left with greater porosity inside the general microstructure after being treated at much higher temperature than the other samples. This is evident in Fig. 59(b) and could be due to the loss of more volatile species and any further shrinkage as a consequence of high degree of graphitization (see the SAD pattern in Fig. 55) as well as cracks due to contractions during the pyrolysing process.

By comparison, the PIP-derived pyC should also contain noticeable porosity, which could have also been created from the evolution of the pyrolysis gases and the shrinkage. This is supported by conclusions made by Choe *et al* [248], who reported that the structure of pyC was very porous. The degree and distribution of porosity was attributed to the heat rate and sample dimensions, which determined the rate of gaseous evolution and escape. High heat rates, such as the 5°C/min used in this study would therefore have promoted the formation of uneven porosity. However, the carbon structures herein were comparatively large, which would have reduced the susceptibility of the carbon to such uneven porosity.

Nevertheless, no support for this could be gained from the TEM micrographs in Fig. 59(c) and (d), unlike the CVI-carbon sample in Fig. 59(a). Based on the kinetics of the gaseous deposition, this sample should be very dense and contain very little if any porosity, which is clearly supported in the TEM micrograph. In order to gain further support for these assumptions, the TEM micrographs were examined in further detail, beginning at the carbon/SiC interface.

4.2.4.2. At the carbon/SiC interface

Comparing the virgin PyC-Phenolic, end-of-life pyC-Epoxy and virgin CVI-C samples in Fig. 61, the structure of the fine SiC between the coarse SiC and pyC was fairly similar. The scale ranged from tens to hundreds of nanometers across the dispersoid band. However, in the graphite sample, this scale was extended up to several microns, as shown in Fig. 61(b).

This observation seems to support the previously proposed mechanism that silicon vapour infiltrated the porous carbon and then developed these fine SiC grains prior to reaching the melting point of the silicon, because as previously highlighted, the industrial grade graphite should be the most porous of all of the samples studied. Greater porosity could facilitate access of the vapour and melt into and throughout the architecture that could account for the increased visibility of the fine SiC particles, as well support the proposed “suck-in” capillary effect. Some support for this theory could be gained measuring the density of the graphite sample using Archimedes method, which revealed a comparatively low density of 1.81 g/cm^3, with an estimated open interconnecting porosity and topographical void content of 9% and 5.17% (±1.5), respectively. Appendix A – Fig. 31 illustrates typical regions of porosity inside the architecture prior to LSI.

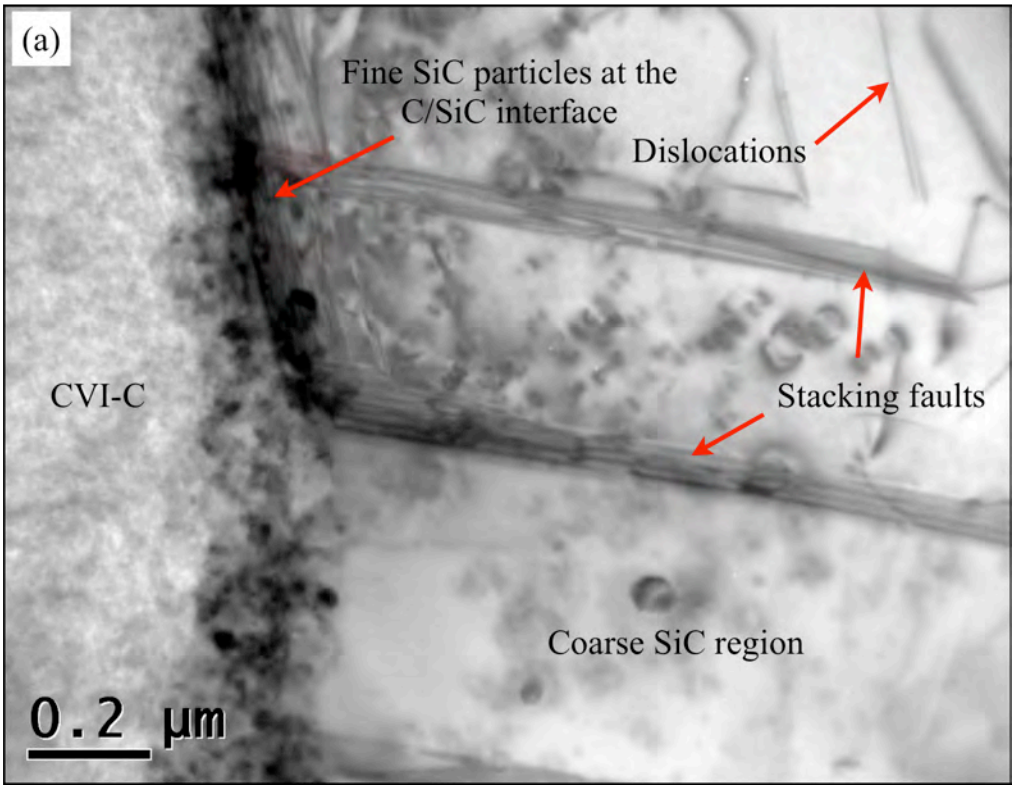
(a)
Fine SiC particles at the
C/SiC interface
Dislocations
CVI-C
Stacking faults
Coarse SiC region
0.2 µm

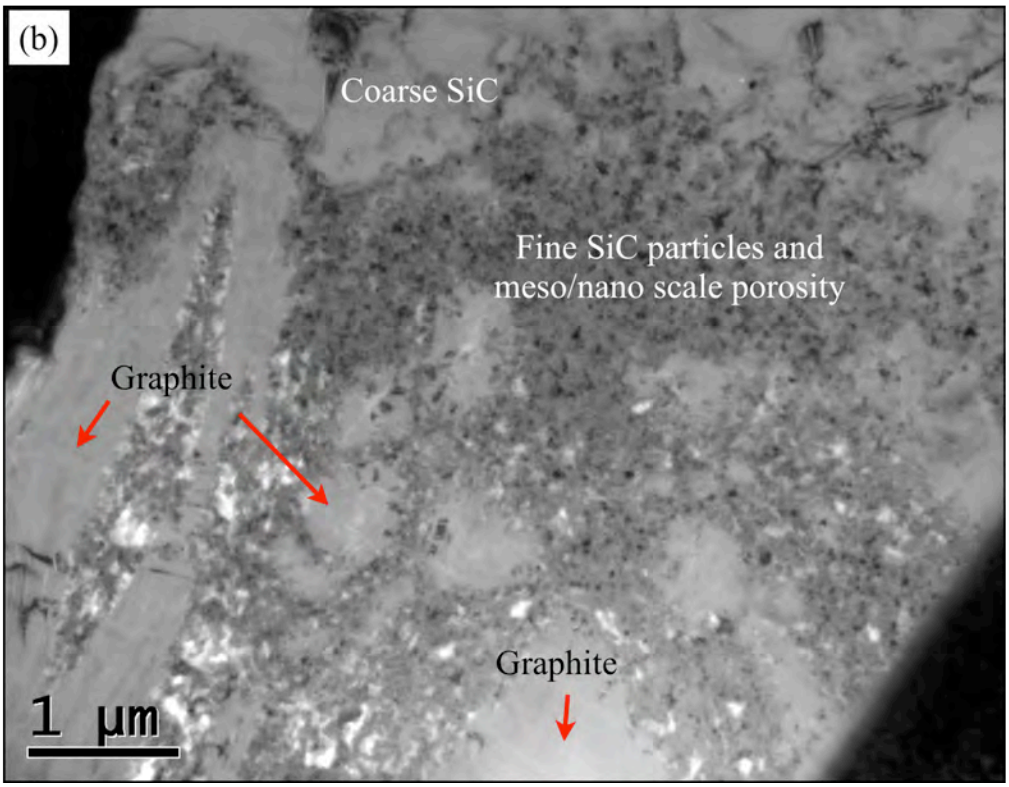
(b)
Coarse SiC
Fine SiC particles and
meso/nano scale porosity
Graphite
Graphite
1 µm

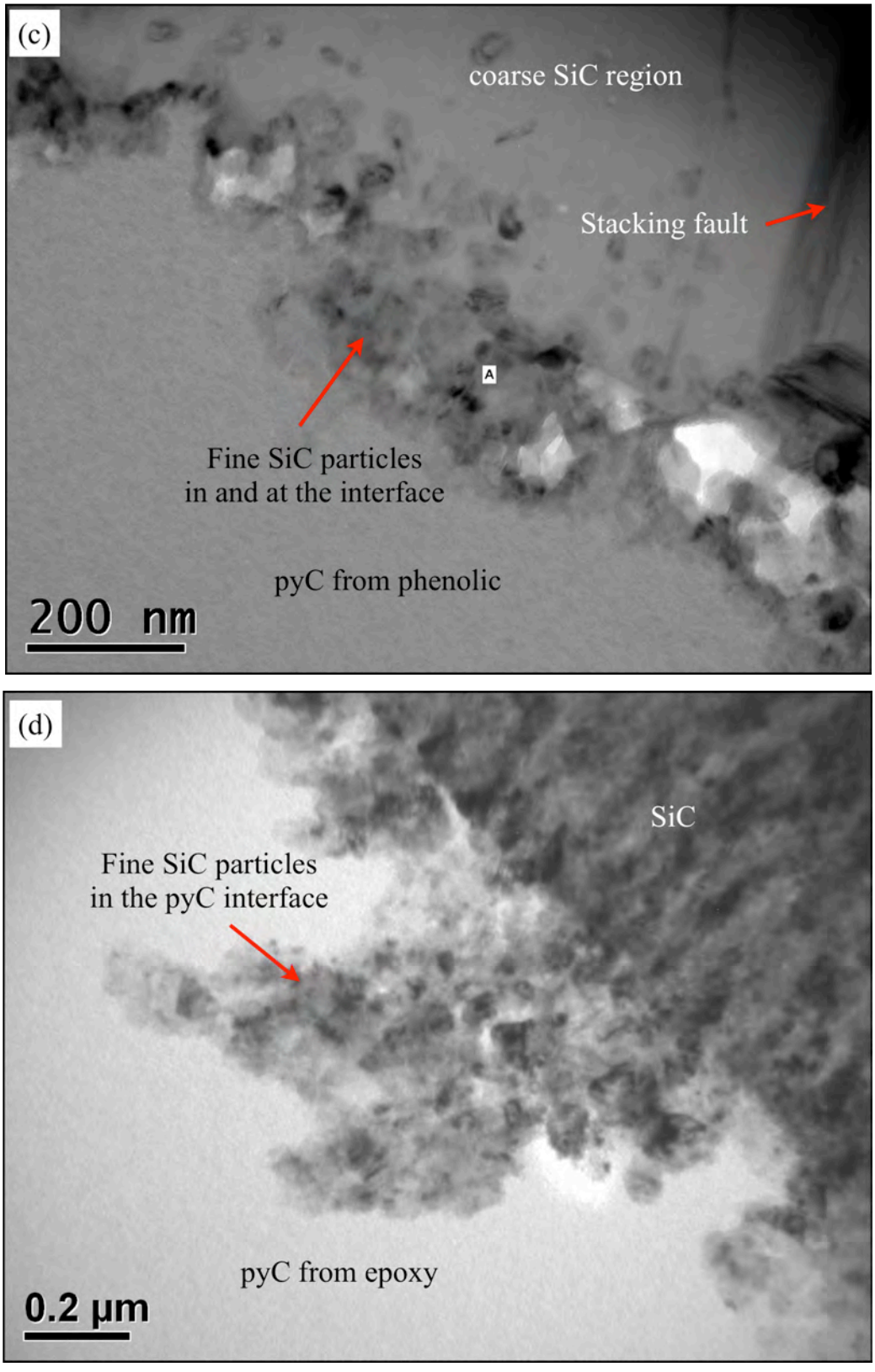

Fig. 61. Cross-section TEM micrographs at the C/SiC interface of: (a) virgin CVI-Carbon, (b) Virgin graphite, (c) Virgin PIP-Phenolic and (d) end-of-life PIP-epoxy.

The fine particles around each interface were originally assumed to have originated from a layer of fine particles between the pyC region and large sized SiC region, as reported by other researchers [144]. However, by carefully examining both bright and dark field images of the PIP-phenolic sample in Fig. 62, it was apparent that, apart from a possible layer composed of the fine SiC particles alone, there might exist two dispersoid regions on either side of the interface layer.

These dispersants are all considered to be SiC and are within the same size range as the interface layer. From Fig. 62(a), near the carbon region, the continuous phase for the dispersoid should be pyC; and near the SiC region, the continuous SiC phase. This fine SiC layer has been noticed in previous investigations [144, 167, 249], but the presence inside the SiC region has not been previously documented. The dispersoids within the pyC are speculated to have developed from the silicon vapour that infiltrated prior to reaching the melting point. Alternatively, they could be an artificial effect due to the large inclination of the interface layer in this observation. However, Wang *et al* [151] showed that the penetration depth of silicon vapour was greater than that of the silicon melt, which seems to support the results herein and is in accordance with the previously highlighted investigations.

Also identified in this region were SiC particles, with a similar morphology to those previously identified in the pyC interface. The presence of the particles was confirmed using a TEM dark field image that was tilted and is shown in Fig. 62(b). It was suspected that they formed from either: migrating carbon matter from the pyC toward the silicon, which converted into SiC, or alternatively; dislodged nano-sized SiC crystals that formed from the silicon vapour on the pyC frontier. Both hypotheses support the previously assumed theory of evolution: dissolution and precipitation.

Meanwhile, further microstructure analysis of the PIP-epoxy seems to provide more evidence to support this proposed “suck-in” process of the silicon vapour/melt prior to a full development of SiC layer. By tuning the polarizing condition of the illumination light, it was noticed that the SiC layer on the polished surface of PyC-Epoxy sample exhibited two distinct contrasts: one in grey near the silicon region, one in a lighter shade of grey near the pyC, as shown in Fig. 59(a). It seems that the thickness ratio is variable between the layer in grey contrast and the one in white grey. A cross-section TEM sample was lifted across the interface of SiC and pyC using the FIB. The TEM image of this region is shown in Fig. 63(b).

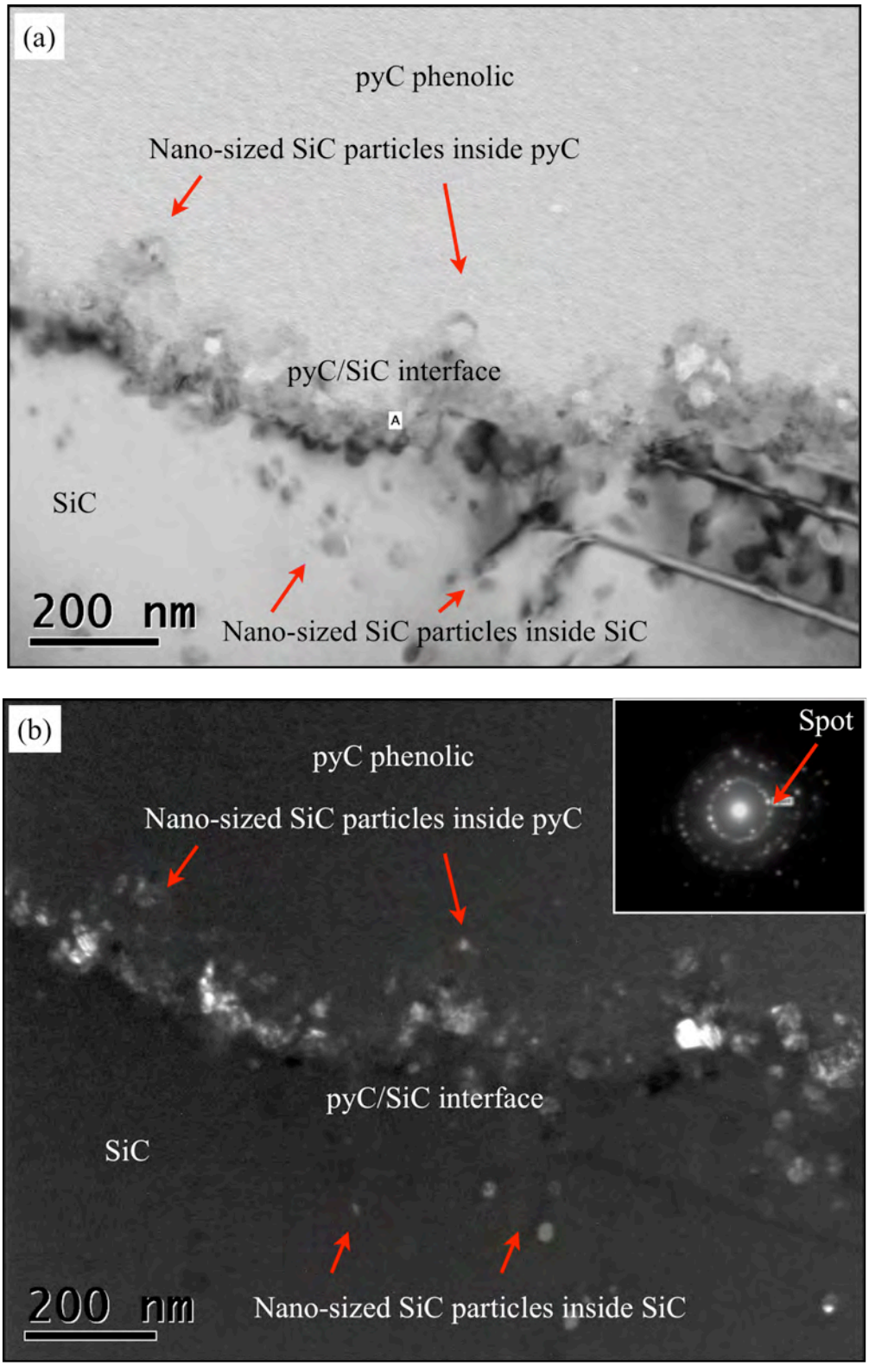

Fig. 62. Cross-section TEM micrographs (a) bright field and (b) supporting dark field micrograph, showing the nano-crystalline SiC layer with evidence of dispersed nano-sized SiC inside the PIP-Phenolic derived PyC and coarse SiC.

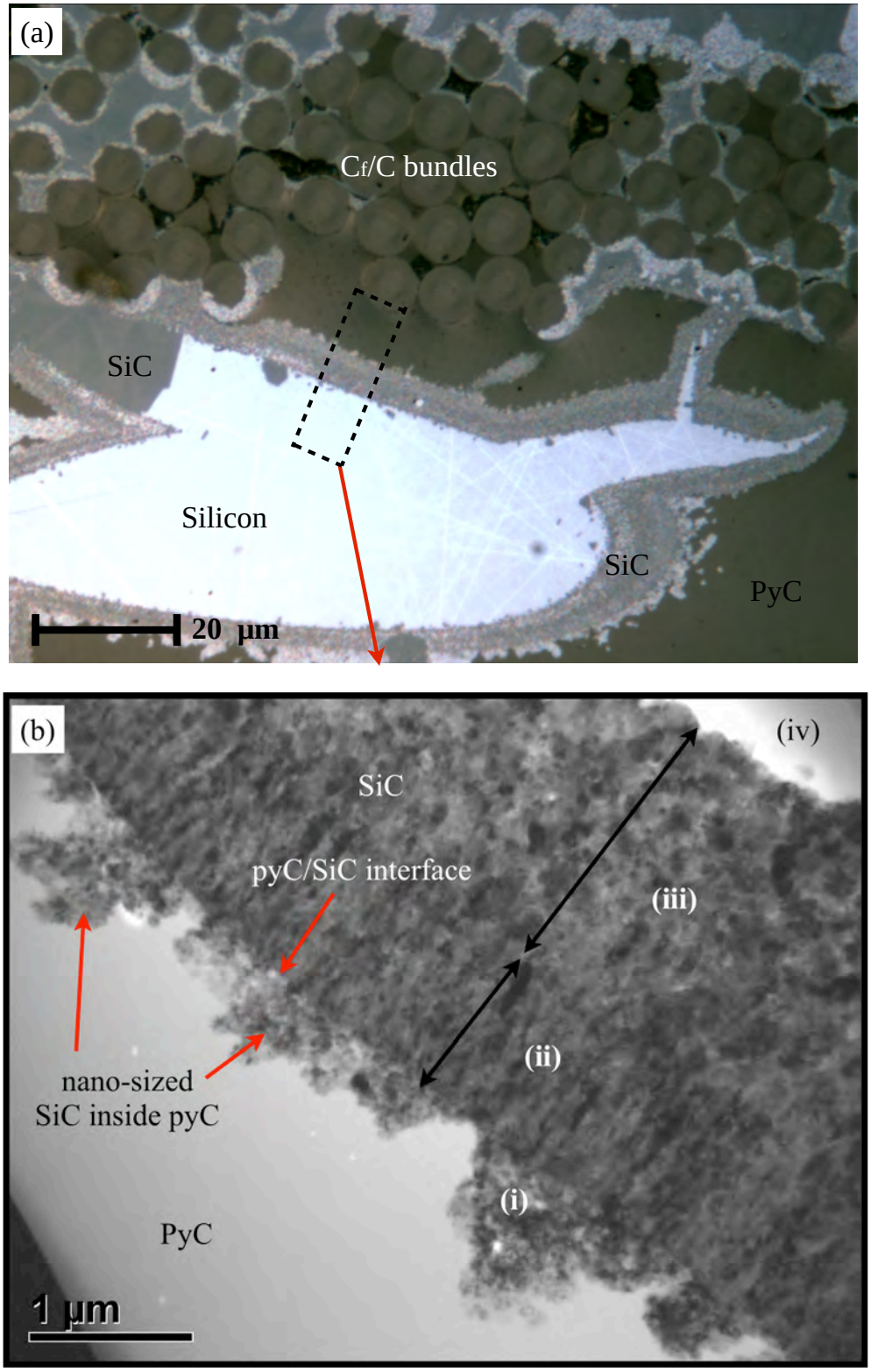

Fig. 63. OM and TEM micrographs illustrating the SiC phase impinging upon the end-of-life PyC inside the PIP-epoxy composite (a) OM as-polished surface under polarised and DIC light conditions; (b) Bright field TEM micrograph, which is highlighted in (a) illustrating 4 different SiC regions.

The formation of this unusual SiC structure could be attributed to a highly porous short-range pyC structure, as opposed to the long range graphite structure, which could have been created by two factors: the low carbon yielding epoxy resin, which could be as low as 5% [221] and/or the evolution of a significant quantity of gaseous emissions during pyrolysis. The subsequent pyC structure would be weak and highly porous, which could easily collapse and be consumed by the silicon melt during LSI. Therefore, according to the evidence inside the TEM micrographs of the CVI-C, graphite and pyC so far, the following schematics in Fig. 64 have been proposed.

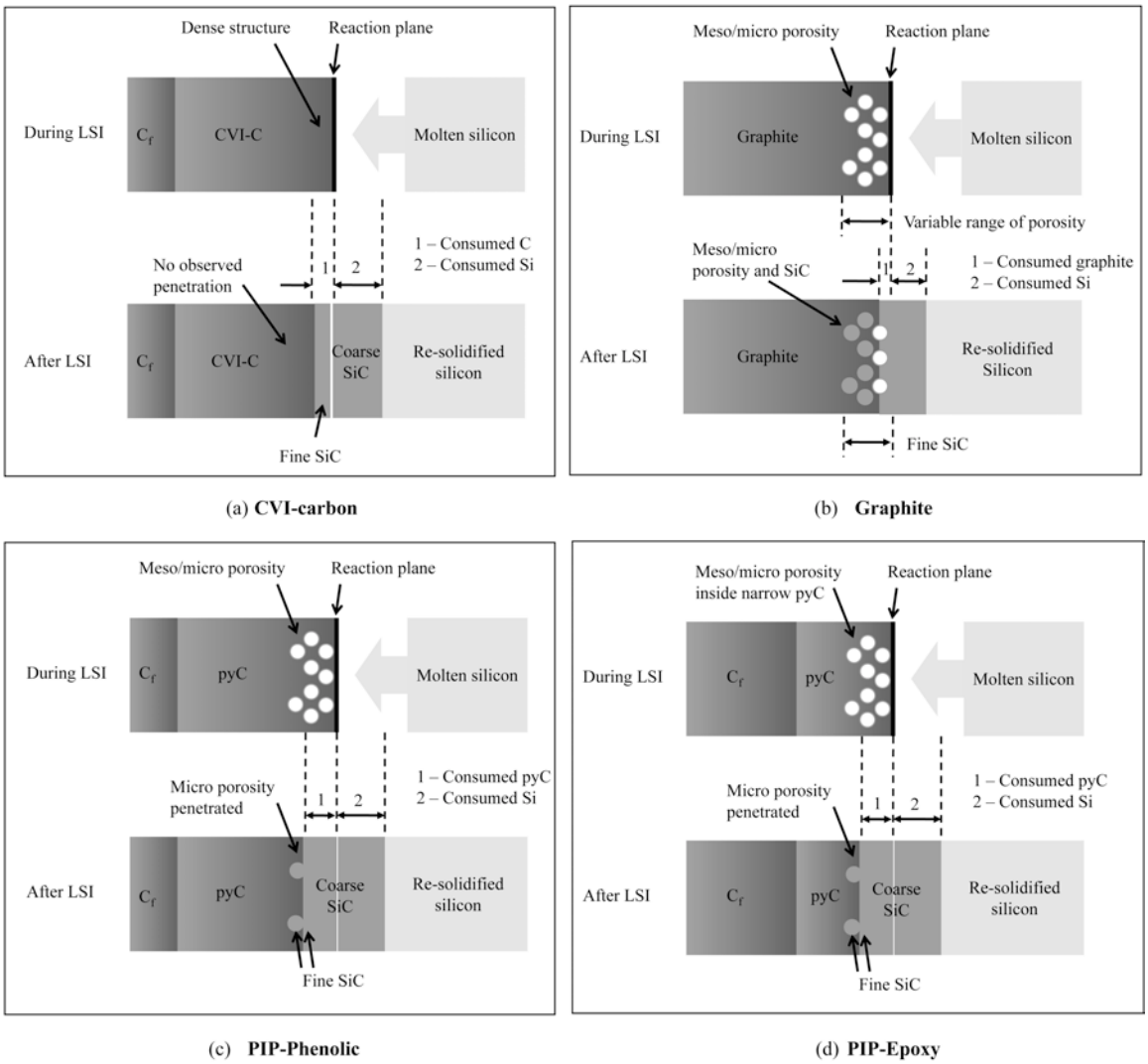

Fig. 64. Schematic describing the proposed LSI mechanism inside: (a) virgin CVI-carbon, (b) virgin graphite, (c) virgin PIP-phenolic and (d) end-of-life PIP-epoxy composites. The schematics are not to scale.

The schematics illustrate each microstructure during and after LSI, and describe: the potential impact of the different carbon architecture inside the different composites; potential mechanisms that could contribute to the observed differences in the SiC thickness; differences and similarities between the virgin and end-of-life composites.

The virgin derived CVI-carbon composite is illustrated in Fig. 64(a), which shows the dense carbon structure that was not accessed by the proposed silicon vapour. Instead the vapour was deposited at the C/SiC interface and reacted to form the fine SiC, which was recognised in all of the microstructures. During LSI, some proportion of the carbon and silicon was undoubtedly consumed during LSI, which is represented by '1' and '2' respectively. More details of the SiC formation are described in the proceeding *Section 4.2.4.3*.

By comparison, the virgin graphite structure was observed to comprise high proportions of meso and nano-scale porosity. This is illustrated in Fig. 64(b) and could be attributed to the manufacture process. Details of the manufacturing route were confidential, however, some evidence might be extrapolated by re-examining the TEM SAD pattern in Fig. 55(b). The structure of the graphite was essentially amorphous and lacking in any defined crystal structure. This is indicative of the 'carbonisation' process, which typically operates at temperatures between 1000 and 1200ºC and not 'graphitilisation' (≥2500ºC) that creates more crystalline graphite. During carbonisation, thermal decomposition i.e. pyrolysis converts the binder into the elementary carbon and volatile components; these volatile species could account for the porosity. In addition, since the volume of the binder is higher than the volume of the carbon formed, there is also an accompanied formation of pores/porosity; the proportion of which is determined by the binder quantity.

It is proposed that prior to and during LSI, the silicon vapour accessed the porosity and converted into a SiC. However, due to the long range of the porosity that extended up to several microns, the vapour was unable to fully densify the porosity prior to reaching 1414°C when the melt entered.

Meanwhile, due to the larger size and higher viscosity of the melt in comparison to vapour from CVI, it was unable to penetrate any of the meso scale porosity, which could account for some of the remaining porosity in the

microstructure after LSI. Instead, as the melt reacted with the outer fringes of the graphite, the melt consumed the graphite generating the observed coarse SiC region.

Both of the PIP-derived pyC architectures were derived from resin under the same manufacturing regime and therefore should have generated a similar and porous structure. Therefore, differences inside the TEM micrographs of the PIP-epoxy could simply be artifacts or anomalies due to the dual interface, which was highlighted in Fig. 63. According to the optical micrographs of the general microstructure (Fig. 56), the hierarchy of the microstructure was the same for both PIP-samples, as well of the CVI-carbon and graphite. However, the PIP-epoxy structure was thinner, which was attributed to the lower carbon yield. Therefore, the key difference between the PIP-phenolic and PIP-epoxy should be the thickness of the pyC, which is illustrated in Fig. 64(c) and (d).

According to the TEM micrographs, the vapour and also possibly the melt penetrated both pyC structures. However, the main difference between the graphite and pyC seems to be that the porosity in the graphite might have been greater and also was not consumed as readily as the pyC. This could explain why there was no porosity evident in the TEM micrographs in both of the pyC composites and account for the increased SiC thickness observed by optical microscopy.

Meanwhile, the schematic in Fig. 65 illustrates the potential impact of the ‘suck-in’ capillary inside the porous graphite and pyC structures. The blue and red arrows represent the potential high and low silicon vapour and melt flow respectively. The narrow tortuous channels generate additional capillary forces, which encourage a greater proportion of the silicon vapour or melt. Furthermore, the impact of the capillary effect could also increase as the SiC builds up in and around the narrow channels in addition to the Venturi effect of adjoining perpendicular channels (Fig. 31).

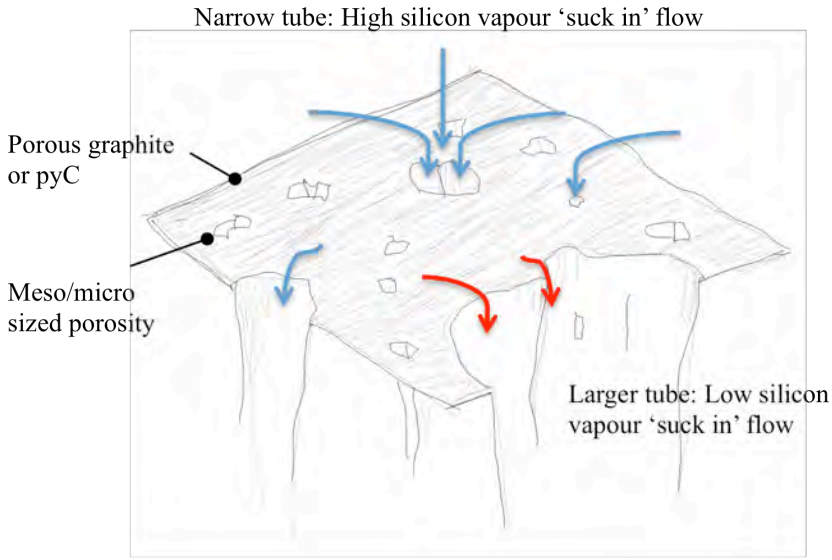

Fig. 65. Schematic illustrating the potential impact of the 'suck-in' capillary effect.

4.2.4.3. In the SiC region

Apart from the PIP-epoxy sample, the SiC in the remaining composites were very similar. All of the SiC crystals contained strain contours and significant stacking faults, which can be seen in Fig. 66(a)-(c). The appearance of stacking faults implies that the SiC region was under strain after the LSI processing, which may have originated from: a). Thermal residual stresses that developed during the cooling down period from the processing temperatures, due to the differences in the thermal expansion coefficients of SiC, silicon and carbon; and/or b). Resistance to the growth of SiC crystallites during the LSI process, due to the space competition of reactants and products. These phenomena have been noticed elsewhere in reaction bonded SiC ceramics [250, 251].

According to the TEM micrographs, even though the SiC polytypes were identified as the same, some of the SiC crystals had more defects in comparison to the others, such as stacking faults. It could therefore be speculated that any non-lattice diffusion process might have been inhibited by such defects, which might have contributed to the observed difference in the thickness of the reaction product.

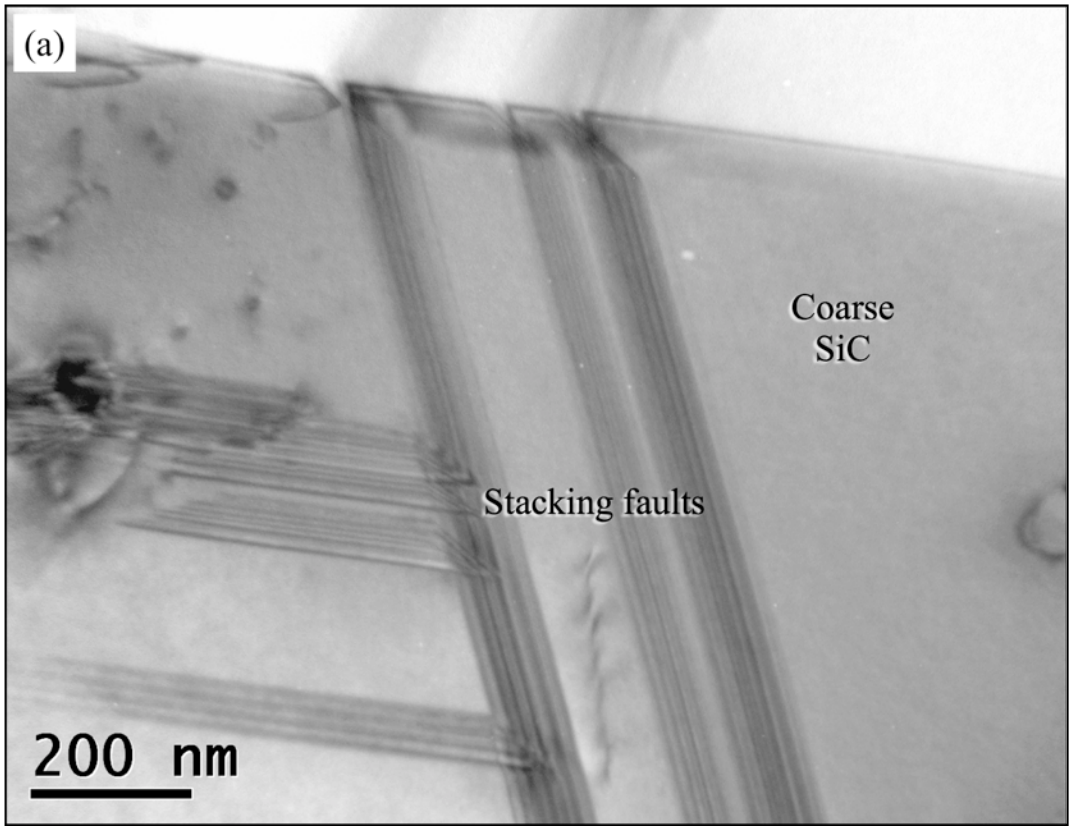
(a)
Coarse
SiC
Stacking faults
200 nm

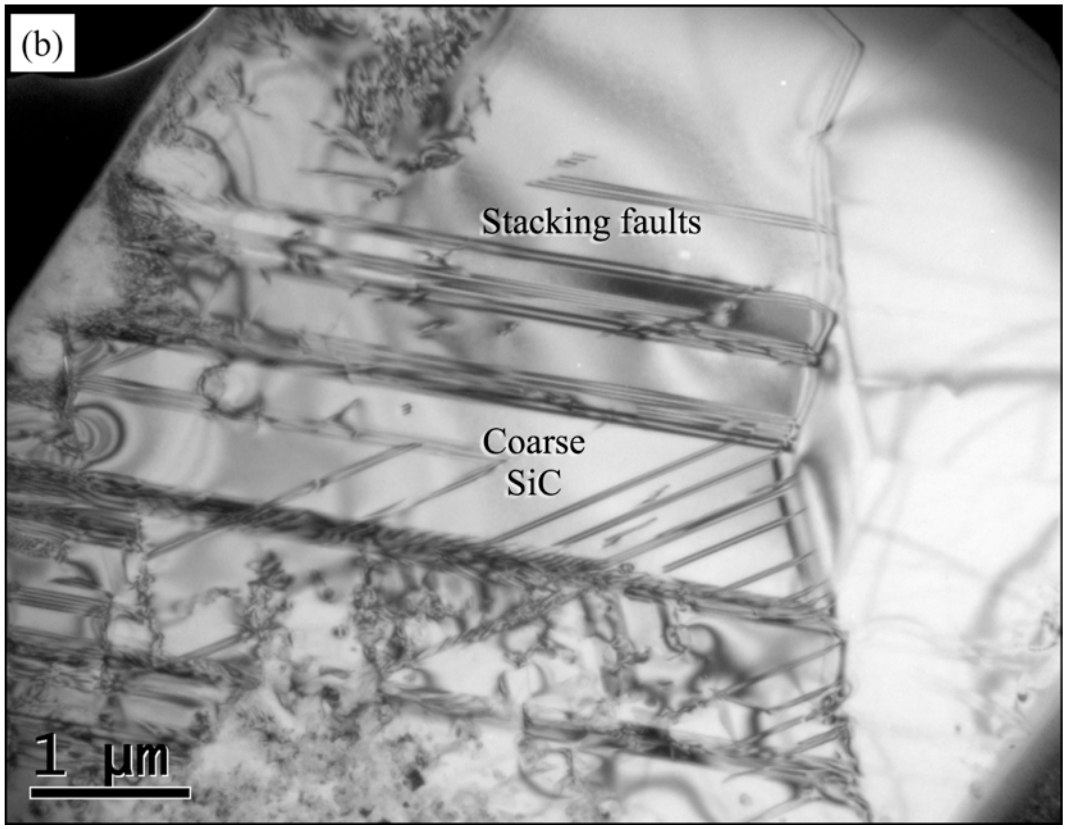
(b)
Stacking faults
Coarse
SiC
1 µm

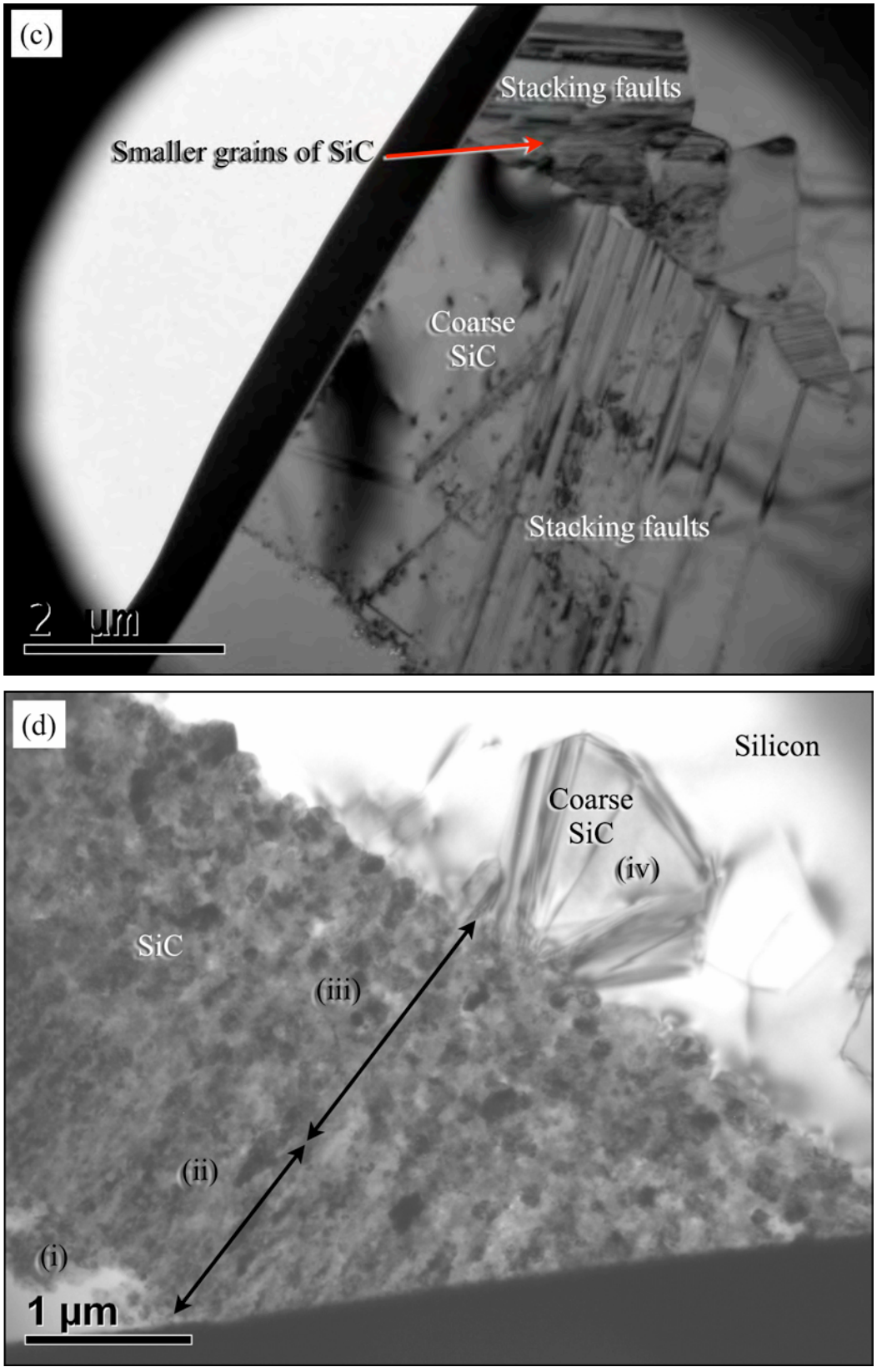

Fig. 66. Cross-section TEM bright field micrographs in the SiC of: (a) Virgin CVI-Carbon, (b) Virgin graphite, (c) PIP-Phenolic and (d) PIP-Epoxy

This is apart from other factors that could influence the growth of the SiC layer, such as topographic effect and the supply of carbon and silicon. The former could be mitigated by continually polishing the same region and observing under microscopy e.g. optical whether the SiC was isolated or part of the general microstructure; the latter could be treated as similar as among all of these samples since almost all of the SiC layers were sandwiched between the residual carbon and silicon regions.

Meanwhile, the particles in the PIP-epoxy sample (Fig. 66(d)) were confirmed as SiC with the support of SAD patterns. The following microstructure was identified: Zone I - nano-sized SiC dispersed inside the pyC with a thickness of up to 1 μm; zone II – densely packed SiC polycrystalline with very fine grain size (about <100 nm) and a thickness of about 1 μm; zone III – another densely packed SiC polycrystalline with grain size inside a few hundred nanometres and a thick of about 2 μm. Development of this microstructure was attributed to the weak porous pyC structure as previously discussed and highlighted in Fig. 63.

4.2.4.4. At the SiC/Si interface

Unlike at the C/SiC interface, there were no fine particles or dispersoids in or around the SiC/Si interface of any of the samples, which are illustrated in Fig. 67. According to these micrographs, the silicon did not typically contain any dislocation lines, except in the case of the PIP-epoxy.

These dislocations are highlighted in Fig. 67(d) and are predominantly located near the SiC/Si interface. However, since there are similar dislocations away from the interface, no support can be gained from this micrograph to explain the cause or development of these dislocations.

Meanwhile, also in this region at the SiC/Si interface are interlocked faceted SiC grains of around a micron in size, which are evident in Fig. 67(c). Following the diffusion-controlled theory for the development of the SiC phase [177], these relatively small particles could be the front of the SiC production during the LSI process. Again, the grains in the front of the reaction were heavily strained with a large density of stacking faults inside.

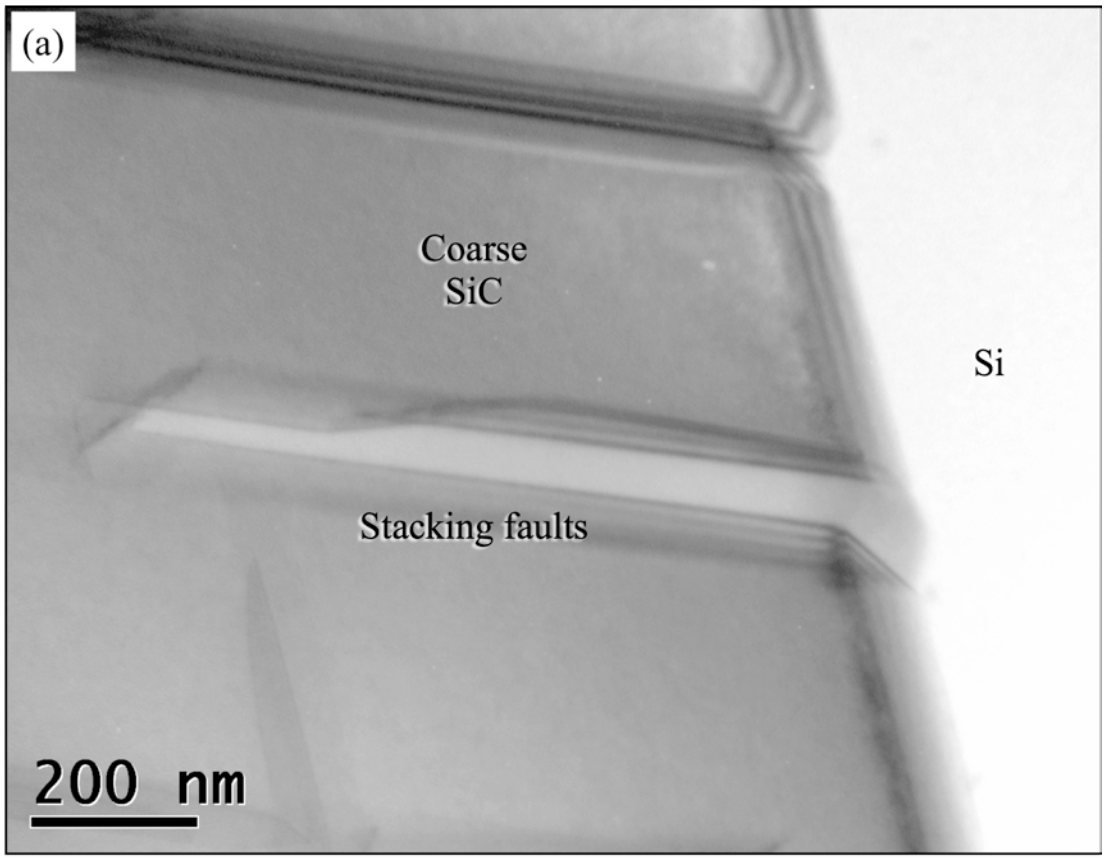
(a)
Coarse
SiC
Si
Stacking faults
200 nm

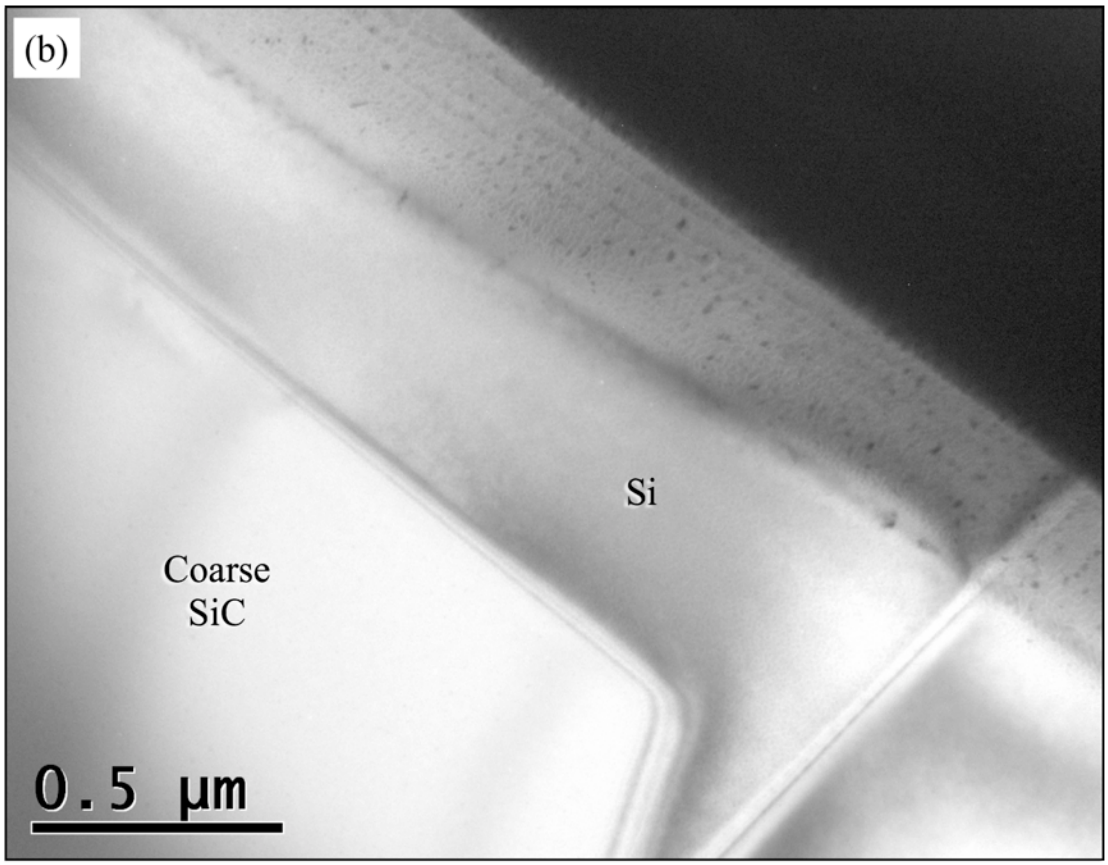
(b)
Si
Coarse
SiC
0.5 µm

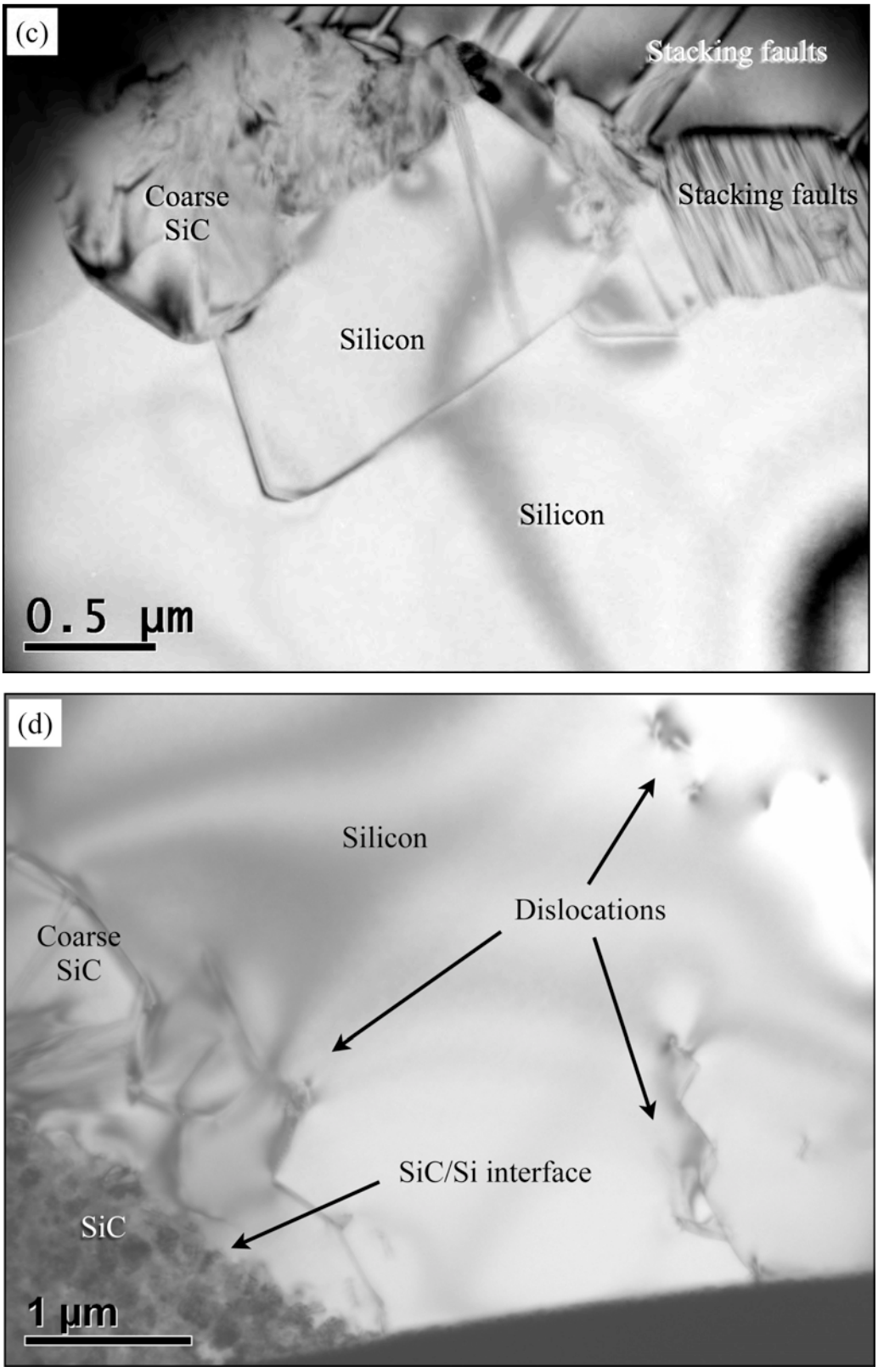

Fig. 67. TEM bright field micrographs at the SiC/Si interface of: (a) Virgin CVI-Carbon, (b) Virgin graphite, (c) Virgin PIP-Phenolic, and (d) End-of-life PIP-Epoxy.

4.2.4.5. Silicon

It was evident in all of the samples, irrespective of the carbon origin that un-reacted silicon was always surrounding the SiC. It is understood that the silicon re-crystallised from the infiltrated silicon melt that failed to react with any carbon. This is supported by TEM SAD patterns that were in a similar fashion to the SiC, correlated with XRD patterns. All of the silicon was of the same polytype: cubic silicon. However, dislocations were also evident several micrometres away from the interface, which are evident in Fig. 67(d). In fact, away from the interface, there was no observed evidence of any other crystal defects.

4.2.4.6. SiC islands

However, in amongst the silicon are interspersed SiC islands, which can be clearly identified in Fig. 56. These islands were evident in all samples and in most cases situated in close proximity to the SiC-Si interface. Through grinding/polishing of the surface, it was revealed that most of these islands were not part of the general architecture of the SiC regions, but isolated islands.

As previously highlighted, the diffusion rate of carbon inside the SiC could be the controlling factor for the development of SiC by the reaction of diffused carbon within the silicon melt. If this mechanism is genuine, it would imply that the developed products through a diffusion-controlled reaction should exist in between the SiC and silicon. Most of the faceted SiC shown in Fig. 56 could be a consequence of this process, but not the isolated SiC islands. These SiC islands could be explained using a process of dissolving-precipitation. According to the Si-C phase diagram [252], carbon can dissolve in silicon melt with a limit of about 5 atm.% at 1500°C, while it's solubility increases with the increase of the temperature. As the melt is cooled down, SiC crystals could precipitate and exist inside the silicon crystal. However, it is clear that further experimental study is needed in order to validate this speculation.

It is not considered likely that the pyC diffused through the entire SiC structure, as there has been no evidence to support this. However, it is possible that the SiC crystals formed and were pushed outward away from the PyC/SiC boundary during the development and evolution of the bulk SiC layer. In this case, the islands

might have developed during the initial stages of silicon melt infiltration, which might have been aided by the violent initial reaction. Alternatively, the islands could have formed through the dislodging of the outer facets of SiC (at point 4), which is also in accordance with Favre *et al* [163]. Instead, it is believed herein that both dissolving-precipitation and dislodgment through violent reaction may have lead to the creation of these SiC islands.

4.2.5. Summary of the microstructural development

OM, TEM and XRD investigations confirmed that: recycled, end-of-life and reclaimed carbon fibres with either virgin and/or end-of-life epoxy can be used to successfully manufacture C_f/C-SiC composites. The microstructure of the resulting composites was very similar to that of virgin derived C_f/C-SiC composites. Fig. 68 illustrates a 3D schematic of a typical microstructure based on the evidence and assumptions made in the preceding sections.

1). Inside the carbon structure

The carbon developed in amongst and surrounding the carbon fibres by either CVI, through direct pyrolysis of resin inside end-of-life pre-pregs or PIP of virgin phenolic resin. TEM micrographs revealed no clear indication that the end-of-life epoxy in the PIP-epoxy sample suffered any degradation.

The TEM micrographs confirmed the existence of nano-sized SiC particles along the PyC/SiC interface of the PIP-derived and graphite samples, while some could have also dispersed inside the pyC and graphite. It was speculated that the particles were generated by silicon vapour that penetrated the meso and micro scale porosity, through a hypothesised ‘suck-in’ capillary phenomenon at temperatures prior to reaching the melting point of the silicon (1414°C), which reacted and spontaneously converted into SiC. The particles extended much further inside the industry grade graphite, in comparison to other samples, which was attributed to the extended porosity that was generated during high temperature processing.

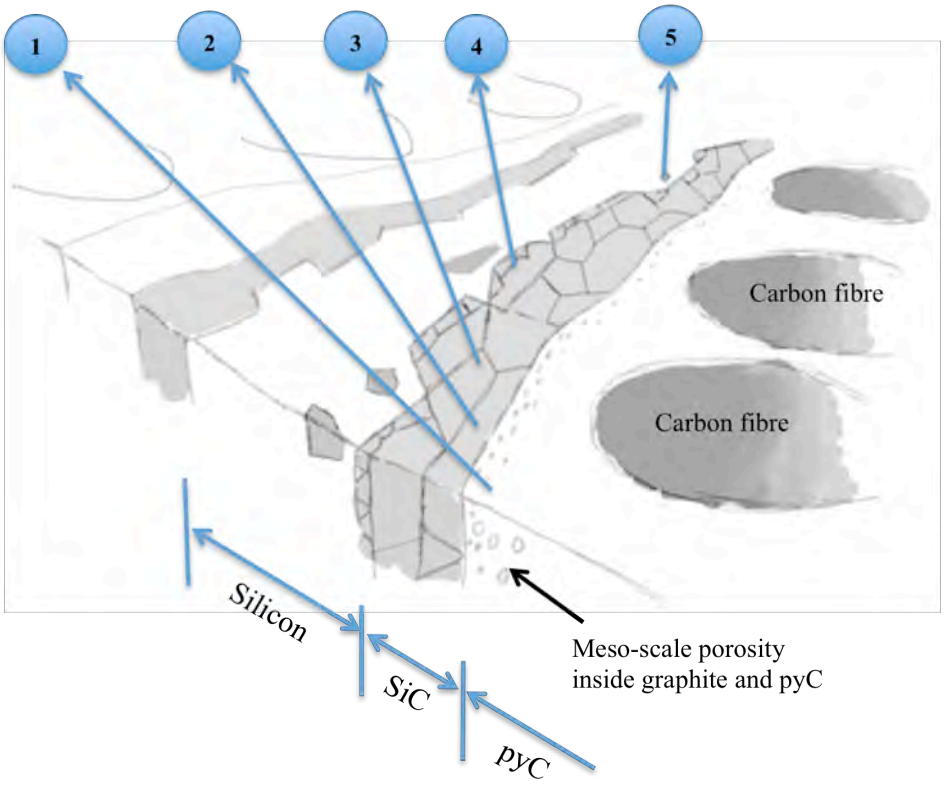

Fig. 68. 3D Schematic illustrating the key features inside a typical microstructure. The phases: carbon fibre (C_f), carbon structure: CVI-C, virgin and end-of-life PyC, SiC and silicon are identified.

By comparison, according to the TEM micrographs, the virgin CVI-carbon structure was dense and hardly accessible by the silicon vapour or melt. There was no evidence of any penetration in either the vapour or liquid melt after LSI.

2 and 3). In the SiC

Point 2 identifies the main reaction plane where the proposed silicon vapour and molten silicon reacted with the carbon prior to and after reaching 1414°C. The coarse SiC layer appeared to comprise multi SiC crystallites, which was approved by TEM micrographs. Combined TEM and XRD results indicated that all of the SiC was of the same polytype, which was FCC β-SiC. The SiC crystallites typically varied in size between 2 and 5 μm (point 3) and possible orientation according to their proximity to the PyC/SiC interface.

Larger SiC crystals were evident at the C/SiC, while smaller SiC crystals were more prevalent nearer the SiC/Si interface. Apart from the PIP-Epoxy, all of the

crystals contained significant quantities of strain contours and stacking faults, which could be indicative of their growth direction. Formation of the multi-layer SiC structure in the PIP-epoxy was considered to be an artifact. However, formation of this structure was likely attributed to the same combination of the meso/micro scale porosity in the PIP-phenolic sample that was generated by the evolution of the pyrolysis gases. The pyC structure would have been fragile due to the porosity, which would have been totally consumed, or at least partly consumed by the silicon melt.

4). At the SiC/Si interface

The SiC crystals at point 4 are at the frontier between the SiC and silicon. The crystals here were smaller, in the 1-3 μm range, which were measured in the TEM micrographs. These crystals comprised similarly dense stacking faults, although were orientated in multiple directions, which again, could relate to their formation direction.

5). Silicon and SiC islands

The silicon contained in all of the samples was considered to have been unable to react with the carbon, with a consequence of re-solidifying back into silicon. This was confirmed by TEM SAD and XRD patterns, which indicated that the silicon was the same type amongst all of these samples: cubic silicon, irrespective of their origin.

SiC islands were present inside all of the samples, just beyond the SiC/Si interface, which was confirmed by optical micrographs (Fig. 56). The islands are thought to have developed through a combination of dissolving-precipitation and dislodgment during the violent LSI reactions.

4.3. Mechanical behaviour of the constituents

According to the literature review, the tribological characteristics of C_f/C-SiC composites, in particular the COF, COF stability (S) and wear rate are typically not favourable and require tailoring for the friction couple to be compatible. It was agreed upon that the mechanisms occurring at the surface directly affect the friction performance, which relates to the properties of the material at the surface. In addition, it is acknowledged that an unmodified surface topography comprises multiple micro and nano-sized phases, interfaces and voids that vary in proportion based on factors already identified. Where the possible impact and role of each phase at the microscopic level during friction has only recently been highlighted [55] and have thus far not been quantified.

Therefore, the properties such as hardness (GPa), Young's modulus (GPa) and fracture toughness (K_{1C}, $MPa.m^{1/2}$) were investigated by nano-indentation at each phase inside three different C_f/C-SiC composites, including those containing end-of-life PAN carbon fibre and epoxy resin. The results are to be used to validate the inclusion of these recycled constituents. Details of the raw materials used to construct the C_f/C-SiC composites are described in Table 14 and included: 1). Virgin PAN-OX carbon fibre with a CVI-C interface inside the 'ST' preform, 2). End-of-life PAN carbon fibre inside the '5417' preform with the dual PIP-epoxy and PIP-phenolic interface, and 3). End-of-life PAN carbon fibre inside the '5417' pre-preg with a PIP-epoxy derived pyC interface.

4.3.1. Carbon fibre

Fig. 69 shows the nano-indentation loading/unloading curves and supporting FEG-SEM micrographs of the different carbon fibre inside the C_f/C-SiC composites. According to the curves and micrographs, there was minimal difference between the virgin PAN-OX and end-of-life PAN carbon fibres, indicating that the end-of-life fibres did not suffer any significant degradation. The virgin PAN-OX fibres recovered slightly slower and exhibited a slightly lower average plastic deformation, which is defined as the depth value (nm) where the unloading portion of the curve crosses the x-axis (Fig. 69(b)).

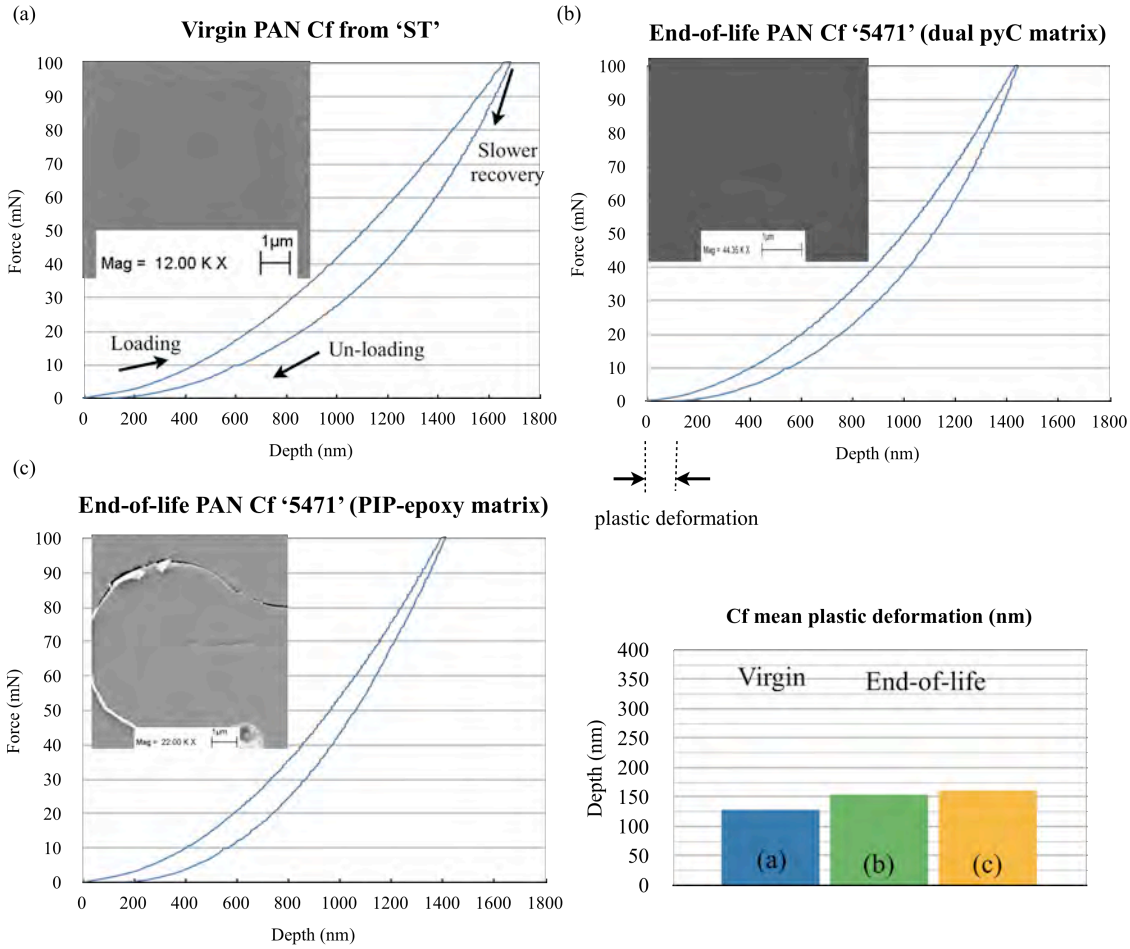

Fig. 69. Nano-indentation curves with supporting FEG-SEM micrographs of carbon fibre inside the different C_f/C-SiC composites. Bar graph represents the mean plastic deformation of each phase.

Imaging the carbon fibre in the microstructures presented a particular challenge for three reasons: firstly, the fibres were very small. According to the micrographs, the virgin PAN-OX fibres inside 'ST' were around 10 micrometres and circular, in comparison to 7 micrometres (also circular) for the end-of-life AS-4 fibres in the other two composites. Therefore, in addition to imaging, striking 'only' the fibre with the indenter and not the interface was also difficult, which was mitigated by performing multiple tests. However, each result could be qualified by examining the indentation curve. If a sudden change in gradient was evident during loading (left side) and/or unloading (right side), then this would indicate a change of phase. A possible example of this is highlighted in Fig. 69(a), while there is no evidence of a sudden change in gradient in the other two curves in (b) and (c).

Secondly, the plastic deformation was very low and was therefore very difficult to resolve. The graphs show that the unloading portion of each curve almost completely returned to their original position, which indicates that all of the fibres were highly elastic.

Finally, the fibres were almost indistinguishable from the adjoining carbonaceous interface (CVI-carbon or pyC) in the secondary electron mode of the FEG-SEM. This was because both phases comprised carbon. Optical microscopy (MEF-3) was initially implemented using the polarised and DIC modes to aid distinction between the phases, although due to the limited maximum operating magnification (x1000) and capability to resolve any propagating cracks, the FEG-SEM had to be used.

4.3.2. Pyrolytic carbon

The indentation curves with supporting FEG-SEM micrographs are shown in Fig. 70. All of the indentations generated inside the CVI-C were indistinguishable in the FEG-SEM micrographs, which is likely due to the very low plastic deformation. The mean plastic deformation of each phase is also shown in Fig. 70, which ranged between 75 and 150 nm for the CVI-C and PIP-derived pyC phases respectively.

According to previous TEM microscopy in Fig. 53, the PyC derived from PIP-phenolic was significant thicker in comparison to the PyC derived from PIP-epoxy. This was attributed to the higher proportion and carbon yield of the phenolic resin. Therefore, inside the C_f/C-SiC composite comprising a dual pyC from PIP-epoxy and phenolic in Fig. 70(b), it would not be unreasonable to assume that the indenter struck the pyC derived from the phenolic. Furthermore, this might have been mitigated further, because all of the indentations were performed away from the C_f/C interface, typically in the tens of microns range.

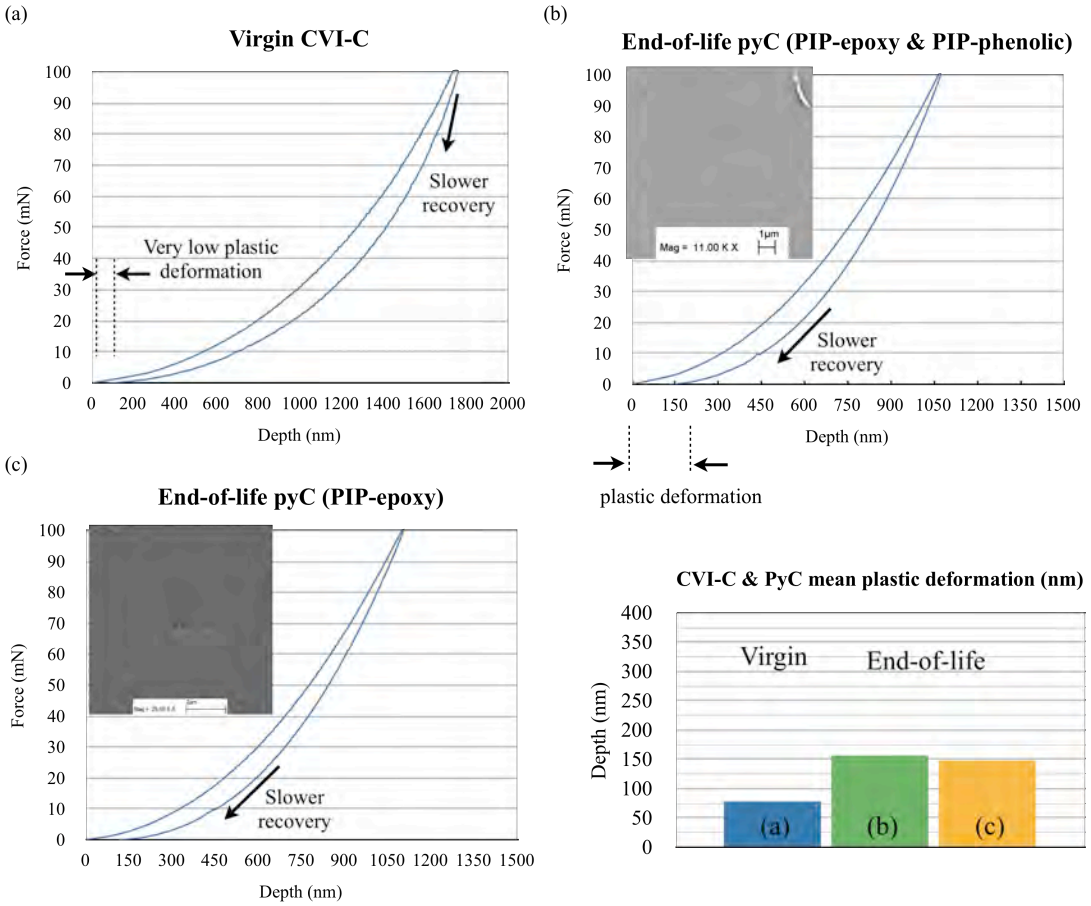

Fig. 70. Nano-indentation curves with supporting FEG-SEM micrographs of the PyC inside the different C_f/C-SiC composites. Bar graph represents the mean plastic deformation of each phase.

Therefore, in this case, these results suggest that the pyC from the PIP-phenolic and PIP-epoxy were very similar because the depth reached, plastic deformation, loading and unloading profiles were almost identical.

Apart from the plastic deformation and depth of penetration, only subtle differences were evident between the profile of the virgin CVI-C and end-of-life pyC loading-unloading curves. A close inspection of the initial recovery periods indicates that the CVI-C recovered slightly slower, which is highlighted in Fig. 70(a). However, the CVI-C generated deeper indents in comparison to both the pyC, both of which were very similar and recovered quite rapidly at first before slowing marginally as the depth reduced.

The obvious differences between the CVI-C and PIP-pyC phases were the depth of penetration and plastic deformation. To help explain these differences, the

mechanical properties: hardness, Young's modulus and structure of crystal structure should be considered.

According to the hardness and Young's modulus results that are reported later in Fig. 75 and Fig. 77 respectively, the CVI-C was both softer and more elastic. Therefore, the deeper indents inside the CVI-C were likely attributed to its significantly lower hardness of approximately 2 GPa in comparison to around 5.5 GPa for the PIP-derived pyC. Meanwhile, it is understandable that if the CVI-C has a lower Young's modulus and is more elastic, then a lower plastic deformation could be envisaged, which was the case in this study. However, because the plastic deformation of the CVI-C was so low, approximately 78 nm in comparison to 150 nm for the CVI-C and pyC phases respectively. Consequently, indents inside the CVI-C were indistinguishable, unlike the indents inside the PIP-derived pyC. Therefore, when using the FEG-SEM, a minimum plastic deformation of between 78 and 150 nm is required in order to distinguish the indentations when a force of 100 mN is used.

Further support might be gained by re-examining the crystal structure of the CVI-C and pyC using the SAD patterns in Fig. 55. The SAD pattern of the CVI-C in Fig. 55(a) clearly showed a diffused ring pattern, which indicates that it was nearly isotropic, very small with no preferred orientation. By contrast, the SAD patterns of the PIP-PyC in Fig. 55(c) and (d) showed long diffused arches, indicating a more preferred orientation and increases size of the graphene units in comparison to the CVI-C. These differences in the size and orientation of the graphene units likely contributes to differences in the hardness and Young's modulus, which are discussed further in 4.3.5 and 4.3.6, and help explain the increased depth of penetration and reduced plastic deformation of the CVI-C.

In addition, as a consequence of the very low plastic deformation in all of the CVI-C and pyC samples, in a similar respect to the carbon fibre, it was unfeasible to induce a crack and estimate the fracture toughness using a force of 100 mN. Therefore, further indentations were performed in the dual pyC C_f/C-SiC composite (b), using higher forces of 250 and 400 mN respectively. The results are shown in Fig. 71.

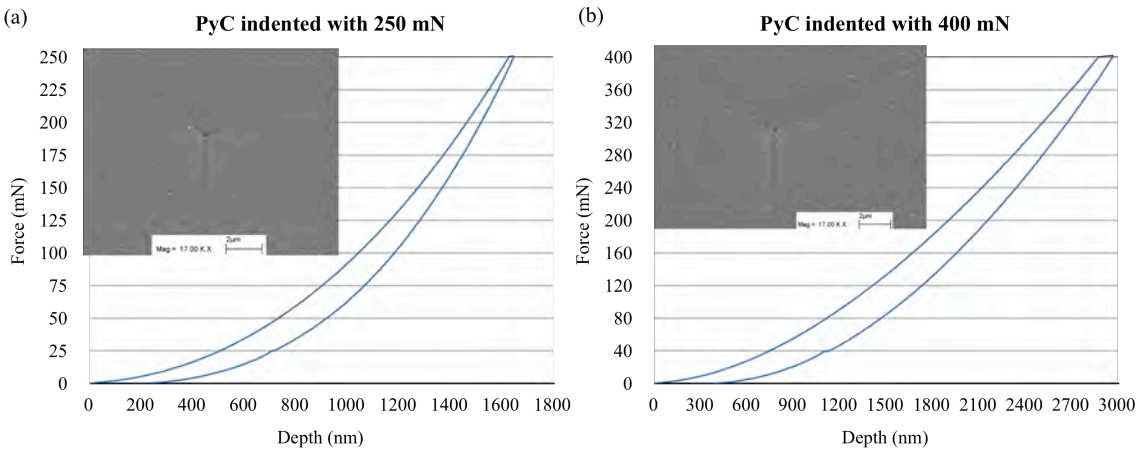

Fig. 71. FEG-SEM micrographs and supporting force-depth graphs of the indentations in the PIP-PyC using a force of (a) 250 mN and (b) 400 mN.

Increasing the force to 250 and 400 mN significantly increased the penetration depth to approximately 1600 nm and 2900 nm respectively. However, still no cracks were generated and both recovered significantly to create plastic deformations of only about 250 nm and 500 nm respectively.

4.3.3. Silicon carbide

The nano-indentation curves with supporting FEG-SEM micrographs from the SiC phases are shown in Fig. 72. The profile of each curve and average plastic deformation depth were all very similar, where the average plastic deformation was approximately 225 nm, which is in accordance with previous TEM and XRD results that indicated that the SiC polytype was the same.

These results closely matched a similar nano-indentation experiment by Fouquet *et al* [1], who tested virgin derived C_f/C-SiC composites and reported almost identical curves, micrographs and plastic deformations. This provides confidence that the nano-indentation was performed correctly.

Meanwhile, in contrast to the carbon fibre and pyC phases, the SiC phases inside all of the composites readily cracked, which permitted the measurement of crack lengths so the fracture toughness (K_{1C}) could be estimated. According to the micrographs, the cracks typically propagated from the corners of the indent, while some also originated from the sides, which are illustrated in Fig. 72(a) and (b), and Fig. 72(c) respectively.

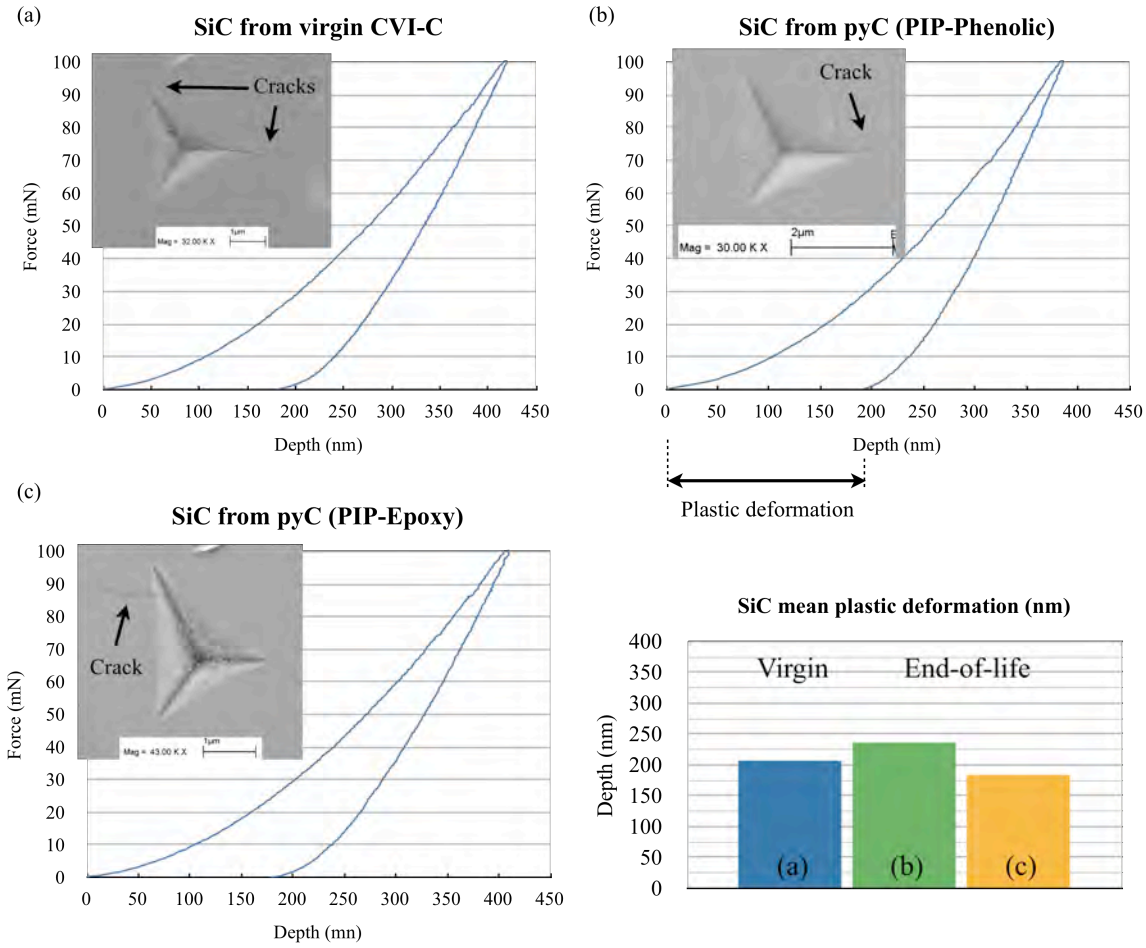

Fig. 72. Nano-indentation curves with supporting FEG-SEM micrographs of the SiC inside the different C_f/C-SiC composites. Bar graph represents the mean plastic deformation of each phase.

After studying all of the micrographs, there was no evidence that could account for these differences. However, the shape and starting location of the cracks were almost identical to those reported by Fourquet *et al* [230].

4.3.4. Silicon

The nano-indentation curves with supporting FEG-SEM micrographs are shown in Fig. 73. In a similar respect to the SiC phases, the loading-unloading curves of the silicon were all very similar amongst these composites, irrespective of the different type and origin of the carbon source. In addition, the mean plastic deformations were also very similar, approximately 350 nm for all of the tested samples. In a similar respect to the SiC, the silicon also readily cracked, most of

which also propagated from the corners of the indent, which can be seen in Fig. 73. These results closely matched the reported data for virgin derived silicon, reported by Fouquet *et al* [1].

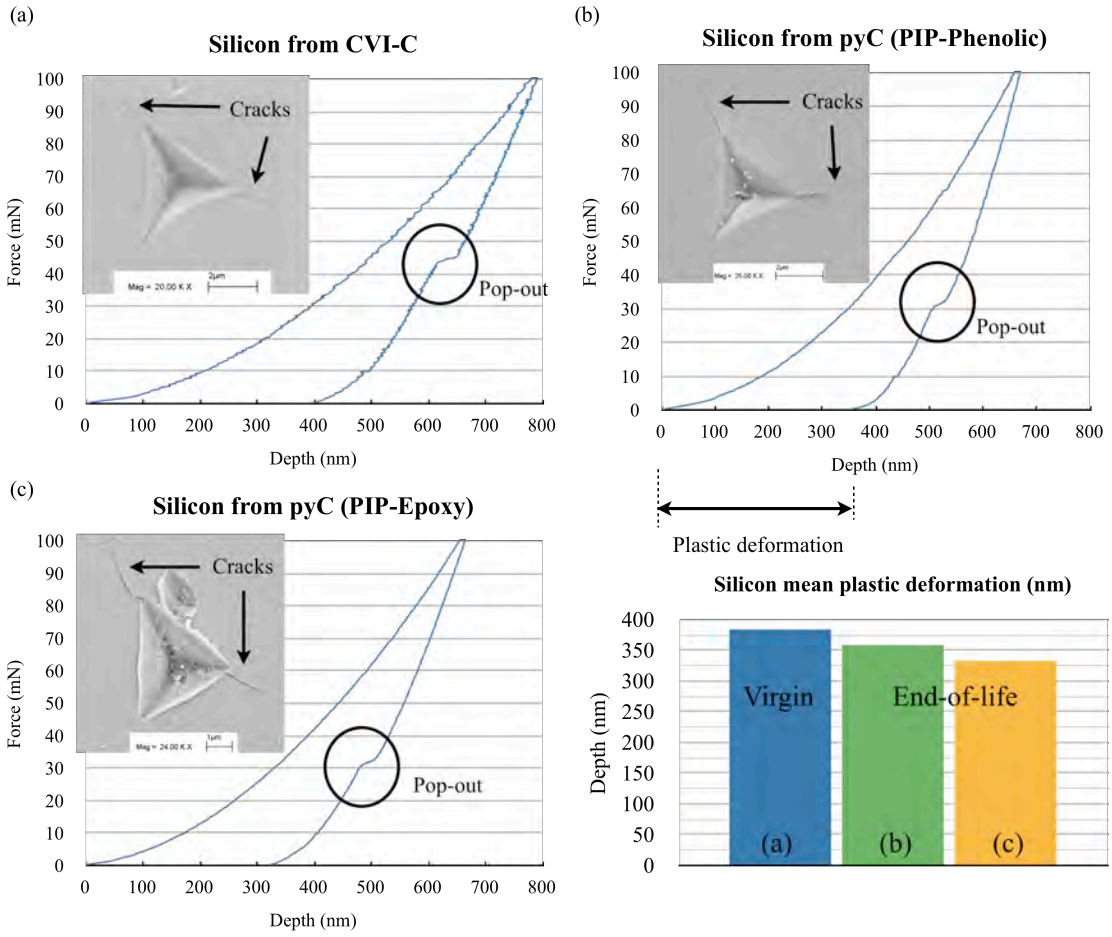

Fig. 73. Nano-indentation curves with supporting FEG-SEM micrographs of the silicon inside the different C_f/C-SiC composites. Bar graph represents the mean plastic deformation of each phase.

The silicon also exhibited a characteristic 'pop-out' feature, which has been reported elsewhere [1, 253, 254] and was evident in all of the samples tested. While there is no supportive evidence herein, one possible factor could be the maximum load, where loads of ≥50 mN were reported to generate pop-out [1]. An additional test was carried out at 200 mN, which is shown in Fig. 74. Increasing the force still resulted in the silicon exhibiting its' characteristic pop-out; phase changes in the silicon to amorphous or BCC, where different phase changes lead to different pop-out loads [253]; loading rate, where a lower unloading rate of 0.5 mNs^{-1} always created pop-out

as opposed to 5 mNs^{-1} that produced only 6 pop-outs from 15 tests [254]. Considering the loading rate used in this study was 2.5 mNs^{-1} and every silicon phases exhibited pop-out, the critical pop-out loading rate should be comparatively high, certainly greater than 2.5 mNs^{-1} and even beyond 5 mNs^{-1} if the phenomenon is to be avoided. Therefore, apart from identifying phase changes in the silicon after indentation, all of these factors could, at least in part account for the results observed herein.

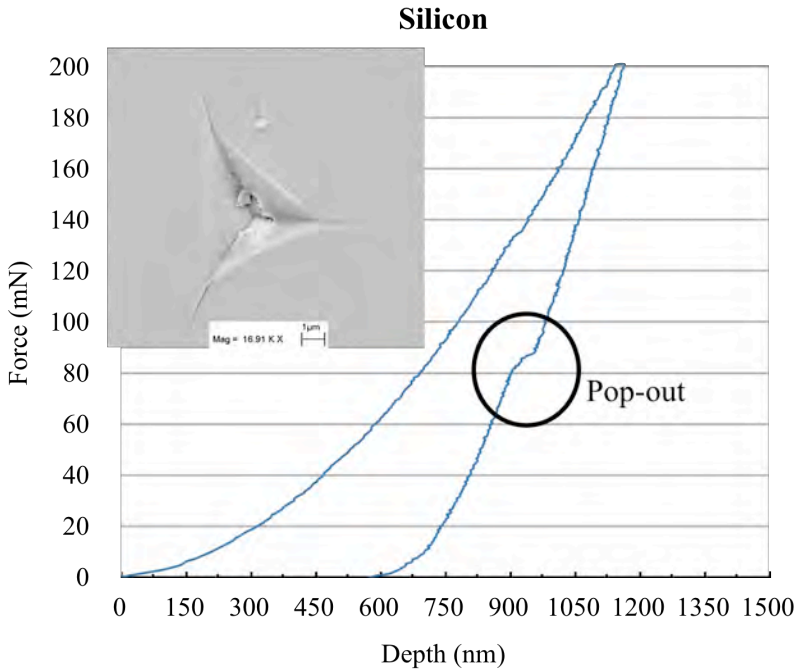

Fig. 74. FEG-SEM micrograph illustrating an indentation in silicon using a 200 mN force, with supporting force/depth graphs showing the pop-out phenomenon still occurs.

4.3.5. Hardness

The hardness (GPa) of each phase inside the virgin and end-of-life samples was estimated using equation (16). The results are shown in Fig. 75, which are tabulated in Appendix B – Table 18. An additional graph with an alternate scale for the carbon fibre and pyC is included (inset) because their values were significantly smaller.

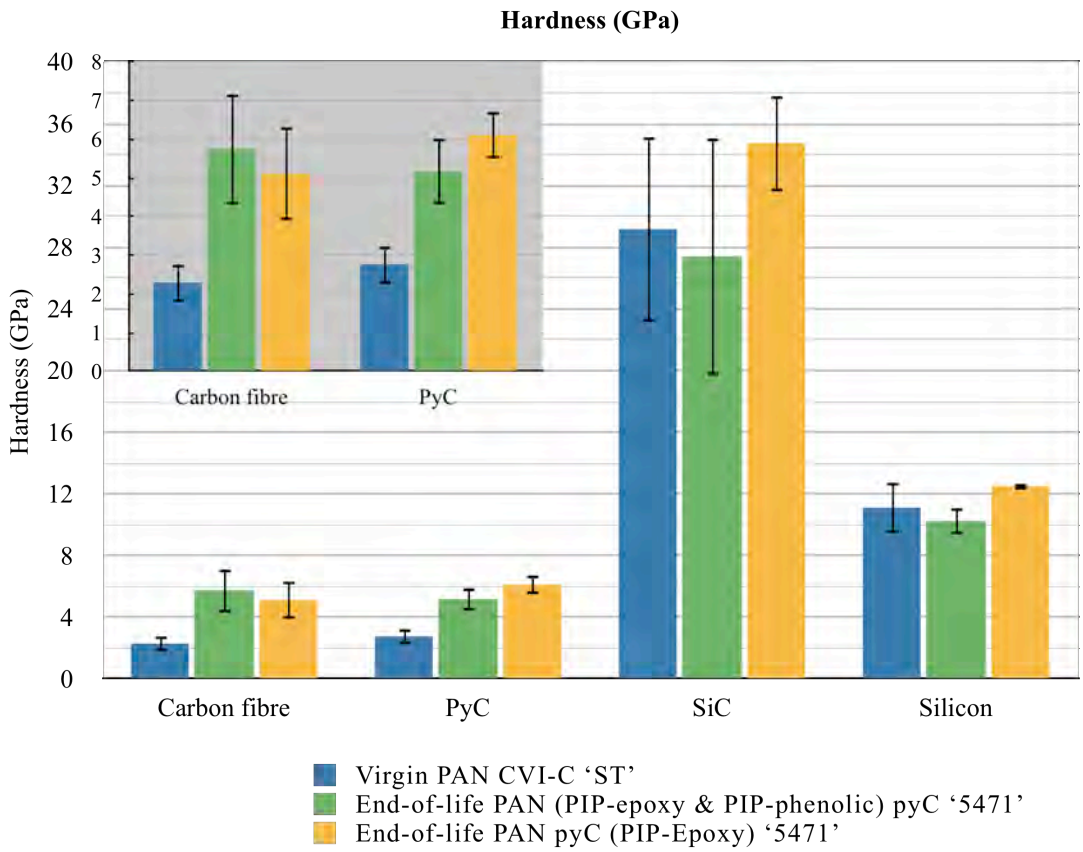

Fig. 75. Bar graphs comparing the hardness of the phases inside the different C_f/C-SiC composites. Error bars represent the standard deviation.

The end-of-life PAN fibre was significantly harder than the virgin PAN-OX fibre, indicating that the end-of-life PAN fibres from the aerospace sector were originally of a higher grade in comparison virgin fibres and that they suffered no significant degeneration. However, since there are no published hardness values for either fibre, further testing would be required to confirm these claims.

The PIP-PyC meanwhile was almost twice as hard than the CVI-C. It was previously highlighted that the pyC interface inside the PIP-phenolic should comprise mainly of pyC derived from phenolic. Therefore, according to the results in Fig. 75, both the PyC-epoxy and PyC-phenolic should posses a similar hardness. In *Section 4.3.2*, differences between the hardness of the CVI-C and both pyC were attributed to differences in the structure of the carbon, where the larger and more orientated graphene units of the pyC should make it harder. Whilst there is no reported nano-indentation data for PIP-derived pyC, the reported hardness of a virgin CVD-derived pyC was 3.6 ±0.2 GPa [255], which is similar to the results herein and further reinforces the potential of the PIP-derived pyC inside these composites.

Variations in the results could be related to the location of the pyC or CVI-C in relation to the fibres and PyC/Si interface. Therefore, pyC and CVI-C samples were indented in a straight line from the fibres to the PyC/SiC interface. The results are presented in Fig. 76, which shows optical micrographs of the indents and supporting force-depth curves.

The hardness and stiffness of the lower indent in the CVI-C sample (Fig. 76(b)) was very high due to the indent making contact with the much harder and stiffer SiC phase. This is supported in the force-depth graph by the sudden variation in the gradient. The hardness of the end-of-life pyC in the PIP-Phenolic and virgin CVI-C increased as the indents approached the PyC/SiC interface, from 4.22 to 4.26 GPa and 2.36 to 3.26 GPa respectively. Considering the very low indentation force of 100 mN, there is no doubt that the bond strength (ILSS) between at the C_f/PyC and pyC/SiC was exceeded. Therefore, it could be easily envisaged that the increase in hardness (and stiffness) could be attributed to the very hard (and stiff) adjoining SiC phase, in comparison to the softer fibres.

Meanwhile, the SiC hardness varied between approximately 28 and 35 GPa, which was in accordance with nano testing by Fouquet *et al* [1] (28-35 GPa) for a similar LSI-derived SiC. There was, however, quite a large variability in the results herein and in those reported by Fouquet *et al*, who attributed it to the preparation process, where the LSI-process created inhomogeneous SiC in comparison to CVI-derived SiC.

Some support for the observed differences could be gained by referring back to the TEM micrographs in Fig. 66. The LSI-derived SiC structure was inhomogeneous and was described further in Fig. 68, which illustrated varying crystal sizes depending on their proximity to the PyC/SiC interface, all of which could also to be at different orientations and contain significant defects and stacking faults. All of these factors might contribute to the observed differences in the hardness, in particular striking the SiC crystal at a different orientation.

(a) **End-of-life pyC**

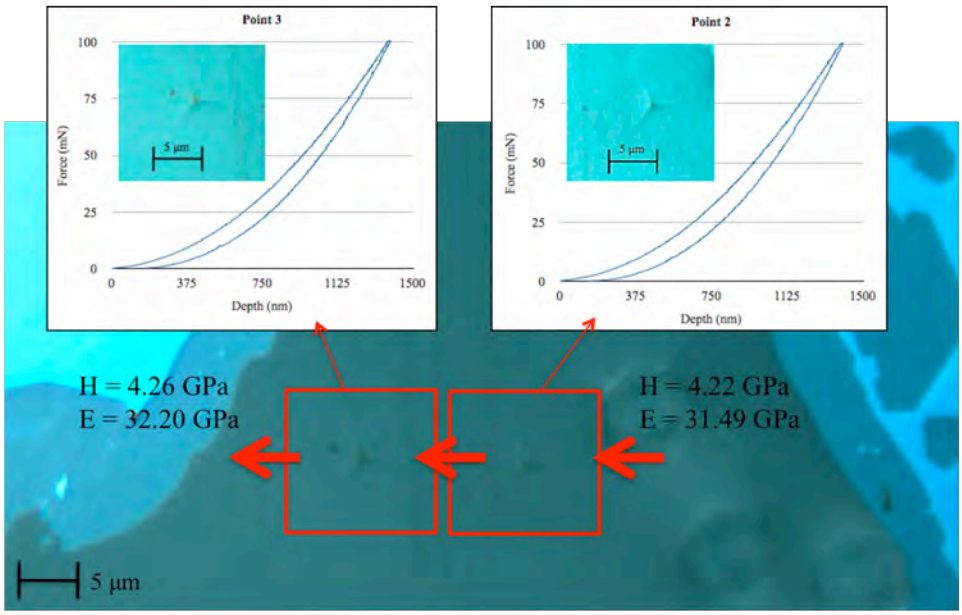

(b) **Virgin CVI-C**

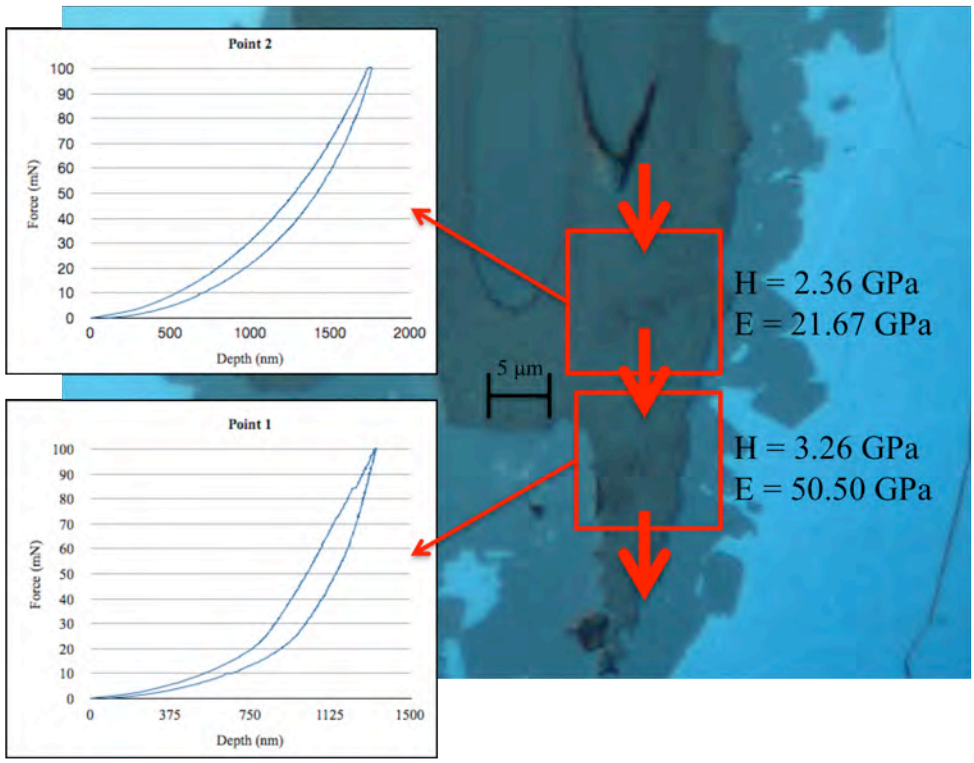

Fig. 76. Optical micrographs under polarised condition illustrating that the hardness (H) and Young's modulus (E) of (a) End-of-life PyC from PIP-phenolic and (b) Virgin CVI-C, increase as the distance from the fibre increases toward the PyC/SiC interface.

The hardness of the silicon phase was very similar in all three of the samples, ranging between 10 and 12 GPa with a correspondingly small standard deviation. This was in accordance with Fouquet *et al* [1] (12 GPa) and the TEM SAD and XRD investigations that identified the silicon as being of the same polytype. Therefore, the properties should be the same, but only if the same orientation is struck each time, which appears to be the case herein.

4.3.6. Young's modulus

The Young's modulus, 'E' results of each phase are shown in Fig. 77, which are tabulated in Appendix B – Table 19. The Young's modulus i.e. stiffness of the end-of-life PAN carbon fibre was at least double that of the virgin PAN-OX fibre. This could offer further support to prior speculation that the end-of-life fibres were originally of a higher grade, in addition to there being no indication of degradation.

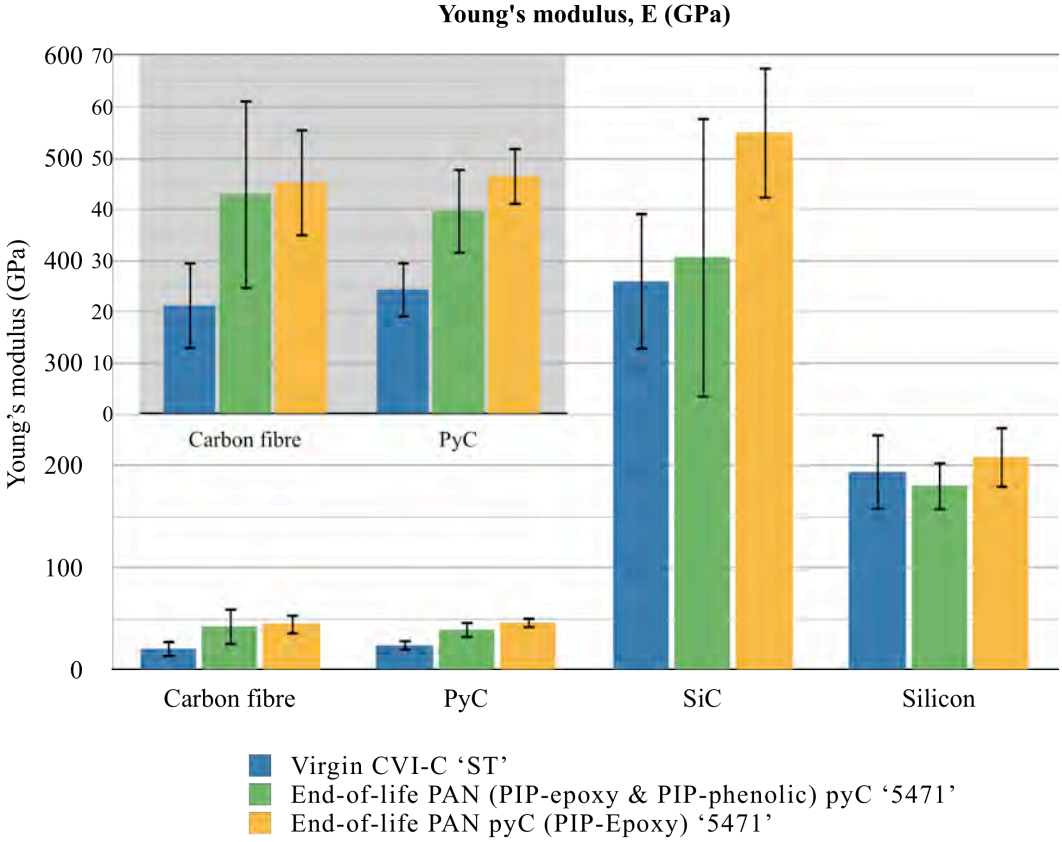

Fig. 77. Graphs comparing the Young's modulus, E (GPa) of the phases inside the different C_f/C-SiC composites. Inset is carbon fibre and PyC enlarged.

Meanwhile, the end-of-life pyC was approximately twice as stiff as the virgin CVI-C, which was represented in Fig. 70 by the lower depths reached by the indenter and the slower recovery. In a similar fashion to the hardness, differences between the CVI-C and pyC are likely attributed to the carbon structure and the position of the indent relative to the fibres and SiC.

The Young's modulus of the SiC varied between approximately 400 and 540 GPa, where the SiC derived from PIP-epoxy was higher. If the polytype of the SiC was the same, then the stiffness should also have been similar, which clearly was not the case herein. By comparison, Fouquet *et al* reported that LSI-derived SiC possessed a lower stiffness of 250 to 360 GPa [1], although the stiffness of a combined CVI and LSI-SiC phase was higher: 450 GPa [230].

As anticipated, the stiffness of the silicon inside all of the samples was similar, where minor differences could easily be attributed to variations in the angle of the crystals. Support for this could be gained from Brantley [256], who found that the Young's modulus varied considerably depending on the orientation.

4.3.7. Fracture toughness

The fracture toughness ($MPa.m^{1/2}$) results are illustrated in Fig. 78 and tabulated in Appendix B – Table 20. Only the SiC and silicon phases are shown because these were the only phases that cracked, where cracks propagating through multiple phases were omitted.

The estimated fracture toughness of the SiC inside each sample varied between approximately 0.71 and 1.16 $MPa.m^{1/2}$. Meanwhile, the silicon was very similar in each composite varying between approximately 0.55 and 0.78 $MPa.m^{1/2}$. The standard deviation was also very small, which indicates the high reliability and reproducibility of testing inside the silicon. Therefore, differences in the results could be related to a number of factors. For example: assumptions made by the calculation in equation (19), differing crack mechanics and/or differences in the SiC itself.

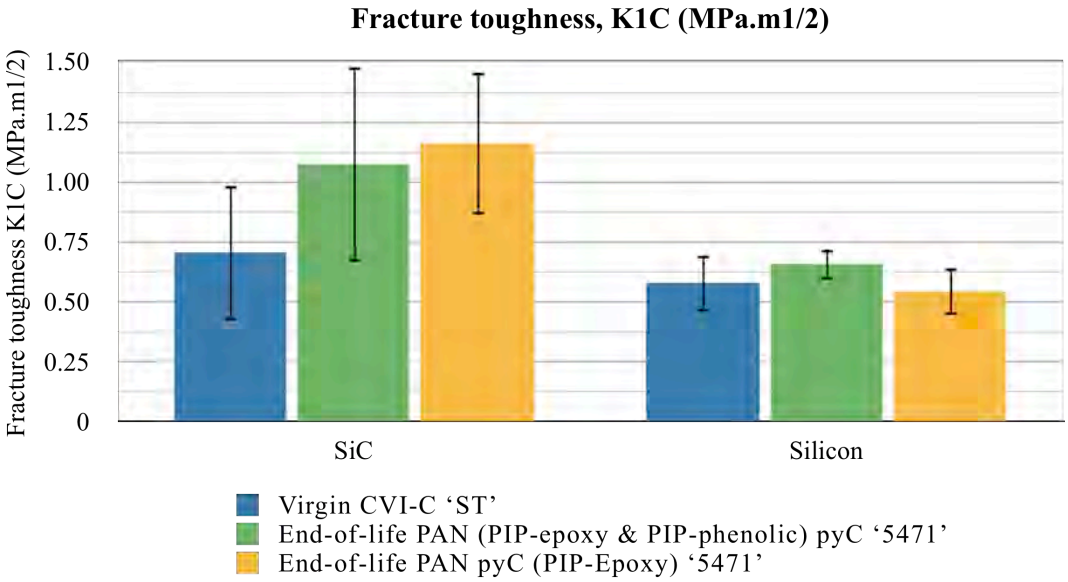

Fig. 78. Graphs comparing the estimated fracture toughness, K_{1C} (MPa.m$^{1/2}$) of the phases inside the different C_f/C-SiC composites. No data for carbon fibre or PyC. Error bars represent the standard deviation.

Assumptions made by the calculation could include: pile up, which can lead to over estimations of the indentation area. However, according to FEG-SEM micrographs, this was not evident herein and therefore any possible significance was neglected; possible extended cracks created by the more narrow Berkovich tip in comparison to the Vickers four-sided indenter; possibility multiple cracks under the surface. Meanwhile, the previously reported differences in the SiC might affect the fracture toughness, in particular, differences in the size and orientation of the SiC crystals.

It is clear however that these results are not a definitive indication of the fracture toughness (K_{1C}). Instead, these results illustrate that the indentation fracture method can be used to estimate the fracture toughness of hard phases such as silicon and SiC inside multi-phase composites. In addition, the fracture toughness of LSI-derived SiC and silicon phases inside different types of C_f/C-SiC, originating from different formats of carbon are comparable.

In summary:

- According to force-depth curves and supporting FEG-SEM micrographs: there was minimal difference between virgin and end-of-life PAN carbon fibre; minimal

difference between virgin CVI-C and end-of-life pyC; negligible difference between the SiC and silicon phases inside the composites comprising the virgin and end-of-life material.

- All of the carbon fibre, pyC and CVI-C phases were highly elastic and did not crack. The SiC and silicon in all of the composites readily cracked using a Berkovich tip, under a load of 100 mN and loading rate of 2.5 mN/s. According to the micrographs, there was no preferential crack initiation. However, cracks typically developed from the corners of the indent.
- The end-of-life carbon fibre and PIP-derived pyC was found to be harder and stiffer in comparison to virgin PAN-OX fibre and CVI-derived carbon. This indicates that the end-of-life fibres were originally of a higher grade in comparison virgin PAN fibres, while neither the end-of-life fibre nor pyC suffered any significant degeneration.
- The hardness, Young's modulus and estimated fracture toughness (K_{1C}) of the SiC and silicon phases inside all of the composites were similar, especially the silicon.
- Variations in the properties of the SiC could be attributed to unaccounted for differing crack mechanics and/or variations in the SiC itself. For example, variations in the SiC crystal size and orientation.

4.4. C_f/C-SiC physical properties and bend strength

4.4.1. Density and porosity

The estimated bulk density (g/cm^3) and open interconnecting porosity (%) of four different C_f/C-SiC composites comprising different recycled carbon fibre were compared at each stage during manufacture; at the CRFP stage, after a single LSI and second LSI. These included: (a) Recycled 'non-woven mat', (b) End-of-life UD '5164', (c) End-of-life 2D woven '5471' and (d) Reclaimed UD 'cured spar', which are detailed in Table 14.

The results for the estimated bulk density and open porosity are shown together in Fig. 79, which can be compared to other reported C_f/SiC or C_f/C-SiC composites similarly manufactured by LPI and LSI, in Appendix A – Fig. 32.

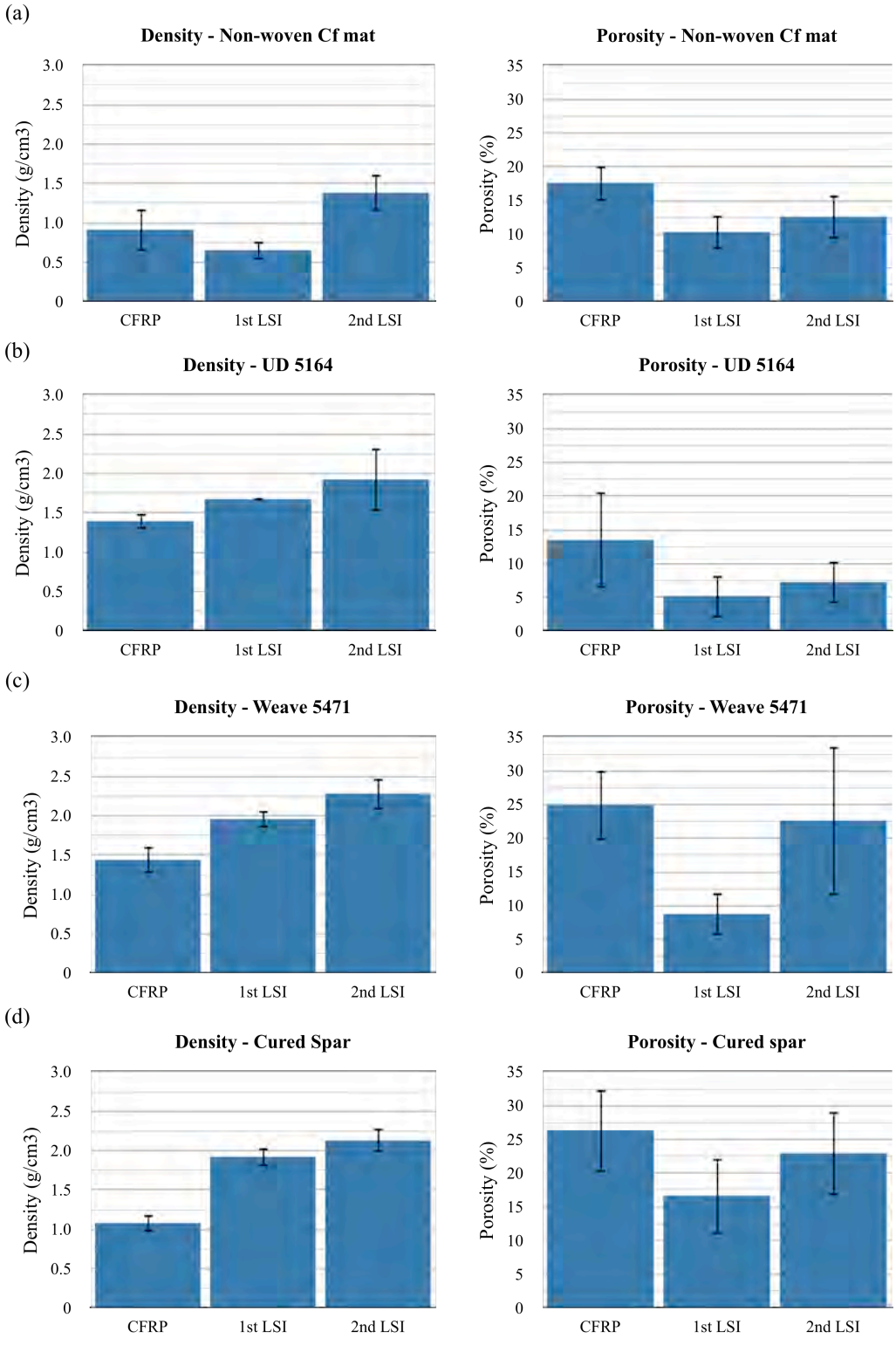

Fig. 79. Estimated bulk density (g/cm^3) and open porosity (%) of different recycled C_f/C-SiC composites: (a) Recycled SF 'non-woven mat', (b) End-of-life UD '5164', (c) End-of-life 2D woven '5471' and (d) Reclaimed UD 'cured spar'. Error bars represent the standard deviation.

All of the composites comprising the waste carbon fibre achieved a comparable bulk density in comparison to the virgin alternatives, apart from the 'non-woven C_f mat' sample. The open porosities were higher, in particular after a second LSI, but were still within a comparable range.

The density increased with successive LSI siliconisations, except in the case of the 'non-woven mat' composite that reduced in density after the first LSI and then increased to a higher density after a second siliconisation (Fig. 79(a)). This was unexpected because the density of a SiC/Si matrix is higher in comparison to the polymer matrix of the CFRP. This could therefore be attributed to either incomplete siliconisation by LSI or weight loss caused by corrosion of the carbon fibres by the silicon melt during LSI.

Some support could be gained by examining the typical microstructures, which are shown in Fig. 80 and clearly illustrate: C_f/C bundles without silicon penetration (dark grey), fully dense PyC/SiC, SiC (grey) and PyC/SiC/Si regions with voids (black) and pools of free unreacted silicon (white).

The former is therefore supported in Fig. 80(a), because there were multiple voids in the microstructure, which must have been mostly closed considering the comparatively low open porosity. Meanwhile, the latter is unlikely because there was no evidence of fibre corrosion. All of the composites increased in density after a second LSI, which would further support theories of incomplete siliconisation after the initial silicon infiltration. It was previously established in the literature review that C_f/C-SiC composites with higher densities performed better as friction materials for disc-on-disc aerospace applications [5]. Zhang *et al* [22] meanwhile identified that the density should reach at least 2.18 g/cm^3, which related to the most beneficial density in terms of both frictional performance and stability (Fig. 11). This was achieved by the end-of-life weave '5471' composite after a second LSI, but not by the remaining preforms, although the UD 'cured spar' composite was close at 2.13 g/cm^3. However, even though there was no additional benefit from densities higher than 2.18 g/cm^3, much of the friction performance benefit was realised at densities as low as 1.85 g/cm^3 [22]. This would therefore include the both of these composites after a single LSI, similar in respect to DLR's Silica woven at 1.9 g/cm^3 (Appendix A – Fig. 32(a)) amongst other virgin-based composites from industry and the UD pre-preg '5164' after a second LSI.

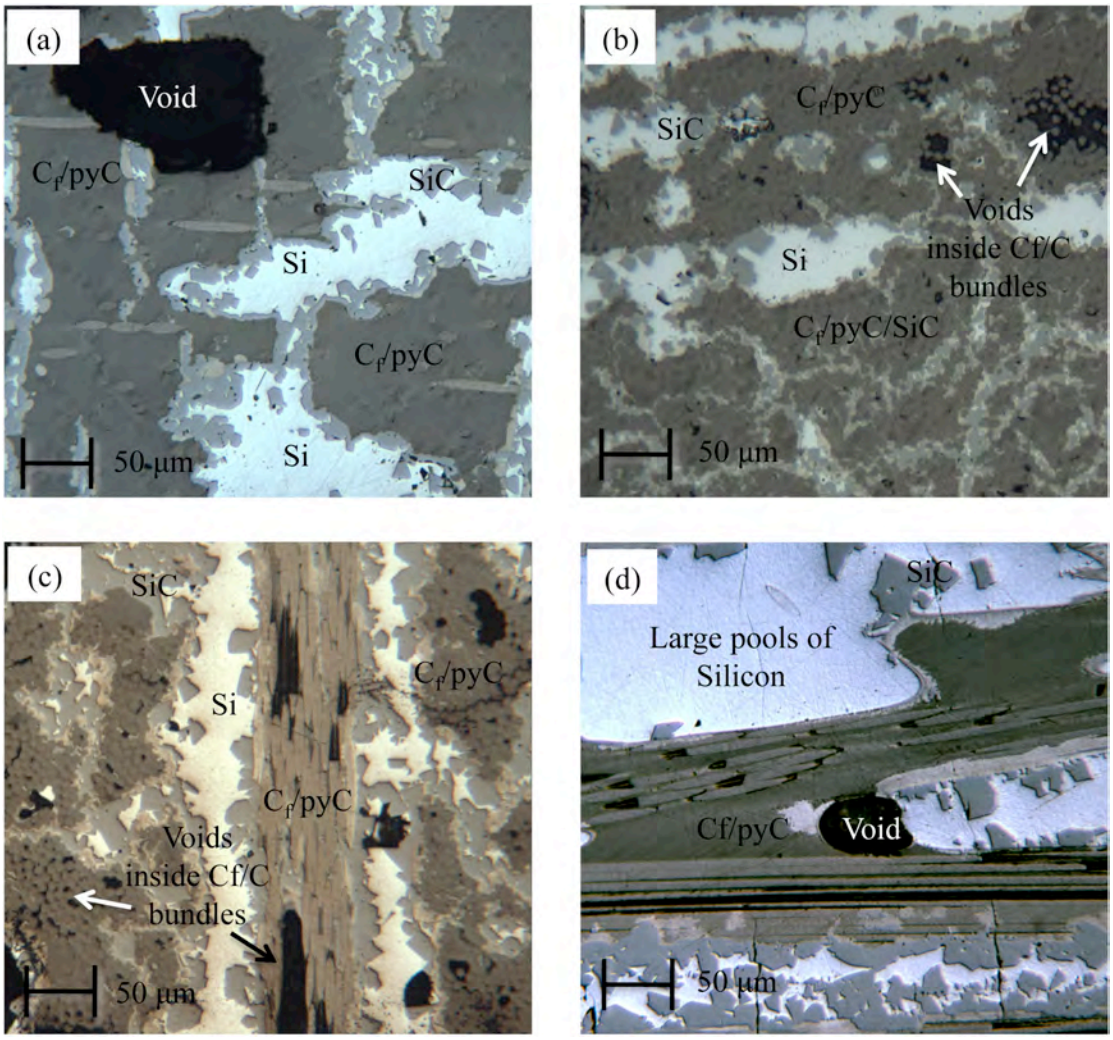

Fig. 80. Optical micrographs illustrating the typical microstructure of the C_f/C-SiC composites: (a) Recycled 'non-woven mat', (b) End-of-life UD '5164', (c) End-of-life 2D weave '5471', and (d) Reclaimed UD 'cured spar'.

Meanwhile, from Fig. 79 (inset), the estimated open porosity of the waste carbon fibre composites all exhibited the same trend: a high initial porosity of the CFRP in comparison to other industrial composites (Appendix A – Fig. 32(b)), apart from the LPI-manufactured sample from MAN; a second lower open porosity that was approximately half the original value and more comparable to the porosities of the industrial composites; followed by an increase after a second LSI, which according to the standard deviations was highly variable.

The initial decrease in the open porosity was due to LSI; the silicon infiltrated into the preform and reacted with the carbon to form a mixture of SiC and silicon, which can be seen in Fig. 80. Meanwhile, the subsequent increase in the open porosity

after the second LSI was likely related to a re-opening the porosity. This trend is in accordance with Bae *et al* [153], who demonstrated that C_f/C preforms with high initial porosities led to C_f/C-SiC composites with high densities. The end-of-life weave '5471' and UD 'cured spar' samples exhibited open porosities between 25 and 26% and created C_f/C-SiC composites with significantly higher densities of 2.34 and 2.13 g/cm^3 respectively.

Therefore, the implication of an additional PIP with two subsequent LSI's was investigated on the end-of-life weave '5471' sample. The results of the bulk density and open porosity at each stage are shown in Fig. 81.

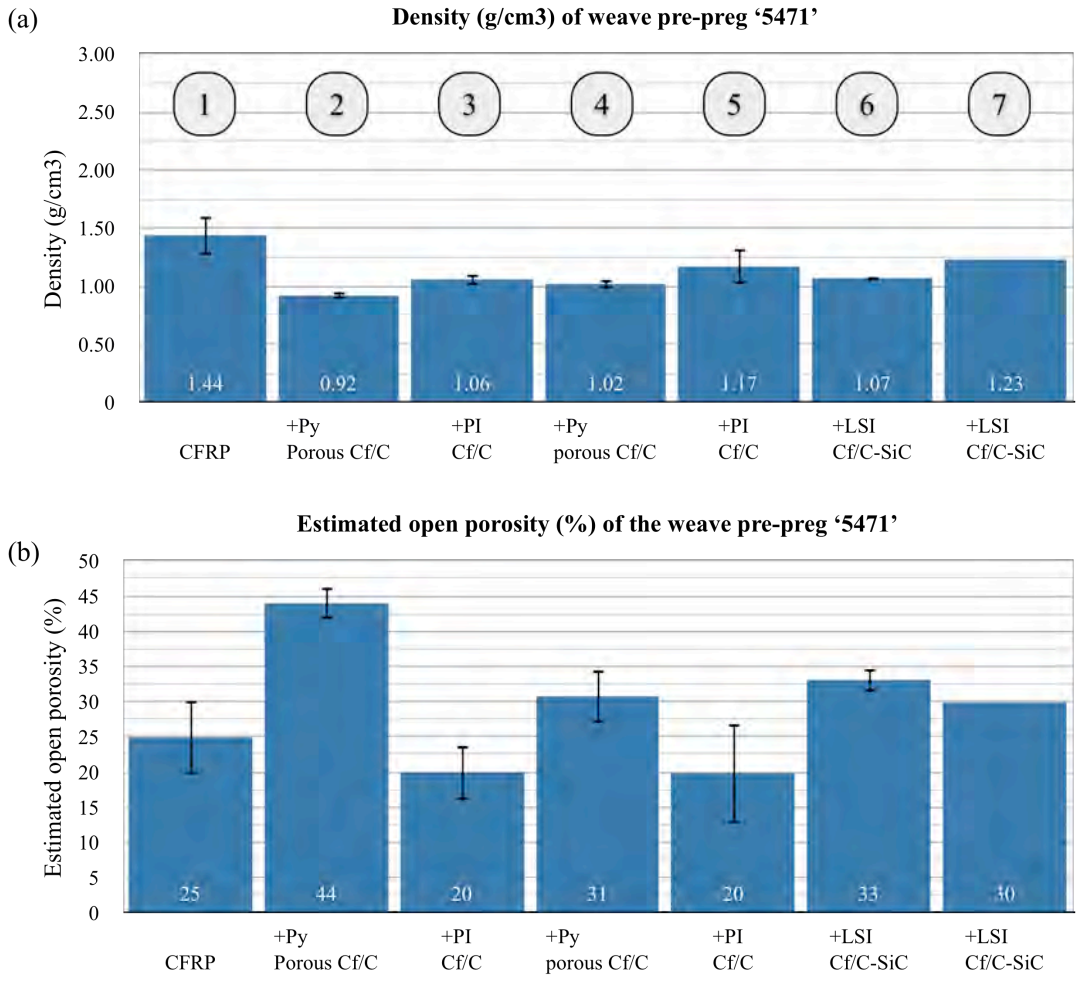

Fig. 81. Graphs showing how the: (a) Bulk density (g/cm^3) and (b) Estimated open porosity (%) changes (1-7) for the end-of-life weave '5471' sample at each stage during processing when manufacture was modified with an additional polymer infiltration and pyrolysis (PIP).

After the initial pyrolysis, the initial density of the CFRP dropped to 0.92 g/cm^3 and the open porosity increased significantly to approximately 44% (point 2). This represents the conditions of the preform prior to LSI. However, instead of being siliconised, the preform was re-infiltrated with phenolic resin (polymer infiltration, PI), which as anticipated increased the density and lowered the porosity to 1.06 g/cm^3 and 20% respectively (point 3). An additional pyrolysis at 900°C (point 4) converted the resin into pyC in addition to the already existing pyC interface, which increased the open porosity to approximately 31%. Meanwhile, a second additional polymer infiltration (point 5) increased the density further still and lowered the porosity, back to about 20%.

Therefore, as the preform was infiltrated and pyrolysed, the density and porosity increased and decreased respectively. This is likely attributed to the progressive increase the pyC as more resin was converted by pyrolysis. However, since the bulk density did not reduce as the preform was progressively infiltrated and pyrolysed, this would also imply that the porosity remained open. This could be related to the open porosity i.e. voids that represent a large volume for their zero mass, although no dimensional measurements were made to confirm this.

The final density of the composite after the first and second LSI was significantly lower and therefore inferior in comparison to the same preform receiving just a single PIP, prior to LSI (Fig. 79(c)). This implies that any additional pyC as a result of the additional PIP inhibited the infiltration of the molten silicon during LSI, which was likely caused by restricting its access throughout the preform.

In summary:

- C_f/C-SiC composites comprising unique waste origins of carbon fibre can achieve comparable densities, open porosities and flexural strengths to similarly processed and orientated virgin-based C_f/C-SiC composites.
- Under the current manufacture regime, none of the preforms were fully densified after a single LSI and required an additional infiltration to reach the typical densities of virgin based C_f/C-SiC composites reported by industry.
- All of the preforms increased with successive infiltrations, apart from the ‘non-woven mat’ preform, which reduced after a single LSI before increasing to a higher density.

- Open porosity measurements revealed the same trend for all of the samples. A comparatively high initial porosity that reduced after the first LSI, which increased after the second LSI. After the initial LSI, the porosities of the composites were comparable to virgin based composites, in particular those also manufactured by a single LSI. However, after a second LSI, the composites exhibited higher porosities, which were also highly variable.
- Additional PIP inside the end-of-life woven '5471' sample appeared to be detrimental to the physical properties. It is speculated that multiple impregnations progressively increased the quantity of pyC, which likely reduced any accessible porosity to the silicon melt during LSI.

4.4.2. Bend strength and failure mode

The next important step was to evaluate the mechanical behaviour and failure mode of these composites and make comparisons to virgin alternatives. This was achieved by measuring the bend strength of each composite and investigating the force-displacement curves.

The results are shown in Fig. 82, which are highlighted in red and includes comparisons to virgin-based composites reported by industry [1, 14]. The results have been split up according to their fibre architecture, because short fibre (SF) composites are known to inherently possess lower mechanical strength in comparison to long fibre (LF) composites [66]. From Fig. 82(a), the flexural strength of the SF 'non-woven mat' was slightly lower in comparison to the other virgin-based composites. Meanwhile, the LF end-of-life and reclaimed composites in Fig. 82(b) exhibited a comparably low strength in comparison to the other LF virgin alternatives.

It was previously highlighted in *Section 2.2.1.1* that there exist a number of possible factors that could influence the bend strength of CMC's. Aside from fibre architecture, which has already been addressed, these include: the manufacture process, fibre volume fraction and the preform architecture.

According to the literature, composites manufactured by CVI or LPI typically create composites with higher flexural strengths, in the range of 450-700 MPa (Table 10) and 330-500 MPa (Table 11), respectively. This compared to typical flexural strengths ranging between 160 and 300 MPa for LSI-derived composites, which was

also reported in Table 11. Therefore, if comparisons were made only between similarly manufactured composites in the LF category, as shown Fig. 82(b). Only the 'DLR Silica woven' composite would qualify, which possessed a comparable bend strength of 160 MPa.

In addition, differences in the flexural strength could be attributed to the higher porosity in comparison to the virgin samples, which are highlighted in Fig. 82. This could offer some support as to why the 'recycled non-woven mat' and 'reclaimed UD' samples exhibited the lowest strengths, because they possessed the highest porosities of about 12 and 23% respectively.

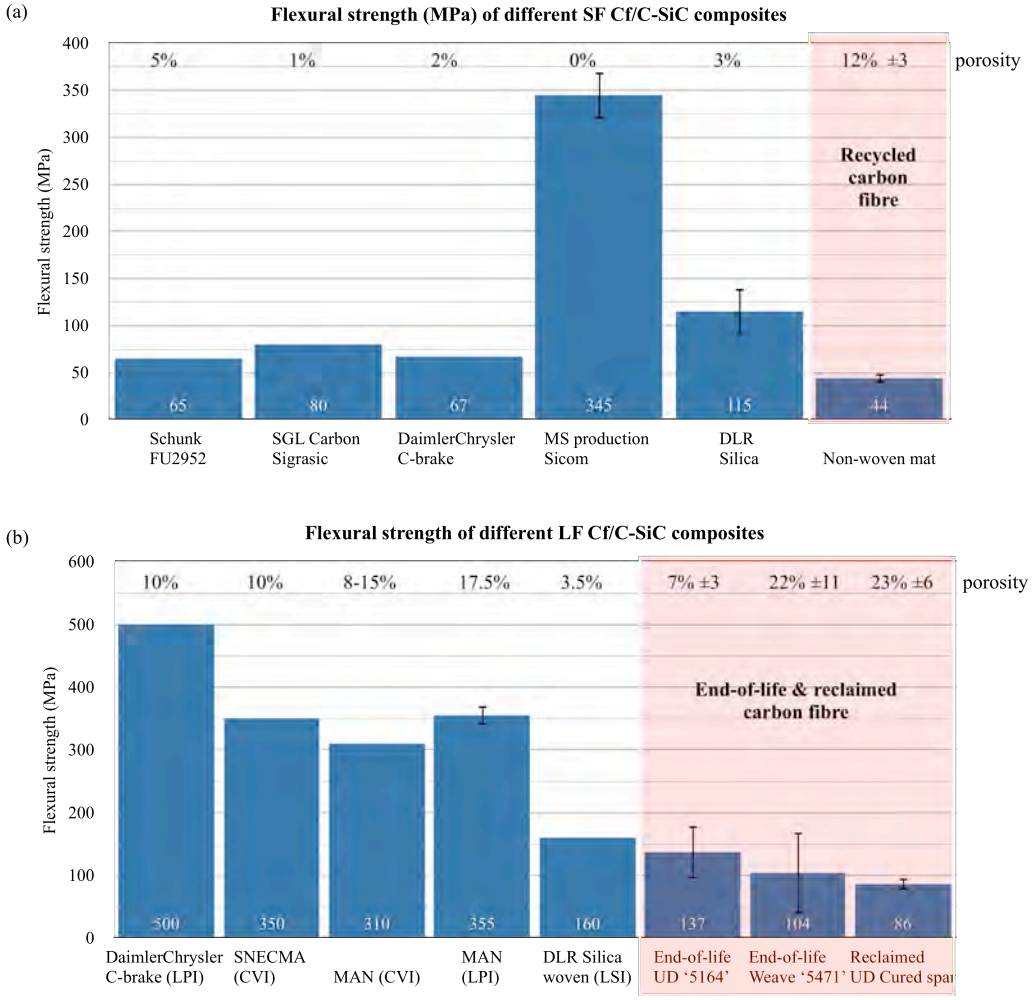

Fig. 82. Graphs showing the bend strength (MPa) of: (a) Virgin and recycled short fibre, and (b) Virgin and recycled long fibre C_f/C-SiC composites. All of the composites were siliconised by LSI, unless otherwise stated. Error bars represent the standard deviation [1, 14].

In terms of the impact of the fibre volume fraction, according to the data previously discussed in Table 10 and Table 11, several of the composites with higher fibre proportions still exhibited a lower flexural strength. Therefore, according to this data, the volume fraction alone does not dictate the flexural strength of the composite.

Meanwhile, variations in the fibre orientation are not likely to vary the strength of the SF composites. By contrast, the fibre orientation has a profound effect on LF composites, which could account for the observed differences between the composites in Fig. 82(b). This is due to the fact that all of the fibres in the UD pre-preg were under stress during bend testing, in comparison to only a proportion of the fibres inside the woven and reclaimed architectures that were bi-directional woven and 0/45/90 respectively.

Further support for the observed differences in the results could be gained by investigating force-displacement curves and breakage photos of these composites, whilst making comparisons to virgin alternatives. The curves and photos are shown in Fig. 83, which could be compared to the stress-strain curve of a virgin C_f/SiC in Fig. 14, taking into consideration the orientation of the UD fibres.

Failure was almost instantaneous for the randomly oriented ‘recycled non-woven mat’ and rapid for the ‘reclaimed carbon fibre’ sample. Meanwhile, the end-of-life UD and woven samples exhibited a characteristic non-catastrophic failure, in particular the woven composite. In fact, the profile of the end-of-life UD (Fig. 83(b)) and virgin UD (Fig. 14(b)) are orientated in the same manner and exhibited a very similar profile.

Evidence inside the photographs support these claims because there the ‘recycled non-woven mat’ exhibited a clean straight break without any of the characteristic fibre pull-out, which was evident from the remaining composites and the UD virgin C_f/SiC composite in Fig. 14(c). Differences between the end-of-life UD and reclaimed UD from the CFRP spar are attributed to the proportion of the orientated fibre in the parallel direction. All of the fibres inside the end-of-life UD composite were orientated in the parallel direction, as opposed to a significantly reduced proportion in the UD 0/45/90 orientated fibres of the inherited cured spar composite. As a consequence of the reduced number of fibres across the break, the recorded bend strength was lower. In addition, due to less evidence of fibre pull-out, failure was more rapid.

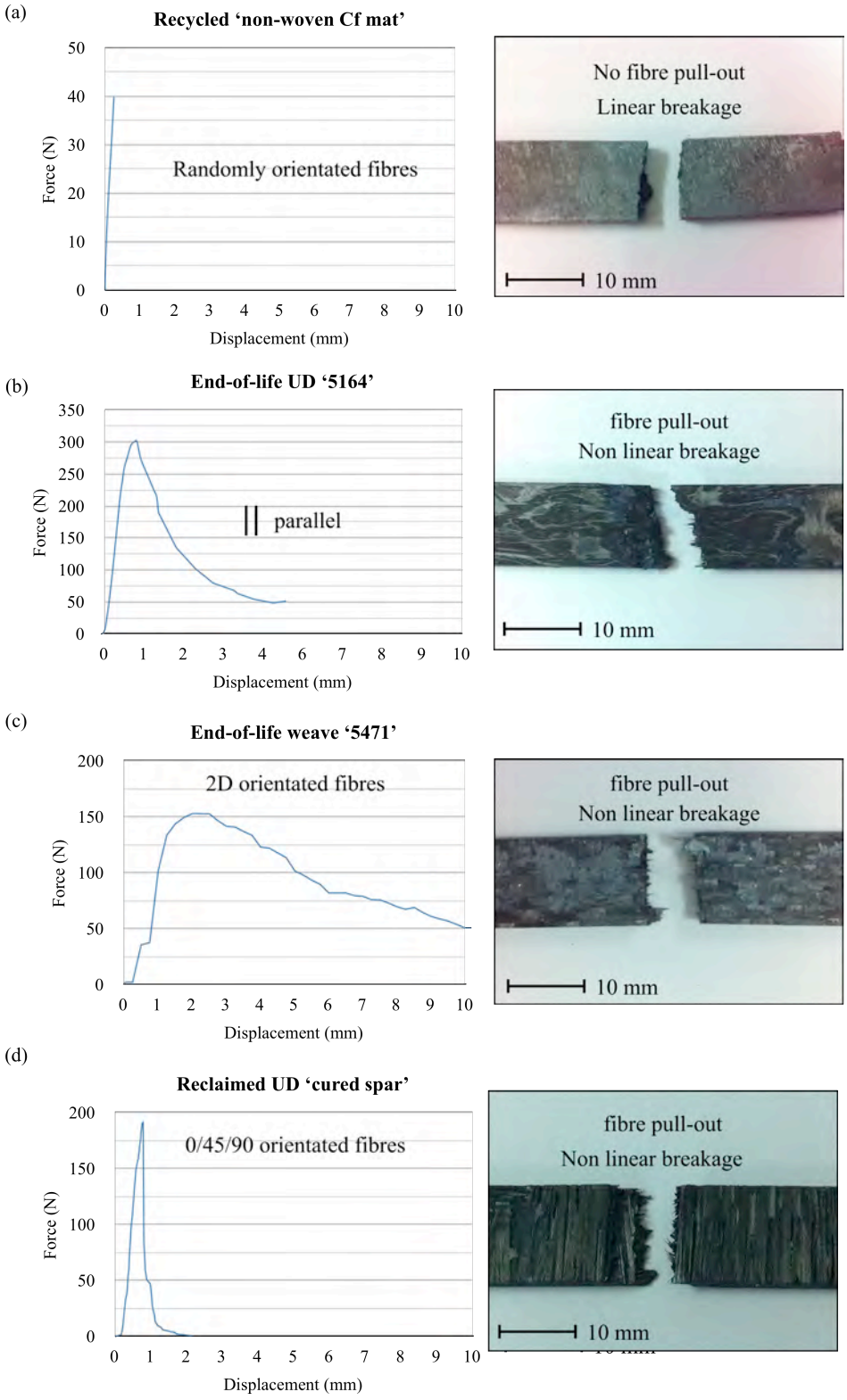

Fig. 83. Force-displacement graphs with supporting photographs comparing the failure modes of the different C_f/C-SiC composites: (a) Recycled 'non-woven mat', (b) End-of-life UD '5164', (c) End-of-life 2D weave '5471' and (d) Reclaimed UD 'cured spar'.

In summary:

- Bend strength testing revealed that C_f/C-SiC composites comprising waste carbon fibre could achieve comparable flexural strengths in comparison to similarly processed virgin alternatives. In addition, testing revealed that the perform architecture of the fibres affected the bend strength and failure mode of the composites.
- The recycled short fibre ‘non-woven mat’ composite exhibited a lower flexural strength in comparison to long fibre end-of-life woven and UD C_f/C-SiC composites.
- The ‘non-woven mat’ failed in a catastrophic manner. This was attributed to the very short fibres and possible incomplete densification by LSI, which left significant voids/porosity in the microstructure.
- In contrast, the long fibre composites exhibited a non-catastrophic failure, in particular the woven structure. This was attributed to fibre pull-out, which was observed in the breakage photographs and was not evident in any of the non-woven mat photos.
- The reclaimed CFRP spar fibre failed in a rapid but not catastrophic manner. The composite withstood a significantly greater force prior to failure in comparison to the non-woven mat composite. It is speculated that catastrophic failure was avoided due to the both the existence of fibre in the parallel direction and fibre pull-out, which was evident of in the photographs.

4.5. Friction trial

The aim of the friction trial was to investigate and make comparisons between the different C_f/C-SiC composites comprising virgin and end-of-life material in terms of their mechanical sustainability and friction behaviour. Three C_f/C-SiC composites were tested using a small-scale dynamometer in a disc-on-pad configuration. The raw materials used to construct these composites included: end-of-life 2D woven '5471' pre-preg and two virgin-derived 2.5D preforms 'ST'.

It was previously acknowledged that the friction mechanisms are complex, dynamic and completely dissimilar to the widely acknowledged mechanisms that occur for traditional cast-iron brake discs. Therefore, recent research focused on identifying the controlling mechanisms [55], which indicated the potential influence of the surface topography and modification of the friction surface that could affect the friction, frictional stability and wear characteristics. Therefore, the discs were imaged prior to dyno testing using an optical microscope and the proportions of the phases at the surface were quantified using image analysis software (Image-J). Relationships were then extrapolated between the dyno testing and the surface proportions of the phases at the surface prior to dyno testing.

Grayscale optical micrographs in Fig. 84 illustrate the generated topographical microstructures of each composite. The phases are identified as: C_f/C (dark grey), SiC (light grey), silicon (white), voids and cracks (black). The bar charts show the estimated proportions of each phase at the surface. The microstructures and surface proportions were very different. Sample '5471' comprised mainly woven C_f/C and void regions with a low mean silicon volume fraction of 0.92% ±0.16. After a single LSI, the estimated bulk density and open porosity was 1.5 g/cm^3 and 9% respectively.

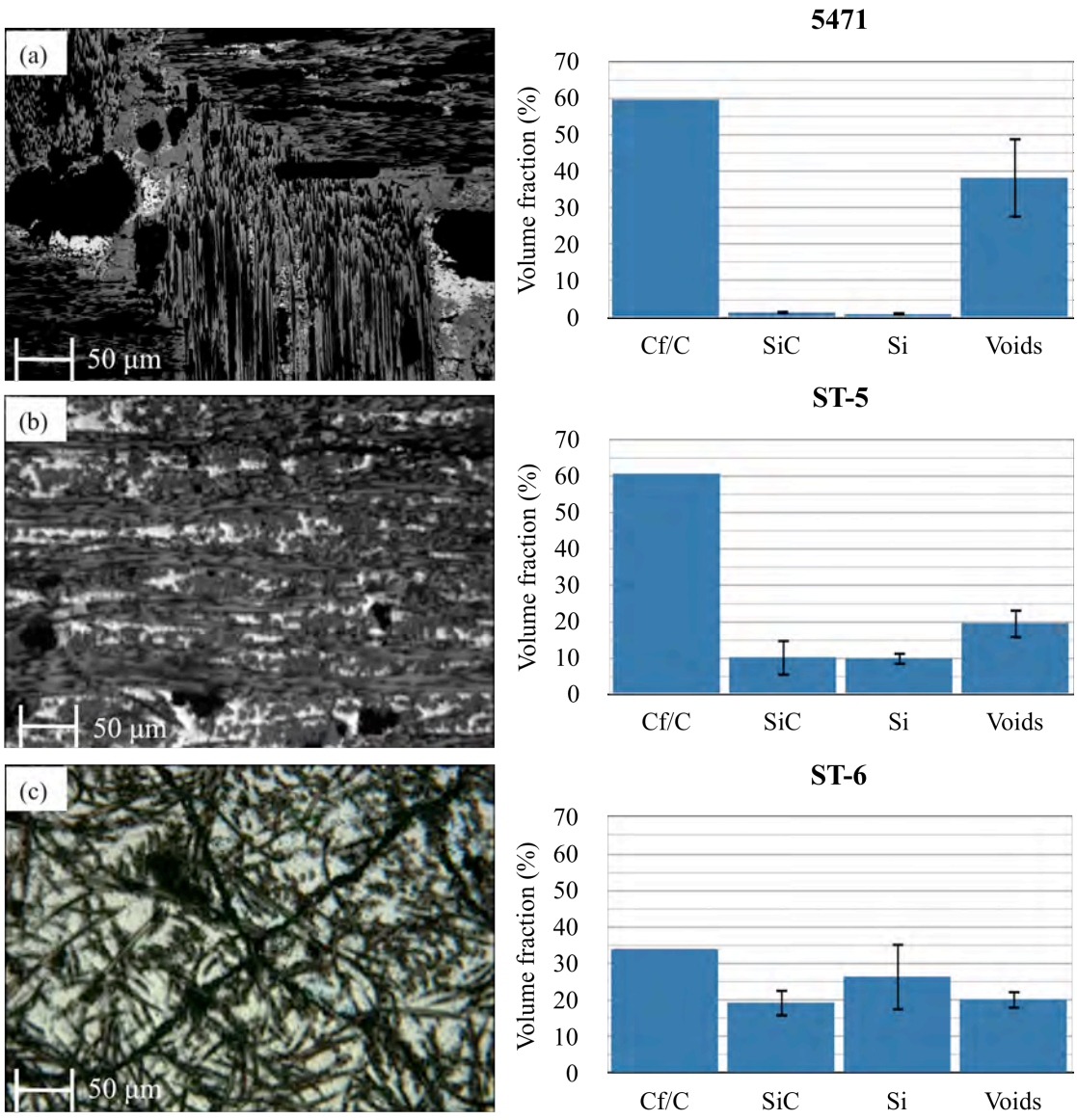

Fig. 84. Greyscale optical micrographs at 50x magnification under polarised light condition of (a) end-of-life 2D woven '5471', (b) virgin 2.5D 'ST'-5 and (c) virgin 2.5D 'ST'-6. Bar graphs illustrating the different estimated mean volume fractions (%) at the surface. Error bars represent the standard deviation.

Meanwhile, the virgin derived samples: 'ST-5' and 'ST-6' were siliconised a second time via LSI to promote the presence of SiC and silicon on the surface. Image analysis revealed that the estimated mean silicon proportions were 9.82% ±1.87 and 26.45% ±9.32 respectively. Notably, as the proportion of SiC and silicon increased, the C_f/C and voids both decreased. The COF profile for each disc-on-pad friction couple over 200 stops is shown in Fig. 85.

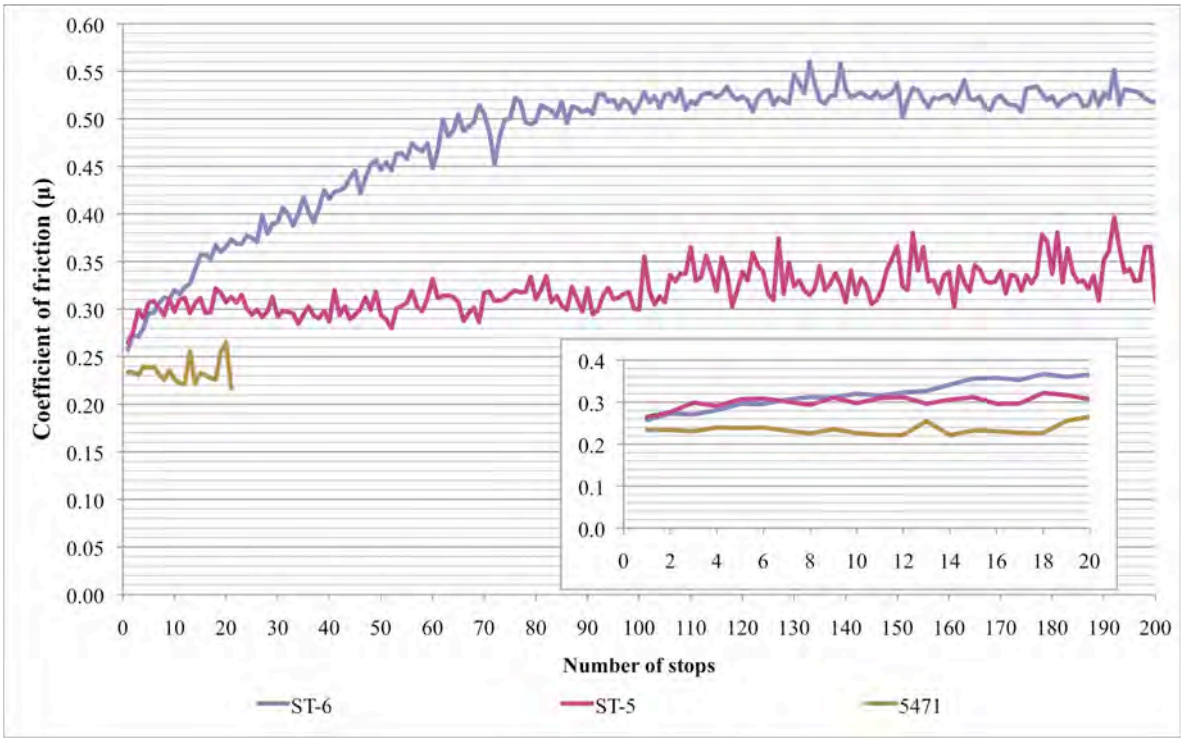

Fig. 85. Small-scale dynamometer testing of the different C_f/C-SiC composites over 200 stops. Inset are the three composites compared up to 20 stops, before 5471 testing ceased.

All three friction couples exhibited a low initial COF, between 0.24 and 0.26, which changed as testing continued. ST-5 rose slightly and then maintained a relatively stable COF over the 200 stops. By comparison, the ST-6 continued to rise gradually over the first 80 stops, before maintaining a relatively stable COF. Meanwhile, '5471' remained low until testing had to be ceased due to excessive wear of the pad and to some extent the disc. A photograph of the '5471' disc and pad is shown in Appendix A – Fig. 33. The pad was almost entirely consumed by the disc, which remained comparatively intact.

Whilst direct comparisons cannot be made to full-scale tests, it was previously identified in the literature review that automotive friction applications desire a sufficiently high and stable COF, of around 0.3-0.4; aerospace requires a stable COF of around 0.4; whilst industry also require a stable COF of approximately 0.3. This compares 0.2 to 0.6 for full-scale dyno testing reported in the literature, where a SiCralee^{TM} coated C_f/C-SiC disc-on-pad friction couple ranged between 0.4 and 0.55 [14]. The profiles, however, were quite different to the full scale testing reported in the literature [14, 19, 22]. This was expected considering the different scale, geometry of the

contact areas, forces used and lack of any surface coating.

Whilst there is no support in this investigation, one possible explanation for the ST-6 profile is the generation of third-party debris during a ‘bedding-in’ period, which built up in sufficient quantities and maintained on the surface. This could be related to the friction profile up to stop 80, where the COF rose to approximately 0.50. The COF then became relatively stable with an average COF of 0.52 until stop 200.

By contrast, a gradual increase in the COF was not obvious in the ST-5 or ‘5471’ friction profiles, which is likely attributed to the absence of any third-party dynamic friction layer on the surface. There is period within the first 5 stops of the ‘ST-5’ profile that could possibly be considered as a bedding-in stage. However, this period is unconventionally very short and would require careful examination of the surfaces after each stop to qualify any claim.

The apparent lack of a bedding-in period could be attributed to either an insufficient surface area for the layer to develop or inadequate properties of the phases. Referring back to the results in Fig. 84, ST-5 possessed almost double the C_f/C, half of the SiC and about 1/3 of the silicon content on the surface, in comparison to ST-6. ‘5471’ meanwhile comprised almost entirely C_f/C and voids, with a very small proportion of silicon and SiC. Therefore, the presence of either C_f/C and voids, or the silicon and SiC promoted the development and maintenance of the dynamic friction layer on the surface. However, considering that ‘5471’ had to be stopped due to its topographical microstructure i.e. high proportions of C_f/C and voids, the latter is more likely.

Therefore, based on speculation in this study and investigations elsewhere [55], this third-party dynamic friction layer could depend on two factors: the properties of the phases and the surface contact area. In this case, the properties of the phases could dictate two factors: firstly, how much of the disc or pad is broken off to create the third-party layer; secondly, how each phase at the surface of the disc and pad reacts to the evolving friction layer. For example, the debris could embed in soft phases or alternatively break up further into smaller debris by the harder phases. The properties of the phases inside C_f/C-SiC composites were investigated in *Section 4.3*, where it was identified that the carbon and pyC phases were very soft and elastic in comparison to the silicon and especially the SiC, which were much harder and stiffer.

Therefore, if the proportions of each material was roughly equivalent (for example in ST-6) a significant share of the load, perhaps proportional to the difference in the Young's modulus i.e. between 10 and 20 times could have been exposed to the silicon and SiC during braking. This additional force exposed to the silicon and SiC could have promoted more of each phase to fracture off and contribute to the third-party layer. Meanwhile, a sufficiently large surface area would be required for the dynamic layer to develop i.e. absence of any voids or cracks. At such a location, a bedding-in period could have been promoted, where the debris could mesh together creating such a dynamic friction layer.

According to the results in Fig. 84 and the COF profile, this was not evident for '5471'. Inside this sample, the carbon fibre and pyC would have acted as a 'ploughing tool'. This would have effectively cut into the pad, creating large quantities of third-party debris as the pad wore down. However, due to insufficient regions to maintain the debris on the surface, combined with the large proportions of voids and crack regions; any third-party debris would likely have been deposited inside such regions and not have contributed to the development or maintenance of the dynamic friction layer that would have promoted a bedding-in period.

The frictional stability (S) was calculated for each friction couple over all recorded stops using equation (1), where higher values are indicative of more stable and thus favourable friction profile. The results were 0.81, 0.88 and 0.89 for ST-5, ST-6 and 5471 respectively. This indicates that 5471 produced the most favourable and stable COF, although was only recorded over the first 20 stops as testing ceased. Therefore, each COF profile was also compared up to 20 stops, which was shown in Fig. 85(inset).

In this brief period, the COF of '5471' was comparatively stable, although was lower in comparison to ST-5 and ST-6 and did not reach a suitably high COF, in a similar respect to ST-5. However, if the previously identified 'bedding-in' period was omitted for ST-6 and 'S' was re-calculated for between stop 80 and 200. The frictional stability would increase from 0.88 to 0.96, now far in excess of ST-5 at 0.81, which would remain at 0.81 even if the 'bedding-in' period of 5 stops was accounted for in a similar re-calculation.

In summary:

- After a single PIP and LSI, the density was of the end-of-life C_f/C-SiC composites '5471' was comparatively low at 1.5 g/cm^3, although did not fail during friction testing, which is a testament to the mechanical sustainability of the composite.
- The surface proportions of the phases seemed to have a significant influence on the wear rate and friction characteristics of the friction couples.
- After a gradual increase in the COF, which could be considered as a bedding-in period, ST-6 exhibited a higher and more stable COF. This was attributed to its apparent surface contact area and balanced surface proportions, which were observed in optical micrographs. The existence of such a surface topography is suspected to have permitted the development and maintenance of a dynamic friction layer comprising third party debris.
- By contrast, ST-5 did not exhibit a gradual increase in the COF, which remained comparatively low and became increasingly unstable as testing continued. This was attributed to the unbalanced surface proportions, in particular the significantly higher proportions of C_f/C, which is suspected to have acted like a ploughing tool; preventing the development and maintenance of a dynamic friction layer.
- The friction results of '5471' were not favorable in this trial. However, this is not necessarily representative of its potential, but rather indicative of the necessity to: increase the surface content of the phases, for example by increasing the number of LSI infiltrations; or introduce a suitable surface coating.

5. Summary

A range of new recycled C_f/C-SiC composites were successfully manufactured that comprised three unique categories of carbon fibre: recycled, end-of-life and re-claimed; in addition to different formats of pyrolytic carbon (pyC) derived from pyrolysis of virgin phenolic resin and end-of-life epoxy from inside carbon fibre pre-pregs. The composites were manufactured in a rapid and cost-effective three-step process: polymer infiltration and hot pressing to create the CFRP, pyrolysis to convert the CFRP into a porous C_f/C composite and liquid silicon infiltration to introduce the SiC matrix. Manufacturing revealed that a desired preform architecture could be either customised or maintained from an original CFRP spar.

End-of-life carbon fibre pre-pregs were used to investigate the characteristics of the preform after pyrolysis and their development into C_f/C-SiC composites: evolution of the microstructure; mechanical properties of the phases; physical and bulk properties; mechanical properties; friction characteristics, where comparisons were made to virgin based C_f/C-SiC composites. The key outcomes are discussed.

5.1. C_f/C development

- After pyrolysing different unidirectional (UD) and woven end-of-life and virgin carbon fibre pre-pregs at temperatures between 300 and 900°C, there was no discernible difference in the carbon fibre tow architecture or fibre architecture.
- Using a heat rate of 5°C/min, the maximum rate of weight loss and corresponding rate of pyrolysis was observed to be between 300 and 400°C for both the end-of-life and virgin pre-pregs.
- Any geometric change in the length, width, and thickness of the pre-pregs during pyrolysis was inhibited in the direction of the carbon fibres. All of the pre-pregs, irrespective of their origin exhibited a dimension change in the perpendicular direction to the fibre orientation. The woven pre-pregs were essentially restricted in both the length and width directions, therefore were observed to ‘bunch up’ and effectively ‘kink’ through a series of expansions and contractions as the pyrolysis temperature increased.
- After pyrolysis at 900°C, individual fibres inside the pre-pregs were observed to fray (spread out) at the ends of each tow, irrespective of the fibre origin: virgin or

end-of-life, resin type or resin quantity.

- Pyrolysis investigations in this study revealed that end-of-life and reclaimed CFRP's were suitable for pyrolysis and further processing toward C_f/C-SiC composites.

5.2. C_f/C-SiC development

- C_f/C-SiC composites manufactured by LSI create the same hierarchy order of the developed microstructure, irrespective of the fibre origin: virgin, recycled, end-of-life or reclaimed; or carbon source: virgin PIP-derived pyC, virgin CVI-derived carbon or end-of-life PIP-derived pyC. This hierarchy was: carbon fibre (C_f) as either single filaments or bundles, pyC or CVI derived carbon, SiC, Si, silicon islands, voids and grain boundaries.
- The volume proportion (%) of the phases: C_f/C, SiC, silicon and voids generated inside these C_f/C-SiC composites via a single liquid silicon infiltration (LSI), indicated the following trends according to the architecture: a non-woven short fibre architecture created minimal SiC and silicon, with large C_f/C and void regions; UD architectures favoured C_f/C regions and low SiC formation with minimal voids; 2D woven architectures promoted a more balanced proportion of each phase, especially SiC; 2D architecture with Z-needling (2.5D) similarly promoted balanced proportions, although favoured C_f/C due to the additional fibre Z-needling.
- Optical and TEM micrographs showed that PIP-derived pyC of epoxy did not sufficiently coat all of the carbon fibres. Consequently, some fibres were clearly siliconised by the silicon melt during LSI. This could be attributed to a low proportion of resin inside the pre-preg and/or a low carbon yield of the resin. TEM micrographs illustrated that the thickness of the PIP-derived pyC was as low as 0.5 micrometres.
- In contrast, PIP-derived pyC from phenolic generated thicker carbonaceous interfaces (PyC) in comparison to PIP-PyC from epoxy and CVI-derived carbon. According to TEM micrographs, the thickness of PIP-pyC from phenolic varied between approximately 5 and 8 micrometres after a single PIP and around 5 micrometres for CVI-derived carbon derived from cracked methane.
- The thickness of the generated SiC layer was proportional to the thickness of the

carbon interface, where thicker pyC or carbon created thicker SiC layers.

- Optical microscopy revealed that enclosed areas of pyC or carbon with a larger contact surface area promoted the formation of greater proportions of SiC.
- Differences in the SiC thickness inside this study were attributed to differences in the structure and morphology of the carbon. TEM SAD patterns indicated differences in the size and orientation of the carbon, where: CVI-derived carbon was very small and practically isotropic; PIP-derived pyC from virgin phenolic and end-of-life epoxy were very similar, possessing some preference in orientation with larger units in comparison to CVI-carbon; commercial graphite possessed larger graphite units in a more preferred orientation in comparison to the pyC and CVI-carbon. In addition, TEM micrographs revealed that the morphology of the carbon differed: CVI-derived carbon was observed to be dense, pyC and graphite contained meso-scale porosity. The range of the porosity inside the graphite extended several micrometres.
- Meso-scale particles could be seen inside TEM micrographs of the PIP-derived pyC and graphite interface, which was attributed to the meso-scale porosity. The presence of these particles was supported using centred dark field (CDF) micrographs inside the TEM. There was no evidence of these particles inside the CVI-derived carbon, which was attributed to the dense carbon structure as a result of the gradual deposition manufacture. TEM SAD patterns indicated that these particles were SiC and were suspected to have formed due to silicon vapour that infiltrated the pyC and graphite at temperatures prior to and during LSI at 1414°C.
- Combined TEM SAD and XRD investigations indicated that the bulk SiC and silicon belonged to the same polytypes regardless of the carbon format: end-of-life pyC, virgin pyC, virgin CVI-C or industrial grade graphite, and that the most likely type was face-centered cubic (FCC) β 3C-SiC and cubic silicon respectively.

- Nano-indentation using a Berkovich indenter, under a load of 100 mN and loading rate of 2.5 $mN.s^{-1}$ was used to investigate and make comparisons between the hardness (GPa) and Young's modulus (GPa) of the phases inside three different composites. These included: end-of-life PAN carbon fibre and virgin PAN-OX carbon fibre; end-of-life PIP-derived pyC, virgin PIP-derived pyC and

virgin CVI-derived carbon; the subsequently generated SiC and silicon by method of LSI.

- According to force-depth curves and supporting FEG-SEM micrographs, there was: minimal difference between virgin and end-of-life PAN-based carbon fibre. FEG-SEM micrographs of the indentations were very faint due to the very low plastic deformation that ranged between 128 and 161 nm; minimal difference between virgin CVI-C and end-of-life pyC. The plastic deformation was similarly very low, in the range of 78 to 156 nm. Consequently, some of the indentations were indistinguishable; negligible difference between the resulting SiC and silicon. The plastic deformations were significantly larger ranging between 184 and 236 nm for the SiC and 332 and 384 nm for the silicon.
- As a consequence of the highly elastic behaviour of the C_f, pyC and CVI-carbon inside all of the composites, none of these phases failed or cracked during indentation. Increasing the indentation force to 250 and 400 mN whilst maintaining the same loading rate did not result in any cracks inside the end-of-life PIP-derived pyC. In contrast, cracks were evident in some of the SiC and silicon micrographs. There was no preferential crack pattern evident as cracks propagated from both the edge and corner of the indentations.
- The estimated hardness (GPa) and Young's modulus, E (GPa) of the phases were comparable and in accordance with other researchers, where data was available. All of the tested carbon fibre, PIP-derived pyC and CVI-carbon were much softer and more elastic in comparison to the SiC and silicon. Measurements inside the SiC were variable, which could be attributed to differences in the size or orientation of the SiC crystal, perhaps as a result of LSI-manufacture.
- Under a load of 100 mN and loading rate of 2.5 $mN.s^{-1}$, all of the indentations into the silicon exhibited a characteristic pop-out phenomenon. Increasing the force to 200 mN still resulted in pop-out. No determining mechanism was found in this study.
- Indentations inside the SiC and silicon that cracked permitted the use of the indentation fracture method to estimate the fracture toughness (K_{1C}, $MPa.m^{1/2}$) of these phases. The toughness was comparable and varied between approximately 0.71 and 1.16 $MPa.m^{1/2}$ for SiC, and between 0.54 and 0.66 for silicon.

- Physical and mechanical property testing revealed that C_f/C-SiC composites

incorporating: recycled, end-of-life and re-claimed carbon fibre could achieve comparable densities, open porosities and bend strengths in comparison to similarly processed LSI virgin C_f/C-SiC composites (as reported by DLR). The achieved open porosities and bulk densities for these composites are highlighted in Table 15 and Table 16 respectively.

Table 15. Achieved open porosity (%) at the CFRP stage, LSI and 2nd LSI stage.

Fibre category	Fibre type	Arch.	Matrix	CFRP	1st LSI	2nd LSI
Recycled	Mixed*	Non-woven short fibre	PIP-PyC + LSI-SiC	17.57± 2.67	10.30± 2.50	12.57± 3.22
End-of-life pre-preg (UD)	AS4-12K	UD		13.47± 7.13	5.17± 3.19	7.22± 3.14
End-of-life pre-preg (weave)	AGP280-3K	2D		24.91± 5.22	8.77± 3.09	22.61± 11.10
Reclaimed UD	AS4-12K	0/45/90		26.32± 6.17	16.65± 5.66	22.92± 6.21

Table 16. Achieved bulk density (g/cm^3) at the CFRP stage, LSI and 2nd LSI stage.

Fibre category	Fibre type	Arch.	Matrix	CFRP	1st LSI	2nd LSI
Recycled	Mixed*	Non-woven short fibre	PIP-PyC + LSI-SiC	0.91± 0.27	0.65± 0.12	1.38± 0.23
End-of-life pre-preg (UD)	AS4-12K	UD		1.39± 0.10	1.67± 0.02	1.92± 0.40
End-of-life pre-preg (weave)	AGP280-3K	2D		1.44± 0.17	1.96± 0.11	2.28± 0.20
Reclaimed UD	AS4-12K	0/45/90		1.08± 0.11	1.92± 0.12	2.13± 0.15

- Small-scale dyno testing of small C_f/C-SiC composites in a disc-on-pad configuration revealed that composites comprising end-of-life fibre could achieve the required mechanical strength and sustainability to perform dyno testing. A surface contact pressure of 1 MPa was sought and achieved using a load of 550 N according to the contact surface area of the pad.
- Testing revealed that the surface topography had a significant influence on the coefficient of friction (COF), COF stability and wear rate. The following phenomenon were evident: High surface proportions of C_f/C and voids at the surface were detrimental to the wear rate of the standard organic pad; high surface proportions of C_f/C in the 60% range with approximately 10% SiC and Si with approximately 20% voids generated a comparatively stable COF of around 0.3;

when more balanced proportions of the phases: C_f/C, SiC, Si and voids, between 20 and 35% were present at the surface, a characteristic bedding-in period was observed, which was characterised as the gradual increase of the COF, followed by a higher COF of approximately 0.52. This bedding-in period could be attributed to the development and maintenance of a third-party friction layer in between the disc and pad.

- These results indicate that if a high and stable COF is to be achieved, a traditional third-party friction layer should develop and be maintained at the surface in between the disc and pad. The development of this layer could be facilitated by the presence of comparatively soft phases such as C_f/C at the surface. However, combinations of both C_f/C the voids should be avoided, where a significant surface void content may deposit the layer and inhibit its maintenance.

5.3. Project achievements

Based on the target baseline properties previously highlighted at the end of the literature review in Table 13, the property achievements of the manufacturing process and different origins of fibre are summarised in Table 17. Any unsuccessful aspects are discussed in *Section 6*.

Table 17. Project achievements

Property	Requirements	Achievements
Recyclability	• Carbon fibre source should be predictable and the potential supply recognised.	✓ Supply from Airbus was predictable.
	• History of the fibre should be traceable.	✓ History of the fibre was traceable.
	• The length of any recovered fibres should be maintained. Minimum length of >5.5mm should be sought to maintain mechanical properties.	✓ Achieved for end-of-life UD and woven, and reclaimed UD C_f/C-SiC ✗ Recycled short fibre was cut too short.
	• Recycling process should aim to recover clean fibres; fibres without any residual carbon or damage.	✗ Recycled fibre possessed residual pyC and was likely oxidised during semi-closed pyrolysis
	• Recycling process should limit any toxic emissions.	✗ Emission of pyrolysis gases. Although, varies according to the polymer matrix material.
Manufacture	• Needs to be capable of being machined to circumferential parallelism.	✓ Achieved
Physical	• Porosity (%) should be as low as possible in order to promote the mechanical strength e.g. bend strength, and thermal conductivity	✓ Achieved porosities between 5 and 23% for recycled, end-of-life and reclaimed C_f/C-SiC.
	• Target density of at least 1.8 g/cm^3 for an automotive disc	✓ Achieved for the end-of-life woven and reclaimed fibre after 1x LSI ✓ Achieved for the reclaimed UD fibre after 2x LSI ✗ Not achieved for the recycled short fibre C_f/C-SiC.
	• Target density of at least 2.1 g/cm^3 for an aerospace disc	✓ Achieved for the end-of-life woven and reclaimed fibre after 2x LSI. ✗ Not achieved for the recycled short fibre C_f/C-SiC or the reclaimed UD C_f/C-SiC after 2x LSI.
Mechanical	• Target density less than grey cast iron, 7.2 g/cm^3 for an industrial disc.	✓ Achieved for all of the C_f/C-SiC composites.
	• Bend strength of 100 MPa for an aerospace application.	✓ Achieved for end-of-life UD and woven C_f/C-SiC. ✗ Not achieved for the reclaimed UD fibre C_f/C-SiC. ✗ Not achieved for the recycled short fibre C_f/C-SiC.
	• Should withstand a pressure of 1 MPa for dyno testing.	✓ Achieved for the end-of-life woven C_f/C-SiC. ✓ Achieved for the virgin 2.5D C_f/C-SiC.
Tribological	• COF between 0.3 and 0.4 for an automotive disc with a pad	✓ Achieved for the virgin 2.5D C_f/C-SiC with a high proportion of C_f/C at the surface. ✗ Not achieved by the end-of-life woven C_f/C-SiC.
	• COF between 0.7 and 0.8 for industrial disc	✗ Not achieved by any C_f/C-SiC.
	• COF of around 0.4 for aerospace applications.	✓ Achieved for the virgin 2.5D C_f/C-SiC with a high proportion of C_f/C at the surface. ✗ Not achieved by the end-of-life woven C_f/C-SiC.
	• COF for all applications should be predictable and stable.	✓ Achieved for virgin 2.5D C_f/C-SiC with balanced proportions of phases at the surface. ✗ Not achieved by the end-of-life woven C_f/C-SiC.
	• No additional wear of the pads at temperatures above 250°C.	✓ Achieved for both virgin 2.5D C_f/C-SiC composites; with a high proportion of C_f/C and balanced proportions of the phases at the surface. ✗ Not achieved by the end-of-life woven C_f/C-SiC.
Cost	• Manufacture process should be rapid to improve the economy.	✓ Achieved for all of the C_f/C-SiC composites.
	• The disc needs to be economically machined, in a short period with minimal tool wear.	✓ Achieved for all of the C_f/C-SiC composites.

6. Suggestions

Due to the time constraints when undertaking any project, there will always be outstanding questions that could be further investigated. Table 17 highlights the successes and opportunities for further development.

In this study, the recycling technique developed and used by Milled Carbon Ltd was not flexible. However, by increasing the fibre length and pyrolysing in a fully inert atmosphere could promote the mechanical properties of the fibres inside the composite and minimise any risk of oxidation. Increasing the length of the fibres could also have a positive impact on the physical properties of the final composite. For example, reducing the open porosity and improving the bulk density. Meanwhile, the 0/45/90 orientation of the fibres inside the reclaimed UD C_f/C-SiC could be re-orientated to an aligned UD architecture that would likely improve the mechanical bend strength, highlighted as a failure in Table 17.

Whilst a number unique carbon fibre sources were investigated, other composites originating from different recycled matter and processes could also be tested. For example the C_f/C disc developed by MABS that was manufactured using hot pressing and CVI. This disc could instead be only partially densified by CVI and converted into a C_f/C-SiC using LSI. The physical, mechanical and tribological properties of this and other composites should then be tested and compared to the results reported in this study. For example, the bulk fracture toughness and COF testing in wet conditions, in addition to investigating the wear rate.

In addition to the work that has already been achieved in this report, a subsequent scale-up methodology is being proposed, which is illustrated in Fig. 86. The first task is to identify a sustainable supply of carbon fibre and implement a suitable recycling process to recover long fibres. Once the fibre has been recovered, the manufacture process can be scaled-up using equipment capable to producing full size discs, which will primarily include a furnace. The next step is to replicate the desired microstructure of the laboratory scale composites, which can then be tested in a feedback loop to the recycling process and manufacture.

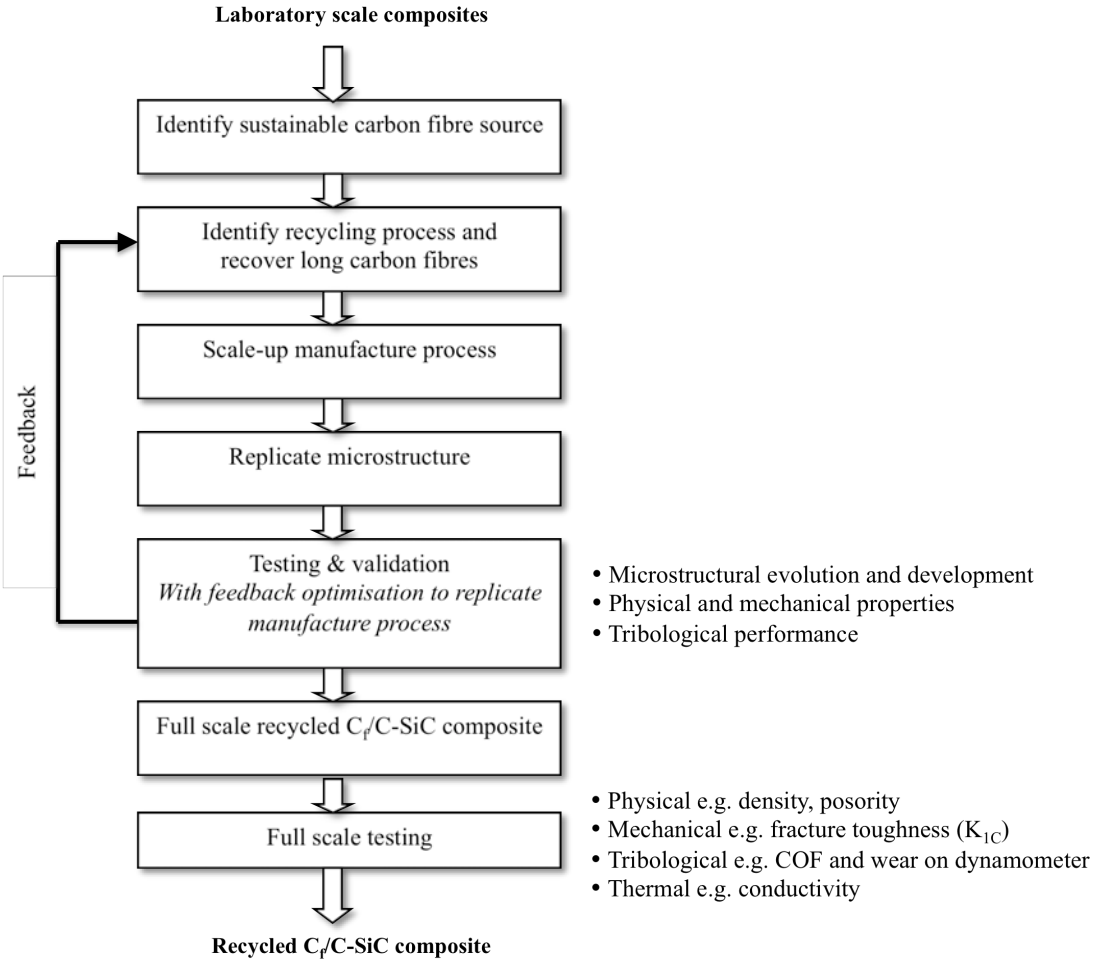

Fig. 86. Flow chart describing the potential scale-up methodology for producing a full-scale recycled C_f/C-SiC composite.

The two main issues that were identified by the consortium members who attempted to manufacture full-scale C_f/C-SiC comprising recycled fibre was achievement of an insufficient density and delamination. It is suspected that a sufficient density was not reached because of the unfamiliar and unpredictable preform architecture and densification process.

Supportive techniques that could be employed include: mercury porosimetry, BET, X-ray CT-Scanner or X-ray micro-tomography (XMT). Mercury porosimetry or the BET method could permit more accurate measurements of the porosity inside the carbon structure and final C_f/C-SiC composite. X-rays could be used to determine a number of parameters. For example, quantifying the connecting and non-connecting porosity, which would be useful in understanding both the gas and liquid phase processing, including the infiltration kinetic mechanisms of LSI. In addition, the X-ray data could be used to identify any flaws, impurities and cracks inside the

composite. This information could be used to modify the parameters of the manufacture process in order to reduce the flaws. Meanwhile, the crack paths could be traced and any beneficial or detrimental phases or interfaces could be identified.

Furthermore, the X-ray data could be transferred directly into the microstructural finite element analysis (FEA) model to predict the bulk properties. A combination of existing FEA programs, such as ‘TexGen’, ‘PATRAN’ and ‘NASTRAN’ could be used to model the impregnation of a polymer during PIP or alternate melt, predict the development or even the evolution of the matrix and mechanical properties. This combination could present a more accurate method compared to existing theoretical models, which are also unable to model and physical or mechanical properties.

Meanwhile, the composites likely delaminated because of the high proportions of the silicon that were infiltrated and expanded during cooling in combination with no vertical (z) needling to inhibit any movement. This could be solved by introducing a third dimension into the composites, for example by Z-needling or the introduction of a fibre web. Once a successful full-scale composite has been achieved, full-scale mechanical and tribological testing can ensue with complimentary ‘real’ testing on the desired application when sufficient properties are achieved.

7. References

1 S. Fouquet, M. Rollin, R. Pailler & X. Bourrat, Tribological behaviour of carbon fibres and ceramic matrix in the Si-C system, *Wear* **264**, 850-856 (2007).

2 J. D. Holme, Disk brake rotor with grey cast iron composition, European Patent EP1034317, (2002).

3 W. Krenkel, R. Renz & T. Henke, Ultralight and wear resistant ceramic brakes, *Mat. for Trans. Tech.*, 89-94 (2005).

4 W. Krenkel, CMC Materials for High Performance brakes, *ISTA Con. on supercars*, 769-775 (1994).

5 W. Krenkel, B. Heidenreich & R. Renz, C/C-SiC Composites for Advanced Friction Systems, *Adv. Eng. Mat.* **4** [7], 427-436 (2002).

6 R. L. Hecht, R. B Dinwiddie & H. Wang, The effect of graphite flake morphology on the thermal diffusivity of gray cast irons used for automotive brake discs, *J. of Mat. Sci.* **34**, 4775–4781 (1999).

7 T. C. Chatterley & M. P. Macnaughtan, Cast Iron Brake Discs - Current Position, Performance & Future Trends in Europe, *SAE Journal* 1999-01-0141 USA (1999).

8 K. Uchida, T. Sato, Y. Kawakami, S. Nishida & N. Hattori, Thermal conductivity of carbon fiber/metal matrix composite prepared by P/M process, *Nippon Kikai Gakkai Kikai Zairyo* **11**, 159-160 (2003).

9 G. Fu, L. Liang, J. Liu & Y. Wang, Fabrication and properties of Al matrix composites strengthened by in situ alumina particulates, *J. of University of Sci. & Tech. Beijing, Mineral, Metallurgy* **13**, [3], 263-266 (2006).

10 R. Duval & E. Lherm, Methods of Manufacturing Carbon-Carbon Composite Brake Discs, US Patent 6183583B1 (2001).

11 B. Wielage, A.G. Odeshi, H. Mucha, H. Lang & R. Buschbeck, A cost effective route for the densification of carbon-carbon composites, *J. of Mat. Processsing Tech.* **132**, 313-322 (2003).

12 W. Kowbel, V. Chellpa, & J. C. Withers, Properties of C/C composites produced in one low cost manufacturing step, *Carbon* **34**, [6] 819-821 (1996).

13 R. Weiss, Carbon fibre reinforced CMCs: Manufacture, properties, oxidation protection, *4th Int. Con. on High Temp. Ceram. Matrix Comp.*, Wiley, Germany, 440-456 (2001).

14 W. Krenkel & F. Berndt, C/C–SiC composites for space applications and advanced friction systems, *Mat. Sci. & Eng.* **A 412**, 177–181 (2005).

15 B. K. Yen & T. Ishihara, The surface morphology and structure of carbon-carbon composites in high energy sliding contact, *Wear* **174**, 112 (1994).

16 Z. Stadler, K. Krnel & T. Kosmac, Friction behaviour of sintered metallic brake pads on a C/C–SiC composite brake disc, *J. of the Euro. Ceram. Soc.* **27**, 1411–1417 (2007).

17 W. Krenkel, Carbon fiber reinforced CMC for high-performance structures, *Int. J. of App. Ceram. Tech* **1**, [2] 194-200 (2004).

18 W. Krenkel, Design of ceramic brake pads and disks, *Ceram. Eng.& Sci. Pro.* **23** [3], 319-330 (2002).

19 S. W. Fan, Y. D. Xu, L. T. Zhang, L. F. Cheng, L. Yu, Y. D. Yuan, F. K. Zhang, G. L. Tian, Z. J. Chen & J.J. Lou, Microstructure and properties of 3D needle-punched carbon/silicon carbide brake materials, *Comp. Sci. & Tech.* **67**, 2390-2398 (2007).

20 P. Xiao, Z. Li, Z. Zhu & X. Xiong, Preparation, properties and application of

C/C-SiC composites fabricated by warm compacted-in-situ reaction, *J. of Mat. Sci. Tech.* **26**, [3] (2010)

21 W. Krenkel, J. M. Hausherr, T. Reimer & M. Frieβ, Design, manufacture and quality assurance of C-C-SiC composites for space transportation systems, *Ceram. Eng.& Sci. Pro.* **25**, [4] 49-58 (2004).

22 Y. Zhang, Y. Xu, J. Lou, L. Zhang & L. Cheng, Braking Behavior of C/SiC composites prepared by chemical vapor infiltration, *Int. J. App. Ceram. Tech.* **2**, [2] 114-121 (2005).

23 K. Kristoffer, S. Zmago & K. Tomaz K, Preparation and properties of C/C–SiC nano-composites, *J. of the Euro. Ceram. Soc.* **27**, 211–1216 (2007).

24 V.K. Srivastava & K. Maile, Measurement of critical stress intensity factor in C/C–SiC composites under dynamic and static loading conditions, *Comp. Sci. & Tech.* **64**, 1209–1217 (2004)

25 W. Krenkel & T. Henke, Design of high performance CMC brake discs, *Key Eng. Mat.* **164-165**, 421-424 (1999).

26 J. Y. Paris, L. Vincent & J. Denape, High speed tribological behaviour of a carbon/silicon carbide composite, *Comp. Sci. & Tech.* **61**, 417 (2001).

27 W. Krenkel, C/C-SiC composites for hot structures and advanced friction systems, *Mat. Sci. & Eng.* **412**, [1-2], 583-592 (2005).

28 J. R. Hyde, E. Lester & S. Kingman, Supercritical propanol, a possible route to composite carbon fibre recovery: A viability study, *Comp.* **37**, 2171–2175 (2006).

29 W. Lui, S. Sun, M. Li & Y. Wei, The preparation of C/C-SiC nanomatrix composites by chemical vapour infiltration, *J. of Mat. Sci. Lett.* **12**, 886-888 (1993).

30 Rey *et al*, Method of densifying a porous substrate by chemical vapor infiltration of silicon carbide, Patent number: 5738908 (1998).

31 R. Naslain, Design, preparation and properties of non-oxide CMCs for application in engines and nuclear reactors: an overview, *Comp. Sci. & Tech.* **64**, 155-170 (2004).

32 W. Krenkel, Carbon fibre reinforced Silicon Carbide composites (C/SiC, C/C-SiC), Handbook of Ceramic Composites, Springer US, 117-148 (2005).

33 W. Krenkel, Cost effective processing of CMC composites by melt infiltration (LSI-process), *Ceram. Eng. & Sci. Pro.* **23** [3], 443-454 (2001).

34 S. Han, D. W. Seo, S. Lee. W, K. S. Hong, S. K. Woo, Y. H. Chung & J. C. Lee, Preparation and morphology of C/C-SiC Composites by Si melt infiltration, *Key Eng. Mat.* **317-318**, 119-124 (2006).

35 W. Krenkel, H. A. El-Hija & M. Kriescher, High performance C/C-SiC brake pads, *Ceram. Eng. & Sci. Pro.* **25**, [4] 191-196 (2004).

36 Y. Ding, S. Dong, Q. Zhao, Z. Huang & D. Jiang, Preparation of C/SiC composites by hot Pressing, using different Cfiber content as reinforcement, *J. of Am. Ceram. Soc.* **89**, 1447–1449, (2006).

37 M. Kermc, Z. Stadler & M. Kalin, Surface temperatures in the contacts with steel and C/C-SiC composite brake discs, *J. of Mech. Eng.* **50**, 346-359 (2004).

38 European end-of-life vehicle directive: Directive 2000/53/EC on end-of-life vehicles. 2000/53/EC, 34-42 (2000).

39 Department of business innovation and skills, The UK Carbon Fibre Composites Industry: Market profile, Net composites (2009).

40 Bosch, Automotive Hand Book 6th Edition SAE, 807 (2004).

41 Bentley website: http://www.bentleymotors.com/models/mulsanne/detailed_specification/ (last accessed 2010).
42 P. J. Blau & H. M. Meyer, Characteristics of wear particles produced during friction tests of conventional and unconventional disc brake materials, *Wear* **255**, 1263 (2003).
43 Sepcarb brakes assistance manual, carbonne industry, France
44 Website: http://www.hitcoracing.com/racing.htm (last accessed 2010).
45 J. R. Gomes, J. R, Silva O.M, Silva C.M, Pardini L.C & Silva R.F, The effect of sliding speed and temperature on the tribological behaviour of carbon-carbon composites, *Wear* **249**, 240-245 (2001).
46 Hitco Carbon website: http://www.hitco.com/ © 2008 (last accessed 2010).
47 Messier-Bugatti Safran Group PDF: http://www.messier-bugattiusa.com/IMG/pdf/pressfile2007en.pdf (last accessed 2010).
48 W. Krenkel & R. Kockendorfer, Brake disk for disk brakes, Patent number: 6308808 B1 (2001).
49 Z. S. Pak, C_f/SiC/C composites for frictional application, *4th Int. Con. on High Temp. Ceram. Matrix Comp.*, Germany, 820–825 (2001).
50 Website: Surface Transforms Plc: http://www.surface-transforms.com/ (last accessed 2010)
51 SGL Carbon Group website: http://www.sglcarbon.com/sgl_t/brakedisc/products/auto.html (last accessed 2010).
52 DLR website: http://www.dlr.de/bk/en/desktopdefault.aspx/tabid-2499/6930_read-10079/ (last accessed 2010)
53 Schunk website: http://www.schunk-group.com/en/sgroup/press/archive/schunk01.c.35390.de (last accessed 2010).
54 SGL Carbon Group website: http://www.sglcarbon.com/sgl_t/fibers/pdf/panox_e.pdf (last accessed 2010).
55 H. Wu & Y.Wang, Friction surface evolution of carbon fibre reinforced carbon/silicon carbide (C_f/C-SiC) composites, *J. of the Eu. Ceram. Soc.* **30**, [15] 3187-3201 (2010).
56 S .Vaidyaraman, M. Purdy, T. Walker and S. Horst, C/SiC material evaluation for aircraft brake applications, *4th Int. Con. on High Temp. Ceram. Matrix Comp.*, Wiley, Germany, 802 (2001).
57 The Aircraft at End of Life Sector: a Preliminary Study, http://users.ox.ac.uk/~pgrant/Airplane%20end%20of%20life.pdf, (2007)
58 J. D. Chen & C. P. Ju, Low energy tribological behaviour of carbon-carbon composites, *Carbon* **33**, [1], 57-62 (1995).
59 A. Lacombe, Friction system using refractory composite materials, Patent number: 5007508 (1991).
60 SGL group website: http://www.sglcarbon.com/sgl_t/fibers/panox.html (last accessed 2010).
61 Website: Messier-Bugatti Safran Group: http://www.messier-bugatti.com/article.php3?id_article=272&lang=en (last accessed 2010).
62 Website: Messier-Bugatti Safran Group PDF: http://www.messier-bugattiusa.com/IMG/pdf/777LR.pdf (last accessed 2010).

63 S. Fan, L. Zhang, Y. Xu, L. Cheng, G. Tian, S. Ke, F. Xu & H. Lui, Microstructure and tribological properties of advanced carbon/silicon carbide aircraft brake materials, *Comp. Sci. & Tech.* **68**, 3002-3009 (2008)

64 Y. Cai, Y. Xu, B. Li, S. Fan, L. Zhang, L. Cheng & L. Yu, Low-cost preparation and frictional behaviour of a three-dimensional needled carbon/silicon carbide composite, *J. of Euro. Ceram Soc.* **29**, 497-503 (2009)

65 Y. Xu, Y. Zhang, L. Cheng, L. Zhang, J. Lou & J. Zhang, Preparation and friction behavior of carbon fiber reinforced silicon carbide matrix composites, *Ceram. Int.* **33**, [3] 439-445 (2007).

66 N. Tucker & K. Lindsey, An introduction to automotive composites, Rapra Technology Limited, (2002).

67 Fibres for reinforcement in composite materials, SP Systems (2001).

68 X. Yin, L. Cheng, L. Zhang, Y. Xu & C. You, Microstructure and oxidation resistance of carbon/silicon carbide composites infiltrated with chromium silicide, *Mat. Sci. & Eng.* **290**, [1=2] 89-94 (2000).

69 J. D. Buckley & D. D. Edie, Carbon-carbon materials and composites, Noyes Publications, (1993)

70 S. Ozbek & D. H Isaac, Strain induced density changes in PAN-based carbon fibre, *Carbon* **38**, [14] 2007, 2007-2016 (2000).

71 P. K. Mallick, Fiber-reinforced composites, Taylor and Francis Group, (2008)

72 V. K. Srivastava, Damage morphology of C/C-SiC composites under impact tests, *Ceram. Trans.* **175**, 181-187, (2006)

73 W. Krenkel, J. Schulte-Fischedick, M. Freiß & B. Thielicke, The interlaminar Shear Strength of C/C-SiC, *4th Int. Con. on High Temp. Ceram. Matrix Comp.*, Wiley, Germany, 181-186 (2001).

74 M. Freiß, W. Krenkel, K. Nestler & G. Marx, CVD-Coating of fabric sheets in combination with the LSI-Process, *4th Int. Con. on high Temp. Ceram. Matrix Comp.*, Wiley, Germany, 199-204 (2001).

75 F. Lamouroux & G. Camus, Oxidation effects on the mechanical properties of 2D woven C/SiC composites, *J. of Eu. Ceram. Soc.* **14**, [2] 177-188 (1994)

76 F. Lamouroux, X. Bourrat & R. Naslain, Silicon carbide infiltration of porous C-C composites for improving the oxidation resistance, *Carbon* **33**, [4] 525-535 (1995).

77 Z. Xingui, Y. Yu, Z. Changmi, H. Boyun & L. Xueye, Effect of carbon-fibre pre-heat-treatment on the microstructure and properties of C_f/SiC composites, *Mat. Sci. & Eng.* **433**, [1-2] 104-107 (2006).

78 K. E. Perepelkin. Oxidized (cyclised) Polyacrylonitrile fibres – OXYPAN. A Review, *Fibre Chem.* **35**, [6], 410-416 (2003).

79 SGL Group website: http://www.sglcarbon.com/sgl_t/fibers/panox.html (last accessed 2010).

80 G. Williams, R. Trask & I. Bond, A self-healing carbon fibre reinforced polymer for aerospace applications, *Comp.: Part A* **38**, [6] 1525-1532 (2007).

81 R. Naslain, The design of the fibre-matrix interfacial zone in ceramic matrix composites, *Comp. Part A* **29**, [9-10] 1145-1155 (1998).

82 R. J. Kerans, R. S. Hay, T. A. Parthasarathy & M. K. Cinibulk, Interface design for oxidation-resistant ceramic composites, *J. of Am. Ceram. Soc.* **85**, 2599-632 (2002).

83 B. Reznik & D. Gerthsen, Microscopic study of failure mechanisms in infiltrated carbon fiber felts, *Carbon* **41**, [1] 57–69 (2003).

84 M. Esfehanian & J. G. Heinrich, Silicide–carbide composites obtained from alloyed melt infiltration, *J. of Mat. Sci.* **42**, [18] 7721–7728 (2007).
85 R. P. Messner & Y. M. Chiang, Liquid-phase reaction-bonding of silicon carbide using alloyed silicon-molybdenum melts, *J. of Am. Ceram. Soc.* **73**, [5] 1193-1200 (1990).
86 J. C. Margiotta, D. Zhang, C. Nagle & C. E. Feeser, Formation of dense silicon carbide by liquid silicon infiltration of carbon with engineered structure, *J. of Mat. Res.* **23**, [5] (2007).
87 F. Lamouroux, S. Bertrand, R. Pailler, R. Naslain & M. Cataldi, Oxidation-resistant carbon-fiber-reinforced ceramic-matrix composites, *Comp. Sci. & Tech.* **59**, 1073-1085 (1999).
88 R. Naslain, SiC-Matrix Composites: Nonbrittle Ceramics for Thermo Structural Application, *Int. J. Appl. Ceram. Tech.* **2** [2], 75–84 (2005).
89 Y. Xu, L. Cheng, L. Zhang, H. Yin & C. You, Effects of chemical vapour infiltration atmosphere on the mechanical properties and microstructure of carbon fibres, *J. of Eu. Ceram. Soc.* **21**, [6] 809-816 (2001).
90 H. Araki, T. Noda, H. Suzuki, F. Abe & M. Okada, Effect of pyrocarbon pre-coating on the mechanical properties of CVI carbon fibre/SiC composites, *J. of Nu. Sci. & Tech.* **32**, [4] 369-371 (1995)
91 S. Labruquere, H. Blanchard, R. Pailler & R Naslain, Enhancement of the oxidation resistance of interfacial area in C/C composites. Part 1: oxidation resistance of B-C, Si-B-C and SiC coated carbon fibre, *J. of Eu. Ceram. Soc.* **22**, [7] 1001-1009 (2002)
92 J. F. Despres & M. Monthioux, Mechanical properties of C/SiC composites explained from their interfacial features, *J. of Eu. Ceram. Soc.* **15**, [3] 209-224 (1995).
93 S. Labruquere, X. Bourrat, R. Pailler & R. Naslain, Structure and oxidation of C/C composites: role of the interface, *Carbon* **39**, [7] 971-984 (2001)
94 M. Guellali, R. Oberacker & M. J. Hoffmann, Influence of heat treatment on microstructure and mechanical properties of CVI-CFC composites with medium and highly textured pyrocarbon matrices, *Comp. Sci. & Tech.* **68**, 1115-1121 (2008).
95 G. A. Slack, Thermal conductivity of pure and impure silicon, silicon carbide, and diamond, *J. of App. Phy.* **35**, [12], 3460-3466 (1964).
96 M. E Westwood, J. D Webster, R. J Day, F. H Hayes & R. Taylor, Review: Oxidation protection for carbon fibre composites, *J. of Mat. Sci.* **31**, [6] 1389-1397 (1996).
97 Y. C Zhu, S. Ohtani, Y. Sato & N. Iwamoto, Improvement in oxidation resistance of CVD-SiC coated C/C composites by silicon infiltration pre-treatment, *Carbon* **36**, [7-8] 929, 935 (1997).
98 X. Yin, L. Cheng, L. Zhang, Y. Xu & J. Li. Oxidation behaviour of 3D C/SiC composites in two oxidizing environments, *Comp. Sci. & Tech.* **61**, [7] 977-980 (2002).
99 S. Wu, L. Cheng, L. Zhang & Y. Xu, Oxidation Behaviour of 2D C/SiC with multi-layer CVD SiC Coating, *Surf. Coatings & Tech.* **200**, [14-15] 4489-4492 (2005).
100 SGL Group website: http://www.sglcarbon.com/sgl_t/fibers/panox.html (last accessed 2010).

101 R. E. Tressler, Recent developments in fibres and interfaces for high temperature ceramic matrix, *Comp. Part A: App. Sci. & Man.* **30**, [4] 429-437 (1999).
102 R. Naslain, X. Bourrat, A. Guette, S. Legallet & F. Rebillat, Oxidation resistance of BN coatings with different textures, *4th Int. Con. on High Temp. Ceram. Matrix Comp.*, Wiley, Germany, 193-198 (2001).
103 N. S. Jacobson, S. C. Farmer, A. W. Moore & H. Sayir, High temperature Oxidation Behaviour of Boron Nitride: I, Monolithic Boron Nitride, *J. of Am. Ceram. Soc.* **82**, [2] 393-398 (1999).
104 K. L. Luthra, R. N. Singh & M. K. Brun, Toughened Sicomp Composites – Process and preliminary properties, *Am. Ceram. Soc. Bull.* **72**, 79-83 (1993).
105 L. Vandenbulcke, G. Fantozzi, S. Goujard & M. Bourgeon, Outstanding ceramic matrix composites for high temperature applications, *Adv. Eng. Mat.* **7**, [3] 137-142 (2005).
106 K. L. Luthra & H. Wang, Silicon carbide-silicon composite having improved oxidation resistance and method of making, US patent 5962103 (1999)
107 Strife J.R and Sheehan J.E, Ceramic coatings for carbon-carbon composites, *Ceram. Bull.* **67**, [2], 369-374 (1988).
108 J. Schulte-Fischedick, J. Schmidt, R. Tamme, U. Kroner, A Arnold & B. Zeiffer, Oxidation behaviour of C/C–SiC coated with SiC–B4C–SiC–cordierite oxidation protection system, *Mat. Sci. & Eng. A* **386**, [1-2] 428-434 (2004).
109 S. Tang, J. Deng, S. Wang & W. Lui, Fabrication and characterization of C/SiC composites with large thickness, high density and near-stoichiometric matrix by heaterless chemical vapor infiltration, *Mat. Sci. & Eng.* **A465**, [1-2] (2007).
110 A. Sakai, J. Gotoh & S. Motojima, Preparation and characterisation of SIC/C and C/SiC/C composites using pulse chemical vapour infiltration process, *Mat. Sci. & Eng. B* **38**, [1-2] 29-35 (1996).
111 N. Igawa *et al.*, Fabrication of SiC fiber reinforced SiC composite by chemical vapor infiltration for excellent mechanical properties, *J. of Phy. & Chem. of Solids* **66**, [2-4] 551–554 (2005).
112 S. W. Fan, Y. D. Xu, L. T. Zhang, L. F. Cheng, L. Yu, Y. D. Yuan, F. K. Zhang, G. L. Tian, Z. J. Chen & J. J. Lo, Three-dimensional needled carbon/silicon carbide composites with high friction performance, *Mat. Sci. & Eng.* **467**, [1-2] (2007).
113 H. Mei, L. Cheng, L. Zhang & Y. Xu, Effect of Temperature Gradients and Stress Levels on Damage of C/SiC Composites in Oxidizing Atmosphere, Science Direct, *Mat. Sci. & Eng.* **430**, [1-2] 314-319 (2006).
114 D. L. Zhao, H. F. Yin, F. Luo & W. C. Zhou, Microstructure and mechanical properties of 3D textile C/SiC composites fabricated by chemical vapour infiltration, *Adv. Mat. Res.* **11-12**, 81-84 (2006).
115 C-H Chu, Y-M Lu & M-H Hon, Growth characteristic of β-SiC by chemical vapour deposition, *J. of Mat. Sci.* **27**, [14] 3883-3888 (1992).
116 T. Noda, H. Araki & H. Suzuki, Processing of high-purity SiC composites by chemical vapour infiltration (CVI), *J. of Nu. Mat.* **212-215**, 823-829 (1994).
117 S. Tang, J. Deng, W. Lui & K. Yang, Mechanical and ablation properties of 2D-carbon/carbon composites pre-infiltrated with a SiC filler, *Carbon* **44**, [14] 2877-2882 (2006).
118 R. Naslain, J. Lamon, R. Pailler, X. Bourrat, A. Guette & F. Langlais, Micro/minicomposites: a useful aroach to the design and development of non-oxide CMCs Composites: Part A, *App. Sci & Eng.* **30**, [4], 537-547 (1999).

119 J. Ma, Y. Xu, L. Zhang, L. Cheng, J. Nie & H. Li, Preparation and mechanical properties of C/SiC composites with carbon fibre woven preform, *Mat. Lett.* **61**, [2] 312-315, (2007).
120 K. A. Appiah, Z. L. Wang & W. J. Lackey, Characterization of interfaces in C fibre-reinforced laminated C-SiC matrix composites, *Carbon* **38**, [6] 831-838 (2000).
121 T. Taguchi, T. Nozawa, N. Igawa, Y. Katoh, S. Jitsukawa, A. Kohyama, T. Hinoki & L. L. Snead, Fabrication of advanced SiC fibre/F-CVI SiC matrix composites with SiC/C multi-layer interphase, *J. of Nu. Mat.* **329-333**, [1] 572-576 (2004).
122 A. H. Wu, W. B. Cao, C. C. Ge, J. F. Li & A. Kawasaki, Fabrication and characteristics of plasma facing SiC-C functionally graded composite material, *Mat. Chem. & Phy.* **91**, [2-3] 545-550 (2005).
123 J. I. Kim, W. J. Kim, D. J. Choi, J. Y. Park & W. S. Yru, Design of a C-SiC functionally graded coating for the oxidation protection of C-C composites, *Carbon* **43**, [8] 1749-1757 (2005).
124 M. Kawase, T. Tago, M. Kurosawa. H. Utsumi & K. Hashimoto, Chemical vapor infiltration and deposition to produce a silicon carbide carbon functionally gradient material, *Chem. Eng. Sci.* **54**, [15-16] 3327-3334 (1999).
125 J. Deng, W. Lui, H Du, H. Cheng & Y. Li, Oxidation behaviour of C/C-SIC matrix composites, *J. of Mat. Sci. & Tech.* **17**, [5], 543-546 (2001).
126 Y. Wang, M. Sasaki, T. Goto & T. Hirai, Thermodynamics for the preparation of SiC-C nano-composites by chemical vapour deposition, *J. of Mat. Sci.* **25**, [11] 4607-4613 (1990).
127 Y. Wang, M. Sasaki, T. Goto & T. Hirai, Thermal properties of chemical vapour-deposition SiC-C nanocomposites, *J. of Mat. Sci.* **26**, [20] 5495-5501 (1991).
128 X. Wei, L. Cheng, L. Zhang, Y Xu & Q. Zeng, Numerical simulation for fabrication of C/SiC composites in isothermal CVI reactor, *Comp. Mat. Sci.* **38**, [2] 245-255 (2006).
129 H. Mei, L. Cheng & L. Zhang, Thermal Cycling Damage Mechanisms of C-SiC Composites in displacement constraint and oxidizing atmosphere, *J. of Am. Ceram. Soc.* **89**, [7] 2330-2334 (2006).
130 S. R. Omena Pina, L. C. Pardini & I. V. P Yoshida, Carbon fibre/ceramic matrix composites: processing, oxidation and mechanical properties, *J. of Mat. Sci.* **42**, 4245-4253 (2007).
131 J. Zhong, S. Qiao, G. Lu, Y. Zhang, W. Han & D Jai, Rapid fabrication of C/C/SiC composite by PIP of HMDS, *J. of Mat. Pro. Tech.* **190**, 358-362 (2007).
132 S. Wang, Z. Chen, F Li & H. Hu, Mechanical properties of C/SiC composites via precursor pyrolysis with pretreated carbon fiber, *Key Eng. Mat.* **336-338**, 1245-1247 (2007).
133 D. Zhu, H. Du, F. Luo & W. Zhou, Preparation and mechanical properties of C-C-SiC composites, *Mat. Sci. Forum* **546-549**, 1501-1504 (2007).
134 F. I Hurwitz, T. A. Kacik, X. Y. Bu, J. Masnovi, P. J. Heiman & K. Beyene, Pyrolytic conversion of methyl- and vinylsilane polymers to Si-C ceramics, *J. of Mat. Sci.* **30**, 3130-3136 (1995).
135 M. F. Gonon, S. Hampshire, J. P. Disson & G. Fantozzi, A polysilazane precursor for S-C-N-O matrix composites, *J. of Eu. Ceram. Soc.* **15**, [7] 638-688 (1995).

136 A. G. Odeshi, H. Mucha & B .Wielage, Manufacture and characterisation of a low cost carbon fibre reinforced C/SiC dual matrix composite, *Carbon* **44**, 1994-2001 (2006).
137 R. W. Olesinski & G.J. Abbaschian, The C-Si (Carbon-Silicon) system, *J. Phase Equilibria* **5** [5], 486-489 (1984).
138 C. C. Evans, A. C Parmee, R. W Rainbow, Silicon treatment of carbon fibre-carbon composites, *4th London Con. on Carbon & Graphite*, 2231-235 (1974).
139 W. B Hillig, R. L Mehan, C. R Morelock, V. I DeCarlo & W. Laskow, silicon/silicon carbide composites, *Ceram. Bull.* **54**, [12] (1975).
140 R. Gadow, Die silizierung von kohlenstoff, Doctoral Thesis, University of Karlsruhe (1986).
141 A. Mentz, M. Muller, H. P Buchkremer & D. Stover, Improving damage tolerance of C/SiC, *4th Int. Con. on high Temp. Ceram. Matrix Comp.*, Wiley, Germany, 317-323 (2001).
142 W. Krenkel, B. Heidenreich & R. Renz, Short fibre reinforced CMC materials for high performance brakes, *4th Int. Con. on high Temp. Ceram. Matrix Comp.*, Wiley, Germany, 809-815 (2001).
143 M. Freiβ, W. Krenkel, R. Brandt & G. Neuer, Influence of process parameters on the thermophysical properties of C/C-SiC, *4th Int. Con. on high Temp. Ceram. Matrix Comp.*, Wiley, Germany, 328-333 (2001)
144 J .Schule-Fischedick, A. Zern, J. Mayer, M. Ruhle, M. Frieß, W. Krenkel & R. Kochendorfer, The morphology of silicon carbide in C/C–SiC composites, *Mat. Sci. & Eng.* **332**, [1-2] 146-152 (2002).
145 Momentive website data sheet for 'celobond J2027L' phenolic resin: http://www.epon.com/Products/TechnicalDataSheets.aspx?id=7770 (Last accessed Dec. 2010).
146 J. P Wang, Z. H Jin & G. J Qiao, Rapid fabrication of C/C-SiC composites, *Key Eng. Mat.* **317-318**, [159-162] (2006).
147 C. Zuber & B. Heidenreich, Development of a net shape manufacturing method for ventilated brake discs in a single piece design, *Materialwissenschaft und Werkstofftechni* **37**, [4], 301-308 (2006).
148 F. Christin, Design, fabrication and application of thermostructural composites (TSC) like C/C, C/SiC and SiC/SiC composites, *Adv. Eng. Mat.* **4**, [12] 903-912 (2002).
149 R. Gadow, T. Haug & A. Kienzle, Melted-infiltrated fibre reinforced composite ceramic, US Patent 6793873B2 (2004).
150 J. Yang & O. J. Llegbusi, Kinetics of silicon-metal alloy infiltration into porous carbon, *Comp. Part A* **31**, 617-625 (2000).
151 J. C Margiotta, D. Zhang & D. C. Nagle, Microstructural evolution during silicon carbide (SiC) formation by liquid silicon infiltration using optical microscopy, *Int. J. of Ref. Met. & Hard Mats.* **28**, 191-197 (2010).
152 Y. Wang, S. Tan & D. Jiang, The fabrication of reaction-formed silicon carbide with controlled microstructure by infiltrating a pure carbon preform with a molten Si, *Ceram. Int.* **30**, 435-439 (2004).
153 D. S. Bae, D. Y. Son, S. P. Lee, H. S. Park, K. S. Kim & J. H. Jeon, Effect of initial porosity on mechanical properties of C/SiC composites fabricated by silicon melt Infiltration process, *Key Eng. Mat.* **261-263**, 1445-1450 (2004).
154 Y. M. Chiang, R. P. Messner, C. D. Terwilliger & D. R. Behrendt, Reaction-formed silicon-carbide. J. of Mat. Sci. & Eng. 144, 63 (1991)

155 W. Krenkel & R. Renz, C_f/C-SiC components for high performance applications, ECCM-8 conference, Woodhead Publishing Ltd, Italy, 23-29, (1998).
156 R. Kochendorfer, N. Lutzenburger & H. Schneider, Applications of CMCs made via the Liquid Silicon Infiltration (LSI) technique, *4th Int. Con. on high Temp. Ceram. Matrix Comp.*, Wiley, Germany, 277-287 (2001).
157 J. Schulte-Fischedick, M. Freiβ, W. Krenkel, R. Kochendörfer & M. König, Crack microstructure during carbonisation of carbon fibre reinforced plastics to carbon/carbon composites, *Pro. of the 12th Int. Con. on Comp. Mat.*, Paris (1999).
158 W. Krenkel, Microstructure tailoring of C/C-SiC composites, *Ceram. Eng. & Sci. Pro.* **24** [4], 471-476 (2003).
159 W. Krenkel, Designing with C/C-SiC composites, *Ceram, Trans.* **153**, 103-123 (2004).
160 Z. Stadler, M. Kermc, K. Tomaz & A. Dakskobler, A motorcycle brake system with C/C-SiC composite brake discs, *Ceram. Eng. & Sci. Pro.* **25**, [4], 179-184 (2004).
161 A. Mentz, M. Muller, H. P. Buchkremer & D. Stover, Improving damage tolerance of C/SiC, *4th Int. Con. on high Temp. Ceram. Matrix Comp.*, Wiley, Germany, 317-323 (2001).
162 S. Kumar, A. Kumar, R. Devi, A. Shukla & A. K. Gupta, Capillary infiltration studies of liquids into 3D-stitched C-C preforms Part B: Kinetics of silicon infiltration, *J. of Euro. Ceram. Soc.* **29**, 2651-2657 (2009).
163 A. Favre, H. Fuzellier & J. Suptil, An original way to investigate the siliconizing of carbon materials, *Ceram. Int.* **29**, [3] 235-243 (2003).
164 F. M. Varela-Feria, J. Ramirez-Rico, A. R. de Arellano-Lopez, J. Martinez-Fernandez & M. Singh, Reaction-formation mechanisms and microstructure evolution of biomorphic SiC, *J. Mat. Sci.* **43**, 933-941 (2008).
165 R. Pampuch, E. Walasek & J. Bialoskorski, Reaction mechanism in carbon–liquid silicon systems at elevated temperature. *Ceram Int.* **12**, 99–106 (1986).
166 R. Pampuch, E. Walasek & J. Bialoskorski, Mechanism of Reactions in the Si-C System and SHS of SiC. *Ceram Int.* **13**, 63-68 (1987).
167 C. Zollfrank & H. Sieber, Microstructure evolution and reaction mechanism of biomorphous SiSiC ceramics, *J. Am. Ceram. Soc.* **88** [1], 51-58 (2005).
168 S. Xu, G. Qiao, D. Li, H. Yang, Y. Liu & T. Lu, Reaction forming of silicon carbide ceramics using phenolic resin derived porous carbon preform, *J. Eu. Ceram. Soc.* **29**, [11] 2395-2402 (2009).
169 V. V. Pujar & J. D. Cawley, *J. of the Am. Ceram. Soc.* 78, 774 – 782(1995)
170 J. Qian, Z Jin & X. Wang, Porous SiC ceramics fabricated by reactive infiltration of gaseous silicon into charcoal, *Ceram. Int.* **30**, 947-951 (2004)
171 A. Favre, T. Birkel & H. Fuzellier, Reaction between liquid Al (or SI) and composite C/C materials, *4th Int. Con. on High Temp. Ceram. Matrix Comp.*, Wiley, Germany, 336-340 (2001).
172 F. Raether, J. Meinhardt & A. Kienzle, Oxidation behaviour of carbon short fibre reinforced C/SiC composites, *J. of Eu. Ceram. Soc.* **27**, [2-3] 1217-1221 (2007).
173 E. W. Washburn, The dynamics of capillary flow, *Phy. Rev.* **17**, [3] 273-283 (1921)

174 F. H. Gern & R. Kochendorfer, Liquid Silicon Infiltration: Description of infiltration dynamics and silicon carbide formation, Comp. **28A**, 335-364 (1997).
175 R. Asthana, Interface- and Diffusion-Limited Capillary Rise of Reactive Melts with a Transient Contact Angle, *Metallurgical & Mat. Trans.* **33A**, 2002-2119 (2001).
176 S. Kumar, A. Kumar, R. Devi, A. Shukla & A. K. Gupta, Capillary infiltration studies of liquids into 3D-stitched C-C preforms Part A: Internal pore characterization by solvent infiltration, mercury, porosimetry, and permeability studies, *J. of Euro. Ceram. Soc.* **29**, 2643-2650 (2009).
177 M. H. Hon & R. F. Davie, Self diffusion of 14C in polycrystalline β-SiC, *J. Mat. Sci.* **14**, [10] 2411-2421 (1979).
178 M. H. Hon & R. F. Davie, Self diffusion of 30Si in polycrystalline β-SiC, *J. Mat. Sci.* **15**, [8] 2073-2080 (1980).
179 R. Gadow, T. Haug & A. Kienzie, Melted-infiltrated fibre reinforced composite ceramic, US Patent 6793873B2 (2004).
180 S. Dong, Y. Katoh & A. Kohyama, Processing optimization and mechanical evaluation of hot pressed 2D Tyranno-SA/SiC composites, *J. of Am. Ceram. Soc.* **23**, 1223-1231 (2003).
181 Y. Liu, L. Cheng, L. Zhang, Y. Hua & W. Yang, Microstructure and properties of particle reinforced silicon carbide and silicon nitride ceramic matrix composites prepared by chemical vapour infiltration, *Mat. Sci. & Eng.* **475**, [1-2] (2007).
182 E. Muller, R. Dittrich & K. Moritz, Studies on a Novel Route to C/SiC, *Adv. Eng. Mat.* **6**, [7], 568-572 (2004).
183 T. Damjanovic, C. Argirusis, G. Borchardt, H. Leipner, R. Herbig, G. Tomandl & R. Weiss, Oxidation protection of C/C–SiC composites by an electrophoretically deposited mullite precursor, *J. of the Eu. Ceram. Soc.* **25**, [2-3] 577-587 (2005).
184 J-M. Lin, C-C. M. Ma, N-H. Tai, W-J. Wu & C-Y. Chen, Preparation and properties of SiC modified carbon-carbon composites by carbothermal reduction reaction, *J. of Mat. Sci. Let.* **18**, [16] 1353-1355 (1999).
185 Y. Zhou, K. Hirao & M. Toriyama, Very rapid densification of nanometer silicon carbide powder by pulse electric current sintering, *J. of Am. Ceram. Soc.* **83**, [3] 654-656 (2000).
186 C. M. Chan & A. J. Ruys, Carbon-fibre-reinforced ceramic matrix composites for high-temperature applications, *Mech. & Mechatronic Eng.* **7**, 17850-17854 (2006).
187 Y. Ding, S. Dong, Z. Huang & D. Jiang, Fabrication of short C fiber-reinforced SiC composites by spark plasma sintering, *Ceram. Int.* **33**, [1] 101-105 (2007).
188 J. Li, J. Tian & L. Dong, Synthesis of SiC precursors by a two-step sol-gel process and their conversion to SiC powders, *J. of the Eu. Ceram. Soc.* **20**, [11], 1853-1857 (2000).
189 Y. Haruvy & V. Liedtke, Sol-gel derived C/SiC composites and protective coatings for sustained durability in the space environment, *Eu. Space Agen.*, [540], 67-74 (2003).
190 K. S. Mazdiyasni, Fibre reinforced ceramic composites, Noyes publications, San Diego, CA, USA, 292 (1990).
191 Website: http://www.gocarbonfibre.com/home.aspx (last accessed 2011)

192 R. E Allred, J. M Goasau & J. M Shoemaker, Recycling process for carbon/epoxy composites, *46th International SAMPE symposium*, 179-192 (2001)

193 A. M. Cunliffe, N. Jones & P. T. Williams, Recycling of fibre-reinforced polymeric waste by pyrolysis: thermo-gravimetric and bench-scale investigations, *J. of Anal. Appl. Pyrolysis* **79**, [2] 315-338 (2003).

194 S. Pimenta & S. T. Pinho, Recycling carbon fibre reinforced polymers for structural applications: technology review and market outlook, Waste management **31**, [2] 378-392 (2011).

195 T. Roberts, The carbon fibre industry: Global strategic market evaluation 2006-2010, Materials technology publications (2006).

196 H. L. H. Yip, S. J. Pickering & C. D. Rudd, Characterisation of carbon fibres recycled from scrap composites using fluidised bed process, *Plastics, Rubber & Composites* **31**, [6], 278 (2002).

197 E. Lester, S. Kingman, H. K. Wong, C. Rudd, S. J. Pickering & N. Hilal, Microwave heating as a means of carbon fibre recovery from polymer composites: a technical feasibility study, *Mat. Res. Bull.* **39**, [10] 1549-1556 (2004).

198 S. J. Pickering, Recycling technologies for thermoset composite materials – current status, *Composites: Part A* **37**, [8] 1206-1215 (2006)

199 J. R Sarasua & J. Pouyet, Recycling effects on microstructure and mechanical behaviour of PEEK short carbon-fibre composites, *J. of Mat. Sci.* **32**, [2] 533-536 (1997).

200 K. Pannkoke, M. Oethe & J. Busse, Efficient prepreg recycling at low temperatures, *Cryogenics* **38**, [1], 155-159 (1998).

201 R. Fukui, T. Odai, H. Zushi, I. Osawa, K. Uzawa & J. Takahashi, Recycle of cabon fiber reinforced plastics for automotive application, The 9th Japan Int. SAMPE symposium (2005).

202 J. Takahashi, N. Matsutsuka, T. Okazumi, K. Uzawa, I. Ohsawa, K. Yamaguchi & A. Kitano, Mechanical properties of recycled CFRP by injection molding method, *16th Int. Con. On Comp. Mat.*, Japan, 1-5 (2007)

203 R. E. Alldred, A. B. Coons & R. J. Simonson, Properties of carbon fibres reclaimed from composite manufacturing scrap by tertiary recycling, *SAMPE Pro. of 28th Int. Tech. Conf.*, Seattle, (1996).

204 R. E. Alldred, J. M. Gosau & J. M. Shoemaker, Recycling process for carbon/epoxy composites, *46th Int. SAMPE Sym. & Exhib.*, CA, USA, 179-192, (2001).

205 M. Nakagawa, K. Shibata & H. Kuriya, Characterization of CFRP using recovered carbon fibers from waste CFRP. *In: 2nd Int. Sym. on Fiber Recycling*, Atlanta, Georgia, USA (2009).

206 R. Pinero-Hernanz, C. Dodds, J. Hyde, J. Garcia-Serna, M. poliakoff, E. Lester, M. J. Cocero, S. Kingman, S. Pickering & K. H. Wong, Chemical recycling of carbon fibre reinforced composites in nearcritical and supercritical water. *Com. Part A* **39**, 454–461 (2008).

207 R. Pinero-Hernanz, J. Garcia-Serna, C. Dodds, J. Hyde, M. poliakoff, M. J. Cocero, S. Kingman, S. J. Pickering & E. Lester, Chemical recycling of carbon fibre composites using alcohols under subcritical and supercritical conditions, *J. of Supercritical Fluids* **46**, [1] 83-92 (2008).

208 G. Jiang, S.J Pickering, E.H. Lester, T.A Turner, K.H Wong & N.A Warrior, Characterisation of carbon fibres recycled from carbon fibre/epoxy resin

composites using supercritical n-propanol, *Comp. Sci. & Tech.* **69**, [2] 192-198 (2009).
209 Y. Liu, L. Meng, Y. Huang & J. Du, Recycling of Carbon/Epoxy composites, *J. App. Polymer Sci.* **95**, [5] 1912-1916 (2004).
210 C. A. Eckert, B. L. Knutson & P. G. Debenedetti, Supercritical fluids as solvents for chemical and materials processing, *Nature* **383**, 313-318 (1996)
211 L. O. Meyer & K. Schulte, CFRP recycling following a pyrolysis route: Process optimization and potentials, *J. of Comp. Mat.* **43**, [9], 1121-1132 (2009).
212 G. Marsh, Reclaiming value from post-use carbon composite, *Reinforced Plastics* **52**, [7], 36-39 (2009).
213 S. H. Alsop, Pyrolysis off-gas processing, In: SAMPE *conf.*, Baltimore, MD, May 18-21, (2009).
214 M. A. Janney, W. L. Newell, E. Geiger, N. Baitcher & T. Gunder, Manufacturing complex geometry composites with recycled carbon fiber. In: SAMPE *Conf.*, Baltimore, MD, USA (2009).
215 CFK Valley Stade Recycling GmbH & Co. KG website: http://www.karl-meyer.de/cfk_recycling/ (Last accessed Dec. 2010).
216 V. P. McConnel, Launching the carbon fibre recycling industry, *Reinf. Plast.* **54**, [2], 33–37, (2010).
217 Karborek website: http://www.karborek.it/fibra/index.php?lang=eng (last accessed 2010).
218 Website data sheet: http://www.hexcel.com/NR/rdonlyres/5659C134-6C31-463F-B86B-4B62DA0930EB/0/HexTow_AS4.pdf (Last accessed Dec. 2010).
219 Website data sheet: http://www.hexcel.com/NR/rdonlyres/9229D78D-51BC-4460-9248-CC256BC6B6A4/0/HexPly_8552_2_22_US.pdf (Last accessed Dec. 2010).
220 Grafil Inc. website: http://www.grafil.com/pyrofil.html (last accessed 2010).
221 G. M. Jenkins & K. Kawamura, Polymeric Carbons: Carbon Fibre, Glass and Char, Cambridge University Press, (1976).
222 H. Ku, F. Cardona & M. Trada, Fracture toughness of phenol formaldehyde composites reinforced with E-spheres, *J. of Comp. Mat.* **43**, [7], 741-754 (2009).
223 Image-J website: http://rsbweb.nih.gov/ij/ (Last accessed Dec. 2010).
224 Gimp website: http://www.gimp.org/ (Last accessed Dec. 2010).
225 British standard test, Advanced technical ceramics – monolithic ceramics – general and texture properties, BS EN 623-5:2009.
226 W. C. Oliver & G. M. Pharr, An improved technique for determining hardness and elastic modulus using load and displacement sensing indentation experiments, *J. Mat. Res.* **7** [6] 1564-1583 (1992).
227 W. C. Oliver & G. M. Pharr, Measurement of hardness and elastic modulus by instrumented indentation: Advances in understanding and refinements to methodology, *J. Mat. Res.* **19**, [1] (2004)
228 M. R. VanLandingham, Review of instrumented indentation, *J. Res. Natl. Inst. Stand. Tech.* **108**, 249-265 (2003)
229 A. C. Fischer-Cripps, Critical review analysis and interpretation of nanoindentation test data, *Surface & Coatings Tech.* **200**, [14-15] 4153-4165 (2006)
230 S. Fouquet, S. Jouannigot, J. Alexis, R. Pailler, X. Bourrat, A. Guette & R. Naslain, Nanoindentation, Microscratch, Friction and Wear Studies of Carbon-Fibre Reinforced SiC-Si Matrix Composite, *Key Eng. Mat.* **264-268**, 917-920 (2004).

231 B. Beake, S. Goodes, S. Jones, R. Parkinson, N. Pickford & J. Smith, NanoTest M manual, Micro Materials Ltd (2004).
232 M. F. Doerner & W. D. Nix, A method for interpreting the data from depth-sensing indentation instruments, *J. of. Mat. Res.* **1**, [4], 601-609, (1986).
233 M. Kutz, Handbook of materials selection, Wiley (2002)
234 Agy ltd. website source : http://www.agy.com/technical_info/graphics_PDFs/Advanced_Materials.pdf (last accessed 2010)
235 L. Ma & G. Sines, Threshold size for cyclic fatigue crack propagation in a pyrolytic carbon, *Mat. Lett.* **17**, [1-2] 49-53 (1993)
236 J. Shackelford & W. Alexander, Mat. Sci. & Eng. Handbook, CRC (2000)
237 P. Hess, Laser diagnostics of mechanical and elastic properties of silicon and carbon films, *App. Surface Sci.* **106**, 429-433 (1996)
238 A. G. Evans & E. A. Charles, Fracture toughness determination by indentation, *J. of the Am. Ceram. Soc.* **59**, [7-8] 371-372 (1976)
239 T. Zhang, Y. Feng, R. Yang & P. Jiang, A method to determine fracture toughness using cube-corner indentation, *Scripta Materialia* **62**, 199-201 (2010)
240 B. R. Lawn, A. G. Evans & D. B. Marshall, Elastic/plastic indentation damage in ceramics: The median/radial crack system, *J. of the Am. Ceram. Soc.* **63**, [9-10] 574-581 (1980).
241 G.R. Anstis, P. Chantikul, B.R. Lawn & D.B. Marshall, A critical evaluation of indentation techniques for measuring fracture toughness: I. Direct crack measurement, *J. Am. Ceram. Soc.* **61**, 533 (1981).
242 G. Quinn, On the Vickers indentation fracture toughness test, *J. of the Am. Ceram. Soc.* **90** [3], 673-680 (2007)
243 J. J. Kruzic, D.K. Kim, K. J. Koester & R. O. Ritchie, Indentation techniques for evaluation the fracture toughness of biomaterials and hard tissues, *J. of Mech. Behaviour of Biomed. Mats.* **2**, [4] 384-395 (2009)
244 D. Chung, Carbon fiber composites, Butterworth-Heinemann (1994)
245 A. Oberlin, Carbonization and Graphilization, *Carbon* **22**, [6], 521-541 (1984).
246 FCC 3C-SiC (00-029-1129), International centre for data diffraction (2009).
247 H. Zhou & R. N. Singh, Kinetics model for the growth of silicon carbide by the reaction of liquid silicon with carbon, *J. Am. Ceram. Soc.* **79** [9], 2456 – 2462 (2005).
248 C. R. Choe & K. H. Lee, Effect of processing parameters on the mechanical properties of carbonized phenolic resin, *Carbon* **40**, [2], 247-249 (1992).
249 S. Xu, G. Qiao, D. Li, H. Yang, Y. Lui & T. Lu, Reaction forming of silicon carbide ceramic using phenolic resin derived porous perform, *J. Eu. Ceram. Soc.* **29**, [11] 2395-2402 (2009).
250 J. N. Ness & T. F. Page, Microstructural evolution in reaction-bonded silicon carbide, *J. Mat. Sci.* **21**, [4] 1377-1397 (1986).
251 O. P. Chakrabarti, P. K. Das & J. Mukerji, Growth of SiC particles in reaction sintered SiC, *Mat. Chem. & Phy.* **67**, [1-3] 199-202 (2001).
252 R. W. Olesinski & G. J. Abbaschian, The C-Si (Carbon-Silicon) system, *J. Phase Equilibria* **5**, [5] 486-489 (1984).
253 I. Zarudi & L. C. Zhang, Structure changes in mono-crysatalline silicon subjected to indentation – explained findings, *Trib. Int.* **32**, 701-712 (1999).
254 L. Chang & L. C. Zhang, Deformation mechanisms and pop-out in monocrystalline silicon under nanoindentation, *Acta. Mat.* **57**, 2148-2153 (2009).

255 G. Hofman, M. Wiedenmeier, M. Freuncl, A. Beavan, G. M. Pharr & J. Hay, Nanoindentation determination of elastic modulus and hardness of pyC samples, *Am. Carbon Soc. 23rd Biennial Conf.* USA, 230-231 (1997)

256 W. A. Brantley, Calculated elastic constants for stress problems associated with semiconductor devices, *J. of App. Phy.* **44**, 534-535 (1973).

Appendices

List of figures

List of tables

Appendix A – Figures

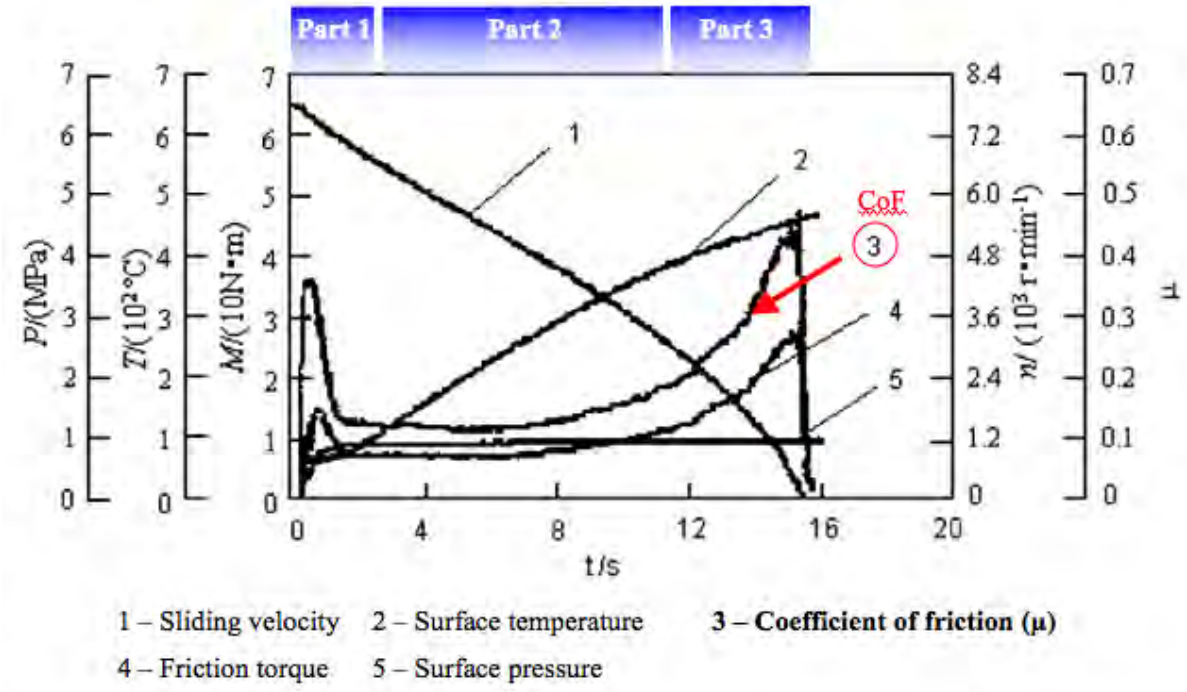

Fig. 1. Dynamometer curve parameters of C_f/SiC discs in a disc-on-disc configuration investigated by Zhang *et al*.

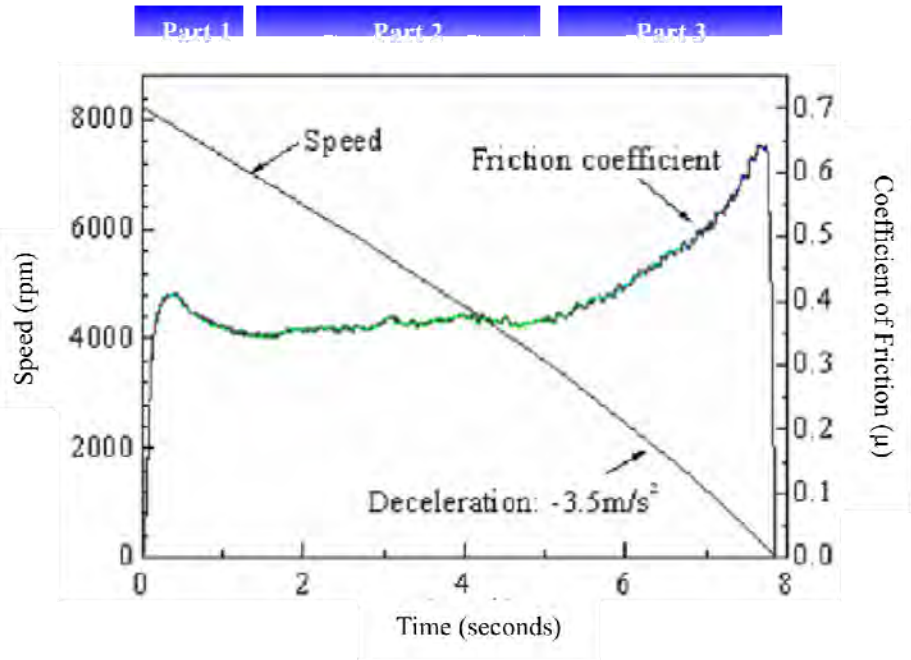

Fig. 2. Dynamometer COF curve for a C_f/SiC disc-on-disc configuration investigated by Fan *et al*.

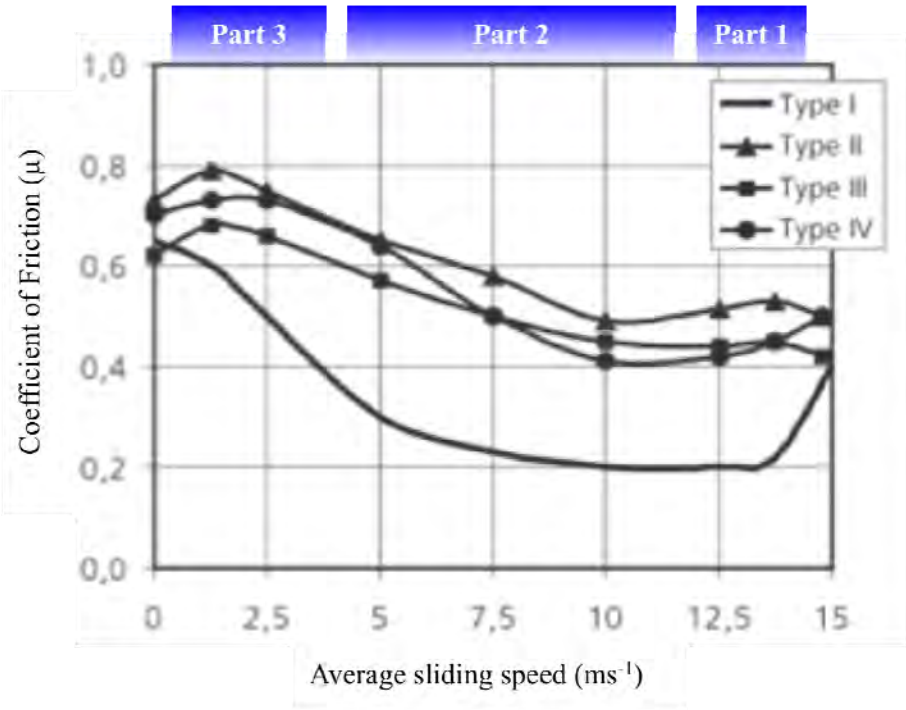

Fig. 3. Dynamometer COF curves, from right to left for the four different types of C_f/SiC reported by Krenkel *et al*. Type 1 represents the sample: Silica XB.

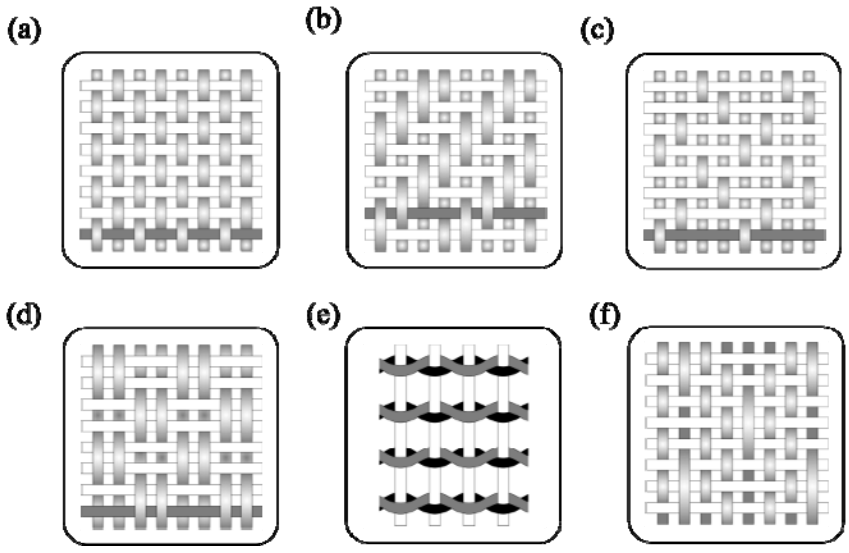

Fig. 4. Schematic illustrating the different types of woven architecture (a) Plain, (b) Twill, (c) Satin, (d) Basket, (e) Leno and (f) Mock leno.

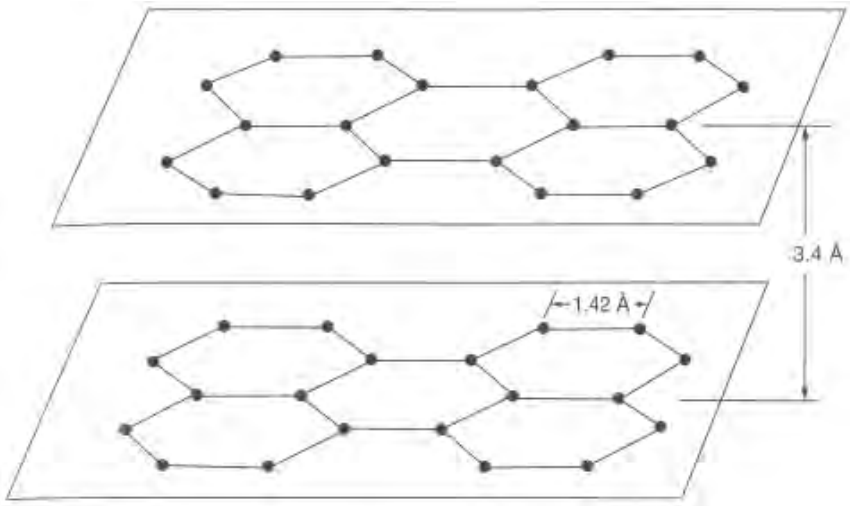

Fig. 5. Schematic of the carbon atoms in a graphite crystal.

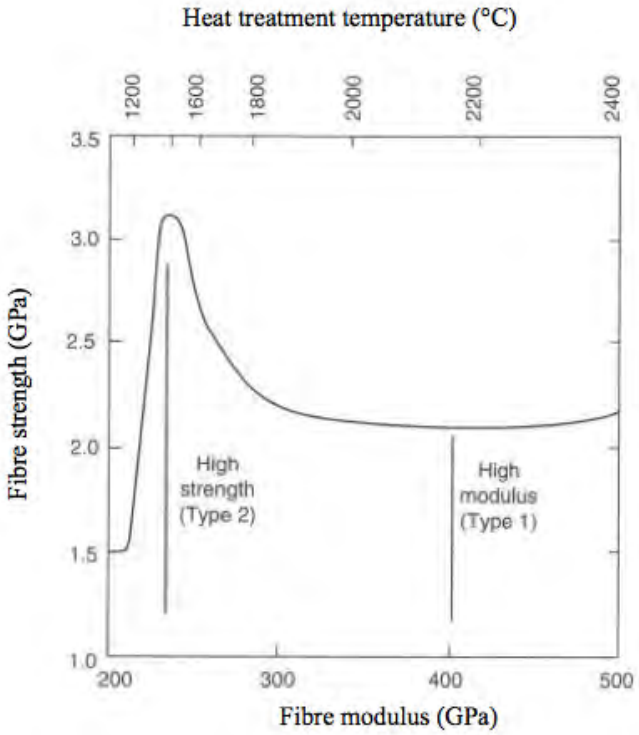

Fig. 6. Influence of heat treatment on the strength and modulus of carbon fibres.

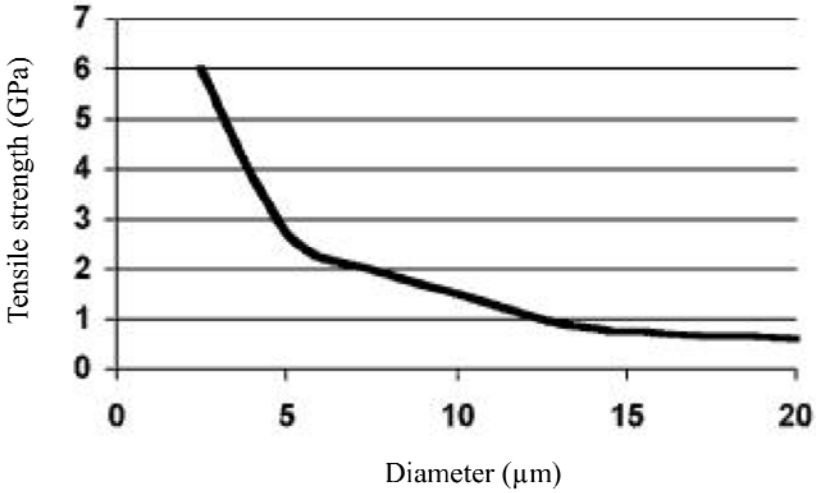

Fig. 7. Graph comparing the tensile strength (GPa) versus fibre diameter (μm) of a carbon fibre.

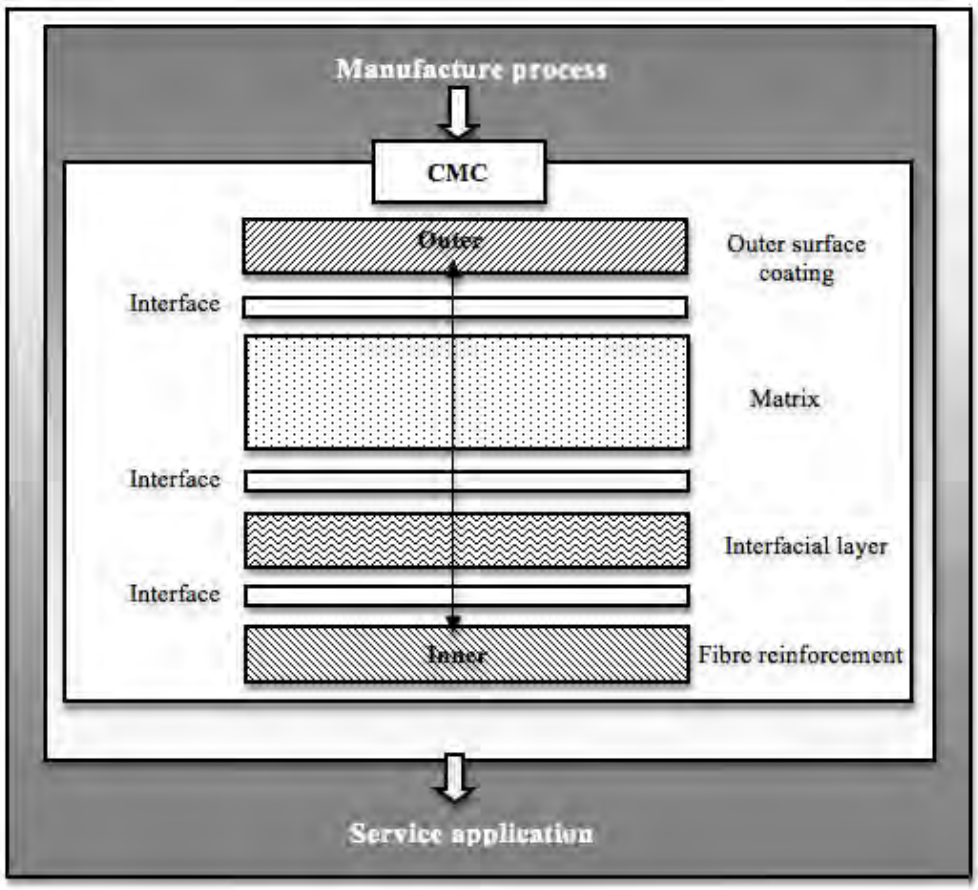

Fig. 8. Flow chart describing the oxidation protection considerations for CMC materials.

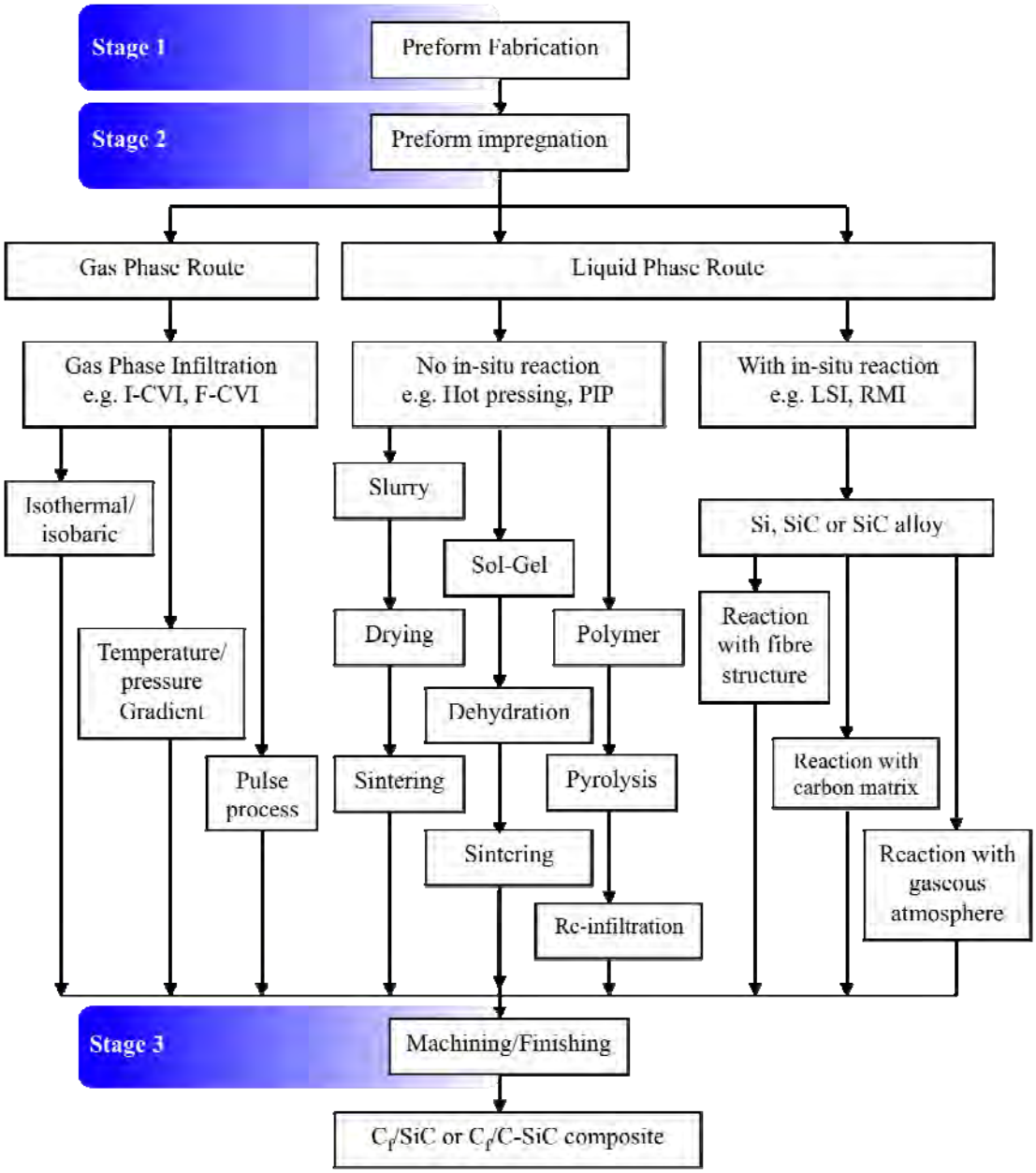

Fig. 9. Typical gas and liquid phase route manufacture possibilities of C_f/SiC and C_f/C-SiC composites.

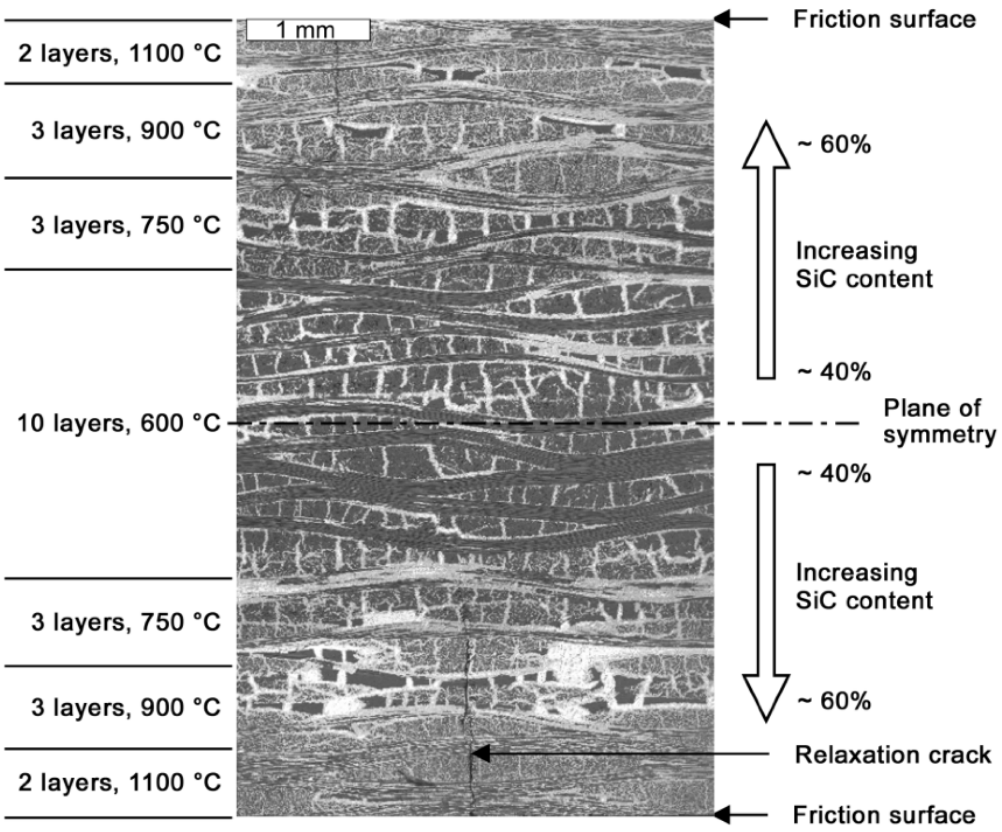

Fig. 10. Graded C_f/C-SiC composite (XG) manufactured by LSI.

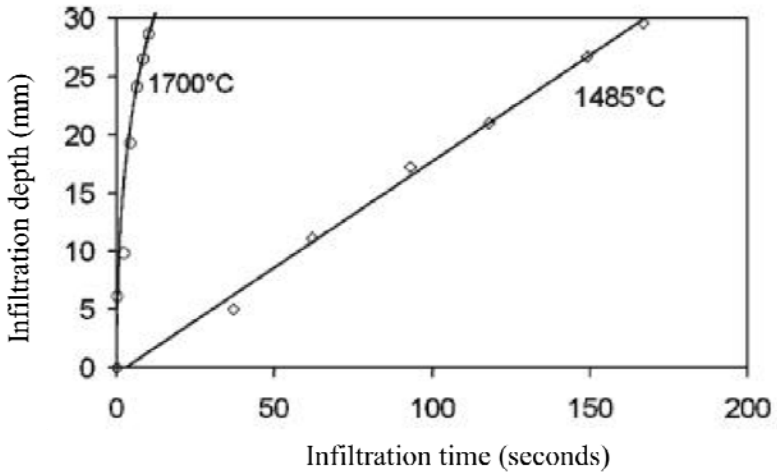

Fig. 11. Silicon infiltration (mm) at 1485ºC and 1700ºC.

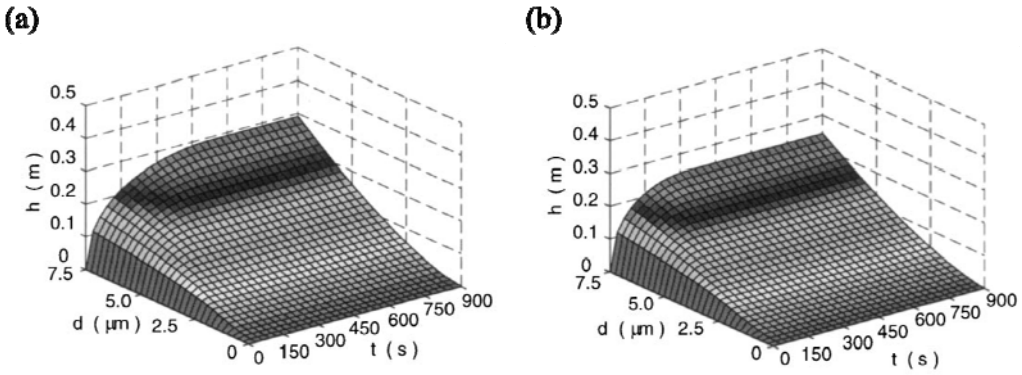

Fig. 12. Theoretical infiltration kinetics of pure silicon (a) at 1527ºC and (b) 1627ºC.

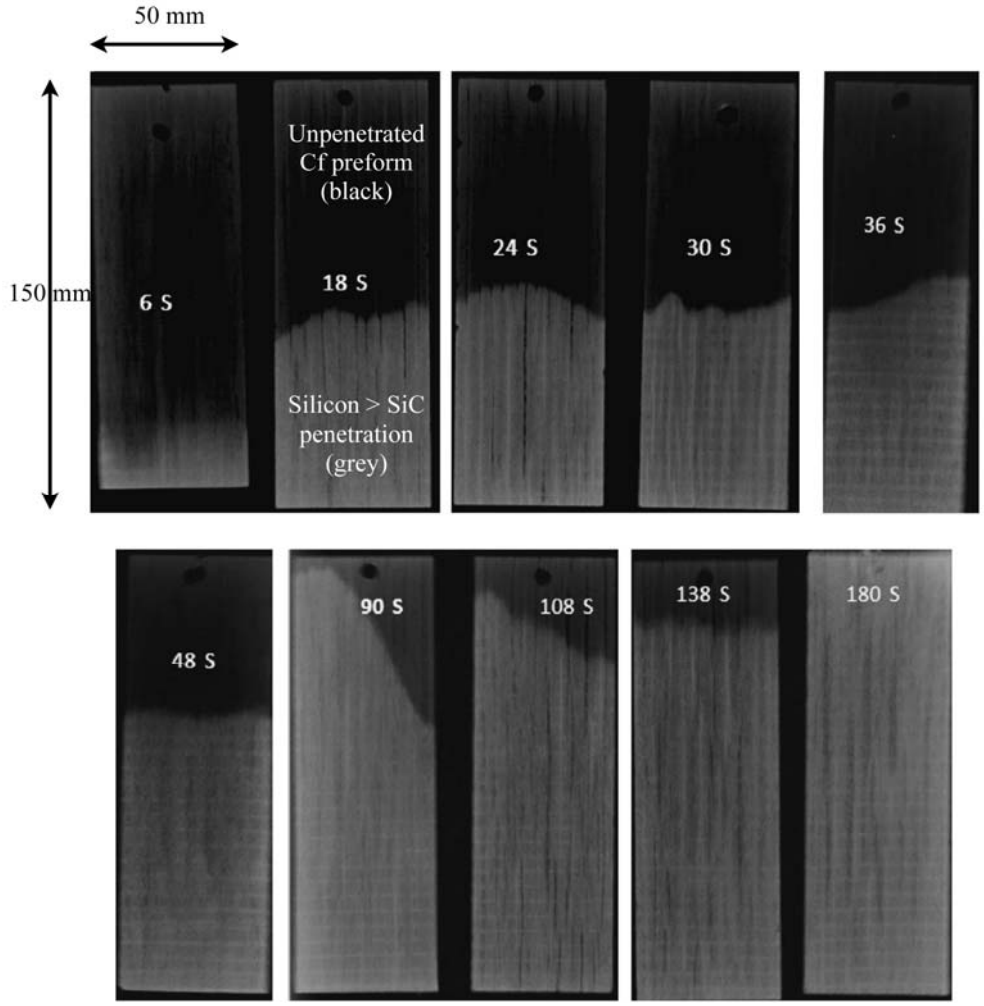

Fig. 13. X-Ray images of the C-SiC composite bars after each siliconisation time (seconds). The grey regions represent the infiltration and conversion height of the silicon into SiC. The black regions represent the non-infiltrated carbon fibre preform.

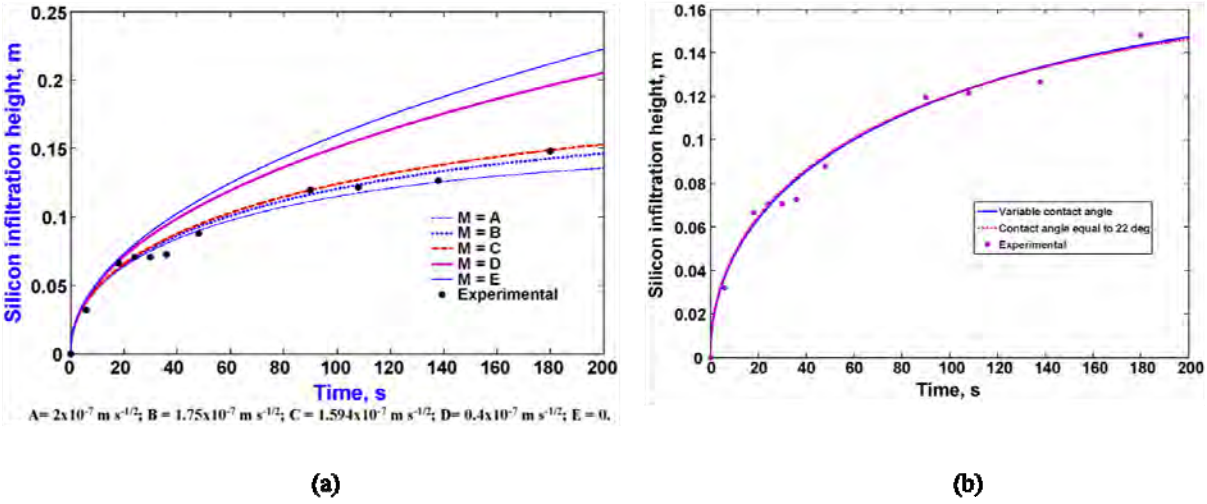

(a) (b)

Fig. 14. Graphs showing (a) Comparison of experimental and estimated silicon infiltration heights by modified Washburn equation (contact angle 22◦) and (b) Comparison of estimated heights obtained from variable angle of contact and contact angle = 22◦ for $M = 1.75 \times 10^{-7}$ m.s$^{-1/2}$.

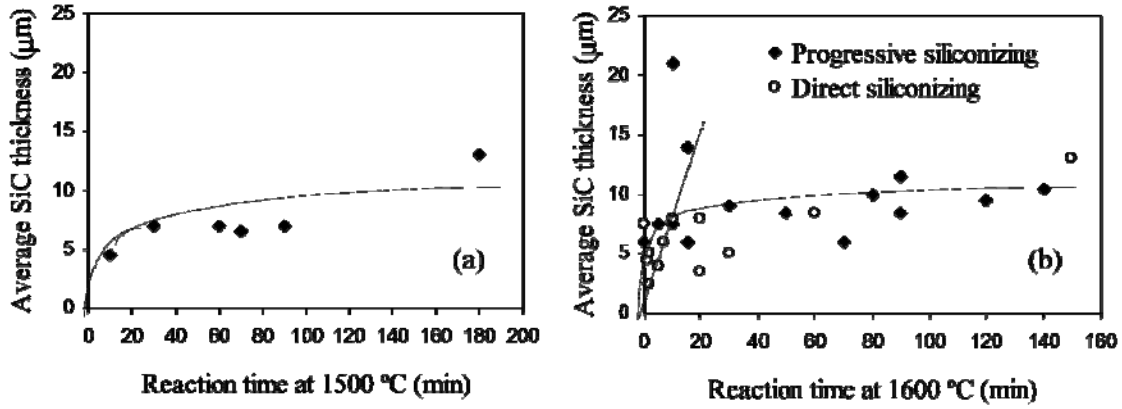

(a) (b)

Fig. 15. Graphs showing changes in the average SiC thickness at a reaction temperature of 1500°C with (a) increasing time (mins) and (b) direct or progressive LSI.

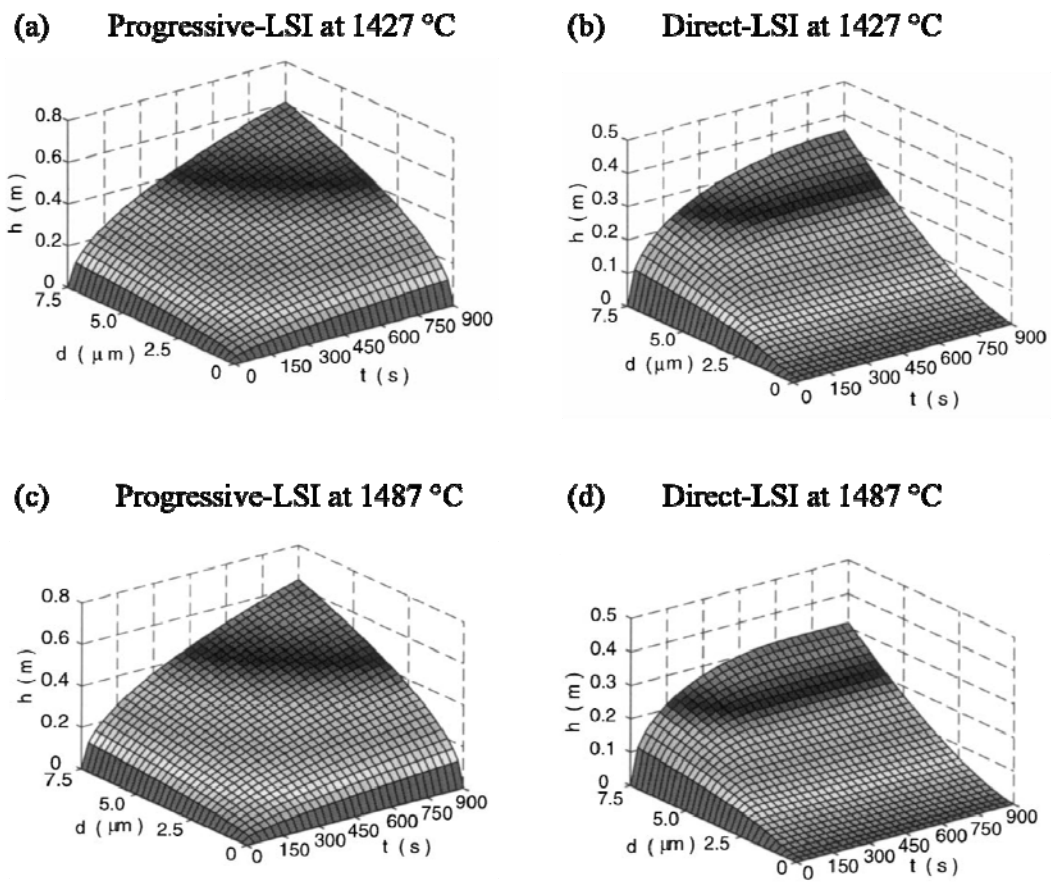

Fig. 16. Theoretical infiltration kinetics: height (m), diameter (µm) and time (seconds) of pure silicon into porous carbon preforms using progressive-LSI or direct-LSI at different temperatures.

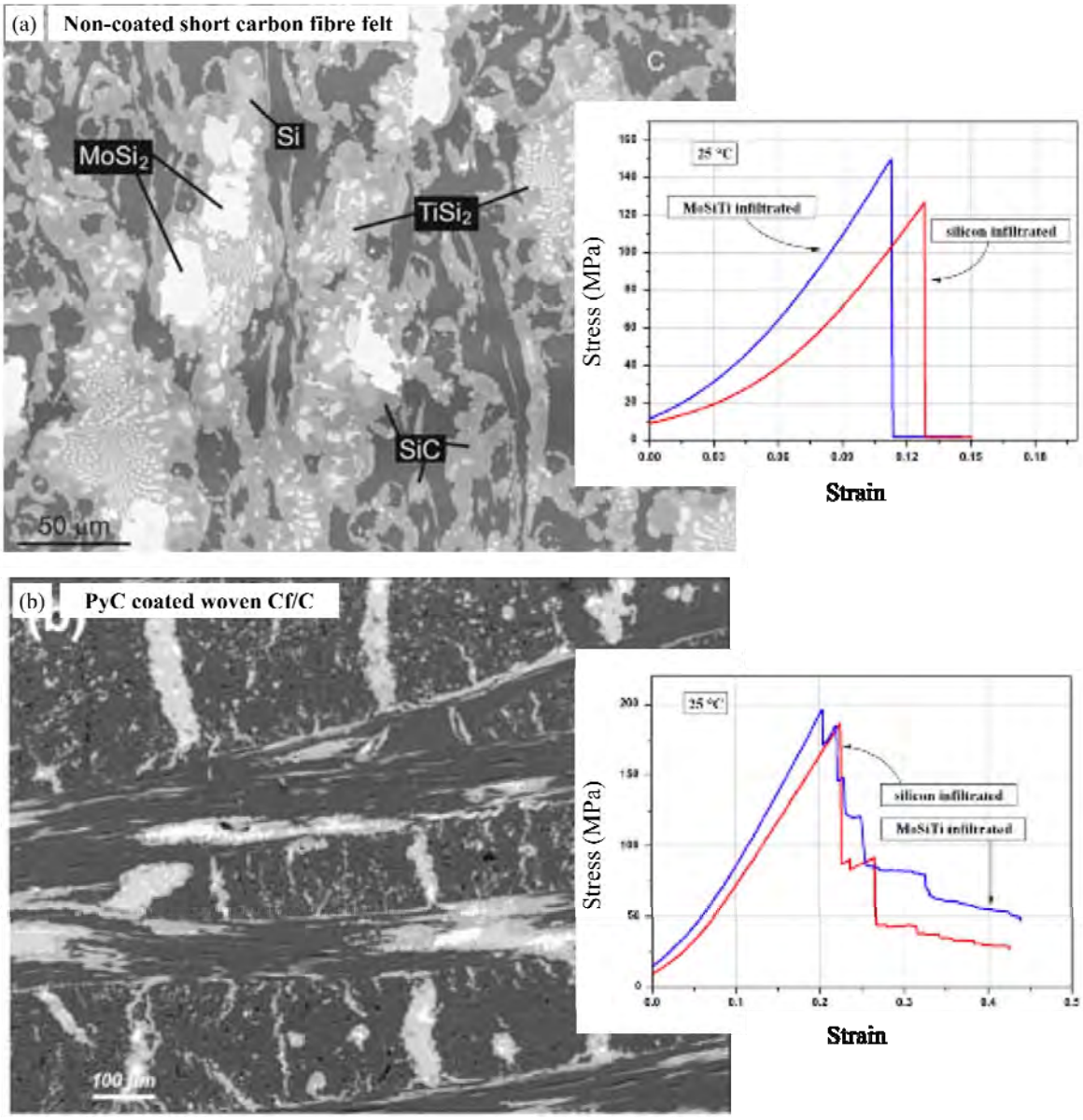

Fig. 17. SEM micrographs comparing C_f/MoSiTi composites with different architectures (a) Short carbon fibre felt and (b) Bi-directional woven C_f/C. Supporting bend strength stress-strain graphs comparing the C_f/MoSiTi composites (Blue) with traditional silicon infiltrated C_f/SiC composites (Red).

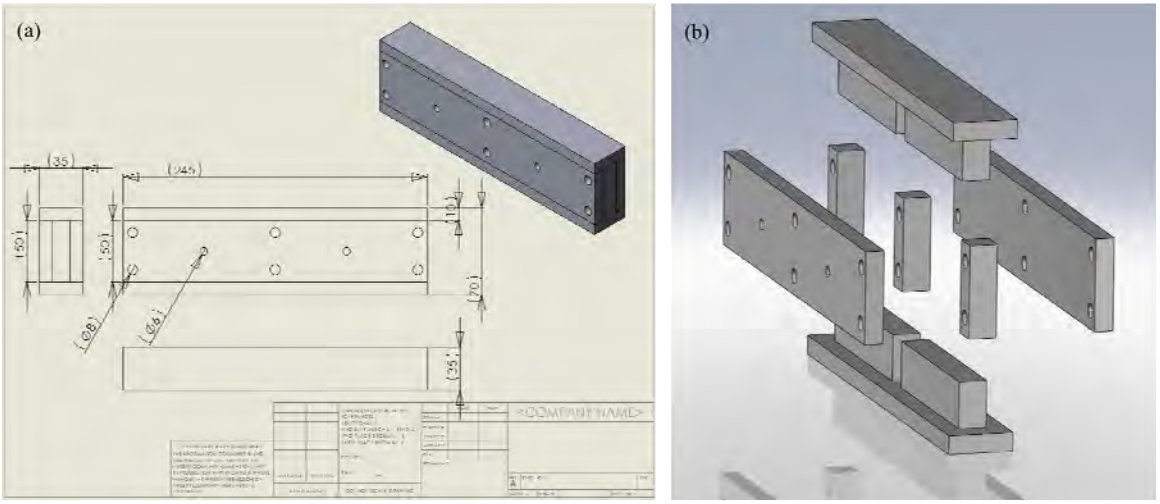

Fig. 18. Schematic of the steel modular die, showing (a) Three-orthographic views, dimensions and a 3D illustration, (b) Exploded view of the die.

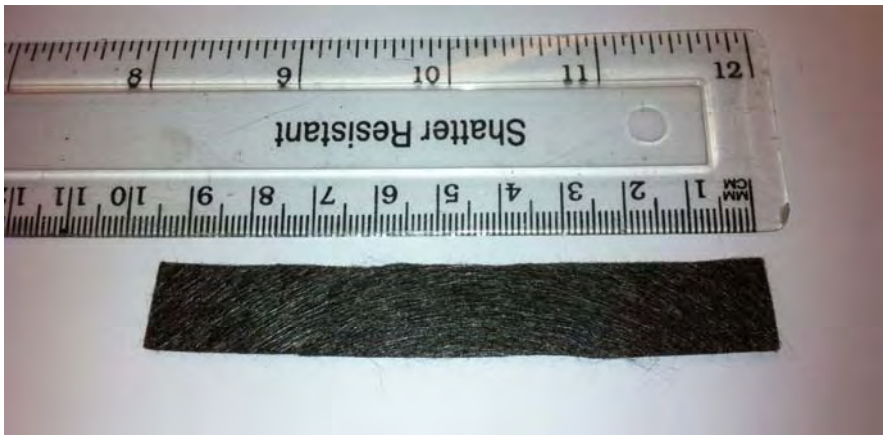

Fig. 19. Carbon fibre mat comprising short carbon fibres (SF), which are randomly orientated.

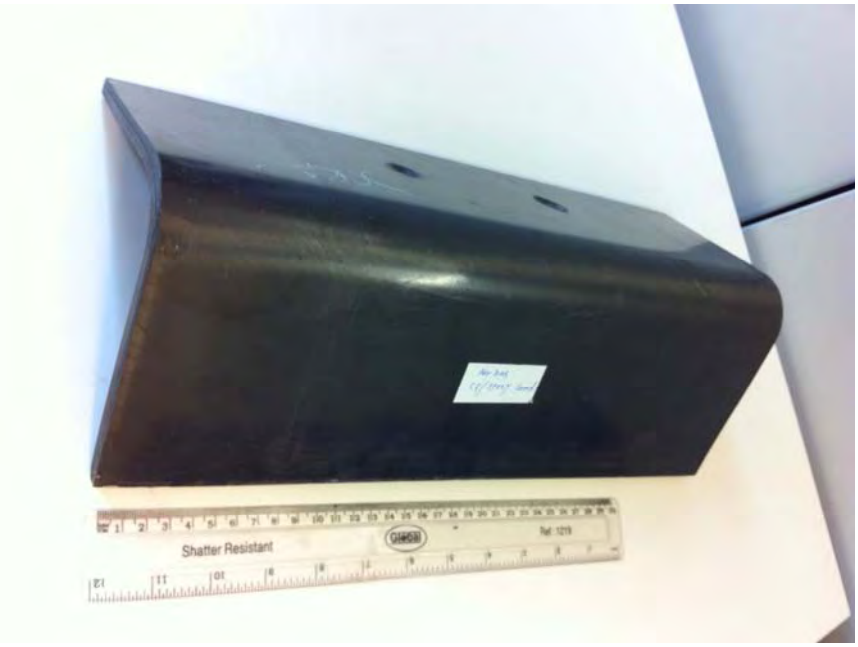

Fig. 20. Photograph of the cured CFRP spar.

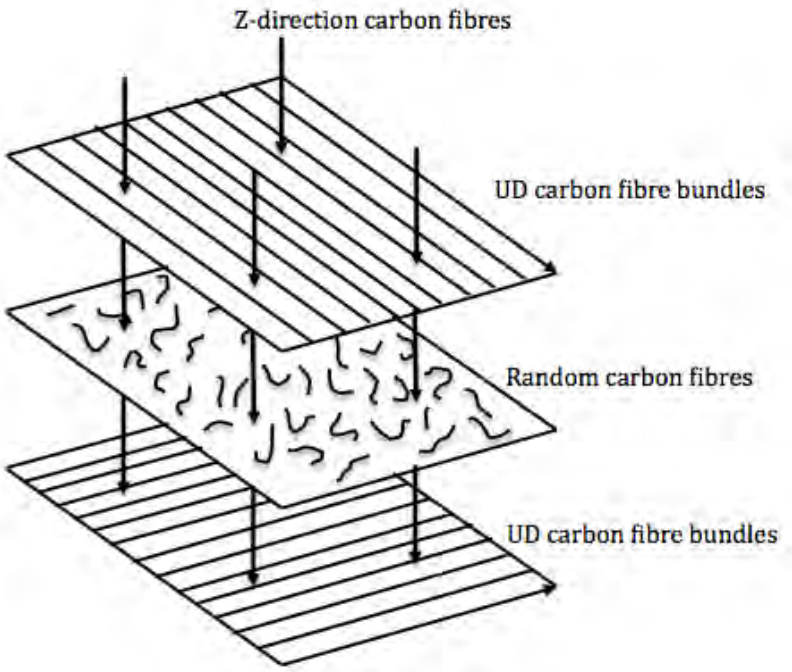

Fig. 21. Schematic of the 'ST' preform architecture. Random carbon fibre web in-between the two uni-directional carbon fibre layers.

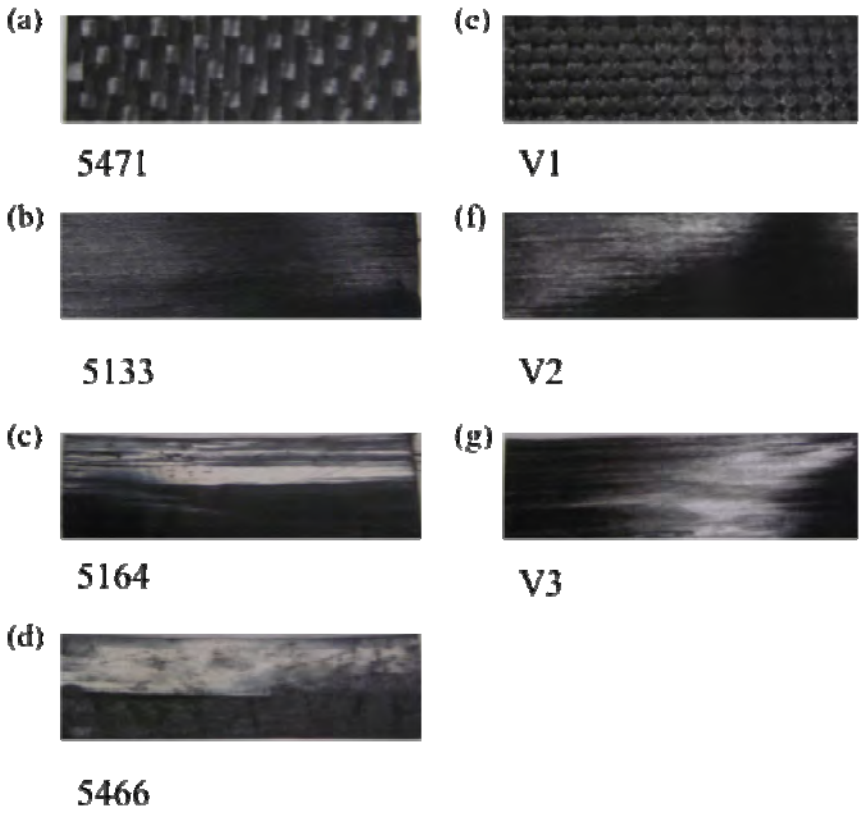

Fig. 22. Photographs of the carbon fibre pre-preg samples: (a). End-of-life woven pre-preg '5471', (b). End-of-life UD pre-preg '5133', (c). End-of-life UD pre-preg '5164', (d). End-of-life UD '5466', (e). Virgin woven pre-preg 'V1', (f). Virgin UD pre-preg 'V2', (g). Virgin UD preg-preg 'V3'.

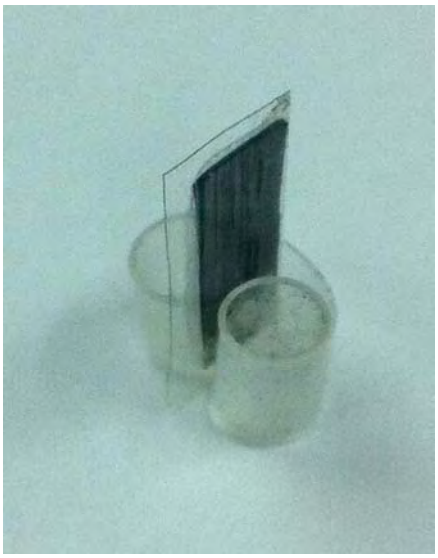

Fig. 23. Typical photograph of the pyrolysed carbon fibre pre-preg enveloped inside standard celotape and held by a plastic clip.

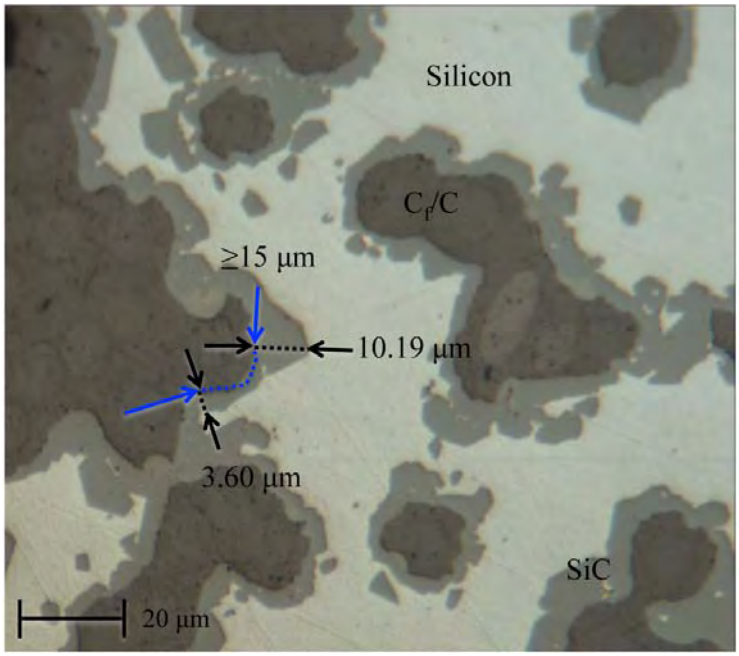

Fig. 24. Optical micrograph under polarized light of the CVI-Carbon sample illustrating how the SiC thickness statistical data was gathered.

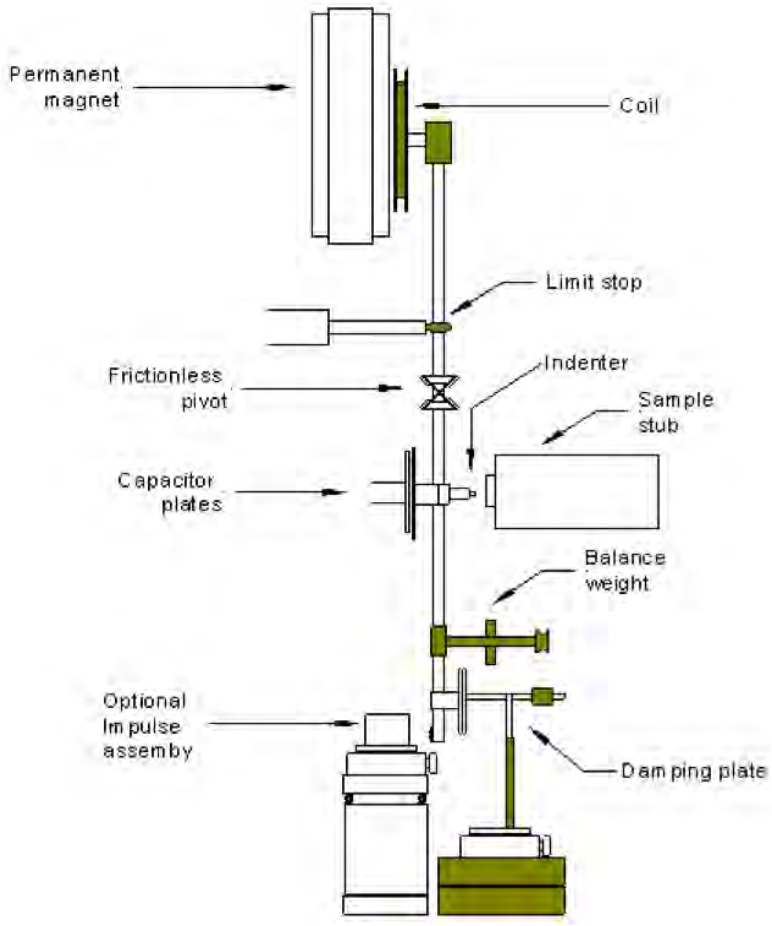

Fig. 25. Schematic of the nano-indenter assembly and all components.

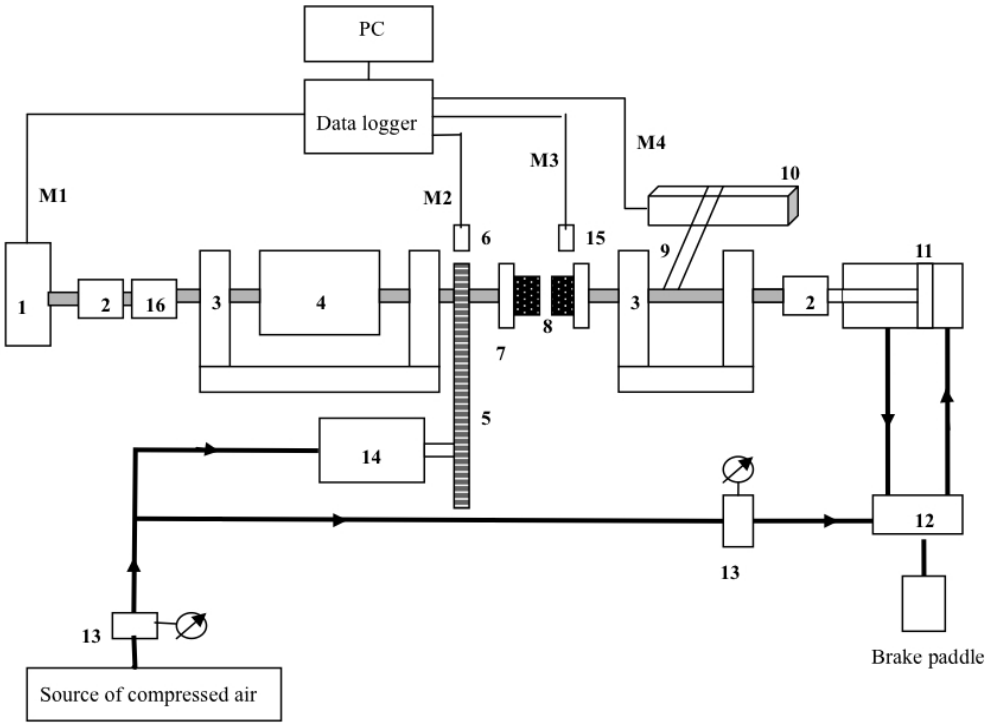

1. Axel load cell
2. Spacer
3. Stand
4. Fly wheel
5. Gear and belt
6. Speed sensor: angular
7. Sample jig/holder
8. Sample
9. Torque arm
10. Linear load cell
11. Pressure cylinder
12. Solenoid valve
13. Pressure valve
14. Air motor
15. Thermal couple
16. Bearing

M1. Break load sensor
M2. Angular speed sensor
M3. Temperature sensor
M4. Torque sensor

Fig. 26. Schematic of the small-scale air-powered dynamometer.

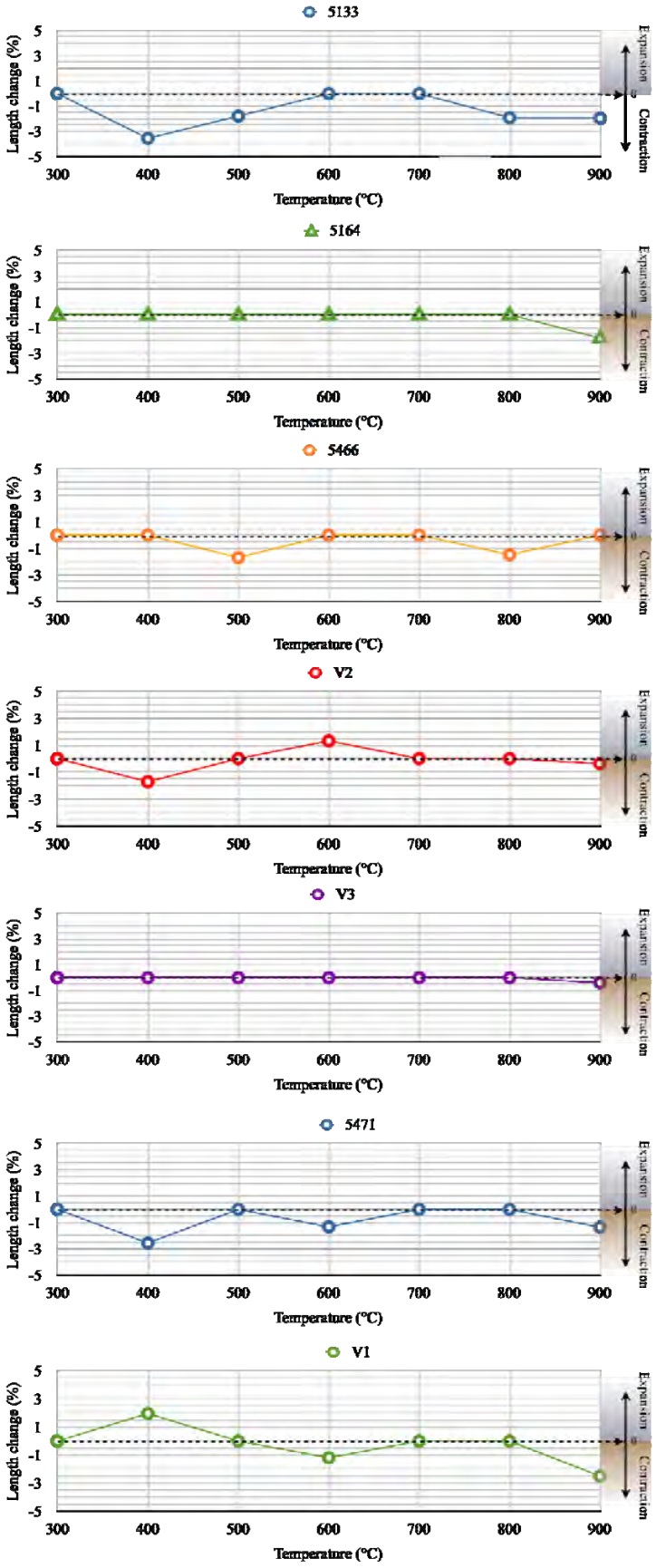

Fig. 27. Graphs illustrating the negligible length change of the UD pre-pregs as they were progressively pyrolysed from 300 to 900°C in 100°C steps for 30 minutes.

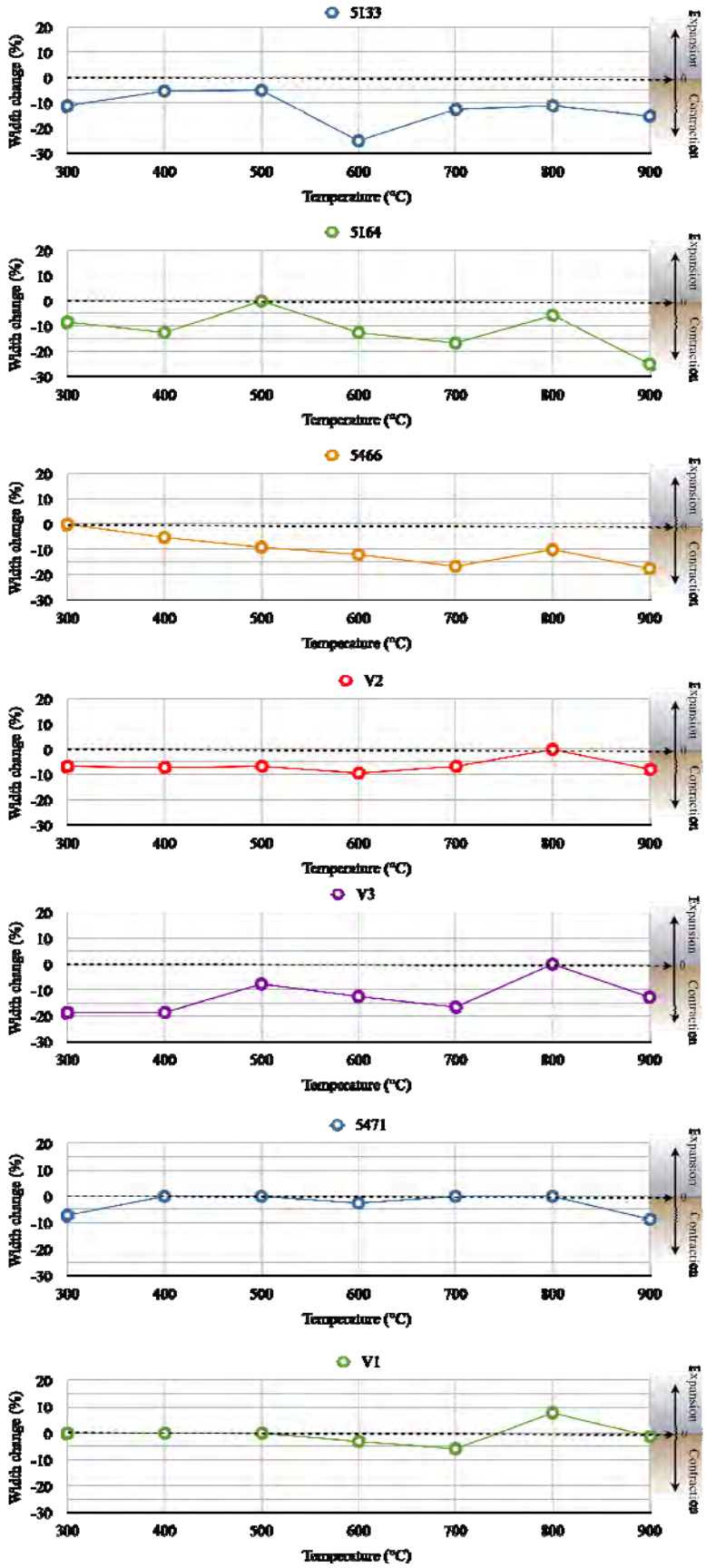

Fig. 28. Graphs illustrating the width change of the UD pre-pregs as they were progressively pyrolysed from 300 to 900°C in 100°C steps for 30 minutes.

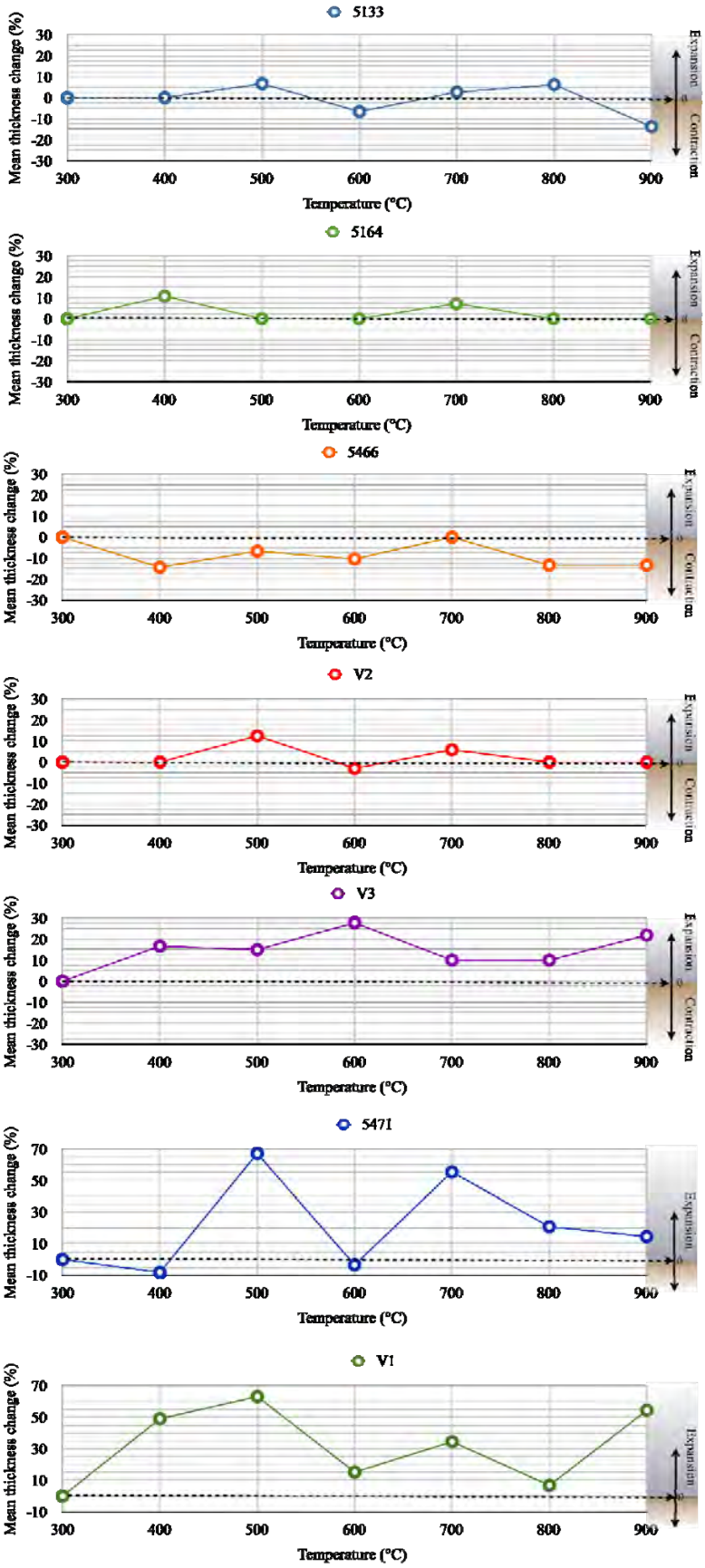

Fig. 29. Graphs illustrating the mean thickness change of the UD pre-pregs as they were progressively pyrolysed from 300 to 900°C in 100°C steps for 30 minutes.

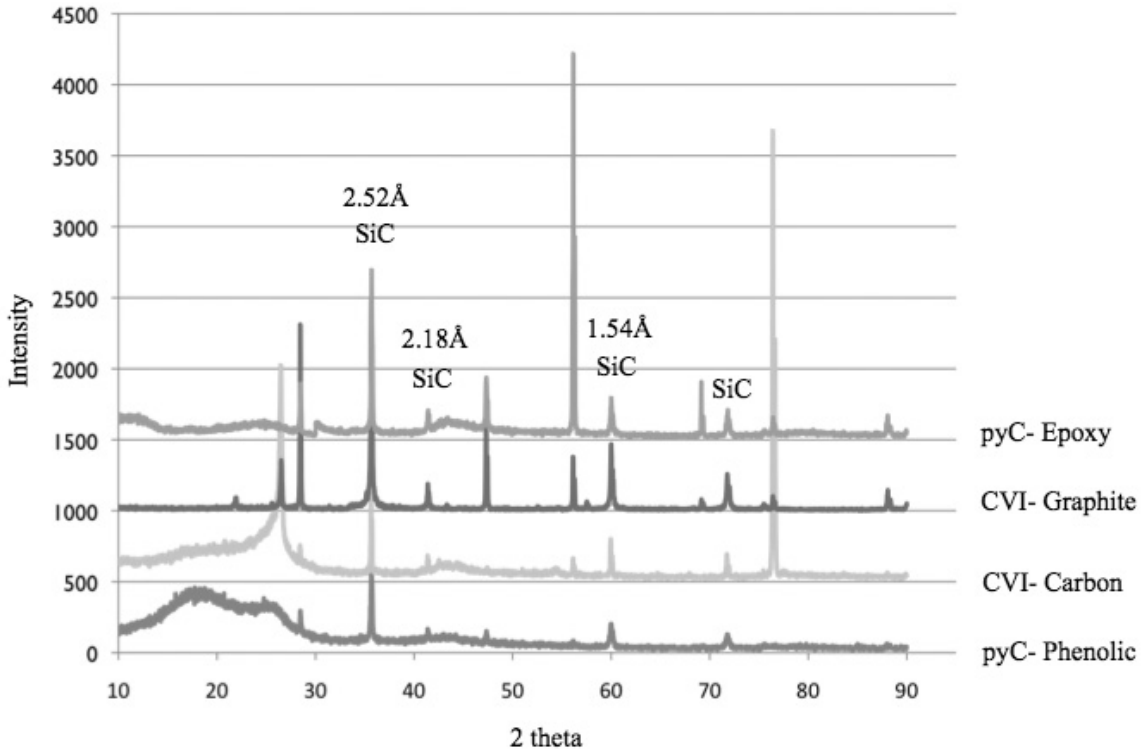

Fig. 30. XRD diffraction pattern of each sample. The four most prominent SiC peaks are highlighted, which correspond to 3C β-SiC.

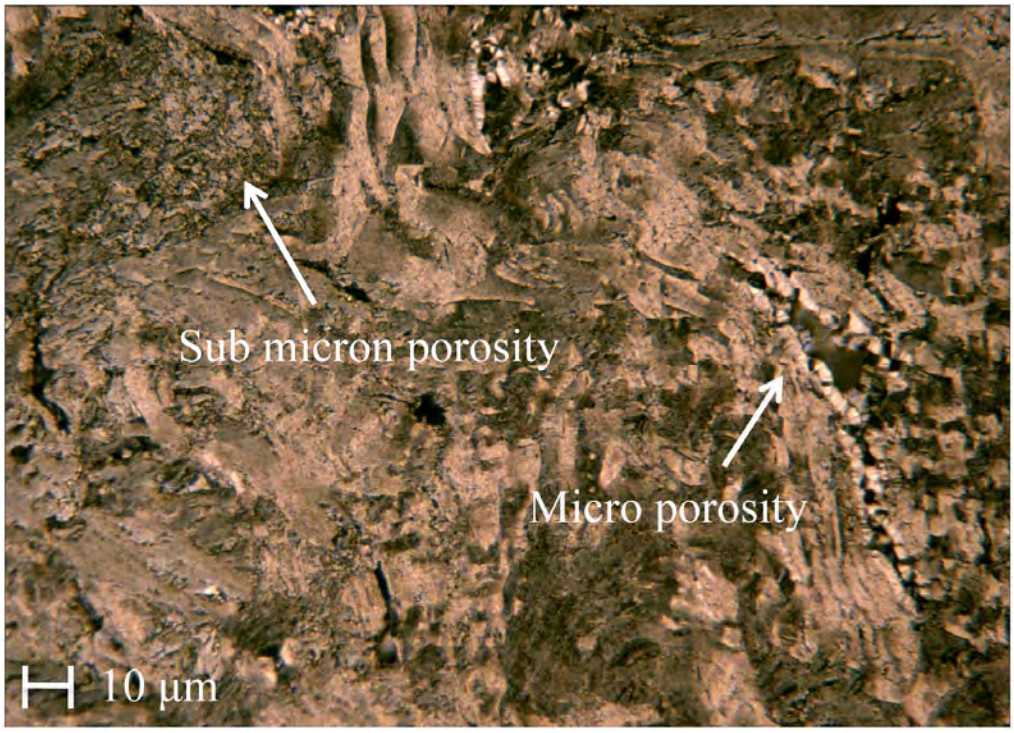

Fig. 31. Optical micrograph of the graphite sample at 400x magnification under polarised light conditions.

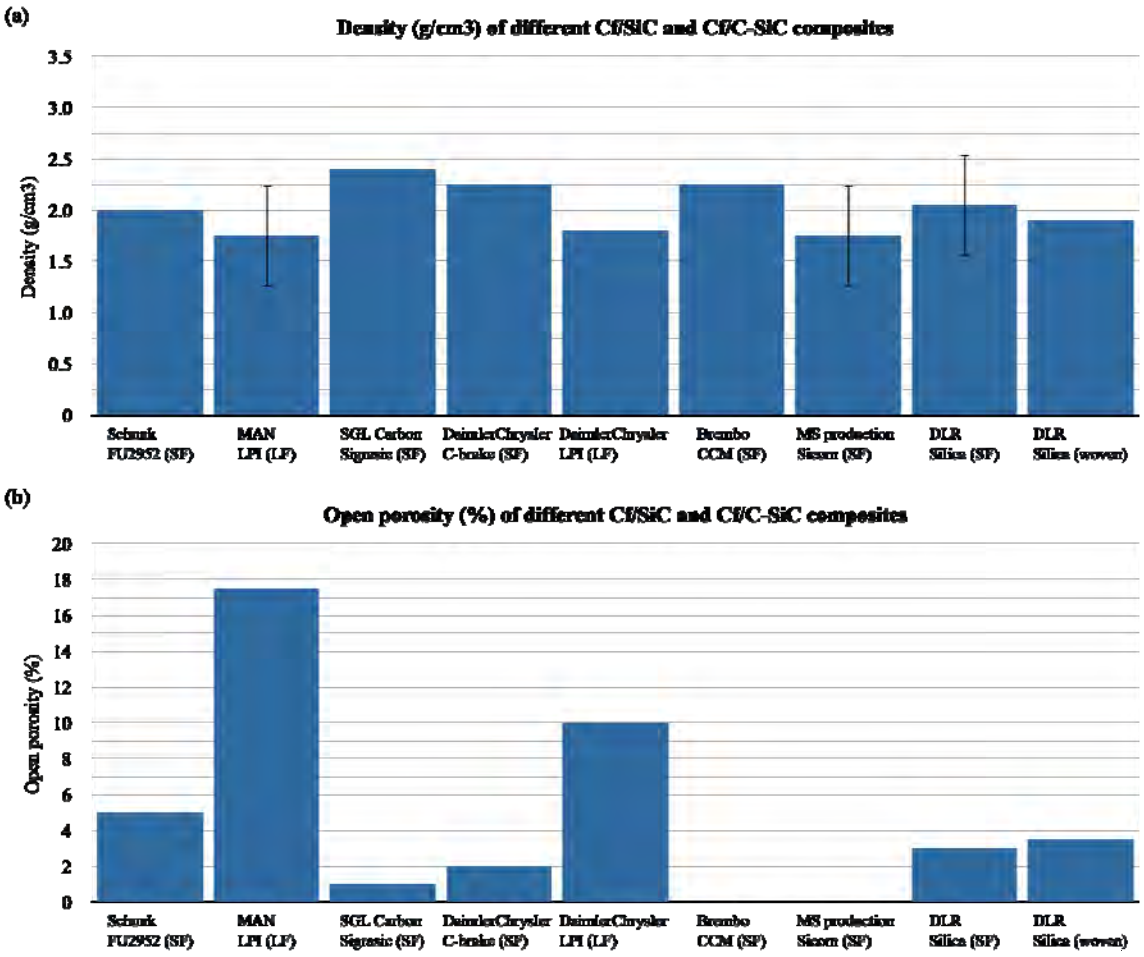

Fig. 32. Graphs showing (a) density (g/cm^3) and (b) open porosity (%) of different industry grade C_f/C-SiC composites. The annotations 'SF' and 'LF' refer to the fibre length: short and long respectively. No data was available for the 'Brembo' and 'MS production' porosities. Error bars represent the standard deviation.

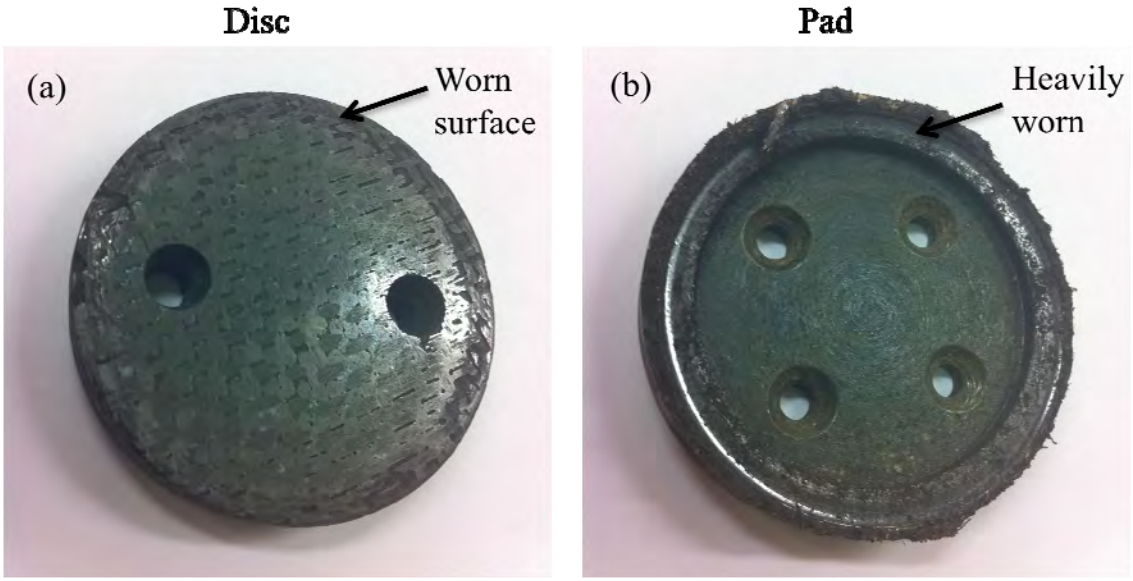

Fig. 33. Photographs of (a) 5471-50 and (b) industry standard pad mounted on a steel plate, illustrating the excessive wear of the pad and to a lesser degree, the disc after dynamometer testing.

Appendix B – Tables

Table 1. Influence of the type of woven architecture on the properties.

Property	Plain	Twill	Satin	Basket	Leno	Mock leno
Good stability	****	***	**	**	*****	***
Good drape	**	****	*****	***	*	**
Low porosity	***	****	*****	**	*	***
Smoothness	**	***	*****	**	*	**
Balance	****	****	**	****	**	****
Symmetrical	*****	***	*	***	*	****
Low crimp	**	***	*****	**	**/*****	**

***** = excellent, **** = good, ***= acceptable, ** = poor, * = very poor

Table 2. Typical properties of PAN and Pitch-derived carbon fibres.

Fibre	Type	Typical diameter (μm)	Density (g/cm^3)	Tensile modulus (GPa)	Tensile strength (GPa)	Strain-to-failure (%)	Coefficient of thermal expansion (10^{-6}/ºC)
T-300	PAN	7 (round)	1.76	231	3.65	1.4	0.6 longitudinal 7-12 radial
AS-1		8 (round)	1.8	228	3.1	1.32	-
AS-4		7 (round)	1.8	248	4.07	1.65	-
IM-7		5 (round)	1.78	301	5.31	1.81	-
HMS-4		8 (round)	1.8	345	2.48	0.7	-
GY-7		8.4 (bilobal)	1.96	483	1.52	0.38	-
P-55	Pitch	10	2	380	1.9	0.5	1.3 (longitudinal)
P-100		10	2.15	758	2.41	0.32	1.45 (longitudinal)

Note: Fibre AS-4 is the fibre used in the Airbus UK MMR samples: 5471, 5164, 5133 and 5466.

Table 3. Properties of commercial PAN-derived carbon fibres. Data from manufacturers data sheets.

Grade	Tensile Modulus (GPa)	Tensile Strength (GPa)	Country
Standard Modulus (<265GPa) (also known as 'High Strength')			
T300	230	3.53	France/Japan
T700	235	5.3	Japan
HTA	238	3.95	Germany
UTS	240	4.8	Japan
34-700	234	4.5	Japan/USA
AS-4	**241**	**4**	**USA**
T650-35	241	4.55	USA
Panex 33	228	3.6	USA/Hungary
F3C	228	3.8	USA
TR50S	235	4.83	Japan
TR30S	234	4.41	Japan
Intermediate Modulus (265-320GPa)			
T800	294	5.94	France/Japan
M30S	294	5.49	France
IMS	295	4.12-5.5	Japan
MR40/MR50	289	4.4-5.1	Japan
IM6/IM7	303	5.1-5.3	USA
IM9	310	5.3	USA
T650-42	290	4.82	USA
T40	290	5.65	USA
High Modulus (320-440GPa)			
M40	392	2.74	Japan
M40J	377	4.41	France/Japan
HMA	358	3	Japan
UMS2526	395	4.56	Japan
MS40	340	4.8	Japan
HR40	381	4.8	Japan
Ultra High Modulus (~440GPa)			
M46J	436	4.21	Japan
UMS3536	435	4.5	Japan
HS40	441	4.4	Japan
UHMS	441	3.45	USA

Table 4. Features and parameters affecting the properties of carbon fibre.

Structural feature	Controlling parameters	Properties	
		Increase	Decrease
Increasing orientation of basal planes parallel to the fibre axis	Fibre drawing, fibre structure, restraint against shrinkage during heat treatment	Longitudinal strength, modulus and longitudinal negative CTE	Transverse strength and modulus
Increasing crystallinity (larger and perfect crystals)	Precursor chemistry & heat treatment	Thermal conductivity, longitudinal negative CTE and oxidation resistance	Longitudinal tensile and compressive strength, transverse strength and modulus
Decreasing defect content	Precursor purity & fibre handling	Tensile strength, thermal conductivity and oxidation resistance	-

Table 5. Physical properties of liquid silicon.

Property	Symbol	Unit	Value
Density	P	g/cm^3	2.33 to 2.34 (20ºC) 2.53 to 2.55 (1420ºC)
Surface tension	Σ	N/m	0.72 to 0.75 (1550ºC)
Wetting angle	Θ	-	0 to 22 (versus C/vacuum) 30 to 41 (versus SiC/vacuum)
Dynamic viscosity	η	Pa.s	$5.10x10^{-4}$ to $7.65x10^{-4}$ (1440ºC) $4.59x10^{-4}$ to $6.38x10^{-4}$ (1560ºC)

Table 6. Mechanical property comparison of different recycling techniques.

Property	Unit	As-received carbon fibre	Treated carbon fibre	
		Manufacturer data	Fluidised bed fibres	Microwave fibres
Tensile strength	GPa	4.5	3.05	3.26
Tensile modulus	GPa	234	243	210

Table 7. Composition of the Hexply™ '8552' epoxy resin.

Composition	Also known as	Chemical data	Quantity (%) Min.	Max
Dapsone Diamino-diphenyl-sulphone	DDS	$C_{12}H_{12}N_2O_2S$	1 10	15 30
Tetraglycidyl methylene dianiline	TGMDA	-	15	40
Triglycidyl-p-aminophenol	TGPAP	-	15	40

Table 8. Composition of the 'Cellobond J2027L' phenolic resin.

Composition	Also known as	Chemical formulation	Quantity (%) Min.	Max
Phenol	Carbolic acid	-	7	10
Formaldehyde	-	H_2CO	2	3

Table 9. Estimated mass change (%) of each pre-preg after 30 minutes pyrolysis at each temperature (°C).

Pre-preg sample	Mass change (%) at each temperature (°C) 300	400	500	600	700	800	900
5133	0.75	18.14	22.17	25.00	25.42	25.23	26.73
5164	0.34	20.26	18.82	23.12	22.87	25.16	29.18
5466	0.45	15.16	24.07	22.90	25.08	24.59	25.54
5471	1.35	24.26	26.07	23.82	24.11	25.39	25.39
V1	0.94	36.63	40.23	41.64	42.24	36.35	43.48
V2	1.32	28.40	23.16	32.80	30.12	31.91	29.29
V3	0.93	24.85	26.13	20.84	22.01	20.68	28.22

Table 10. Estimated mass change of pre-preg '5471' after repeated pyrolysis for 30 minutes at 500°C.

No.	Mass change (g) of '5471' at Before	After	Mass change (%)
1	0.1889	0.1430	-24.30
2	0.2063	0.1573	-23.75
3	0.1804	0.1362	-24.50
4	0.2224	0.1698	-23.65
5	0.1994	0.1503	-24.62
6	0.2076	0.1587	-23.55
7	0.1786	0.1359	-23.91
Mean			**-24.04 ±0.43**

Table 11. Estimated mass change of pre-preg '5471' after repeated pyrolysis for 30 minutes at 700°C.

No.	Mass (g)		Mass change (%)
	Before	After	
1	0.1790	0.1335	-25.42
2	0.1734	0.1293	-25.43
3	0.1826	0.1367	-25.14
4	0.1678	0.1250	-25.51
5	0.1726	0.1290	-25.26
6	0.1822	0.1363	-25.19
7	0.1815	0.1351	-25.56
Mean			**-25.36 ±0.16**

Table 12. Estimated mass change of pre-preg '5471' after repeated pyrolysis for 30 minutes at 900°C.

No.	Mass (g)		Mass change (%)
	Before	After	
1	0.2071	0.1533	-25.98
2	0.2009	0.1489	-25.88
3	0.1963	0.1443	-26.49
4	0.2036	0.1512	-25.74
5	0.2085	0.1539	-26.19
6	0.1974	0.1446	-26.75
7	0.1999	0.1487	-25.61
Mean			**-26.09 ±0.41**

Table 13. Estimated length change (%) of each pre-preg after 30 minutes at each temperature (°C).

Pre-preg sample	Length change (%) at each temperature (°C)						
	300	400	500	600	700	800	900
5133	0.00	-3.56	-1.79	0.00	0.00	-1.92	-1.96
5164	0.00	0.00	0.00	0.00	0.00	0.00	-1.83
5466	0.00	0.00	-1.69	0.00	0.00	-1.47	0.00
V2	0.00	-1.72	0.00	1.32	0.00	0.00	-0.38
V3	0.00	0.00	0.00	0.00	0.00	0.00	-0.39
5471	0.00	-2.56	0.00	-1.33	0.00	0.00	-1.36
V1	0.00	1.96	0.00	-1.19	0.00	0.00	-2.50

Table 14. Estimated width change (%) of each pre-preg after 30 minutes at each temperature (°C).

Pre-preg sample	Width change (%) at each temperature (°C)						
	300	400	500	600	700	800	900
5133	-11.11	-5.26	-5.00	-25.00	-12.50	-11.11	-15.22
5164	-8.33	-12.50	0.00	-12.50	-16.67	-5.66	-25.02
5466	0.00	-5.26	-9.09	-12.00	-16.67	-10.00	-17.57
V2	-6.67	-7.14	-6.67	-9.38	-6.67	0.00	-7.89
V3	-18.75	-18.69	-7.69	-12.50	-16.67	0.00	-12.79
5471	-7.14	0.00	0.00	-2.56	0.00	0.00	-8.70
V1	0.00	0.00	0.00	-3.13	-5.88	7.69	-1.20

Table 15. Estimated mean thickness change (%) of each pre-preg after 30 minutes at each temperature (°C).

Pre-preg sample	Mean thickness change (%) at each temperature (°C)						
	300	400	500	600	700	800	900
5133	0.00	0.00	6.67	-6.67	2.67	6.21	-13.79
5164	0.00	10.71	0.00	0.00	7.14	0.00	0.00
5466	0.00	-14.29	-6.67	-10.34	0.00	-13.33	-13.33
V2	0.00	0.00	12.50	-3.03	5.88	0.00	0.00
V3	0.00	16.67	15.00	27.78	10.00	10.00	21.90
5471	0.00	-8.10	67.05	-3.39	55.34	20.85	14.60
V1	0.00	49.10	63.16	15.20	34.50	6.78	54.47

Table 16. Average composition by volume (%) of the phases inside C_f/C-SiC composites with different architectures and fibre origins.

Average volume fraction (%)	2.5D: CVI-C	Non-woven: PIP-LSI	2D: PIP-C	UD: PIP-C
C_f/C	43.07	45.23	29.68	63.53
SiC	30.12	14.12	44.78	22.35
Silicon	22.92	5.10	17.43	9.17
Voids	3.90	35.55	8.10	4.95

Table 17. d-spacing's measured by X-ray diffraction.

Sample	Measured 2θ	h	k	l	Measured, d (Å)
CVI-Carbon	35.64	1	1	1	2.52
	42.28	2	0	0	2.14
	59.96	2	2	0	1.54
Graphite	35.66	1	1	1	2.52
	41.40	2	0	0	2.18
	59.96	2	2	0	1.54
PyC-Phenolic	35.28	1	1	1	2.54
	41.26	2	0	0	2.19
	59.20	2	2	0	1.56
PyC-Epoxy	35.66	1	1	1	2.52
	41.42	2	0	0	2.18
	59.98	2	2	0	1.54

Table 18. Nano-scale hardness (GPa) of different C_f/C-SiC composites.

Hardness (GPa)	CVI-C C_f/C-SiC	PIP-Phenolic C_f/C-SiC	PIP-Epoxy C_f/C-SiC
Carbon fibre	2.30	5.76	5.12
PyC	2.77	5.18	6.12
SiC	29.18	27.40	34.76
Silicon	11.11	10.25	12.52

Table 19. Nano-scale Young's modulus, E (GPa) of different C_f/C-SiC composites.

Young's modulus, E (GPa)	CVI-C C_f/C-SiC	PIP-Phenolic C_f/C-SiC	PIP-Epoxy C_f/C-SiC
Carbon fibre	21.27	43.02	45.32
PyC	24.39	39.75	46.54
SiC	379.95	403.55	525.28
Silicon	193.95	180.54	208.67

Table 20. Nano-scale fracture toughness (MPa.m$^{1/2}$) of different C_f/C-SiC composites.

Fracture toughness (K_{1C})	CVI-C C_f/C-SiC	PIP-Phenolic C_f/C-SiC	PIP-Epoxy C_f/C-SiC
SiC	0.71	1.07	1.16
Silicon	0.58	0.66	0.54